IN-PROCESS MONITORING OF FORMULATED PRODUCT MANUFACTURING

By

Giuseppe Forte

A thesis submitted to the School of Chemical Engineering at the University of Birmingham for the degree of

DOCTOR OF ENGINEERING (EngD)

School of Chemical Engineering

College of Engineering and Physical Sciences

University of Birmingham

B15 2TT

September 2019

UNIVERSITY OF BIRMINGHAM

University of Birmingham Research Archive

e-theses repository

Abstract

The implementation of smart manufacturing and digitisation on industrial plants is undergoing rapid development. One of the enablers of this innovation process is the availability in real time of data accurately describing the manufacturing process: inline measurement techniques. This study investigated sensing techniques characterised by low cost, fast response and non-invasiveness, with the aim to apply them to Johnson Matthey production lines.

Among the investigated methods, Electrical Resistance Tomography was used for fluid mixing operations. This technique was applied for multiphase mixing detection, both in a stirred tank (gas-liquid) and in a pipeline (liquid-liquid), allowing to gather quantitative information over mixing performance.

Acoustic Emission was used to characterise gas-liquid mixing regimes within a stirred tank. The data processing was carried out employing machine learning algorithms to correlate the acquired signal with the operating fluid regime. Obtained results suggest the potential of Acoustic Emission in monitoring mixing processes.

Electrical Capacitance Tomography was investigated as a tool for interface detection and powder mixing monitoring. A data processing approach, alternative to the traditional thresholding, was developed to identify boundaries between phases and applied to Johnson Matthey processes.

This work has made step forwards within the process analytics technology application in the chemical industry.

Acknowledgements

Firstly, I would like to thank the EPSRC, Johnson Matthey, and the University of Birmingham for funding and giving me the opportunity to take part in this program.

This book is the result of 4 years of work, persistence and sacrifice which would have been impossible to achieve without the contribution of a bunch of great people around me. It is my pleasure to acknowledge them here.

Hugh, thanks for the trust, the esteem and the guidance. You have provided me with both direction and space to learn, grow and improve as a researcher. Mark, I am grateful for the continual encouragement and the long-distance support. Thanks also for never giving up on editing my ever-expanding sentences. I am immensely grateful to both of you for allowing me to work flexibly when my family needed me most.

Fede, thanks for encouraging me to start this adventure and for both providing technical advice and keeping morale high. I cannot list here all the fun we had with our trips around the world; from Puerto to Chicago. Thanks for a friendship that will certainly outlast this EngD.

The EngD program would not exist without you, Richard. Thanks for making sure everything was running smoothly and showing enthusiasm every time I came up with a new exotic conference proposal.

To all the people in JM that have helped me during these years, my deepest thanks. I have learned a lot throughout this experience from each interaction, discussion and collaboration. I would like to thank Bev and Lynn for being essential within JM. To my JM friends Michele, Giuseppe (the other), Andrea, Tom, Javier and Becca I have enjoyed spending time together, discussing both work and more casual affairs that have made this adventure richer. In

particular, to Domenico and Alessandro, the Sabini; I cannot picture how these four years would have been without your friendships. To Rosita and Graziano, my piece of family and home breathe in the UK.

To the people that have actively contributed to this work, Peter, Phil, Andrea, Matteo, Michele, Goce, James, Simona thank you for your invaluable help.

To my family and my close friends for being my first supporters and my motivators; to Andrea, for being there, always; to my grandparents Angelo, Giovanna and Nunzia who have given away their time for me, an immense thank you. This goal is also yours.

No book is worth reading if you cannot find love in it. If the reader does find it in these pages, the merit is yours Rossana. If that is not the case, then I must have kept it too close to me (sorry!). It has inspired me every day.

To my sister Gabri, for her ability to smile (when she wants), even over the phone, and for being a piece of me, thank you.

To my mom Franca and dad Franco, no words can do justice for how much you taught me. Your strength is mine, we achieved this together. It is to you that I dedicate this doctoral thesis, with all the love and affection I am capable of.

Table of Contents

List of Figures:

Figure 7.3 – Block diagram representing the catalyst converter production process (a). And a pictorial representation of the coating process on the line (b): a bare substrate is placed on the coating bench by a robot (1), then a controlled quantity of washcoat is placed on top (2) and pulled through the channels applying a vacuum from the bottom of the part (3); the part is then weighed (4) and is dryied with hot air (5). Some parts are sampled before drying for X-ray measurements of the dosing length (4') and if

List of tables:

List of abbreviations:

2D	Two-Dimensional
3D	Three-Dimensional
AE	Acoustic emission
AGT	Advanced Glass Technology
AI	Artificial Intelligence
API	Active Pharmaceutical Ingredient
AT	Aluminium Titanate
BFE	Basic Flowability Energy
BU	Business Unit
CARPT	Computer Automated Radioactive Particle tracking
CBD	Conditioned Bulk Density
CCPS	cyber-physical production system
CFD	Computational Fluid Dynamics
CMC	Carboxymethylcellulose
CPU	Core Processing Unit
CT	Computer Tomography
DAS	Data Acquisition System
DEM	Discrete Element Method
DNS	Direct Numerical Simulation
DPF	Diesel Particulate Filters
ECT	Electrical Capacitance Tomography
EngD	Engineering Doctorate
ENR	Efficient Natural Resources
ERR	Electrical Resistance Rheometry
ERT	Electrical Resistance Tomography
FEM	Finite Element Method
FIR	Flow Index Rate
FT	Flow through
FTSE	Financial Times Stock Exchange
G/L	Gas/liquid
GPF	Gasoline Particulate Filters

G-S-L	Gas-Solid-Liquid
GUI	Graphic User Interface
HB	Herschel-Bulkley
IPA	Isopropyl alcohol
IR	Infrared
ITS	Industrial Tomography Systems
JM	Johnson Matthey
JMTC	Johnson Matthey Technology Centre
k-NN	k-nearest neighbors
LBP	Linear Back Projection
LDA	Laser Doppler Anemometry
MF	Main flow
ML	Machine Learning
MMTC	Multi-Modality Tomography Configurator
MRI	Magnetic Resonance Imaging
MSBP	Modified Standard Back Projection
NIR	Near Infrared
NMR	Nuclear Magnetic Resonance
NN-MOIRT	Neural Network Multi-criteria Optimization Image Reconstruction Technique
NOSER	Newton One-Step Error Reconstruction
NOx	Nitrogen Oxides
OEM	Original equipment manufacturer
PAT	Process Analytical Technology
PCA	Principal Component Analysis
PE	Polyethylene
PEEK	Polyether ether ketone
PEPI	Positron Emission Particle Imaging
PEPT	Positron Emission Particle Tracking
PET	Positron Emission Tracking
PGM	Platinum Group Metals
PIV	Particle Image Velocimetry
PL	Power Law

PLIF	Planar Laser Induced Fluorescence
PM	Particulate Matter
PMMA	PolyMethyl Methacrylate
PSD	Particle Size Distribution
RDT-6	Rushton Disc Turbine (6 blades)
S/L	Solid in Liquid
SE	Specific Energy
SEM	Scanning Electron Microscope
SF	Secondary flow
SI	Stability Index
SiC	Silicon carbide
SOx	Sulphur Oxides
SR	Size ratio
SVM	Support Vector Machine
USD	United States Dollar
UV	Ultra-violet
VOC	Volatile Organic Compounds
Vvm	Volume per Volume per minute

All nomenclature is given within the single chapters with appropriate definitions and units.

1.
Introduction and Business case

1.1 Project Context

The concept of "Industry 4.0" or smart manufacturing has recently undergone intense scrutiny by manufacturing industry and is close to becoming a reality (Kusiak, 2018). Industry 4.0 integrates data generation, automation, cloud computing and high-sensitive analytics driving a new control and manufacturing platform that is being implemented on modern plant (Hermann et al., 2016; Kagermann et al., 2013). Digitalised manufacturing industries of the future are forecast to become modular structures equipped with cyber-physical systems to monitor physical processes and promote instantaneous and effective communication, facilitating information exchange and decision making. The ultimate vision of Industry 4.0 sees future industrial companies fully digitalized, creating global networks through which machinery, factories and different divisions connect and share information, influencing each other actions (Lasi et al., 2014). The advantages of this approach are improvements in quality control, leaner supply chain and reduction of waste but will also integrate the customer experience (McKinsey & Company, 2016).

The capability of generating large amounts of data rapidly forms the basis of this revolutionary trend. Awareness of the importance of data has increased so that companies at the forefront of this process are tackling business problems with a whole new mentality. Recently, a survey was carried out by Microstrategy Analytics and Mobility (Microstrategy, 2018) globally across more than 500 professionals working in analytics and intelligence industries. Of the interviewed sample, 57% (60% for UK) declared that their company has a

Chief Data Officer (CDO); 64% (59% for UK) of enterprise organisations stated that over the current year they had planned to invest more in data analytics structure and personnel. It is, hence, undoubtable and inevitable that manufacturing companies are equipping themselves to face the "Fourth Industrial Revolution" (Schwab, 2016).

As well as an improved management of data, the process involves increasing the quality and the speed at which information from production lines are available to the controller and operators. Indeed, one of the challenges that industries are facing is the improvement of current process analytic technologies (PAT) that could offer relevant information on the process in real time and without being invasive. The ease with which existing facilities can be retrofitted with new PAT is also an important consideration. Unlike the previous industrial revolution, this process will not lead to a huge replacement of existing equipment (Figure 1.1).
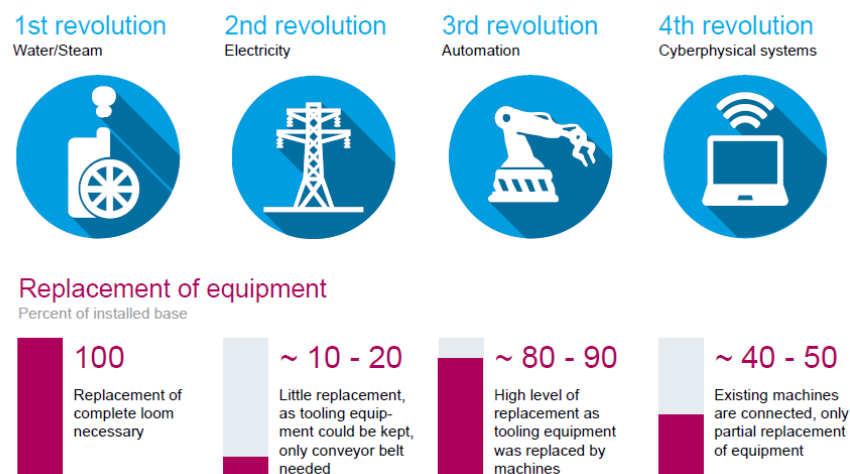
Figure 1.1 – Explanatory graphic of percentage of estimated replaced equipment during the fourth industrial revolution compared with previous revolutions: the first one brought the introduction of the steam machine: the technology was novel and replaced all man powered machines; the second revolution empowered previously installed machine with a wide net of electrical power supply; while the third revolution needed the installation of complex robotics and automation devices (McKinsey & Company, 2016).

Although some current techniques have fulfilled the immediate needs for information of controllers, often it is required to sample at the end of a process (e.g. for final quality checks/customer approval). This can lead to product rework or waste which damages both profit and environmental impact.

This work aims to explore the field of process analytics via the investigation of potential in-line measurement solutions for the monitoring of manufacturing processes operated by the sponsoring company of this Engineering Doctorate (EngD) project, Johnson Matthey (JM). JM has a highly differentiated structure and range of products (Section 1.3), amongst which is catalytic converters for automotive emission control. The in-line measurement techniques investigated in this thesis are directed towards, but not limited to, the manufacture of these catalysts.

1.2 Technical background

1.2.1 General overview

One of the goals of Industry 4.0 is maximum flexibility in production, where products can be highly customised according to demand, with processes which are capable of adjusting accordingly. The basis of this is to be able to capture the current system state and rapidly adapt it as required to meet the product specification. In this context, measurement technology plays an essential role in capturing the process condition and translating it into digital information in real-time. This is done through a cyber-physical production system (CPPS), integrated into the production control, which is able to capture and evaluate data in real time enabling process interventions to be made (Imkamp et al., 2016).
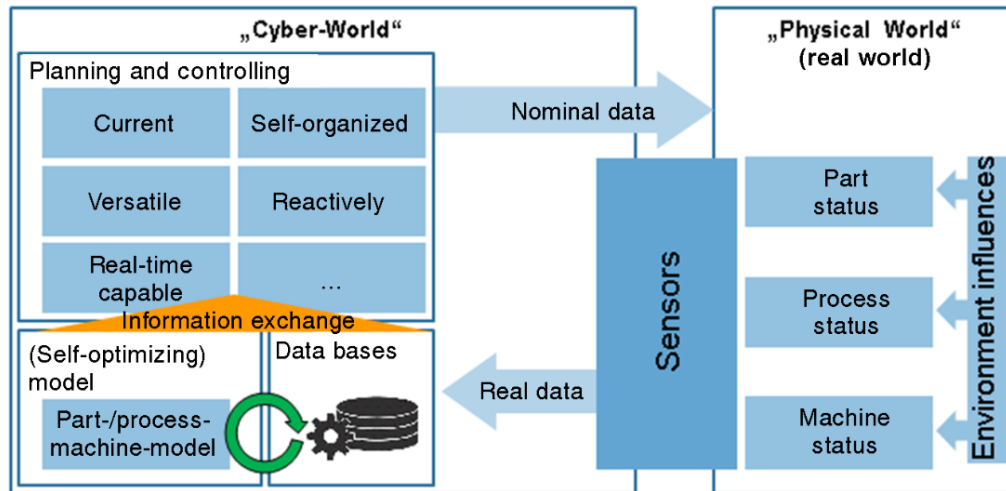
Figure 1.2 – Scheme of a cyber-physical production system (CPPS) (Imkamp et al., 2016). The sensors represent the interface between the physical world and the cyber world. They allow collecting information from the process and make them available for modelling. The computational models will generate a response that will be fed to the process as data.

As shown in Figure 1.2, the sensors/measurements box has a critical role in connecting the "two worlds" as well as the implementation of complex multivariate models that would ideally be capable of self-optimisation following the process evolution captured by the inline measuring tools. A critical issue is that it is not trivial to be able to identify the right data necessary, hence, the right measurement technique to be implemented, at the right stage of the process.

Aligned with the requirements of Industry 4.0 are the developing challenges in metrology. Zeiss's analysis (Berthold and Imkamp, 2013) identified some crucial points to be addressed for supplying manufacturing plants with enabling techniques:

- Speed: it is essential that data can be acquired, processed and made available in real time. Avoiding affecting the cycle time when implementing the technique on a plant makes it not only desirable, but also easy to be adopted and effectively integrated in the process.

- Accuracy: reducing the tolerances of quality parameters, hence achieving better accuracy would guarantee a better control. The improvement in this area is ongoing (Weck, 2005), with studies focused on innovative sensors, transducers and on introducing new calibration procedures (Imkamp et al., 2016).

- Reliability: especially for safety-critical products (pharmaceuticals and medical products) it is crucial to reduce as much as possible the measurement uncertainty. The goal is to achieve an understood and appropriate failure rate enabling accurate prediction of lifetime.

- Flexibility: given the growing variety of measurement systems used on plant, they will have to adapt to capture different features and take into account signals combined from different sensors. (Weckenmann et al., 2009). In addition, the use of "smart sensors" will allow multiple features to be captured simultaneously.

The improvements in the cited areas will ultimately converge and contribute to the creation of holistic models that bring together relevant characteristics for the final goal of targeting the desired product quality. In this field, use of Artificial Intelligence (AI) has promised the achievement of adjustable real time models, bringing together both statistical and physical features (Venkatasubramanian, 2019). The models constitute the link between the measurements made and the quality and specification of the final product (Brecher et al., 2014). This perspective is, however, impossible to put into practice without the availability of real time data which is only obtainable with innovative, real time, information rich measurement techniques.

The research described in this thesis aims to evaluate innovative applications of existing measurement techniques that respond to the characteristics and needs of modern manufacturing. An overview of the current field of inline measurement techniques with a

brief focus on those employed in this work is covered in the section 1.2.2 below. A full theoretical description of the employed techniques is given in subsequent chapters (2-7).

1.2.2 Inline Measurements

The deployment of inline measurements on industrial plant is a continuously evolving field that embraces many manufacturing sectors. The pharmaceutical industry has spearheaded recent advances with the adoption of PAT (Dickens, 2010). Generally, PAT is defined as the application of on-field instrumentation and chemometrics from measuring chemical or physical properties or other characteristics that are impossible to be inferred from conventional process variables (temperature, pressure, etc.) (Dickens, 2010). What distinguish PAT from the traditional techniques are the applicability on-field and most importantly the timescale, in the order of seconds or sometimes minutes, versus the laboratory offline techniques which need hours or in some cases days to obtain results.

The use of PAT in industry goes back to the 1940's, for the massive empowerment of German industrial plants prior to World War II (Gregory et al., 1946), employing amongst other techniques infrared photometers, distillation analysers and conductivity sensors. Its application has seen in the following decades the extension to chemical, refinery and nuclear plants worldwide. More recently the technology has evolved from the introduction of real-time gas chromatography (1950's - 1960's), mass spectroscopy (1970's) to the in-process Raman and particle size instrumentation (2000's). In Table 1.1, a summary of the recent most common PAT applications is reported. Nonetheless, given the wide range of available technologies and the continuous strive to improve them, it includes only a representative portion of the research carried out in the field.

Table 1.1 – Summary of the commonest PAT and their applications.

Technique type	Applications
UV-visible Spectroscopy	Composition monitoring (Coates, 2010; Saltzman, 2006), pulp colouring (Schmidt, 2000), pharmaceutical syntheses (Brittain, 2006), Clinical chemistry (Upstone, 2013), pollution detection (Ojeda and Rojas, 2009), catalysis activating deactivation (Schoonheydt, 2010), solid mixing (Weinekötter and Reh, 1995).
Near Infrared (NIR) & Infrared (IR) Spectroscopy	Moisture content detection (Cervera-Padrell et al., 2012), tableting (Wahl et al., 2014), fluidised bed (Obregón et al., 2013), granulation (Alcalà et al., 2010), milling (Chablani et al., 2011), composition monitoring (Coates, 2010), polymerisation (Ouzineb et al., 2003).
Raman Spectroscopy	Reaction monitoring (Li et al., 2003) bioreactors (Lee et al., 2004) Powder blending (Hausman et al., 2005), calcination (Leugers and Lipp, 2006). catalyst activation (Jestel, 2010).
NMR	Reaction monitoring (Barrios Sosa et al., 2011; Chanda et al., 2015) separation processes (Maiwald et al., 2003).
AE and ultrasonics	Granulation (Whitaker et al., 2000) tool condition monitoring (Elforjani and Shanbr, 2018; Li et al., 2015) structural integrity (Ohtsu, 1996)
Fluorescence	Pharmaceuticals manufacturing (Rashidi, 1997) biofouling (Lemke et al., 2005) water quality (Dickens, 2010), bioreactors (Li and Humphrey, 1991).
Microwave and Terahertz	Polymer synthesis (Wietzke et al., 2009) Polymer deposition (Soppe et al., 2005).
Industrial tomography	Mineral transportation (Tan and Dong, 2015), fluidised beds (Kantzas, 2015; Wang et al., 2015), bubble columns (Holland, 2015) reaction monitoring (Ali Othman and Takei, 2015; Mosorov, 2015), food processing (Del Nobile et al., 2015), nuclear waste (Primrose, 2015).

Amongst the wide fields of metrology and PAT, previous EngD students in Johnson Matthey have carried out significant work in the field of industrial tomography. Ukachukwu Oguh (Oguh, 2012) thoroughly studied Platinum Group Metal (PGM) hydrometallurgy related processes with a particular focus on the use of ERT to monitor gas-liquid mixing in stirred tanks. Peter Clark (Clark, 2016) widened the range of used measurement techniques to include Electrical Impedance Spectroscopy and 2-D Electrical Capacitance Tomography for monitoring processes related to catalytic converters production.

This thesis uses these previous conducted studies as its foundation, with the overall aim of translating the research to the manufacturing plants. The research is focused on three techniques whose applications are disclosed in the following results chapters:

- Electrical Resistance Tomography (ERT)
- Electrical Capacitance Tomography (ECT)
- Acoustic Emission (AE).

The former two techniques belong to the industrial tomography family where the output data are reconstructed images; for AE the outcome of the measurement is the acoustic spectrum. However, all the used techniques have many points of commonality: high speed of measurement, non-invasiveness (that enables processes to be monitored with minimum interference) and the still fully not achieved potential of deployment in or at-line. These characteristics and their applicability to wide range of unit operations involving multiphase intermediates have constituted reason for investigation in this work.

The two electrical tomographic techniques, ERT and ECT, are characterised by the use of data acquired in situ to reconstruct an image. Electrical tomography is a soft-field technique, meaning that the sensitivity of the measurement within the sensing region depends also on the spatial variation of the physical parameters being measured. For a hard-field technique (e.g.

X-ray and gamma-ray tomography), the sensitivity is only a function of the excitation parameters (Tapp et al., 2003). In all kind of tomographic techniques, a source able of emitting energy (whose nature depends on each case) is coupled with a receiver that collects it after it is gone through a sample. In practical terms, the hard-field techniques make use of high-energy electromagnetic radiations: the presence of the sample, although having an effect on the recorded energy magnitude at the detector, does not modify the direction of travel of the energy waves. Hence, it is possible to obtain high-resolution images with relatively little computational effort. Instead, in soft-field tomography, the low-energy field involved is affected by the presence of the sample and therefore its shape cannot be known a priori. This characteristic of soft field methods makes the image reconstruction an ill-posed mathematical problem leading generally to a low-resolution image. Nonetheless, the uses of electrical tomography for industrial applications are many, thanks to the high time resolution (up to 200 frames per second), robustness, low-cost and the limited invasiveness.

Both ECT and ERT are characterized by the presence of an array of electrodes (often arranged in circular fashion) and a data acquisition unit that controls excitation and acquisition, although their functioning principle differs. ECT detects electrical permittivity variations in very low (or non-) conductive materials. Typically, one electrode is energized with a known voltage and the induced capacitance on the remaining electrodes is measured, this is a function of the dielectric properties of the monitored system. ERT instead requires the electrodes to be in contact with a conductive material and works on the principle of induced charge migration due to an applied current through the electrode pairs in sequence.

The applications of electrical tomography are usually associated with the presence of multiple phases. Sharifi and Young (2013) review ERT applications in chemical engineering applications including flow analysis (Machin et al., 2018; Ren et al., 2017), blending and

mixing studies (Edwards et al., 2009; Holden et al., 1998; Pakzad et al., 2013) and phase detection (Takriff et al., 2013; Wang et al., 2000) in various units (pipes (Dong et al., 2003; Ma et al., 2001), mixing vessels (Mann et al., 1997), fluidized beds (Stanley and Bolton, 2008) and separators (e.g. Williams et al., 1999). ERT is recognized as amongst the most advanced techniques in terms of industrial implementation (Primrose, 2015) but can encounter some resistance from plant operators because the traditional sensor geometry (electrodes arranged around a circumference) is not easy to retrofit to existing equipment such as stirred tanks.

ECT has been applied to many operations concerning multiphase flow, including trickle beds (Wang et al., 2015), fluidized beds (Halow, 1997; Zhang et al., 2016) bubble columns (Al-Masry et al., 2010) and offshore oil-gas transport pipelines (Hansen et al., 2019). Although widely employed in research laboratories, ECT has been implemented less frequently on industrial plants when compared with ERT, mostly because of the difficulty of obtaining quantitative information. Most of the past literature has focused on planar 2-D or pseudo 3-D measurements (obtained by interpolating between multiple 2-D planes); however, in recent years the advancement in data processing, involving the use of Neural Network approaches (Rymarczyk and Klosowski, 2019; Zainal-Mokhtar and Mohamad-Saleh, 2013) and the upgrade to full 3-D (Clark et al., 2016a; Wei et al., 2015) has made it more desirable for industry.

The Acoustic Emission technique differs in both the physics and the output. In most applications, a piezoelectric sensor, in contact with the measured system, acquires the generated vibrations and transmits them to an oscilloscope or a computer. The acquired signal is then processed to characterise the system. Widely used in civil engineering for structure monitoring (Di Benedetti et al., 2013; Ohtsu, 1996), AE has also been applied in

chemical engineering for fault detection (Boyd and Varley, 2001) and condition monitoring (Rozak et al., 2018). Recent studies have also looked at applications involving multiphase monitoring in pipelines (Addali et al., 2010) and to characterize bubble sizes in bubble columns (Al-Masry et al., 2005). However, the complex nature of the generated signal has, most of the time, limited the applications to simple systems and a controlled environment. This limitation can be, however, overcome with the employment of powerful statistical and machine learning approaches to extract relevant information for process control (Li et al., 2015).

The three techniques described above have been investigated as potential inline tools for monitoring JM processes. The aforementioned advantages in terms of costs and flexibility are desirable for applications in the catalytic converter production but also for processes involving multiphase systems across the different divisions of the Company.

1.3 <u>Johnson Matthey structure</u>

Johnson Matthey plc is a leading science and technology company operating traditionally in the market of precious metals, catalysts, process technology and more recently in the health and energy storage businesses. JM is a FTSE 100 company employing more than 14,000 professionals across its 30 sites in Europe, North America and Asia. In 2018/19 JM had a revenue of £10.75 billion and an underlying profit of £525 million (Johnson Matthey, 2019a). JM operations include a diverse range of sectors: emission control, process technologies, precious metals, batteries and pharmaceuticals, and it is organized into four main divisions. Each of JM sectors is described below.

1.3.1 Clean Air

The Clean Air division operates in the applications of catalysts for reducing emissions from automotive and other sources. The primary focus of the Clean Air sector is producing

catalysts for the automotive industry, both for light-duty and heavy-duty vehicles. According to Acres and Harrison (Acres and Harrison, 2004), JM has been the supplier of one third of all the emission control catalysts ever assembled on any vehicle. Furthermore, amongst Clean Air products, the stationary emission catalysts have, as an application, the reduction of emissions in industrial effluent flows, particularly for energy generation and storage.

The Clean Air division has been directly involved in this project, being one of the focuses of the investigated measurement techniques and having hosted on its plants extensive trials, as described in Chapter 7.

1.3.2 Efficient Natural Resources

The Efficient Natural Resources (ENR) division in JM has as an objective to develop and use advanced technology to achieve greater efficiency and optimal yields in the use of natural resources. The main related businesses of ENR include:

- *Catalyst Technologies* which supplies catalysts and licensed processes to the oil and gas and process industries. Its specialty applications include hydrogen plants, ammonia production, methanol and formaldehyde synthesis and bio-renewable production of bulk chemicals.

- *Platinum Group Metals Services* which has a focus on refining and recycling precious metals, producing platinum group metals (PGMs) based products and precious metal related support services.

- *Advanced Glass Technologies* (AGT) which produces functional glass-based materials, primarily for the automotive glass, advanced ceramic, electronic, and tableware industries. Among the main products are the black obscuration enamels widely used on car windscreens, precious metal inks, coatings and decorative enamels.

- *Diagnostic Services* also known as Tracerco operates in the oil and gas space and is a world leading diagnostic and measurement business with high-technology products including subsea pipeline diagnostics and radiation monitoring and protection devices.

1.3.3 Health

The Health division sector of JM operates in many stages of pharmaceutical production. The main focus is on the production of active pharmaceutical ingredients (APIs), supply of catalysts for the pharmaceutical industry, and in providing precision components for medical devices. Among the different products, the Health sectors also provides business to business services to tackle quality and safety related chemical challenges.

1.3.4 New Markets

The New Markets division covers a wide spectrum of applications to explore future major growth areas. Currently at the core of this division is the development of alternative powertrain and energy storage technology such as battery materials, battery technology and fuel cells. JM is the world's leading supplier of fuel cell catalysts and membrane electrode assemblies and one of the leading manufacturers of cathode materials for batteries (Johnson Matthey, 2019b).

1.3.5 Johnson Matthey Technology Centre

Aside from the different business sectors, Johnson Matthey Technology Centre (JMTC) is the Research and Development division at the core of the innovative science applied across the different divisions. JMTC has provided the financial support for this EngD project.

1.4   <u>Business Case</u>

Johnson Matthey is undergoing a digitisation process to align its development and production to smart manufacturing (Johnson Matthey, 2018), to continue striving towards its mission of "making the world a cleaner and healthier place" (Johnson Matthey, 2018).

The trend of catalyst products use worldwide is positive, with applications ranging from automotive catalytic converters to catalysis for production of feedstock chemicals. The global market size was estimated at $25 billion USD in 2018 and expected to expand at a CAGR of 4.5% by 2025 (Grand View Research, 2019). Focusing on the automotive sector, the global market size was evaluated at $0.23 billion USD in 2017 and projected to grow at a similar rate of 4.2% in the same time frame (Allied Market Research, 2018). This growth is expected because of the input in the market of innovative products as well as the introduction of more stringent legislation (having an objective of reducing emissions from both consumers and industrial processes) (Armor, 2011).

The formulation of catalysts includes base metal oxides, rare earth metals and precious metals. Examples are given in Figure 1.3.
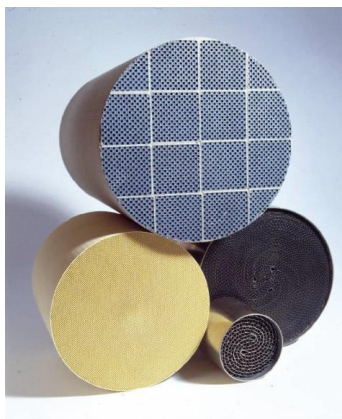
Figure 1.3 – Example pictures of different catalytic products: (a) Automotive catalytic converter, (b) Methanol synthesis and reforming catalyst, (c) Platinum metal (Johnson Matthey, 2017a).

The first introduction of legislation concerning the after treatment of automotive exhaust gases goes back to 1975, USA, California, shortly followed by the other states of the USA, Canada and Japan, before spreading worldwide. Nowadays, over 98% of new cars are sold equipped with automotive catalysts (International Platinum Group Metals Association, 2019).

These devices are complex products consisting of cylindrical or elliptical cross section prisms, made either from metal or ceramic, characterised by a fine honeycomb covered in a ceramic washcoat containing the active catalyst (generally Platinum, Rhodium and Palladium compounds). These items are installed in vehicle exhaust lines and intercept the gases coming from the combustion chamber with the objective to remove nitrogen oxides (NOx), sulphur oxides (SOx), volatile organic compounds (VOC's), carbon monoxide and particulate matter (PM) through chemical reduction (or physically in the case of particulate). The catalyst formulation is strictly

dependant to the type of engine. In a comprehensive review, Twigg (Twigg, 2011) analyses in detail the characteristics of emission control systems. To convert the pollutants, it is necessary to offer a high surface area, keeping at the same time a low pressure drop to minimise exhaust backpressure and maximise fuel consumption. The honeycomb ceramic design represents an ideal solution to meet both the mentioned requirements and has been adopted since the mid-1980s.

The manufacture of the catalyst consists of different unit operations involving multi-phase mixtures. The scheme in Figure 1.4 shows the principal processes involved.
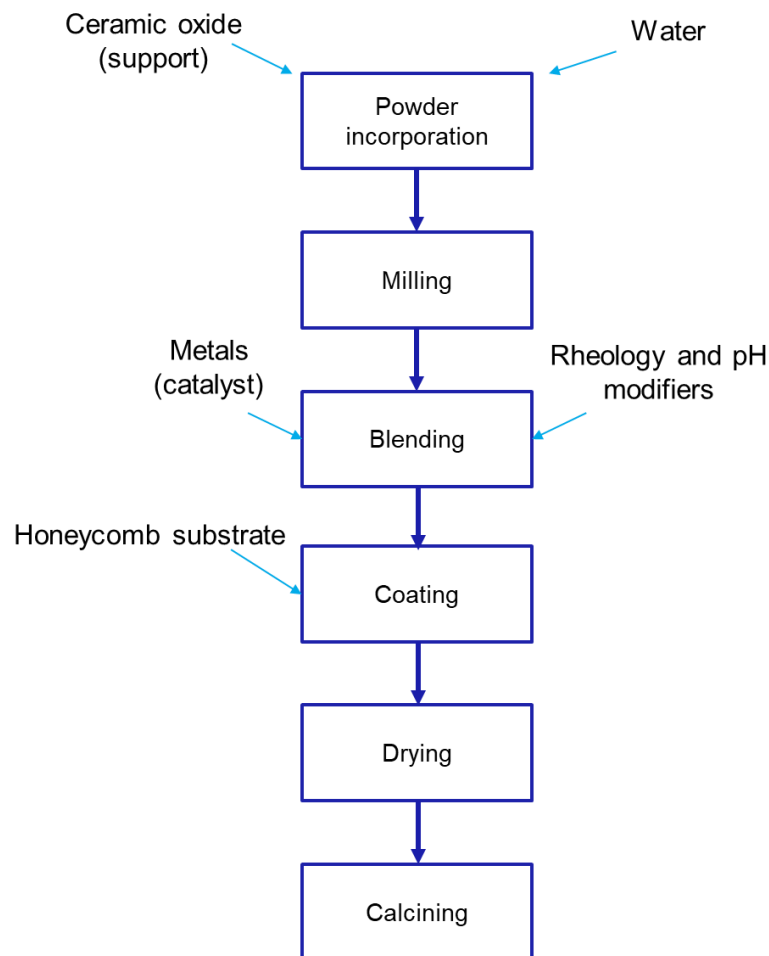
Figure 1.4 – Flow diagram of catalytic converters production process. Ceramic oxide is added to water constituting a suspension, called slurry. The slurry is milled for reducing particle size and is then enriched with metals and rheology and pH modifiers in a blending step. The intermediate, also called washcoat, is then used to coat honeycomb substrate. The substrates are then dried and calcined before being ready for packaging and dispatch.

In principle, ceramic oxide powder is incorporated into water, constituting a slurry that will be the "carrier" of the active catalyst. The obtained solid-liquid suspension undergoes a milling step, during which the particle size is adjusted to specifications. The active part of the catalyst constituting of PGM salts is then added to the mixture and blended. In this delicate step the pH and most importantly the rheology is adjusted by adding inorganic and organic compounds. The intermediate product resulting from the blending is called the washcoat and it is a non-Newtonian fluid which is used to coat the substrates. The rheological behavior of the mixture is critical to enable the following step of coating to meet specification. At this stage, the solid-liquid suspension meets the solid ceramic (or metallic) substrate and it is spread onto the channels through a coating process. The parts then are dried with hot air and calcined at high temperature.

As briefly described above, the manufacture of catalytic converters is composed of many unit operations. Amongst the different studies involved in the continuous improvement of the whole process, being able to monitor some of the operations in real time is an enabler for consistency in meeting quality standards and reducing as much as possible waste and downtime.

The research presented in this thesis investigates measurement solutions on some of the described processes, but it also includes potential applications for different sectors (other catalysts, pharmaceutical products, batteries). Indeed, while there has been a specific focus on delivering a measurement solution to support the coating step in catalytic converter production, other investigations have been more cross-functional. The investigations on fluid mixing and particularly on gas-liquid mixing, indeed, find perfect application in the case of pharmaceutical fermenters and platinum refining processes. Although the main interactions

with the JM business divisions were with Clean Air, the breath of the conducted work is wider as explained in detail in Section 1.5.

1.4.1 Thesis scope and aim

Research in the field is constantly moving towards highly complex holistic measurement systems that can provide useful information in short time in order to enable more accurate and fast responding process control strategies. The work carried out in this EngD project lies in the wider context of empowering modern plants with accurate, fast and reliable analytics that can improve process control in both terms of productivity and sustainability.

As well as the development of novel measurement strategies, their application to complex system combined with data processing and statistics require effort from the research community. In this work the scientific aims consist in:

- Investigating the ERT using the linear probe as a source of quantitative information about the gas hold-up in a small scale (3 L) gas-liquid stirred tank. So far, ERT has been used only for R&D purposes, believed to be source of qualitative information and not applicable on industrial systems. Being this technique a fast responding method, being also able able to translate tomograms into quantitative data is critical to the success of the technique as a plant widespread method. The ERT data are processed to extract information about the gas spreading through a stirred tank. The objective is to gather information about the global gas hold-up but also to extract local information at different regimes as flooding, loading and complete dispersion. Although the carried out work is made on a 3 L scale, the design of the probe and its ease of retrofitting make it, in perspective, a desirable sensing method for bigger scale as JM production mixing tanks. (Chapter 2)

- Proposing a methodology to make use of Acoustic Emission as a diagnostic tool in multiphase mixing. On a similar system as for ERT, AE has been used for the first time as a classification method for gas-liquid mixing regime. The objective is to develop a data processing method, involving machine learning, which can be used to extract information from the data-rich acoustic spectrum. Such method was tested in recognising different regimes (ungassed, loading, complete recirculation) with the target of establishing capability of the technique to be used in such applications. (Chapter 3)

- Establishing capabilities and limitations of ERT for in pipe mixing of non-Newtonian fluids. Such fluids are characterised by resistance to be mixed in condition of low-shear. Therefore, for continuous processing applications, static mixers are used to encourage blending. One of the difficulties encountered is to make sure the desired grade of mixing has been achieved. This is the reason why in this work ERT is investigated as a potential diagnostic in this application. The technique is used to evaluate mixing of solutions of Carbopol 940 (well described by a Herschel-Bulkley rheology) and carboxymethylcellulose (CMC) (Power law model) in comparison with a laser based high-resolution technique as Planar Laser Induced Fluorescence (PLIF). The aim is to investigate whether ERT, although being characterized by low resolution, could be used to collect information representing the achieved blending performance in a 25.4 mm pipe equipped with 6 elements Kenics® KM static mixers. (Chapter 4)

- Applying Electrical Capacitance Tomography (ECT) to powder blending in order to identifying capabilities in detecting good blending and segregation. ECT has been identified as a potential ground-breaking tool for such unit operation. Powders with

different electrical permittivity have been mixed in a FT4 Freeman rheometer (Freeman Technology ®) and ECT has been challenged to identify blending conditions. The application of ECT had, so far, not been extended to such unit operations. The purpose is to evaluate a novel use of this technique for a well-known complex application. (Chapter 5)

- Improving data interrogation of 3D ECT. Its upgrade to three-dimensional reconstruction has only recently become available. In this work, a volumetric method to evaluate reconstruction error in cases of plastic PEEK phantoms immersed in glycerol is proposed with the objective of make the performance evaluation easer. Nonetheless, in cases of multiphase systems, one of the limitations of the technique was to be in need for a thresholding value to distinguish the different phases. Such a priori information makes it difficult to be applied in cases of dynamic systems. The objective is to propose a method that does not need a priori information about the permittivity of the involved phases and that, in a simple case of horizontal interface, could be used to automatically place the interface (Chapter 6). An additional objective related to ECT is to evaluate its applicability in terms of speed and robustness on a real industrial application such as coating in catalytic converters production. This takes the method developed in Chapter 6 and brings it in a factory environment to challenge it on a production intermediate (Chapter 7).

1.4.2 Thesis business objectives

To ensure that JM retains its position among the leaders in the market and at the same time being able to respect the mission of using natural resources in an efficient way, the Company is on the route towards the implementation of smart manufacturing practices.

The work in this thesis aims to make a step forward in this direction, increasing knowledge in the field of advanced in-situ characterisation techniques and looking at their direct applications on existing unit operations on industrial plants. The project is in line with the diversification of JM market coverage, having investigated methods for monitoring processes present in catalyst production as well as for pharmaceutical and precious metal refining.

The overall aims of the present work with respect to the needs of JM are summarised below:

- Increase JM expertise in the field of process tomography and in-line measurement methods with a broad range of applications.

- Develop data processing approaches for extracting key parameters to support decision making on plant.

- Extending work done at laboratory scale to industrial environment to demonstrate capabilities and opportunities of implementation.

The present EngD project is part of a long going relationship between the University of Birmingham and JM, building on previous EngD and PhD projects. The conducted studies, although being thought around JM processes, aim to progress research within the measurement and control area. As a result, journal papers and conference presentations have arisen from this work, reported in §1.7, demonstrating the impact of this work to the wider scientific community.

The overall aim of the conducted work was to investigate innovative applications and data interpretation of existing measurement techniques with the primary objective of contributing to the shared need of improving real time data acquisition methods for industrial processes and identify opportunities of implementation within JM production plants.

The present work has looked at different areas of multiphase processing with the objective to contribute to the scientific research in the field. Current methods for monitoring state of dynamic processes are often based on traditional process monitoring parameters, *e.g.* pressure, temperature, conductivity. Although these parameters are extremely useful for monitoring the overall state of the process, they do not, sometime, give enough information to picture local dynamics. Within JM interests, with reference to the objectives outlined in Section 1.4.1 some specific aims have been addressed:

- Further develop the capability to capture multiphase mixing in stirred tanks. Traditionally, the employed monitoring methods are recipe control, operator experience and sometime only the quality of the final product. The investigation of ERT and AE for this unit operation aims to allow real time monitoring of the gas dispersion in stirred tanks in a Nickel nitrate hexahydrate solution. Such choice is made on the basis of applications in the refinery division of JM (e.g. leaching, platinum salts dissolution). Specifically:

  o The ERT data, often used qualitatively in industry, have been processed with the intention of establishing a methodology that could provide, together with the non-traditional linear probe geometry, an implementable online tool for gas hold-up measurements. The investigated system was a 3L stirred tank, in which an electrolytic aqueous solution is mixed with air in absence or presence of a third solid phase. The objective was to use ERT to capture local information about the gas distribution within the tank and detecting the gas hold-up at different mixing regimes.

o The AE technique in this application was not tested before on similar systems, therefore, it was explored as a potential condition monitoring tool in combination with Artificial Intelligence (AI) characterised by low-cost and ease of retrofitting. A method to process AE information making use of machine learning algorithm was proposed. The objective was to investigate whether it be possible to gather reliable information about the mixing regimes in a 3L multiphase system using AE. Conditions of ungassed (monophasic) mixing, loaded and completely dispersed (often the desired status) were investigated and the developed method was challenged to recognise the operating regime.

- Evaluate the potential and limitations of ERT for pipeline applications. The tendency in industry is, where possible, to shift production from batch to continuous processes (Hakansson, 2018; Lee et al., 2015); however this transition often encounters technical limitations including measurement and control strategies. Amongst the most challenging unit operations to monitor, fluid mixing using static mixer can represent a critical step in production, especially in cases of non-Newtonian fluids. Such fluids (Carbopol 940 solutions and CMC) were accurately prepared to mimic rheological behaviour of catalytic carrier, also known as washcoat, a critical component of automotive catalytic converters. ERT was identified as a potentially ground-breaking tool for this purpose.

- Develop a methodology for using ECT for monitoring industrial processes. Powder blending, and catalytic converters coating represent critical steps in JM processes:

  o Powder blending is a common unit operation across the different divisions and the development of an inline technique capable of assessing when segregation

may affect the homogeneity of the intermediate. Zeolite and mannitol were used in this investigation as powders. Although the choice was made based on their electrical and good flowability properties, the blending of this two powders and the capability to monitor it may represent advantages in processing of pharmaceutical tablets.

- o The monitoring of the coating step within the catalytic converter production was identified as one of the key areas of improvement for improving productivity and reduce downtime. It is to fulfil this need that three-dimensional ECT was thoroughly scrutinised and studied for establishing a robust methodology and evaluate its accuracy against current at-line methods.

- Conduct tests on a JM plant in order to assess robustness, practical limitations and potential improvements of the ECT technique and ultimately provide the business with a powerful tool for inline monitoring of catalyst converter coating.

1.5   Structure of the thesis

This thesis comprises of 8 chapters. The diversity of the analysed topics mimics the variety of processes and measurement techniques available on a manufacturing plant. For this reason, as mentioned above, the appropriate state of the art for the different combination of diagnostics and processes are reported in the various chapters as well as details on the theory and functioning principle for the employed techniques. Although the chapters can be read as stand-alone (apart from Chapters 6 and 7 which are intimately connected), structurally, the thesis is divided in two sections. The first part, Chapters 2-4, addresses the complex problem of multiphase mixing detection.   Different techniques, such as Electrical Resistance Tomography and Acoustic Emission are investigated as possible solutions for fluid mixing monitoring. In the second section, Chapters 5-7, Electrical Capacitance Tomography is

identified as a promising technique to be used for measurements of powder mixing and as a quality assurance diagnostic tool for coating in the catalyst converters production line. In Figure 1.5, a roadmap of the thesis structure is shown.
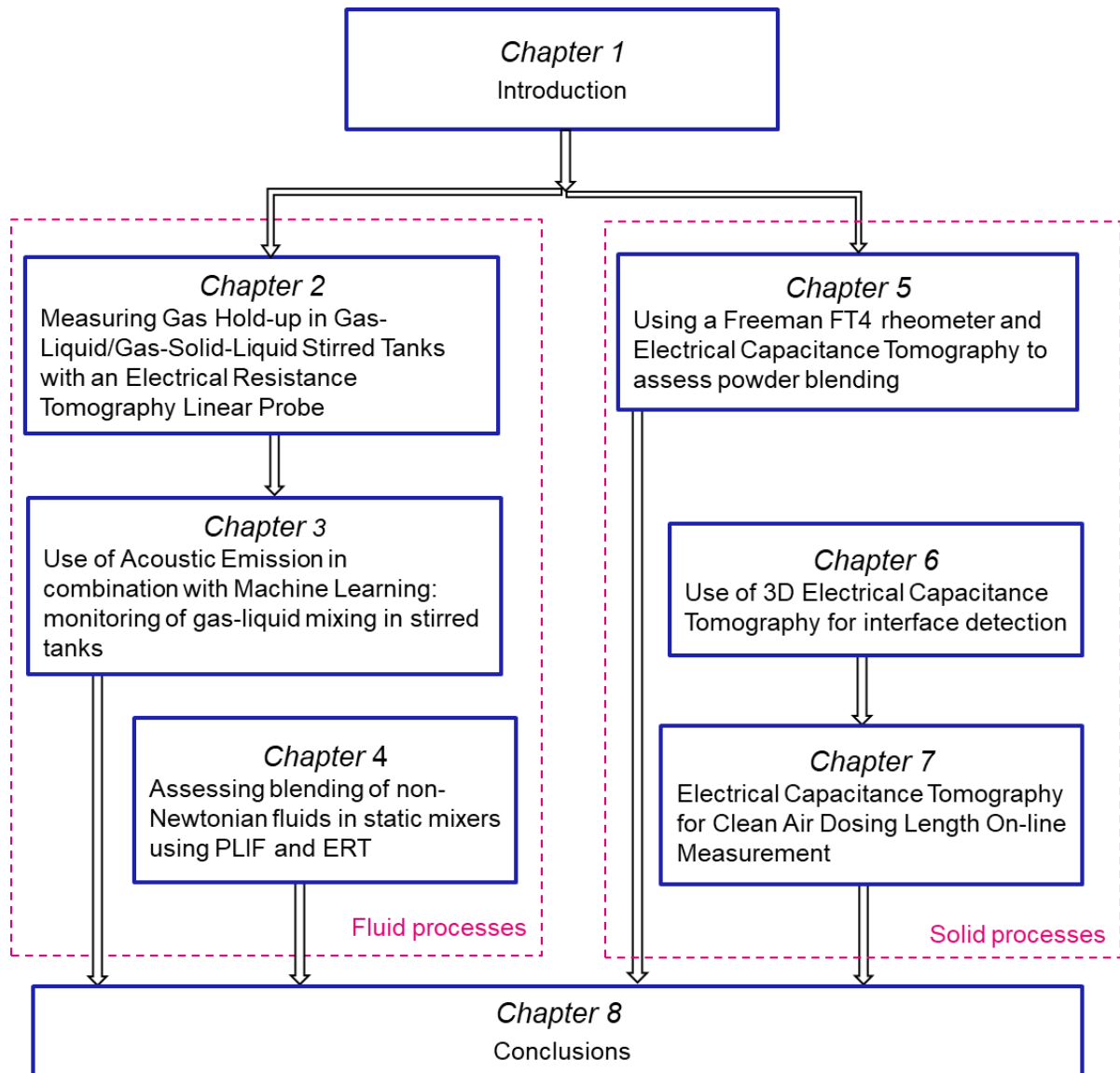
Figure 1.5 – Thesis roadmap. The introduction chapter gives the context and establishes the objectives and aims. The thesis is then divided in two parts: the fluid process section composed and the solid process section both composed of three chapters.

Looking at each of the chapters in detail:

Chapter 2 - Measuring Gas Hold-up in Gas-Liquid/Gas-Solid-Liquid Stirred Tanks with an Electrical Resistance Tomography Linear Probe

This chapter addresses the problem of detecting the gas hold-up in the case of multiphase mixing in stirred tanks. Although ERT has been previously investigated as a possible solution, the traditional design of ring cages does not meet the retro-fitting requirements for practical inline installation. The linear probe design instead is portable and easily adaptable to existing equipment. This chapter develops and test a method to evaluate overall and local gas hold-up in cases of bi-phasic (gas-liquid) and three-phase (gas-solid-liquid) mixtures.

Chapter 3 – Use of Acoustic Emission in combination with Machine Learning: monitoring of gas-liquid mixing in stirred tanks

The same unit operation described above is tested with an alternative technique to identify the different gas sparging regimes in a non-invasive fashion. Acoustic Emission receives as input vibrations caused by the gas bubbles breakup and interaction with the main fluid and the mixing equipment. Being a data-rich technique, the generated signal is often difficult to interpret. In this study, machine learning algorithms are used to recognise patterns in the signal that can allow gas-liquid regime identification.

Chapter 4 – Assessing blending of non-Newtonian fluids in static mixers using PLIF and ERT

Although many fluid mixing operations are still carried out in batches, they are also interested by the tendency of moving to continuous processes. Amongst the various challenges connected to this, detecting the level of blending can represent an obstacle for the implementation. In this Chapter, blending of non-Newtonian fluids in a pipe line, obtained using motionless mixers, is monitored with Electrical Resistance Tomography (ERT). The potentially plant suitable technique is compared with a well-established optical technique, Planar Laser Induced Fluorescence (PLIF), that represents a powerful term of comparison for evaluating the detecting performance of ERT.

Chapter 5 - Using a Freeman FT4 rheometer and Electrical Capacitance Tomography to assess powder blending

This Chapter moves away from the fluid mixing to face the non-trivial challenges of powder blending. An Electrical Capacitance Tomography (ECT) sensor is fitted on a Freeman FT4 rheometer, a commonly used tester for characterising powder flow properties. The FT4 is equipped with a blade that moves into the powder bed recording the used total energy and torque; this movement results also in powder blending. Exploiting the electrical properties of two different powders, ECT is able to identify cases in which the powders are well-blended and, at the opposite, condition of segregation. ECT observations are in agreement with the FT4 measurements, demonstrating ECT suitability for powder blending applications when the used materials are characterised by different electrical permittivities.

Chapter 6 – Use of 3D Electrical Capacitance Tomography for interface detection

This Chapter investigates the use of ECT in the three-dimensional space. Traditionally being used for planar measurements, in this work ECT is, at first, challenged to image plastic phantoms immersed in glycerol and then to reconstruct horizontal gas-liquid interfaces. An alternative binary gating method based on the maximum gradient of the voxel values profile is introduced and tested against the traditional thresholding approach. The interface recognition method is built and tested with the purpose of being the foundation of an industrial application described in the following chapter.

Chapter 7 - Electrical Capacitance Tomography for Clean Air Dosing Length On-line Measurement

The 3-D ECT technique is applied in this Chapter for monitoring substrate coating, a JM critical process in the manufacturing of catalytic converters. Initially, ECT is tested in a laboratory environment to evaluate feasibility, accuracy and challenges related to its

application. In a second stage, the technique is tested on a production line in comparison with the well-established X-ray scan machine, the standard currently utilised for coating length measurements. The X-ray method is a powerful tool, limited though by the high cycle time that does not allow to monitor 100% of the items. This work shows the advantages and limitations of ECT and it has recently led to a wider campaign of trials for industrial implementation.

1.6   List of publications and awards

1.6.1 Publications (chronological)

- Clark P.J., Forte G., Simmons M.J.H., Stitt E.H., 2016, 'Towards 3D-Electrical Capacitance Tomography for interface detection', *Johnson Matthey Tech. Review*, 60 (2), 164. https://doi.org/10.1595/205651316X691537

- Forte G., Clark P.J., Yan Z., Stitt E.H., Marigo M., 2018, 'Using a Freeman FT4 rheometer and Electrical Capacitance Tomography to assess powder blending', *Powder Technology*, 337, 25-35. https://doi.org/10.1016/j.powtec.2017.12.020

- Forte G., Alberini F., Simmons M.J.H., Stitt E.H., 2019, 'Measuring Gas Hold-up in Gas-Liquid/Gas-Solid-Liquid Stirred Tanks with an Electrical Resistance Tomography Linear Probe', *American Institute of Chemical Engineers (AICHE) Journal*. https://doi.org/10.1002/aic.16586

- Forte G., Albano A., Simmons M.J.H., Stitt E.H., Brunazzi E., Alberini F., 2019, 'Assessing blending of non-Newtonian fluids in static mixers using PLIF and ERT', *Chemical Engineering & Technology J.* https://doi.org/10.1002/ceat.201800728

- Forte G., Alberini F., Simmons M.J.H., Stitt E.H., 2019, 'Use of Acoustic Emission in combination with Machine Learning: monitoring of gas-liquid mixing in stirred tanks', submitted to *the Journal of Intelligent Manufacturing*.

- Antonelli M., Forte G., Simmons M.J.H., Alberini A., Stitt E. H., 'Flow regime identification in aerated stirred vessel of different materials using passive acoustic emission and machine learning' to be submitted to Journal of Advanced Manufacturing and Processing.

1.6.2 Conferences (chronological)

- Forte et al., 2016, 'Extending the application of Electrical Resistance Tomography in fluid mixing diagnosis', *8th World Congress of International Process Tomography*, Foz do Iguazu, Brazil.

- Forte et al., 2017, 'Towards Increased Quantification of Electrical Resistance Tomography using Linear Probes in Fluid Mixing Diagnosis'. *9th International Symposium on Mixing in Industrial Processes,* Birmingham, UK.

- Forte et al., 2018 'Validation of Discrete Element Modelling (DEM) on a Freeman FT4 rheometer using Electrical Capacitance Tomography to assess powder blending', *Powder Flow 2018: Cohesive Powder, Royal Society of Chemistry,* London, UK.

- Forte et al., 2018, 'Using a Freeman FT4 Rheometer and Electrical Capacitance Tomography to Assess Powder Blending', *8th World Congress on Particle Technology*, Orlando, USA.

- Forte et al., 2018, 'Measuring Gas Hold-up Profiles in G/L Stirred Tanks using an Electrical Resistance Tomography Linear Probe', *XXVI North American Mixing Forum*, San Juan, Puerto Rico.

- Forte et al., 2018, 'Use of PLIF and ERT to assess mixing performance for blending of non-Newtonian fluids using static mixer', *16th European conference on Mixing (Mixing 16)*, Toulouse, France.

- Forte et al., 2019, 'Dynamic drying monitoring of a fixed bed using 3D-Electrical Capacitance Tomography', *19th Conference on Advances Process Analytics and Control Technology (APACT)*, Chester, UK

- Forte et al., 2019, 'Use of Acoustic Emission in combination with Machine Learning: recognition of gas-liquid mixing regime in stirred tanks', 15th International Conference on Fluid Control, Measurements and Visualization (FLUCOME), Naples, Italy.

- Forte et al., 2019, 'Use of Acoustic Emission for identifying Gas-Liquid mixing regime in agitated vessel applying machine learning', 61th Acoustic Emission Working Group Meeting & 9th International Conference on Acoustic Emission, Chicago, USA.

1.6.3 Awards

- Best presentation at the IChemE Fluid Mixing Processes SIG Research Student event, 2018, 'Measuring Gas Hold-up Profiles in G/L Stirred Tanks using an Electrical Resistance Tomography Linear Probe', Manchester UK

- Student award in the Acoustic Emission Working Group student competition, 2019, 'Use of Acoustic Emission for identifying Gas-Liquid mixing regime in agitated vessel applying machine learning', Chicago, USA.

2.

Measuring Gas Hold-up in Gas-Liquid/Gas-Solid-Liquid Stirred Tanks with an Electrical Resistance Tomography Linear Probe

An electrical resistance tomography (ERT) linear probe was used to measure gas holdup in an aqueous two-phase (gas–liquid) and three phase (gas–solid–liquid) solution within a stirred-tank system equipped with a Rushton turbine. The ERT linear probe was chosen rather than the more commonly used ring cage geometry to achieve higher resolution in the axial direction as well as its potential for use on manufacturing plant. Gas-phase distribution was measured as a function of flow regime by varying both impeller speed and gas flow rate. Global and local gas hold-up values were calculated using ERT data by applying Maxwell's equation for conduction through heterogeneous media. The results were compared with correlations, hard-field tomography data, and computational fluid dynamic simulations available in the literature, showing good agreement. This study, thus, demonstrates the capability of ERT using a linear probe to offer, besides qualitative tomographic images, reliable quantitative data regarding phase distribution in gas–liquid systems.

This chapter is published in the American Institute of Chemical Engineers (AIChE) journal in the following paper (Forte et al., 2019b):

Forte G., Alberini F., Simmons M.J.H., Stitt E.H., 2019, 'Measuring Gas Hold-up in Gas-Liquid/Gas-Solid-Liquid Stirred Tanks with an Electrical Resistance Tomography Linear Probe', *AIChE Journal.* https://doi.org/10.1002/aic.16586.

2.1   Introduction

Gas-liquid stirred tanks are widely used in biochemical and chemical manufacture, driven by the process requirements for bulk mixing and interphase contact. As a consequence, substantial work has been conducted in the past few decades aimed towards the understanding of two-phase turbulent mixing in these units (Ranade and Deshpande, 1999; Smith and Warmoeskerken, 1985). Studies on overall gas hold-up and gas dispersion have been carried out both experimentally and using computational simulations (Wang et al., 2014).

A significant challenge remains in the application of diagnostic methods and sensors which can provide local information on mixing performance, flow regime and phase distribution at process scale, either for troubleshooting or as a means of controlling process or product attributes during production. The most common methods are limited to either transparent media or global observations. For example, bulk gas volume fraction in a stirred tank is commonly obtained by determination of the increase in liquid height given by the presence of the gas with respect to the non-gassed condition, either visually (Rushton and Bmbinet, 1968; Saravanan and Joshi, 1996; Yawalkar et al., 2002) or using level probes (Gao et al., 2001). Applied techniques for local parameter investigations (velocity fields, local bubble size and interphase contact) and for overall gas content remain the tools of the industrial or academic researcher on the grounds of practicality or cost, *e.g.* Computer Automated Radioactive

Particle tracking (CARPT) (Chen et al., 1999; Khopkar and Ranade, 2008), ultrasonics (Cents et al., 2005; Chaouki, et al., 1997; Stamatiou and Muller, 2017; Utomo et al., 2001), Particle Image Velocimetry (PIV) (Chung et al., 2009; Laakkonen et al., 2005) Positron Emission Particle Tracking (PEPT) (Fishwick et al., 2005) and Laser Doppler Anemometry (LDA) (Dudukovic, 2000).

Tomographic methods, however, have some considerable potential. Whilst X-ray (Ford et al., 2008) and γ-ray (Veera et al., 2001) tomography and Magnetic Resonance Imaging (Sederman and Gladden, 2001) have been used successfully to obtain local values in opaque media, the need for high energy radiation, and thus significant health and safety precautions, often represent a practical limit for these techniques on plant. An alternative is the use of electrical tomography (Chaouki, et al., 1997; Holden et al., 1998; Sardeshpande et al., 2017; Wang et al., 2000), though image reconstruction is more complex and error prone since the methods are soft field rather than hard field (Wang, 2015) and the applicability of the method is dependent upon the conductivity of the phases present. Electrical Resistance Tomography (ERT), which is applicable for a conductive continuous phase, has been applied for mixing studies for single phase systems for a little under twenty years (Holden et al., 1998; Mann et al., 1997), at first using a cylindrical 8 plane electrode cage each containing 16 electrodes. Subsequently, this technique has been employed on a qualitative and quantitative basis for gas-liquid systems in bubble columns (Jin et al., 2007), stirred tank reactors (Abdullah, 2017; Sardeshpande et al., 2017; Wang et al., 2000), for immiscible liquid-liquid systems (Kourunen et al., 2008), and to assess homogeneity in solid-liquid suspensions (Harrison et al., 2012; Ricard et al., 2005). Data obtained from multiplane sensors are commonly linearly interpolated to reconstruct volumetric conductivity and therefore phase distribution. Some attempts have been done in resolving three phase systems using ERT in combination with

other techniques. For example, circular array ERT was used in combination with a fibre optic probe to investigate gas-liquid-solid circulating fluidized bed (Razzak et al., 2009).

Although circular array ERT gives useful information (Carletti et al., 2016), the issues related to plant installations and re-engineering of existing reactors make this sensor design essentially suitable only for pilot and laboratory scale studies. Thus, alternative sensor designs which are sufficiently robust and are easy to engineer within the process environment have been sought; such a design is a linear array, or probe. The first works reporting the use of the linear arrangement of electrodes for ERT were by Richardson (Richardson and Holdich, 2001) and Bolton (Bolton et al., 2002) for monitoring solids distribution in a conductive liquid phase. Despite employing the same measurement strategy as the circular design, the linear configuration allows acquisition of data with higher resolution in the axial direction, therefore giving information of axial homogeneity and distribution, useful in multiphase applications. It is reasonable to state that in industrial application (e.g. for evaluating solids deposition or local gas hold-up), for rotationally symmetrical tanks, axial mixing efficiency, rather than the radial distribution, is the most important parameter in terms of quality control. Although potentially applicable on larger scale and for in situ monitoring, this configuration has received little attention in the literature after Bolton's (Bolton et al., 2002) work. Ricard et al. (Ricard et al., 2005), for example, applied a linear sensor in combination with CFD modelling to investigate L-L dispersion and solids suspension in stirred tanks.

This paper describes the application of ERT using a linear probe for quantitative measurement of gas and liquid phase distribution and overall hold-up in a stirred tank reactor equipped with a Rushton turbine operating in the turbulent flow regime. The capability of the linear probe to discriminate the gas and liquid phases, as a function of gas-liquid flow pattern is assessed.

These data are analysed using Maxwell's equation, already successfully used for investigating bioreactors (Hamood-ur-Rehman et al., 2013; Khalili et al., 2018) for similar gas fraction using an ERT cage sensor, to determine global and local gas hold-up.

For validation purposes, the two-phase results were compared with results for similar systems from the literature using hard-field techniques and computational methods. Ford et al. (Ford et al., 2008) used X-ray computed tomography (CT) to measure gas dispersion in a 0.21 m diameter stirred tank agitated with a Rushton turbine (Fr = 0.09-1.1, Fl = 0.03-0.08, with gas flow rate between 0.86 and 1.7 vvm). Experiments were carried out at three different regimes (flooding, loading and complete dispersion) and both gas hold-up maps and axial distribution plots were produced, deriving local time-averaged gas hold-up in the axial direction at different velocities. The CT measurement domain covered one third of the tank height (with the impeller at the bottom of the field of view), focusing on the impeller zone where the gas hold-up was observed to be at its highest value in the loading and complete recirculation regimes. At the flooding condition, inefficient gas dispersion was observed with a flatter vertical profile characterising the axial gas volume fraction: the power input is insufficient to retain gas that flows through the impeller to the surface.

Khopkar et al. (2008), instead, have combined γ-ray CT measurements with CARPT and computational fluid dynamic studies (CFD) on a stirred tank with diameter of 0.20 m also equipped with a Rushton turbine. This study was carried out at low impeller speed (Fr = 0.0755) and at a volumetric gas flow rate of 0.4-0.8 vvm (Fl = 0.042-0.084), therefore with the system working in the flooding regime. The CT measurements showed higher hold-up in proximity of vessel wall with CFD capturing an inward movement of the gas in the rise through the tank, generating a secondary loop in the top half of the vessel. Both techniques

captured the low level of sparging achieved in the flooding regime and the obtained axial gas hold-up profile does not exceed 5% v/v.

As an extension to the two-phase system study, the present work also considers the capability of the method to discriminate the presence of an additional dispersed solid phase as a means of providing a first step towards the translation of this technology to the operation and control of three-phase reactors.

The chosen system is an aqueous solution of Nickel nitrate hexahydrate (99,99% Sigma Aldrich®) into which air is sparged. In the case of three-phase mixing stainless steel particles are added. The choice of such system is made to mimic the leaching process in the PMG refining JM group. In such operation, the liquid is an aqueous solution in which metals are dissolved. Throughout the process, the addition of chloride makes platinum salts dissolve while impurity metals remain in solution. The system investigated in this study is not reactive in order to simplify experiments; however the objective is to evaluate potential of ERT for multiphase mixing detection with the intention of making it available for more complex systems.

2.2   Theory

2.2.1 Gas – liquid flow regimes and hold-up

Gas hold-up is one of the most important parameters for scale-up, performance evaluation and for model development, directly influencing the G/L interfacial area. Amongst others, Smith (Smith, 1985) identified three key parameters in such applications: the scale of vessel, the impeller shape and dimension and the volumetric gas flow rate. The main flow patterns, or regimes characterising gas-sparged stirred tanks (generally dependent upon tank geometry, gas flow rate, Q_g, and impeller speed, N) are defined as flooded, loaded, completely dispersed,

and gas recirculation (Nienow, et al., 1985). In flooded condition ($0 < N < N_f$), minimum dispersion is achieved, and a plume of gas rises centrally close to the impeller. At higher impeller speeds, when $N_f < N < N_{cd}$, the system is in the loaded regime: the gas is more radially distributed but does not occupy the entire volume of the tank due to the buoyant forces exceeding the radial drag force given by the impeller action. In the completely dispersed regime ($N_{cd} < N < N_r$) the gas is well dispersed through the whole reactor at low power. Beyond N_r, the full gas recirculation regime is observed. The two dimensionless numbers used to characterise the operating regime are the Froude number $\left(Fr = N^2 D / g\right)$ and the Flow number (Warmoeskerken and Smith, 1985) $\left(Fl = Q_g /(ND^3)\right)$ and based upon these parameters a characteristic regime chart (Middleton and Smith, 2003) can be drawn to identify the operating regime.

Many empirical correlations have been published to estimate gas hold-up. Based on the parameters described above and the Reynolds number $\left(Re = \frac{ND^2 \rho}{\mu}\right)$, Smith (1991) proposed a correlation for tanks with T > 0.44 m:

$$\varepsilon_g = 0.85 (Re \cdot Fr \cdot Fl)^{0.35} \left(\frac{D}{T}\right)^{1.25} \qquad \textbf{(2.1)}$$

Another common approach to predict gas fraction in agitated vessel refers to the power dissipated by the impeller:

$$\varepsilon_g \propto \left(\frac{P_g}{V}\right)^A \upsilon_s^{\ B} \qquad \textbf{(2.2)}$$

The parameters A and B are system dependent but generally are within the range of 0.2-0.7 with a higher value for A in the case of non-coalescing systems compared with coalescing systems (Yawalkar et al., 2002).

For three-phase mixing, many studies have been carried out with focus on solids suspension and effect of gas presence on the Zwietering "just suspended" impeller speed (Zwietering, 1958), N_{js}, defined as:

$$N_{js} = S\nu^{0.1}d_p^{0.2}(g\Delta\rho/\rho)^{0.45}X^{0.13}D^{-0.85} \qquad \textbf{(2.3)}$$

It is reported that the presence of gas, unsurprisingly, affects suspending power of the impeller (Kasat and Pandit, 2005) and that in three-phase systems the solid suspension mechanism is mainly determined by the gas-liquid interaction hydrodynamics at the impeller blade (Rewatkar and Joshi, 1991). For this reason, it is usually advised that the $N_{js,g}$ in presence of gas is higher than N_{js} in the bi-phasic system (Nienow and Bujalski, 2002). Studies conducted by different researchers have shown various different effects of solids presence on the gas holdup depending on relative density and solid concentration (Bao et al., 2006); Chapman (Chapman et al., 1983b) reports no significant influence on gas distribution in presence of solids for X lower than 20%.

2.2.2 ERT for gas hold-up

ERT has been applied to reconstruct the gas volume fraction over the height of the tank and to calculate overall hold-up. Maxwell's model given in Equation (2.4), was used to compute gas volume fraction ε_g within the tank (Maxwell, 1881):

$$\varepsilon_g = \frac{\left[1 - \left(\dfrac{\sigma_m}{\sigma_c}\right)\right]}{\left[1 + 0.5 \cdot \left(\dfrac{\sigma_m}{\sigma_c}\right)\right]} \tag{2.4}$$

Where σ_c is the conductivity of the continuous phase and σ_m the conductivity of the biphasic mixture. An alternative approach was proposed by Montante and Paglianti (Montante and Paglianti, 2015) and applied extensively by Jamshed (Jamshed et al., 2018), which used a dimensionless conductivity ε ($\varepsilon = 100(1 - \sigma_m / \sigma_c)$) proportional to the gas hold-up to describe sparging performance of different impellers, however the authors indicate this parameter as proportional to the gas hold-up and not as an absolute value. Furthermore, in the investigated range of gas hold-up (approximately 1-15%), the simplification used by Montante (Montante and Paglianti, 2015) can be considered proportional (with a factor of approximately 0.7) to the Maxwell's equation. For this reason, Maxwell's equation is used in this work. Limitations to the application of this method could be encountered when approaching very high or very low (next to monophasic) hold-up.

2.3   Materials and Methods

2.3.1 Stirred tank configuration

The investigated system for two-phase and three-phase experiments was an agitated cylindrical Perspex tank equipped with a ring sparger at the bottom of the vessel. The tank, with diameter T, was equipped with four baffles with width B equal to $T/10$. The impeller used in this study was a stainless steel six blade Rushton Disc Turbine (RDT-6) with diameter 0.056 m (D/T= 2/5), additional information on system design is given in Table 2.1.

Table 2.1 – Geometric properties of stirred tank

Vessel Property	Ratio with Tank Diameter, T	Absolute Value (m)
Tank Diameter, T	-	0.14
Impeller Diameter, D	2/5	0.056
Baffle width, B	1/10	0.014
Impeller clearance, C	4/14	0.04
Fluid Height, H	3/2	0.21
Ring sparger diameter	7/10	0.04

The impeller was earthed to the tomographic acquisition system to reduce electro-magnetic disturbance on the imposed electric field. In order to cover all the electrodes within the vertical linear probe, the liquid level H was set to 0.21 m (H/T=3/2).

Nickel nitrate hexahydrate (99,99% Sigma Aldrich®) solution in demineralised water, having a conductivity of 2.7 mS cm^{-1}, was used as the liquid phase. Air was sparged into the tank using a metal ring sparger located at the bottom of the vessel concentric with the impeller shaft. The diameter of the sparger was 0.04 m; designed smaller than the impeller diameter in order to allow the rising bubbles to be caught in the radial flow induced by the impeller (Middleton and Smith, 2003). The ring was equipped with 8 orifices of diameter 0.5 10^{-4} m and connected to a compressed air source. The air flow rate was set within a range of 8.33×10^{-5} - 16.7×10^{-5} m^3 s^{-1} using an inline rotameter, corresponding to 1.5 and 3 vvm respectively. In Figure 2.1, the operating conditions are reported in a *Fr-Fl* chart redrawn from Middleton (Middleton, 1997). The boundaries between the flow regimes are obtained by the equations reported in (Lee and Dudukovic, 2014; Nienow, et al., 1985).
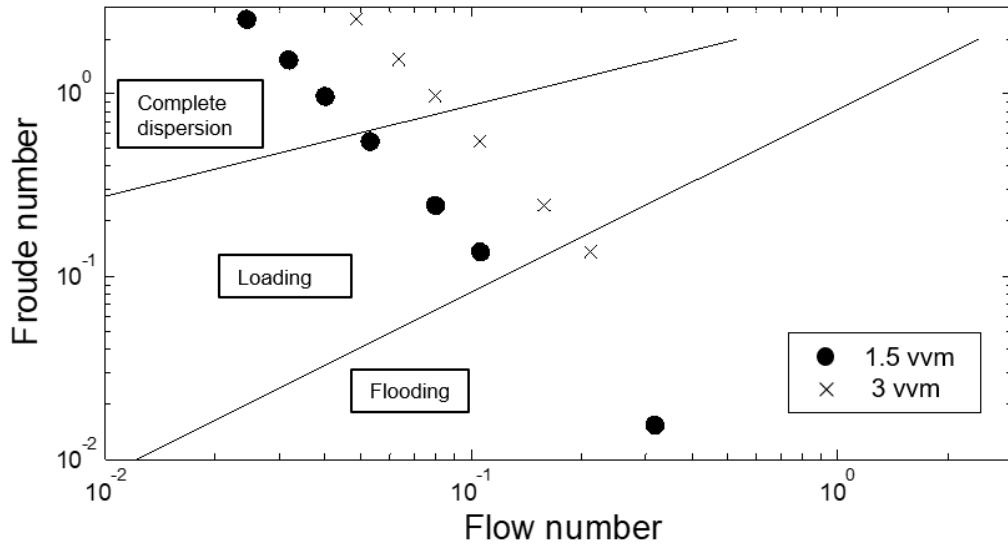
Figure 2.1 – Flow map for the Rushton turbine with operated condition at different gas flow rate redrawn from Middleton et al. (Middleton, 1997). The desirable condition is the top left region, where the complete dispersion is. This regime allows high surface contact between the phases. Moving towards the centre of the plot, the loading condition guarantees less volume of the tank covered by the gas bubbles, making the dispersion less performing. On the bottom right the flooding condition has the worse gas dispersion through the tank; the gas bubbles have large dimension and leave the tank flowing through the impeller shaft.

Flow number was varied between 0.024 and 0.32, whilst the value of *Fr* was kept between 0.016 and 2.5. The Reynolds number was thus between 15,000 and 60,000 ensuring the system was maintained in the turbulent regime.

For the three-phase mixing experiment, stainless steel particles were used as dispersed phase (ρ_s = 8000 kg m^{-3} and particle size between 0.177×10^{-3} and 0.420×10^{-3} m) at concentrations of 3, 4 and 5 % w/w. Conductive particles have been chosen for having an opposite effect on conductivity compared to the gas. The "just suspended" impeller speed was calculated using the Zwietering correlation (2.3). The achievement of such state was optically verified with particles being present on the bottom of the tank for not longer than 2 seconds. Biphasic

measurements (solid-liquid) were taken at different impeller speeds (1/3 N_{js}, 2/3 N_{js} and N_{js}) for comparison with the three-phase measurements. The effect of gas on suspending potential of the system was taken into account correcting the N_{js} speed as suggested by Nienow (Nienow and Bujalski, 2002), resulting in an insignificant increase in the investigated conditions (3 rpm at the most).

2.3.2 Measurement Configuration

The ERT apparatus used in the experiments is comprised of a linear probe and a four-channel p2+ Data Acquisition System (DAS) supplied by Industrial Tomography System (ITS Ltd., Manchester, UK). The linear probe was equipped with 18 electrodes arranged in a 140 mm long strip as shown in Figure 2.2(a, b).
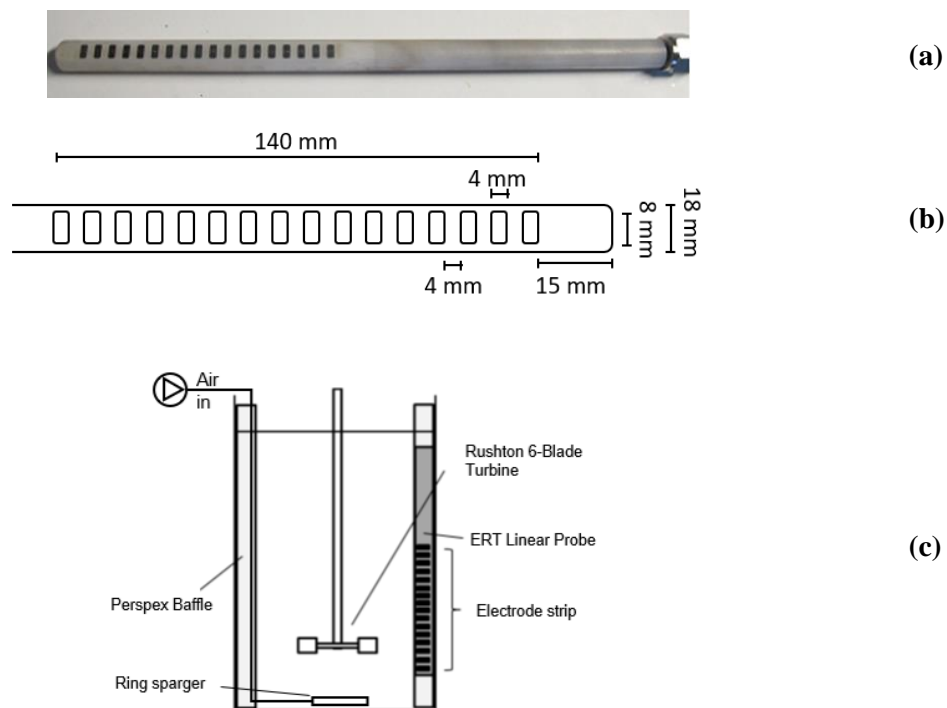
Figure 2.2 – Picture (a) and schematic (b) of the ERT linear probe and (c) its position in the tank (Clark, 2016). The probe covers the lower part of the tank and requires that all the electrodes are covered by the liquid. Its field of view covers approximately from the wall to the centre of the tank. Tank design details are reported in Table 2.1.

The stainless-steel electrodes are uniformly spaced 4 mm apart and have a width of 8 mm and a length of 4 mm. The bottom and the top electrodes do not actively take part in the measurement, instead they are earthed and act as guard electrodes. The polyether ether ketone (PEEK) support forming the body of the probe, isolates the coaxial cables that connect each electrode to the DAS, from the aqueous system.

The linear probe was placed behind one of the baffles (in the direction of impeller rotation), to minimise its influence on the flow field, as shown in Figure 2.2(c). The electrode array was placed so that it faces the interior of the vessel across a chord to avoid the noise caused by the stirrer. The latter was grounded to the DAS to avoid any electric potential difference between the mixing equipment and the tomographic apparatus. The portion of fluid covered by the ERT extends approximately 70 mm from the surface of the probe and the obtained output is a tomogram 10×20 pixels in size (specified by the supplier). The field of view of the probe extends from the baffle to the impeller zone, however the penetration is a function of the gas hold-up and will decrease dramatically in case of very high gas hold-up. In this work, where hold-up does not exceed 20%, the penetration is considered constant throughout the investigated cases, and equal to the minimum suggested by the manufacturer.

The excitation scheme is analogous to the traditional cage geometry: each pair of adjacent electrodes is used to input a current through the fluid, while the potential difference is measured for each pair of remaining neighbour electrodes along the sensor. The acquired data are processed using the ITS p2+ software that runs a Linear Back Projection (LBP) algorithm in order to reconstruct the conductivity distribution across the field of view of the probe. The chosen algorithm guarantees a fast response and has been previously applied in similar studies for gas liquid (Montante and Paglianti, 2015; Takriff et al., 2013) and solid-liquid (Hosseini et

al., 2010). The intensity of the injected current was 30 mA for all the experiments and the frequency was kept at 9600 Hz and 60 frames were taken at each condition.

The probe was specifically selected to evaluate axial conductivity in the stirred tank and to guarantee certain flexibility in installation. Unlike the circular cage, its geometry causes the covered portion of space to not have the same electric field density: the periphery of the probe (top and bottom) has a lower density of measurement than the central region. The effect of this is that the accuracy of the projected image is not uniform, with the top and bottom corners away from the probe reported as having poor reliability (Bolton, 2006). Previous investigations (Forte et al., 2016) suggest the periphery of the tomogram is characterised by low reliability due to the linear geometry of the sensor, therefore in the conducted data processing, the tomograms are reduced to an 8×16 pixel grid. Specifically, the top and bottom two rows and the last two columns of pixel are removed from the analysis.

The tomograms are commonly displayed using conductivity scale, showing zones with higher or lower conductivity. To facilitate reading of gas volume fraction, the tomograms were converted into local gas hold-up tomograms, by applying Maxwell's equation (2.4) to each pixel, taking a reference values obtained from monophasic runs. Figure 2.3, in which tomograms are represented using a smoothing graphical tool, gives an example of a tomogram converted from conductivity to gas hold-up map.

(a)

(b)
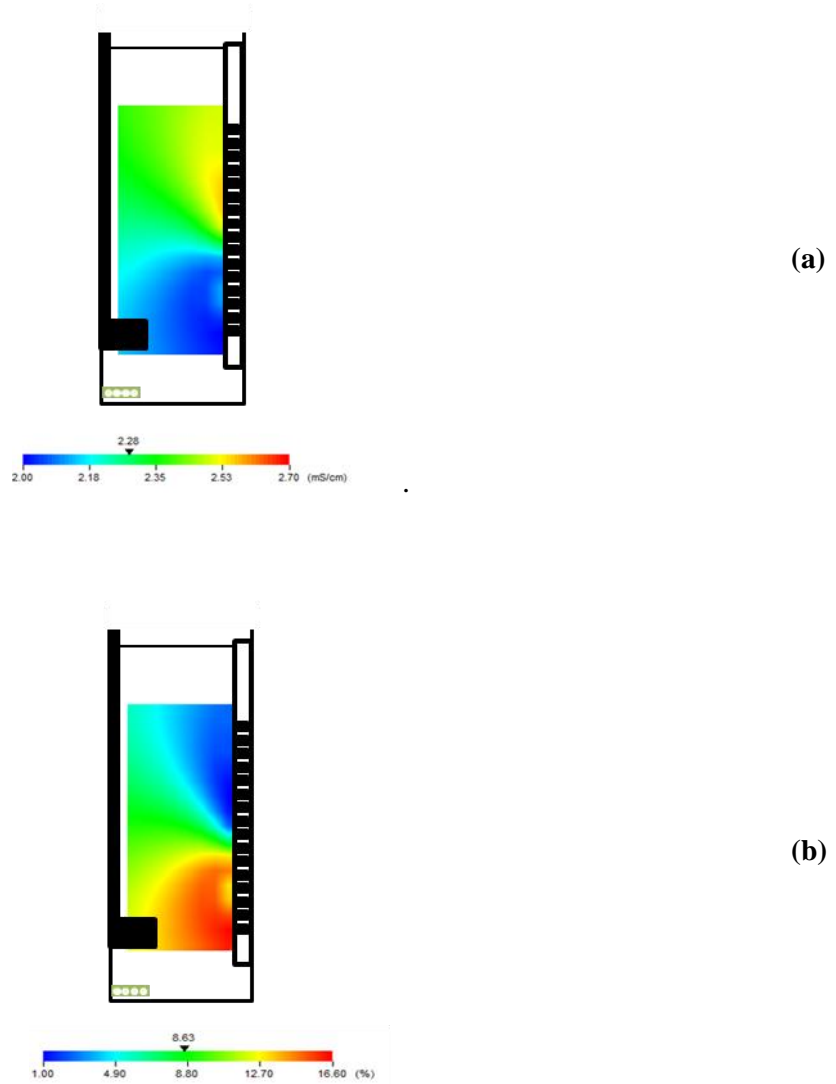
Figure 2.3 – ERT tomograms representing conductivity map (a) and gas holdup (b). The tomograms are reported with a scheme of the tank for identifying the measurement covered area. It is also reported in black the impeller, in grey the gas sparger. The condition used as example in this figure is the loading regime.

2.4   Results and Discussion

2.4.1 Two phase Gas-Liquid Mixing

2.4.1.1   Global gas hold-up

To evaluate the impact of gas presence on the average conductivity across the tank, a monophasic test was run with gas feed valve shut and the impeller speed was varied between

0 and 1300 rpm. In Figure 2.4, a flat trend is visible up to 1000 rpm, after which the average

conductivity moves towards lower values because some air is entrained at the surface. In the

same figure, conductivity values derived from the ERT measurement, with standard deviation

error bars are shown for the bi-phasic system at the two different gassing rates used.
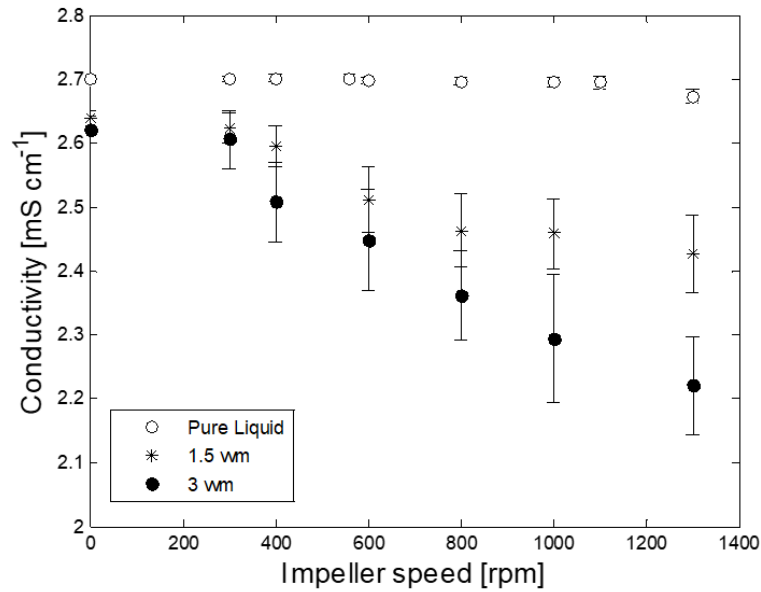
Figure 2.4 – Average conductivity for monophasic and biphasic system at different impeller speeds. The pure liquid presents a constant conductivity even when increasing the impeller speed. Instead, the gassed condition sees a decrease in conductivity as the impeller speed is increased.

The higher the feed rate, the lower the detected average conductivity, indicating an increasing

gas hold-up. The same trend is observed when the impeller speed is increased. The obtained

values for conductivity are converted into gas hold-up data applying Maxwell's Equation

(2.4). In Equation (2.4), the used value for conductivity for mixture and continuous phases

are taken at corresponding impeller speeds. Figure 2.5 plots interpreted global gas phase

fraction against the product of the Froude number, Fr, the gas flow number, *Fl,* and impeller

Reynolds number, *Re*, according to Equation (2.1).

In Figure 2.5, as proposed by Smith (Smith, 1991), the calculated values can be approximated by a straight line. The calculated gradient for this experimental dataset is 1.8, different from the value of 0.85 derived by Smith. Nonetheless, the work reported by Smith was on a larger system (T > 0.41 m), and it can be reasonably argued that the size of tank may affect the proportionality constant as well as the different properties of the used aqueous solution. More importantly, it should be noted that the holdup data derived from ERT measurements correspond well to Smith's linear hypothesis, leading to the conclusion that the observed trend well represents the evolution of gas retained in the liquid bulk.
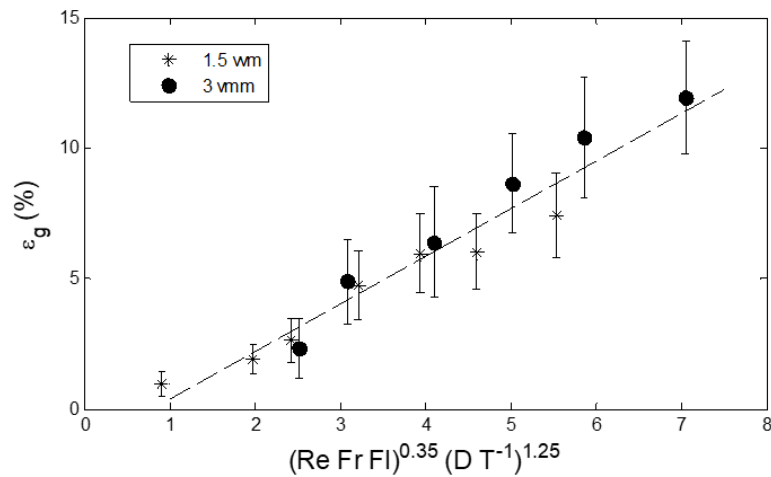
Figure 2.5 – Global gas holdup values at 1.5 and 3 vvm. (Equation of trend line: y = 1,8182x - 1,4008; R² = 0,9161). On the x-axis the correlation derived by Smith (1991).

2.4.1.2   Local gas hold-up

The linear probe geometry allows the use of ERT to visualise in real time (measurement frequency up to 50 s^{-1}) the presence of gas in the tank and to assess quantitatively the homogeneity of distribution within the tank.   Figure 2.6 shows a comparison between

tomograms and images taken by a camera for the different flow regimes obtained for the lower gas feed rate (1.5 vvm).
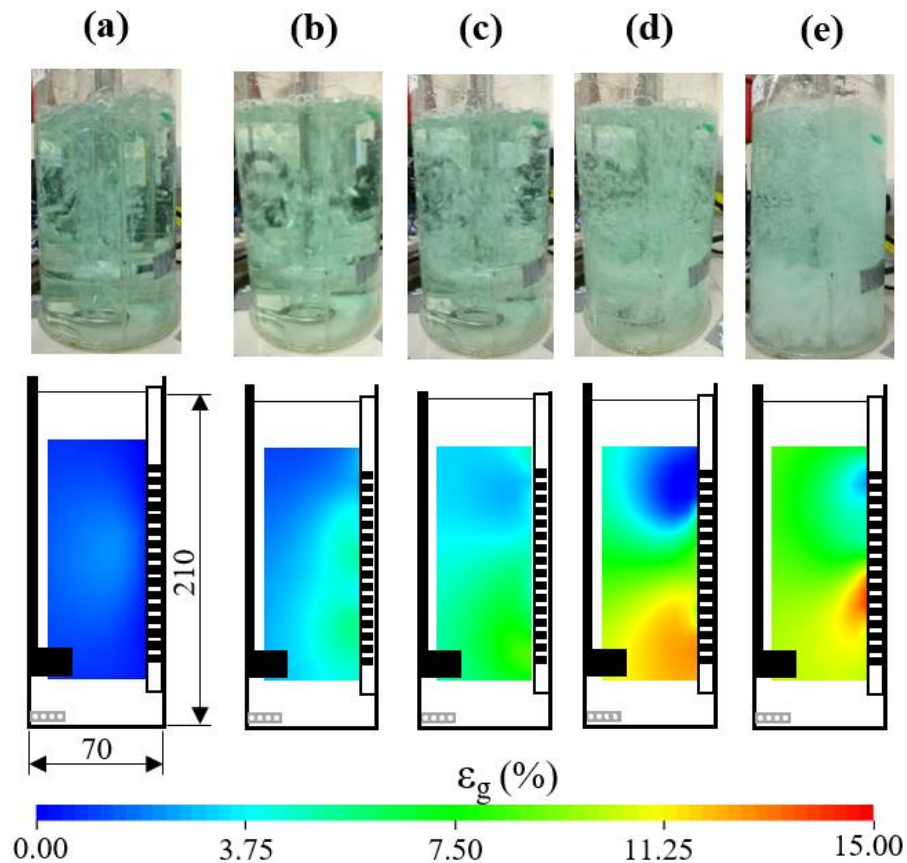
Figure 2.6 – Comparison of pictures and conductivity tomograms for flooding (a), loading (b, c) and completely dispersed (d, e) for 1.5 vvm. The tomograms are reported with reference to their position in the tank. It is highlighted in the figure: the position of the impeller on the left, the gas sparger on the bottom and the liquid level at the top. The gas dispersion performance improves as the regime moves from the flooding though the loading to the complete dispersion conditions (left to right).

The effect of increasing the impeller speed, as expected, cause the total hold-up to shift towards higher values, as noticeable comparing the colour shift from blue (low values) towards red (higher values). In particular, the impeller zone seems to be most influenced.

Similar effects can be seen in Figure 2.7, reporting pictures and gas hold-up tomograms for the different regimes but with a gas feed rate of 3 vvm.
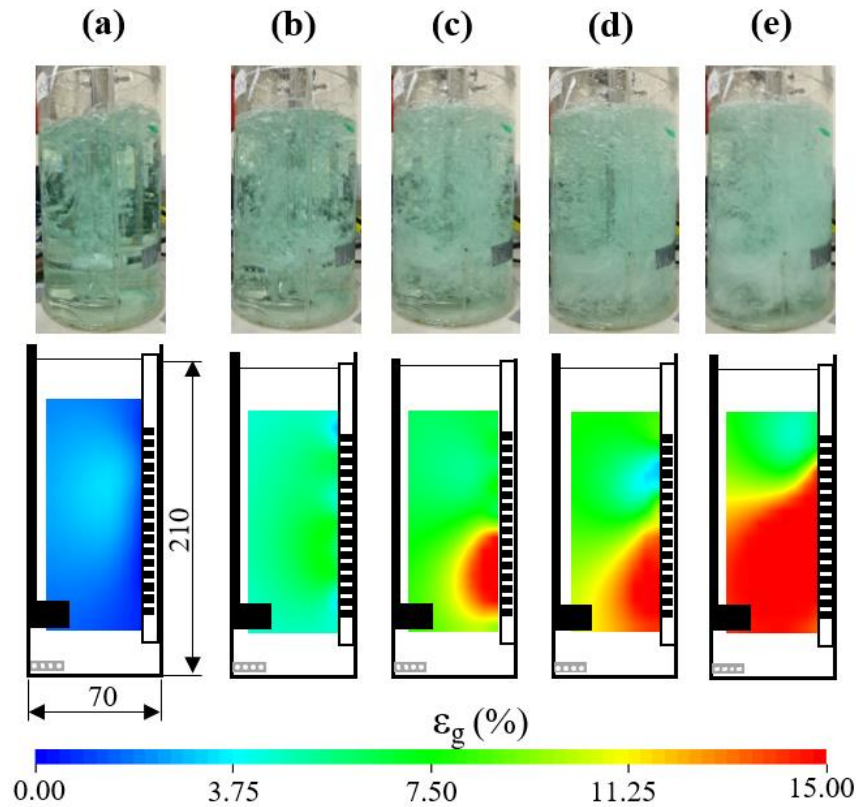
Figure 2.7 – Comparison of pictures and conductivity tomograms for, flooding (a), loading (b, c) and complete dispersion (d, e) for 3 vvm. The tomograms are reported with reference to their position in the tank. It is highlighted in the figure: the position of the impeller on the left, the gas sparger on the bottom and the liquid level at the top. The gas dispersion performance improves as the regime moves from the flooding though the loading to the complete dispersion conditions (left to right).

A direct visual comparison can be drawn between the two figures. As would be expected, increasing the air flow rate causes an increase of gas hold-up, although in both cases the distribution has a similar profile, with the gas volume fraction decreasing towards the top of the tomogram (and thus the tank).

To better visualize the variation of the gas fraction over the height of the vessel, an axial gas hold-up plot can be obtained, shown in Figure 2.8, by averaging the pixel values along each horizontal row in the tomogram.
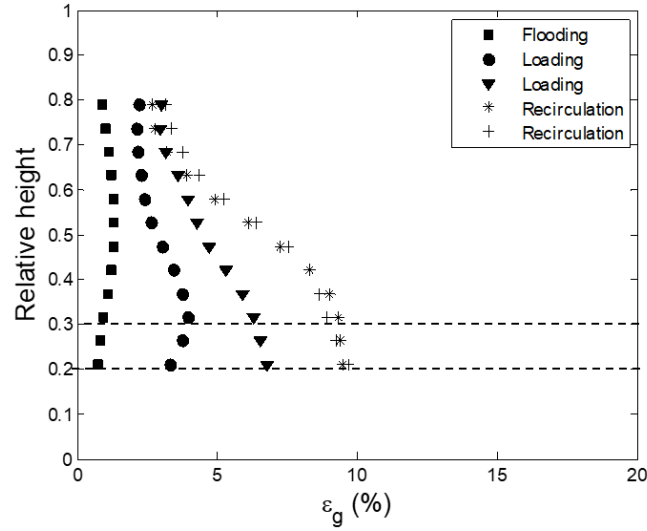
(a)
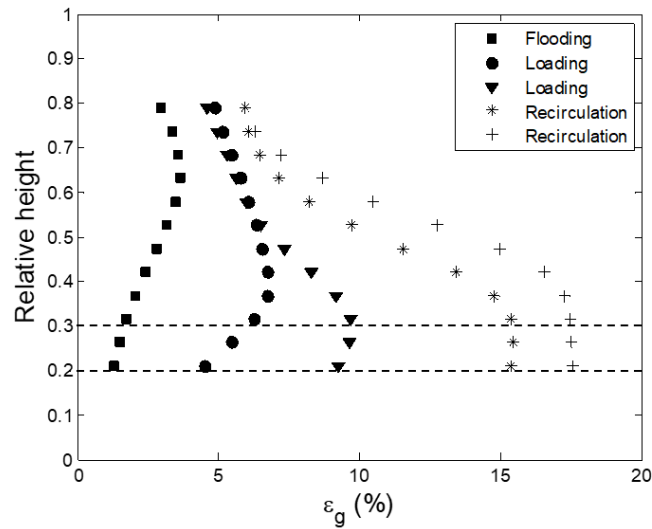
(b)

Figure 2.8 – Axial gas hold-up at Flooding (Fr=0.016, Fl=0.32), Loading (Fr=0.11, Fl=0.14 for circles and Fr=0.24, Fl=0.080 for triangles), and Recirculation regimes (Fr=0.98, Fl=0.040 for asterisks, and Fr=1.5 Fl=0.032 for crosses), for 1.5 vvm (a); axial gas hold-up at Flooding (Fr=0.14, Fl= 0.21) Loading (Fr= 0.24 Fl=0.16 for circles, and Fr=0.55 Fl=0.11 for triangles) and Recirculation regimes (Fr=1.5, Fl= 0.063 for asterisks, and Fr=2.5 Fl=0.049 for crosses) for 3 vvm (b). The dashed lines delimit the impeller zone.

Figure 2.8 emphasizes observations made, that similar trends are obtained for 1.5 and 3 vvm, with the latter having significantly higher gas retention. The profile is relatively flat at low impeller speeds (in flooding condition), with the impeller having little effect on gas

dispersion: the gas flows along the shaft, with a slightly higher hold-up towards the top of the tank. At loading, the profile gains more inflection, with hold-up increasing in the impeller region. It can be observed that the higher the value of impeller speed, the higher is the gas concentration around the impeller. This parabolic profile in the impeller area is due to the gas capture caused by the impeller motion (Van't Riet and Smith, 1975). The increase in impeller speed has relatively less effect on dispersion towards the top of the tank and even at complete dispersion regime gas hold-up does not exceed 5% and 8% at the top of the tank, for the lower and higher gas rates respectively.

2.4.1.3   Comparison with literature

Axial gas hold-up profiles extracted from Ford's X-ray (Ford et al., 2008) and Khopkar's (Khopkar and Ranade, 2008) γ-ray tomography and CFD are compared with data obtained using ERT at similar regimes, in Figure 2.9. Given the difference in set up of the different studies as well as hard rather than soft field measurement methods, this comparison has the objective of validating the capability of ERT to detect meaningful gas hold-up profiles and at the same time, to analyse its limitation in accurately representing axial variations in gas distribution.
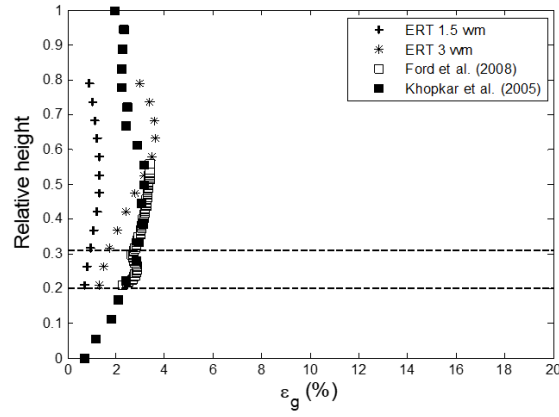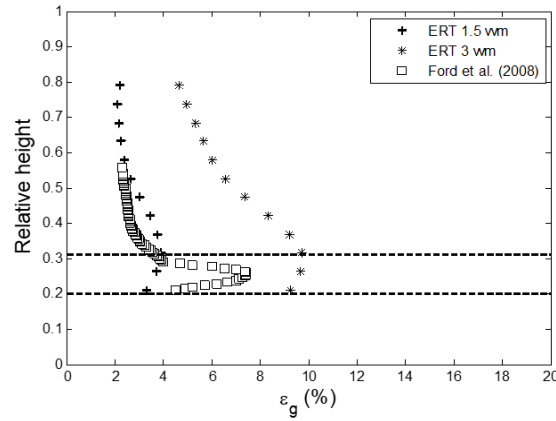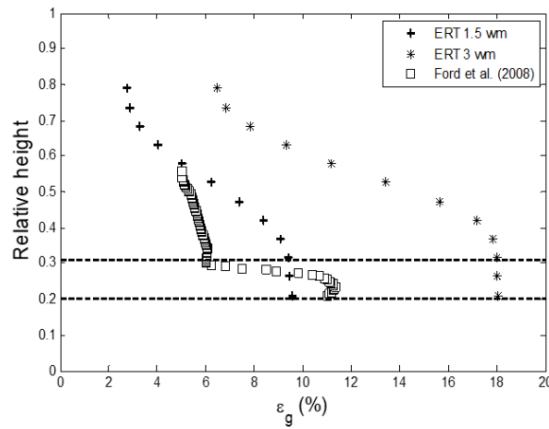
Figure 2.9 – Comparison of axial gas hold-up between ERT experimental data and data from the literature at different regimes: flooding (a), loading (b) and complete dispersion (c), with the dashed lines delimiting the impeller zone. In (a) the comparison includes Khopkar et al. (2005) CFD and Ford et al. (2008) experimental data . The gas dispersion profile is flat as the impeller fails in sparging the gas radially. In (b) Ford et al. (2008) data are compared to ERT measurements. The gas dispersion is improved particularly at the impeller. In (c) the two datasets are compared at complete dispersion with similar profiles in terms of relative shape rather than in absolute terms.

CT and CFD data are compared with ERT at flooding condition (Figure 2.9(a)). As expected at this regime, the axial profile is rather flat, with air flowing axially through the impeller and along the shaft; sometimes also referred to descriptively as "bubble column mode". Data from the three studies agree with the theoretical expectation and describe similar profiles. Gas hold-up does not exceed 4% and its maximum can be located approximately at half way up the tank, with little or no axial variance.

Increasing the impeller speed, moving to the loading condition, the gas now locates mainly around the impeller where is "thrown" radially by the impeller. Visually, bubble size decreases, and the gas covers a higher portion of the tank, as was shown in the corresponding tomograms reported in Figure 2.6(b,c) and 2.7(b,c). This condition is picked up in the axial plots (Figure 2.9(b)) where both data from the literature and ERT show an overall increase in hold-up compared to the flooding condition, together with an increase in axial variance. Indeed, the impeller region is characterised by a significantly higher hold-up compared to the rest of the tank. It is possible to notice how the profile obtained by CT measurements quickly decreases tending to a constant value as exiting the impeller region; differently ERT shows a smoother trend with no sudden changes in the axial profile. Nonetheless, all studies are in agreement, indicating a significantly higher gas hold up in the impeller region.

A similar trend is observed for the complete dispersion regime. In this regime the optical images (Figure 2.6(d,e) and 2.7(d,e)) show decreased bubble size with particularly high concentration in the impeller zone. Although the ERT technique does not allow observation of the recirculation loops in the tank, it is able to capture the high gas fraction around the impeller region coming from sparging in the first place and the radial motion given by the impeller discharge and recirculation. The high-hold up is also well depicted in Figure 2.9(c) in which ERT and CT gas hold-up profiles are compared. Both techniques indicate a similar

trend to loading condition with a significant overall shift toward higher values of gas fraction. Although the comparison shows an overall condition of higher aeration achieved in this work (due to higher vvm gas rate), a good agreement in trends is observed. A smoother profile from the ERT data is again observed. This apparent smoothing is most probably related to the lower resolution of ERT and in particular to the inherent smoothing caused by the linear reconstruction applied to derive the conductivity tomograms. Nevertheless, in this comparison, ERT is not presented as a direct replacement for hard field CT in terms of accuracy for research studies, but rather as a lower cost alternative that is additionally deployable into manufacturing vessels.

2.4.2 Gas-Liquid-Solid System

The addition of stainless-steel particles to the system has an influence on the electric field generated by the ERT electrodes and therefore it affects the measured conductivity. Given the conductive nature of the used solids, the measured average conductivity increases from the monophasic condition as more solids are suspended from the bottom of the tank. This increase is however very small relative to the impact of the presence of gas. Indeed, the relative increase in conductivity at N_{js} for 5 w/w % in the solid-liquid case is approximately 0.4% while the addition of gas causes a decrease in the average conductivity between 8-20% from the base conductivity of the continuous phase. This difference can be seen in Figure 2.10 where axial profile in conductivity are shown for the Solid-Liquid run at different impeller speeds and, with a different conductivity (x axis) scale, the same runs are plotted in comparison with Gas-Solid-Liquid run at the same impeller speeds.
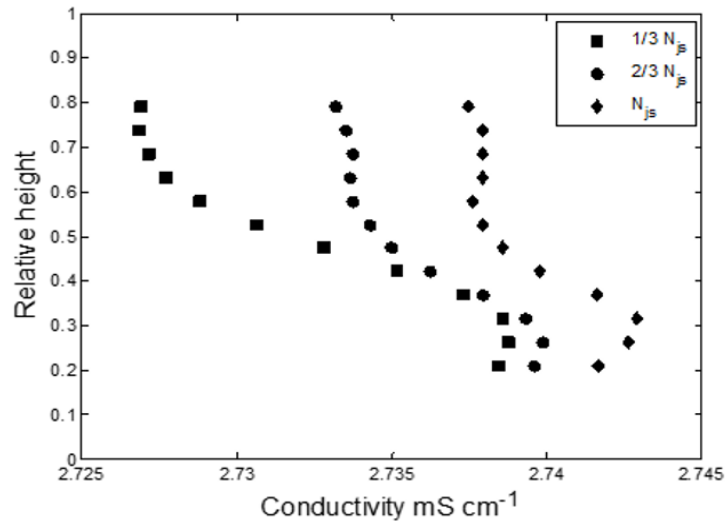
(a)
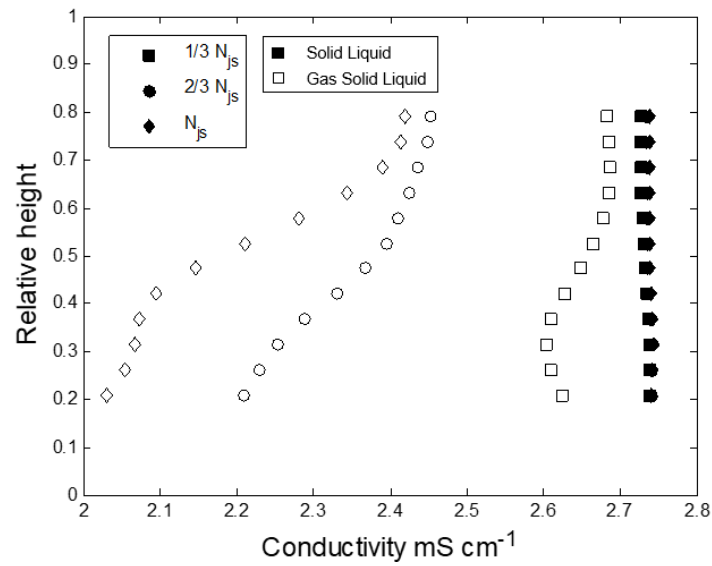
(b)

Figure 2.10 – Axial conductivity plot for 5% w/w solids content in the case of Solid-Liquid mixing (a) and in the case of Solid-Liquid mixing compared with Gas-Solid-Liquid mixing with gas feed flow of 3 vvm (b). The comparison between the two plots highlights how by adding the gassed dataset (b) the contribution given by the presence of solids (a) is negligible.

Figure 2.10(a) shows how increasing the impeller speed causes a global increase of conductivity, given by the higher number of conductive particles suspended. At 1/3 Njs, a few particles are suspended, and they are concentrated in the bottom part of the tank. Moving towards Njs, it is possible to see how the profile becomes flatter and globally higher than the profiles at lower speed. However, reaching the N_{js} condition does not guarantee a homogenous dispersion of the particles across the tank; this condition is picked up by the ERT profile that still shows higher values in the impeller region than in any other height in the tank. The obtained profiles are consistent to what observed in Carletti's work (Carletti et al., 2014) in which glass beads were suspended in aqueous solution. Although the different electrical properties of the solids used in this case cause an opposite effect on conductivity, similar trends are observed as the impeller speed is increased.

Figure 2.10(b) reports conductivity profiles for the same conditions (viz. with solids), but now with a gassing rate of 3 vvm. The scale in changes of conductivity is markedly larger with the gas. From this, it can reasonably be argued that, despite the presence of solids, the ERT system can still measure substantially the gas hold-up in the tank, with only minor influence from the dispersion of the particles.

In Figure 2.11, the trend of global gas hold-up for the three-phase case is compared with data for the Gas-Liquid only system.
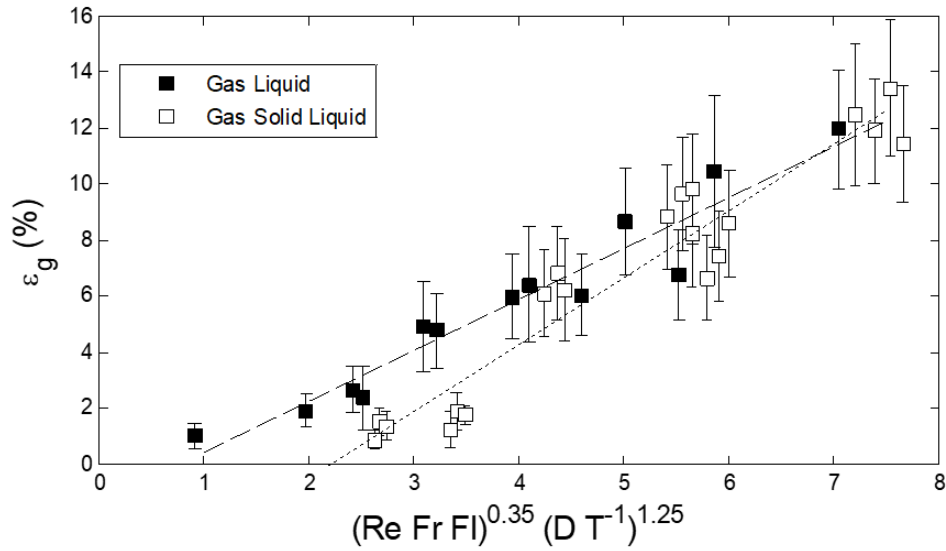
Figure 2.11 – Global gas hold-up trend for two-phase and three-phase systems. The straight line for the biphasic condition has as equation: y = 1,8182x - 1,4008 (R² = 0,916). The straight line for the three-phase condition has as equation: y = 2,3793x - 5,2467 (R² = 0,92). The major differences between the two systems are identified at low impeller speed.

The data show similar values of gas hold-up for the three-phase case at the higher impeller speeds; the right-hand side of the plot. For the condition of low agitation, however, the presence of the solids at the bottom seems to inhibit the retention of gas as already observed by Chapman (Chapman et al., 1983b). However, increasing the power provided by the impeller, the presence of solids seems to have little effect on the gas hold-up, as previously reported by Warmoeskerken (Warmoeskerken et al., 1984).

2.5 Conclusions

In this work, an ERT linear probe was used to visualize and measure gas distribution in a two-phase and three-phase stirred tank at different regimes. ERT was able to successfully measure global gas hold-up in every observable regime in agreement with predictions from the literature. Local gas distributions were also measured and agreed with measurements on

comparable systems conducted using hard-field techniques. Suspension of conductive solids was measured using ERT and it was assessed that they have little or no effect on the measurement of gas hold-up, therefore it can be concluded that the technique is suitable for measuring gas volume fraction also in presence of particles.

Differently from the traditional circular cage where the focus is on radial concentration, the chosen geometry of the probe allows to observe the axial profile of gas fraction within the tank in a quantitative fashion. The linear probe has the portability, ease of retrofitting and flexibility characteristics that make it a desirable tool for real-time measurements in an industrial environment. Overall, ERT has proven to offer, beside qualitative visual information on gas location, quantitative measurements of gas hold-up in a small scale stirred tank with high potential to be scaled for inline monitoring of multiphase operations at industrial scale.

2.6   <u>Nomenclature</u>

B	Baffles length, m
D	Impeller diameter, m
D_p	Diameter of suspended particles, m
Fl	Flow number
Fr	Froude number
g	Standard acceleration due to gravity, m s^{-2}
H	Liquid level, m
N	Impeller rotational speed, rps
N_{cd}	Complete dispersion critical impeller speed, rps
N_f	Flooding critical impeller speed, rps

N_{js}	'Just suspended' impeller speed, rps
N_r	Recirculation critical impeller speed, rps
P_g	Gassed power, W
Q_g	Volumetric gas flow rate, $m^3 \, s^{-1}$
S	Geometrical constant in Zwietering correlation
T	Tank diameter
V	Volume of the tank, m^3
v_s	Superficial velocity of the gas, $m \, s^{-1}$
X	Mass fraction

Greek letters

ε_g	Gas volume fraction
ε	Dimensionless conductivity
μ	Dynamic viscosity of liquid, $kg \, m^{-1} \, s^{-1}$
ν	Kinematic viscosity of liquid, $m^2 \, s^{-1}$
ρ	Density of liquid, $kg \, m^{-3}$
ρ_s	Density of solid particles, $kg \, m^{-3}$
$\Delta\rho$	Difference between solid and liquid density, $kg \, m^{-3}$
σ	Electrical conductivity, $mS \, cm^{-1}$

3.

Use of Acoustic Emission in combination with Machine Learning: monitoring of gas-liquid mixing in stirred tanks

Operations involving gas-liquid agitated vessels are common in the biochemical and chemical industry; ensuring good contact between the two phases is essential to process performance. In this work, Acoustic Emission (AE), using a piezoelectric sensor, was applied to evaluate the gas-liquid mixing regime within two-phase (gas-liquid) and three-phase (gas-solid-liquid) mixtures in a 3L stirred tank equipped with a Rushton Turbine and a ring sparger. The system was operated in each of the different flow regimes (non-gassed condition, loaded and complete dispersion) with the objective to use features in the acoustic spectrum to univocally identify the different conditions.

Machine learning was used to process the acquired data. The dataset was divided into a training set, used to train the machine in recognising features in the spectrum corresponding to each condition, and a testing set, unseen by the machine, used to evaluate accuracy of regime prediction. Obtained results show that the system successfully recognises acoustic spectrum corresponding to the different regimes with an accuracy higher than 90% both in absence and presence of suspended particles.

This chapter has been submitted for publication in the Journal of Intelligent Manufacturing:

Forte G., Alberini F., Simmons M. J. H., Stitt E.H., 2019, 'Use of Acoustic Emission in combination with Machine Learning: monitoring of gas-liquid mixing in stirred tanks'.

3.1   <u>Introduction</u>

Improving process monitoring is a common need within the process industry, including chemical, food, biochemical and pharmaceuticals (Boyd and Varley, 2001). Desirable features for process measurements are to be non-invasive and suitable for in-line application with real time response, in order to avoid delays in intervening with control measures. Amongst several potential sensing methods, Acoustic Emission (AE) is a low cost, data-rich technique with applicability for in-line monitoring. Traditionally acoustic techniques are categorised as either with active or passive acoustics. The former consists of a transmitter generating an acoustic wave within the system and a receiver acquiring the response of the stimulated system. The latter, also known as acoustic emission (AE), is composed only by a sensor recording acoustic waves generated by the process itself.

The signal will often be a combination of numerous acoustic events all propagating to the sensor via different paths. Most of AE research has focused on fault detection (leakage, failure, ...) (Boyd and Varley, 2001), corrosion (Cole and Watson, 2005) and tool wearing (Elforjani and Shanbr, 2018; Li et al., 2015). More recent studies have also investigated AE as a mean of monitoring physic-chemical changes within processes involving powder and fluids. For example, Aldrich et al. (2000) used directional microphones to estimate particle size in a ball mill using continuous regression. Other studies have applied AE to powder pneumatic conveying (Esbensen et al., 1998) and V-blenders (Crouter and Briens, 2015).

Applications in multiphase mixing are also reported in the literature. Nordon et al. (2004), for example, applied AE to a jacketed stirred tank for monitoring of a heterogeneous reaction. While the first known reference on gas-liquid flow dates from the 1920's (Bragg, 1921), more recent works (Addali et al., 2010) have used AE energy information to predict gas phase fraction in a two phase (air-water) slug flow. In this work, AE is applied to monitor gas-liquid mixing in a 3L stirred tank, with the objective to identify the operating bubble dispersion regime. Although, many researchers have investigated various methods to determine multiphase mixing regimes in stirred tanks in real time, as reported in subsequent sections, their applications have been limited to R&D. This is mainly due to difficulties in retrofitting the devices to existing plants as well as to slow responses. In this work, AE is applied to monitor gas-liquid mixing in a 3L stirred tank, with the objective to identify the operating bubble dispersion regime. The system is chosen as for the previous chapter (Chapter 2) to mimic in small scale a common application in the metal refining division, as leaching. The aim is to propose a methodology to obtain real time information by installing an acoustic piezoelectric sensor on the outside of a stirred tank. The data-richness and high time resolution of the used technique represent desirable features for modern control system strategies.

3.1.1 Gas-liquid mixing

Gas-liquid reactors are very common unit operations in the biochemical and chemical industries, where ensuring appropriate interphase contact and gas dispersion is critical. Different regimes are observed when sparging gas into stirred tanks; namely flooded, loaded, completely dispersed, and gas recirculation (Nienow, et al., 1985) depending on gas flow rate, tank design and fluids properties (e.g. rheology, density, interphase tension). The different regimes (shown in Figure 3.1) characterise how well the gas is sparged within the volume of

the tank: in the flooding regime the impeller speed N does not overcome the flooding critical speed N_f, therefore the gas dispersion is minimum, where a plume of gas rises from the sparger up to the surface along the impeller. At higher impeller speeds when the N is higher than N_f, but lower than N_{cd} (the completely dispersed critical speed), the system is in the loading regime; where the gas is more dispersed but does not cover the whole volume of the tank. as the radial drag force is overcome by the buoyancy forces. At higher impeller speed ($N_{cd} < N < N_r$), in the completely dispersed regime, the gas is well dispersed through the whole vessel at low power, but it is beyond N_r (the recirculation critical speed) that the full gas recirculation regime is observed. The latter two are generally the desirable conditions for unit operations requiring good contact between the two phases.
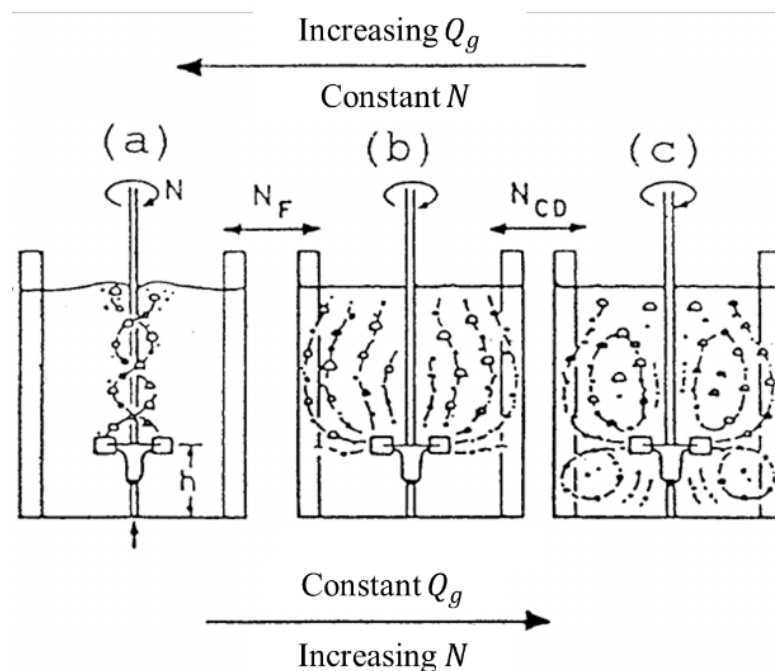
Figure 3.1 – Pictorial representation of the main gas-liquid regime: (a) flooded, (b) loaded and (c) completely dispersed (Nienow, et al., 1985). Contact between the two phases increases moving from the flooded (a) towards the completely dispersed condition (b).

Commonly, the operating regime is estimated based on a characteristic regime chart (Middleton, 1992) based on the definition of two dimensionless numbers: the Froude number

$(Fr = N^2 D/g)$, defined as the ratio of the flow inertia to the gravity field and the gas Flow number (Warmoeskerken and Smith, 1985) $\left(Fl = Q_g/(ND^3)\right)$ representing the ratio of the gas inlet rate to the impeller pumping .

3.1.2 Sensing and measurement techniques

Existing measurement techniques for identifying the different regimes are multiple, including optical (Yawalkar et al., 2002), level probes (Gao et al., 2001), ultrasonics (Cents et al., 2005; Chaouki, et al., 1997) and tomography (Electrical Resistance ERT (Forte et al., 2019b, Chapter 2; Jamshed et al., 2018), X-ray (Ford et al., 2008), γ-ray (Veera et al., 2001)), but are often limited by practical considerations (invasiveness, retrofitting, opacity, safety) and cost issues. The mentioned systems all require high investment cost in terms of devices and operations. They are also usually fixed solutions characterized by rather heavy retrofitting. Furthermore in cases of high energy based methods (X-ray, γ-ray) an additional cost is represented by the safety measures needed to ensure safe use of the technique. The AE device is, instead, composed by a simple hardware which does not require retrofitting and is also a portable solution. The sensor can be placed on a tank and moved to another quickly, being installed on the outside wall. This, together with the low investment and operational cost make it convenient to use and furthermore devoid of safety issues. The AE system applied in this study has, therefore, the potential to be a cheap, easy to install (and retrofit) alternative technique that can offer reliable information on the operating gas-liquid regime.

In this work, AE emission data are acquired at loaded and completely dispersed regimes as well as in ungassed condition, to simulate accidental shut down of air feed. Machine learning (ML) supervised algorithms are used to identify and recognize the different conditions. To evaluate the robustness of the technique in correctly identifying the operating regime, a deviation from the biphasic condition is also introduced, by adding solid particles to the bulk

up to a concentration of 5% w/w. This occurrence is not unusual in case of chemical reactions, as for example solid precipitation, occurring from mixing reactive gas-liquid mixtures in stirred tanks (Zhao et al., 2016, 2017). The presence of solids will cause an increase in the emitted signal because of impacts of the particles with the wall, the impeller and with each other, but the system will be challenged to correctly predict the gas-liquid operating regime. The regime is considered unchanged at fixed air volumetric flow and impeller speed: for low concentration (< 20% w/w (Chapman et al., 1983b)) of solids, works in the literature report little effects of the presence of the particles on the gas sparging dynamics (Bao et al., 2006; Chapman et al., 1983b).

3.1.3 Machine learning algorithms

The use of machine learning algorithms in AE applications has recently and successfully been applied by other researchers in the literature for condition monitoring of cutting tools (Chen et al., 2011; Li et al., 2015). The implementation of such techniques in chemical and manufacturing industry has recently seen increasing interest, since such data-driven and statistical approaches fit well with the smart manufacturing / Industry 4.0 trend (Wuest et al., 2016).

Techniques involving Artificial Intelligence (AI) have been applied in several fields including game playing, robotics, facial and speech recognition (Venkatasubramanian, 2019) with the first attempt to chemical engineering applications reported in the 80s for catalyst design (Bañares-Alcántara et al., 1985; 1987), an application that is still the object of current studies (Ulissi et al., 2017). Recent applications in researches of industrial interest can be found in estimation of physical properties of organic molecules (National Academies of Sciences, 2018), shape memory alloys design (Xue et al., 2016) and studies on colloidal self-assembly systems (Spellings and Glotzer, 2018). The spreading of such investigations have in the last

years interested a much wider range of operations thanks to cheaper and faster calculators and fast access to large memory storage (cloud) (Venkatasubramanian, 2019). Furthermore, also the psychological barriers within organization, both within management and manufacturing have lowered thanks to spreading of AI devices within domestic and personal application (Amazon Alexa is an example).

Many ML techniques including both unsupervised and supervised algorithms have been developed. In this study, some of the more common machine learning methods are used for processing the AE data in the frequency domain, to recognize the different operative conditions; solving a classification problem (Wu et al., 2008). The herein used algorithms are: logistic regression, support vector machine (SVM), K-nearest neighbour (K-nn) and decision tree; of which the last three were implemented in MATLAB® classification learner application within the Statistic and Machine Learning toolbox.

Logistic regression has already been applied in processing acoustic emission data for predicting reliability of cutting tools and for condition monitoring of bearing elements (Rozak et al., 2018) to provide adequate maintenance schedules (Li et al., 2015). It is a nonlinear statistical method which has been extensively used also beyond machine reliability and life prediction (Caesarendra et al., 2010; Yan et al., 2004; Yan and Lee, 2004) in the field of economics (Martin, 1977) and health (Bender and Kuss, 2010). The algorithm itself can be defined as a binomial regression (Hilbe, 2009), where the output is a probability h_θ of a condition being verified, in the specific case the belonging of the signal to one specific class. Logistic regression makes use of a logistic function, also known as sigmoid function:

$$h^i_{\theta^i}(x) = 1/(1 + e^{-\theta^{iT}x}) \tag{3.1}$$

In the equation above $h_\theta^i(x)$ is the obtained probability, that the input variable x (the AE spectrum in this study) belongs to a given class i (one of the three operating conditions). θ^i is the vector of parameters (frequency features in the spectrum), that the machine tunes in the learning step. For each condition i a parameter θ^i is obtained in the learning process. Such process consists of an optimisation on the parameter θ^i run by the machine, using the gradient descent strategy, to correctly classify the training data set. The test, instead, sees the machine providing the probability that the fed spectrum belongs to the three classes and it will assign it to the one with highest probability $h_\theta(x)$.

The decision tree algorithm (Murthy, 1998) has a node structure for addressing the classification problem using hierarchical, sequential binary classifications. The tree structure is built with an increasing number of nodes moving from the top of the tree towards the bottom branches. The nodes composing the tree are ranked during the learning process where the features flagged as highly informative are positioned at the top nodes of the tree; moving towards the bottom level features, where less informative scores are placed. This algorithm is widely used because of its transparent mechanism that helps users to visualise how the classification algorithm takes its decision (Jang, 1993). Among different decision tree algorithms (Kotsiantis, 2007), one of the most frequently used due to its effectiveness and simplicity, is the Iterative Dichotomiser 3 (ID3) (Soofi and Awan, 2017). This algorithm is described by a parameter called maximum number of splits, which is a control parameter of the final depth of the tree (Safavian and Landgrebe, 1991): the higher this number, the larger, more detailed and complex will be the tree. Within MATLAB® Classification Learner toolbox, two decision tree algorithms were selected for test based on this control parameter: fine tree (100 maximum number of splits) and medium (20 maximum number of splits).

A different classification logic characterises the k-Nearest-Neighbour (k-NN) algorithms (Cover and Hart, 1967). Each instance is assigned to a certain class based on the class to which its nearest neighbours belong. The principle is that, in the vector space defined by the number of used features, instances within a dataset will be closer to instances belonging to the same class. The definition of distance between data points was computed using the Euclidean definition (Wu and Zhang, 2002), although many other methods can be used (Canberra, Chebyshev, Minkowsky etc.) (Prasath et al., 2017). One of the critical parameters defining the algorithm is k which describes the number of nearest neighbours that the algorithm considers in assigning each instance to a class. In this work, three values of k are used for the analysis: 1 (termed as fine k-NN), 10 (medium k-NN) and 100 (coarse k-NN). k-NN algorithms are widely used in applications such as face recognition (Kasemsumran et al., 2016), traffic forecasting (Zhang et al., 2013) and speech recognition (Rizwan and Anderson, 2014), achieving high performance when large training datasets are available. It is robust to noisy data and easy to visualize, but it often requires large memory allocation (Soofi and Awan, 2017).

Support vector machine (SVM) is considered one of the most accurate and robust algorithms among the common methods (Vapnik, 2000). It is an efficient and quick method, especially in the training step. Given a dataset, SVM finds the best classification function that divides the instances in two classes. The "best" function is identified geometrically and can be a hyperplane in the case of linear classification, or it can have different shapes depending on the definition of the kernel function that characterises the method. Amongst others, this function may be linear, parabolic, hyperbolic. Defined the kernel function, the SVM finds the parameters within this function that maximise the margin between the classes (Suykens and Vandewalle, 1999). The margin corresponds to the shortest distance between the closest

69

points to the boundary hyperplane function. SVM is able to deal with a large variety of classification problems including high dimensional and non-linear problems (Soofi and Awan, 2017). Although SVM is very powerful, it is difficult to visualise (Karamizadeh et al., 2014) and require accurate often a priori selection of a number of parameters within the kernel function.

Among the wide spectra of algorithms and kernels available in the literature, in this work, some of the most established methods are used to process data-rich AE signal in order to identify the operating gas-liquid regime in two-phases and three-phases conditions. The objective is to develop a flexible method that can be extended to different systems and evaluate expected accuracy using a supervised machine learning approach.

3.2   Material and Methods

3.2.1 Stirred tank configuration

The agitated system, already used by Forte et al. (Forte et al., 2019b, Chapter 2), was a cylindrical Perspex tank equipped with a gas sparger (ring shape) at the bottom of the tank. The vessel, having a diameter, T, of 0.14 m, was equipped with four Perspex baffles with width, B, equal to $T/10$. A stainless steel six blade Rushton Disc Turbine (RDT6) with diameter $D = 0.056$ m ($D/T = 2/5$) was used for stirring. The used liquid was an aqueous solution of Nickel nitrate hexahydrate (99,99% Sigma Aldrich®) (as reported in Chapter 2) and its level was set to 0.21 m ($H/T=3/2$). In Figure 3.2 a schematic of the tank is reported, together with the AE measurement device scheme.
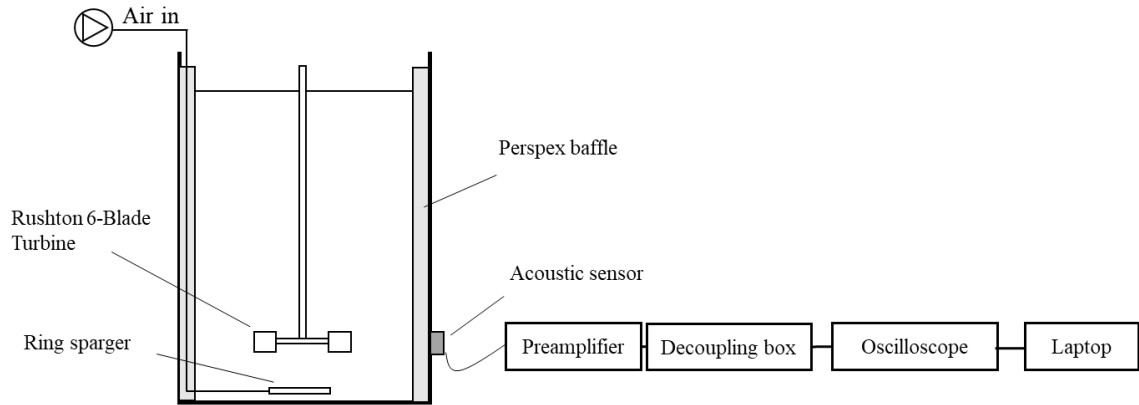
Figure 3.2 – Schematic of the stirred tank and the AE equipment. The acoustic piezoelectric is placed on the outside of the vessel at the impeller height. The sensor is connected to a preamplifier, a decoupling box and an oscilloscope. The oscilloscope transforms the electric signal in digital signal and transfers the data to a laptop where the data are recorded and stored.

The air flow (ranging between 5-10 L min^{-1}, corresponding to 1.5 and 3 vvm respectively) was fed from a ring sparger positioned at the bottom of the tank and equipped with 8 orifices of 0.5 mm. During the different experiments, the Reynolds number was kept between 15,000 and 60,000 in order to have, in all cases, turbulent regime. The impeller speed (300-1300 rpm) and the gas flow rate were changed to set one of the operating regimes (loading, complete dispersion) and then the same conditions of impeller speed were recorded with no air fed to the system (to mimic failure of gas feed unit). The achievement of the different regimes was theorised using flow regime maps and visually checked throughout the experiments, (using optical methods as per (Forte et al., 2019b, Chapter 2)). In Table 3.1, operating conditions for the different regimes are reported.

Table 3.1 – Operating conditions for the different regimes.

Regime	Fr	Fl	Impeller speed N (rpm)	Air flow rate Q_g (vvm)
Ungassed	0.24-2.55	-	400-1300	-
Loading	0.24-0.55	0.08-0.0529	400-600	1.5-3
Complete dispersion	1.0-2.55	0.0244-0.08	800-1300	1.5-3

In the three-phase experiment, stainless steel (AISI 316) spherical particles (Alpha Aesar ©) were used as solid phase. The particles, used at concentrations of 3, 4 and 5 % w/w had a density ρ_s of approximately 8000 kg m^{-3} and size between 0.177 and 0.420 mm. The same operating points as for Table 3.1 were taken.

3.2.2 Acoustic emission

The used apparatus has been assembled as for similar works in the literature (Nordon et al., 2004): a piezoelectric sensor (Vallen Systeme GmbH, Icking, Germany) with resonance frequency of 375 kHz and diameter 20.3 mm, was attached to the tank using a silicone based vacuum grease to ensure acoustic coupling with the tank. A preamplifier (40 dB gain, Vallen Systeme GmbH) was also part of the measurement rig as well as a decoupling box (Vallen Systeme GmbH) that removed the electrical noise introduced by the preamplifier before feeding the signal to the oscilloscope (5243A Pico® Technology Limited), used to record data, arranged as for Figure 3.1. The sensor was placed on the vessel outside wall at a height of 0.04 m from the bottom of the tank, corresponding to the impeller region. Twenty-five measurements at each combination of impeller speed and gas flow rate were taken for 0.2 s with a sampling rate of 1000 kHz, over a maximum recording capability of 20 MHz.

3.2.3 Data processing and Machine Learning

The purpose of the present work is to develop a methodology to interrogate the information from the acoustic spectrum to determine the operating regime based on a previously trained model. The acquired signals were pre-processed before they were fed to the machine learning algorithm. A schematic summary of the data processing is shown in Figure 3.3.
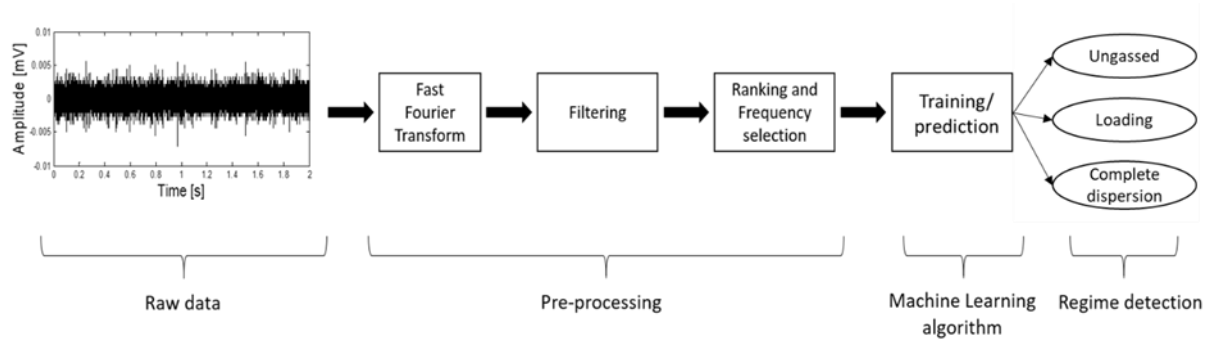
Figure 3.3 – Flow diagram summarising the data processing of AE signal. The raw data acquired in the time domain are transformed using the Fast Fourier transform. The data in the frequency domain are then filtered and the data dimension is reduced by selecting the data belonging to the most variable frequency. These are then fed to the machine learning algorithms for training and prediction.

The time-domain signals were processed using the Fast Fourier Transform function (Cooley et al., 1969) to obtain the corresponding dataset in the frequency domain. Examples of time domain and frequency domain signals for loading and complete dispersion conditions are reported in Figure 3.4.
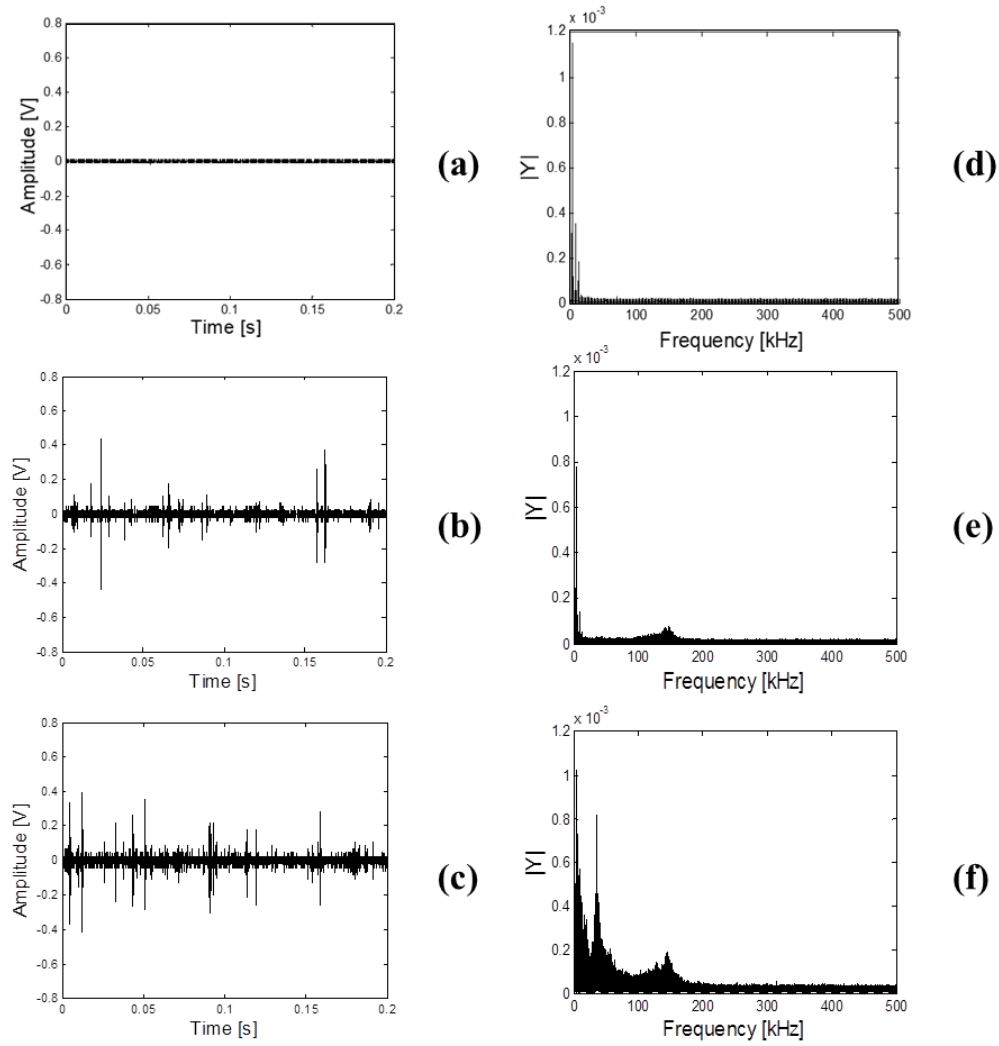
Figure 3.4 – Time domain (a,b, c) and frequency domain (d, e, f) signals for ungassed(a,d), loaded (b,e) and complete dispersion conditions (c,f). The first row shows the ungassed condition: gas is not sparged and the acoustic waves produced by the stirring of liquid does not excite the acoustic sensor, the only frequency visible in the spectrum (b) is given by environmental noise and is present in all three conditions. When gas is sparged in both loading (b) and completely dispersed (c) regimes, the interactions between the two phases produce detectable signal. The two conditions are not clearly distinguishable in the time domain, while in the frequency domain the completely dispersed (f) regime presents peaks at 40-50 kHz, not visible in the loading regime (e).

A feature scaling and mean normalisation were then applied to the obtained spectra, in order to have values at each frequency ranging from -1 to 1, to avoid biasing the processing towards the features exhibiting the highest amplitude (Kouroussis et al., 2000). Low frequencies are

notoriously prone to noise propagation and environmental interference (Nordon et al., 2006; Whitaker et al., 2000), therefore frequencies below 4 kHz were removed from the analysis.

Implementation of machine learning algorithms requires a high number of computational operations. At the same time, high number of points may be cause of bias in the implementation of the classification algorithm. In order to reduce the interrogated features, a method based on the highest variance in the data is proposed. The frequencies in the spectrum are ranked based on their variability across the data, with the most variable ranked as 1st and so on. Based on this ranking, a number n of the most variable frequency peaks was selected as features characterising each instance before being fed to the machine. This is done to reduce the amount of processed data, as the objective of the study is to investigate AE suitability for inline real-time installation. The selection of n number of used features is investigated with $n_{max} = 30'000$ being the maximum value. In Figure 3.5, an average frequency domain plot is reported for the three conditions for $n = n_{max}$ to show the span of used frequencies across the whole spectrum.
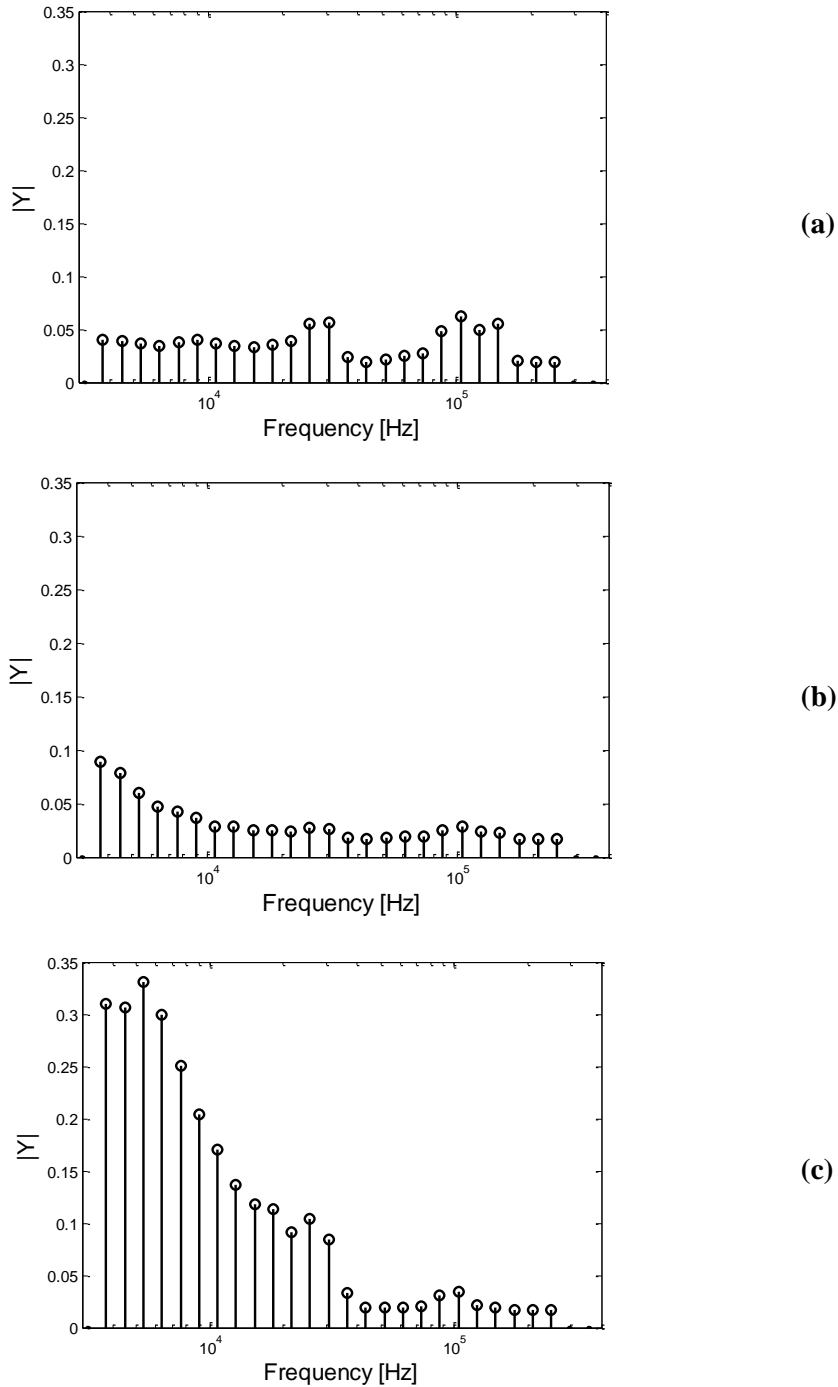
Figure 3.5 – Frequency distribution across the spectrum for ungassed (a), loaded (b) and complete dispersion (c) regime. The ungassed condition presents a flat frequency signal, where no specific frequency range prevails on the others. In the loading condition instead there is a higher predominance of low frequency. At completely dispersed condition the region below 50 kHz has the predominance over the high frequency region.

As seen in Figure 3.5, reducing the used frequencies in the spectra for the three conditions neglects the frequencies over 200 kHz, but it does not narrow down effectively the range of observation within the spectrum. However, it must be noted that the logarithmic grouping will use a wider range for the higher frequencies, hence, the most present features in the case of $n = n_{max}$ are for frequencies in the audible range (< 20 kHz). This is more evident by increasing the dispersion of gas, where the peak at lower frequencies increase in intensity.

Following the feature selection step, the data are divided in three datasets for the assessment:

- A training dataset, consisting of 60% of the acquired data, was fed to the machine for the training process, together with their own corresponding class of belonging.

- A cross-validation dataset, consisting of 20% of the acquired data, used for selecting the optimum number of used features.

- A test dataset, consisting in the remaining 20% of the data, unseen by the machine was used to evaluate the final accuracy of the method.

The three dataset are built taking for each operating point (fixed impeller speed and gas feed rate) the corresponding portion in percentage (Example: for a given operating point, a number of 25 AE data points (spectra) are recorded, of which 15 are included in the training dataset, 5 in the cross-validation dataset and the remaining 5 in the test dataset)

The task is addressed as a classification problem: in the training step, the system gets, as an input, the spectra and the corresponding class (ungassed, loaded, completely dispersed). Depending on the used algorithm, the machine builds criteria to identify the correspondence between the AE data and their known operating condition. When the training is complete,

given a new AE set of data the system will provide as an output the predicted operating condition.

The training process is carried out by obtaining acoustic signal at different impeller speed and air flow rate at the three regimes. The cross-validation step consists of identifying the optimum number of features (*n*) to use for the analysis. The criteria to automatically select *n* are dependent on two selected parameters:

- the processing time; in this case identified as the time taken by the CPU to process the learning step, arbitrarily decided to be lower than 1 second;

- the average accuracy of the methods; four variants are chosen from each family of the used algorithms and their accuracy is averaged for identifying the zone of optimum.

In the test step, the performance of the algorithms are calculated using two factors, one being the accuracy of the method, calculated as the ratio between number of cases correctly predicted and the total cases number; the second factor is known as the F1-score (Powers, 2011). It is widely used in medical applications for diagnosis methods (Ferizi et al., 2019; Rink et al., 2011) and it takes into account positive prediction as well as false negative. It is defined as:

$$F_1 = 2\frac{P \cdot R}{P+R} \tag{3.2}$$

Where P is the precision and R is the recall, defined, for a binary classification, in (3.3) and (3.4) respectively:

$$P = \frac{True\ positive}{True\ positive + False\ positive} \tag{3.3}$$

$$R = \frac{True\ positive}{True\ positive + False\ negative} \tag{3.4}$$

For each condition, the precision is the relative fraction of correctly assigned instances amongst all the cases assigned to that specific class, while recall is the fraction of correctly recognised instances over the total amount of instances belonging to the same class (Apte et al., 1994). Such definitions are valid for binary classification, when the algorithm is challenged to identify the belonging of a certain dataset on the positive or negative classes (medical diagnosis is an example). In cases of multiclassification, the F1-score is calculated for each condition and successively weighted. Therefore, in this work the comparison is made on the average weighted F1-score (Al-Salemi et al., 2018): the closer F1-score is to 1 the more reliable and precise is its prediction power.

The process of training and testing the machine learning algorithm is repeated for ten times, where for each repetition, the datasets included in the training and testing are randomly selected. This is done to avoid bias in evaluating the algorithm accuracy that may be achieved by selecting a "lucky" training dataset. The reported results are the average values obtained in the ten repletion steps.

In this study, two test cases datasets were analysed: one at the same conditions of gas flow rate and impeller speed with the bi-phasic mixture, and a second one in which solids are added to the mixture.

3.3   Results

3.3.1 Parameter tuning

One of the potential issues for the application of AE as a real time tool is the computational time; it is essential that the analysis can be carried out in short time to evaluate the operating condition. However, AE are usually acquired at high frequency, resulting in a large amount of data; this can cause delay in processing and, at the same time, represents a challenge for the

algorithms to avoid biasing and overfitting. For this reason, an initial study is carried out by manipulating n, the number of used features, in the spectrum for the classification. After ranking the frequency spectrum based on decreasing variance, a variable number, n, of frequencies is fed to the training process of the different algorithms. The obtained methods are then challenged to correctly classify the cross-validation dataset; as done for the training dataset, the corresponding n of the cross-validation spectra are used for the optimisation step. For this initial test, carried out on the biphasic case, one algorithm of each family is used for the analysis. The objective is to identify the optimal number of features that would represent a good compromise of obtained accuracy and processing time for the different algorithms. The results, in terms of accuracy, are shown in Figure 3.6.

Figure 3.6 highlights how critical the choice of the parameter n is in ensuring good prediction performance.
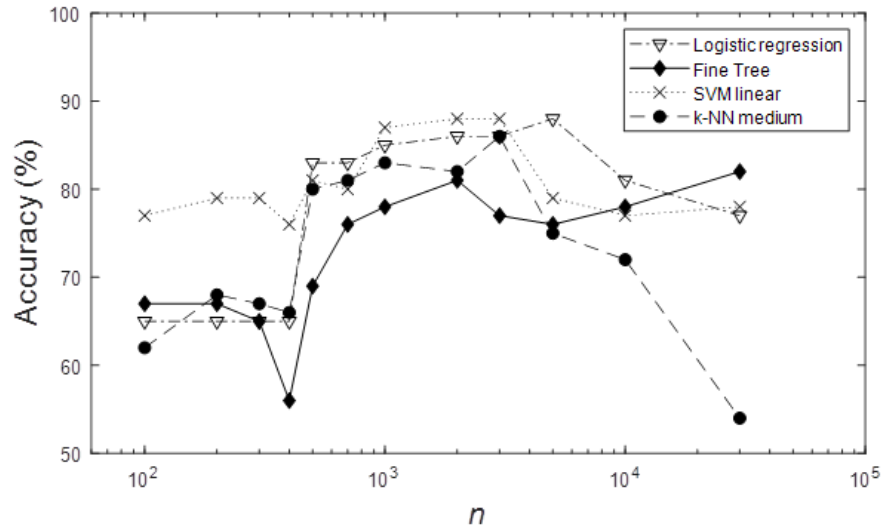
Figure 3.6 – Accuracy over the cross-validation dataset varying the number of n number of features for Logistic regression, Decision tree (fine), SVM (with linear kernel) and k-NN (with k=10) in the gas-liquid case.

While the SVM starts already with performance around 75-80% even with a small number of features (n = 100) with a local maximum in the range between 1000 and 3000 features, the other three algorithms perform significantly worse at low number of features. Their accuracy progressively increases with increasing n, until the same range of SVM maximum is reached. In this condition all performance, except the decision tree, are in the same order of SVM. By increasing the number of features over 10,000, all the algorithms, except the decision tree, performance are worse. This is due to the fact that when increasing the vector space dimension, the algorithms may be misguided by unimportant parts of the spectrum that tend to "homogenise" the acquired data at different conditions. The decision tree is less affected mainly because it is not based on geometrical parameters. Training time is reported in Table 3.2 for the different data points for the three methods built in MATLAB® Classification learner (the logistic regression algorithm was not considered in this comparison because it was manually coded by the authors).

Table 3.2 – Training time for Fine Tree, SVM (linear kernel), k-NN and the average value.

n	Training time [s]			
	Fine Tree	SVM Linear	k-NN medium	average
100	0.41	0.18	0.089	0.2263
200	0.47	0.207	0.115	0.264
500	0.53687	0.336	0.1803	0.351
1000	0.77	0.544	0.361	0.558
2000	1.25	1.03	0.8016	1.02
5000	3.81	3.608	3.54	3.652
30000	106.5	124.06	106.83	112.46

When *n* is increased over 1000, the processing time takes longer than 1; moreover, *n* = 1000 corresponds to the maximum region of three of the four tested methods (Figure 3.6), therefore, this is identified as the operating number of features for further analysis.

3.3.2 Two-phase test

The training was carried out for the chosen number of features based on the training dataset acquired for the biphasic condition. The test dataset, unseen by the machine in previous step was used to obtain the prediction performance of the set of chosen algorithms. Results in terms of accuracy for each algorithm at different regimes are reported in Table 3.3.

Table 3.3 – Average accuracy of the machine learning algorithms for the different regimes in the gas-liquid case. The last row reports the overall accuracy together with the standard deviation obtained in the 10 repetitions.

Regime	Method Accuracy (%)								
	Logistic regr.	Fine Tree	Medium Tree	Linear SVM	Quad. SVM	Cubic SVM	Fine KNN	Medium KNN	Coarse KNN
Ungassed	89	93.1	93.1	86,7	94,9	96.1	100	84	88.4
Loading	85	87.8	87.8	83.2	97.1	97.1	89.2	83.2	30
Complete dispersion	94.7	84.0	84.0	97.6	87.6	90	84.0	82	0
Global	90.2 ±2.9	88.9 ± 4,2	88.9 ± 4,2	86.7 ± 3,8	93.8 ±3.8	94.4 ±3.7	91.6 ±3.9	83.8 ±5.10	44 ±8.6

In terms of accuracy, all the methods exception made for the Coarse KNN have accuracy over 84%. Among the tested algorithms, the SVM with quadratic and cubic kernels seem to outperform the linear based SVM and the other algorithms, with accuracy equal to or higher than 90% in the three investigated conditions. Logistic regression also presents a high

accuracy comparable to the other methods, while it is interesting to observe that k-NN performance inflects as the number of considered *k* neighbours is increased from 1 (fine *k*-NN) to 100 (coarse *k*-NN). In cases of classification problems, accuracy is often not enough to correctly describe the performance of the algorithm, therefore, for further comparison a weighted F1-score (Powers, 2011) is calculated for the different algorithms as an average among the 10 repetitions. It is showed in Table 3.4.

Table 3.4 – Weighted F1 score obtained in the gas-liquid regime prediction case. The value is averaged over the 10 repetitions.

Regime	Logistic regr.	Fine Tree	Medium Tree	Linear SVM	Quad. SVM	Cubic SVM	Fine KNN	Medium KNN	Coarse KNN*
F1 score	0.914	0.892	0.892	0.845	0.938	0.951	0.911	0.841	-

* No value was calculated for the Coarse k-NN because of a null denominator

Quadratic and cubic SVM achieve the highest result in F1-score, confirming what has already been observed from the accuracy comparison. By way of example, a parity plot from one of the repetition, showing the correct predictions and the failures of the SVM cubic algorithm is reported in Figure 3.7. The points on the identity line identify the correct assignments, while the misclassifications are in one of the other regions of the plot.
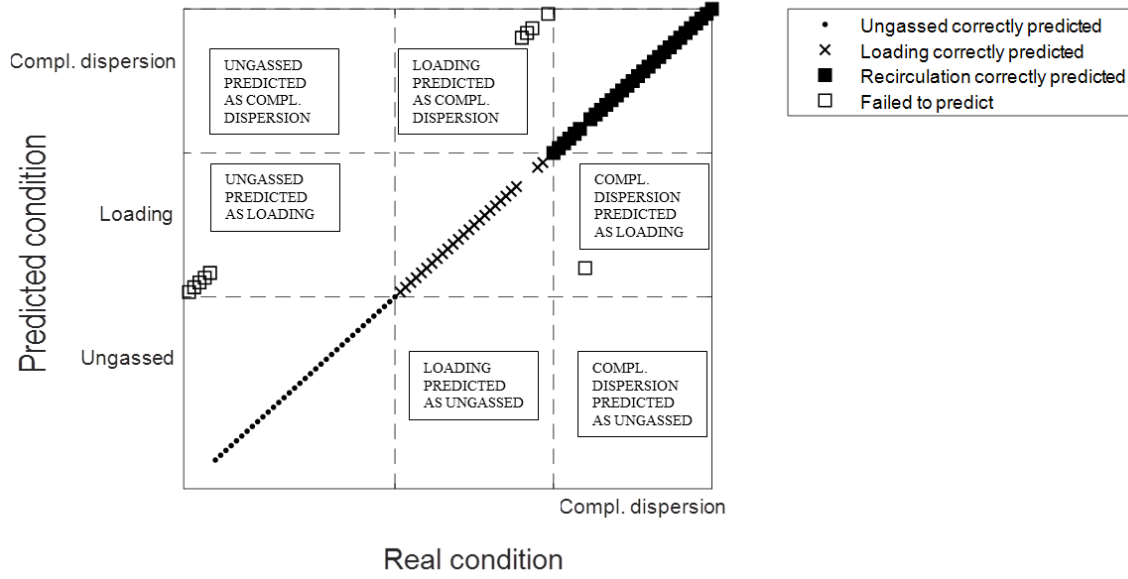
Figure 3.7 – Parity plot reporting SVM quadratic results in classifying the different test datasets in the biphasic case. The points on the bisector are correctly predicted, contrariwise the prediction is incorrect for the points off the bisector. Data show one of the repetitions (the median dataset) reported in Table 3.3.

All the ungassed cases are correctly identified by the algorithm, while three datasets for both loading and complete dispersion are misclassified. The three points belong to the points at the edge between the two regimes, respectively $N=600$ rpm for loading and $N=800$ rpm for complete dispersion (both at a gas feed rate of 1.5 vvm), capturing oscillations among the two very close conditions.

3.3.3 Three-phase test

In the second part of the study, stainless-steel particles are added at different concentration and the acoustic signal is acquired at the three regimes. The same algorithms used for the biphasic system are applied for assessing the ML capability in this case, maintaining unchanged also *n,* the number of used features. The obtained results in terms of overall accuracy and F1-score are summarised in Table 3.5.

Table 3.5 – Overall accuracy and weighted F1-score for the different algorithms in gas-solid-liquid regime prediction Data are calculated over 10 repetitions.

Regime	Logistic regr,	Fine Tree	Medium Tree	Linear SVM	Quad. SVM	Cubic SVM	Fine KNN	Medium KNN	Coarse KNN
Overall accuracy (%)	90.1 ±3.4	83.1 ±4.2	83.8 ±4.9	78.8 ±4.6	93.8 ±4.2	94.2 ±3.9	92.5 ±2.9	90.9 ±3.4	56.5 ±9.5
Weighted F1-score	0.931	0.852	0.881	0.813	0.939	0.941	0.912	0.888	0.734

In the three-phase cases the obtained performance of all algorithms are high, with fine and medium k-NN achieving comparable performance to the cubic and quadratic SVM, (still being the highest performing algorithms) and the logistic regression algorithms. Figure 3.8 shows the parity plot obtained in the three-phase case.
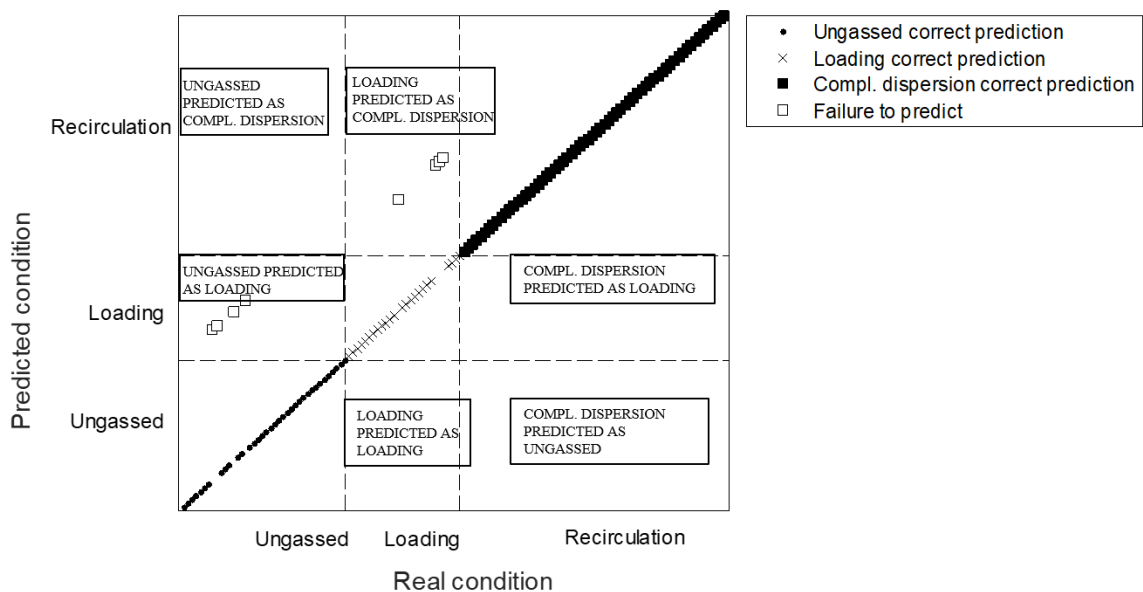
Figure 3.8 – Parity plot reporting SVM quadratic results in classifying the different signals in the gas-solid-liquid test. The points on the bisector are correctly predicted; contrariwise the prediction is incorrect for the points off the bisector. Data show one of the repetitions (the median dataset) reported in Table 3.5.

This result confirms that as the presence of solids, at low concentration, does not have major effects on the gas-liquid sparging dynamics within the tank, in similar fashion it does not significantly affect the ability of the ML tools to infer acoustic emission features to characterise the bi-phasic mixture. The algorithms are able to be trained to recognise the acoustic emission caused by the bubbles presence and interaction with the other phases and therefore it is possible for the system to identify the corresponding regime.

3.3.4 Dynamic condition

To further challenge the technique, and in order to verify its flexibility over deviations from an initial well-defined condition, an additional test was run. The dataset used to achieve a performance closer to the performance median in section 3.3.2 was used for all the algorithms trained and tested in the gas-liquid condition are challenged to recognise the corresponding regimes in the three-phase condition. Such a situation is realistic in cases in which a system is characterised in a certain starting bi-phasic condition and then during the operation dynamic, a third phase is generated by reaction or addition to the mixture. Therefore, the acquired data used for the three-phase experiment are fed to the biphasic algorithm. The results, reported in Table 3.6, show the significant decrease in accuracy and F1-score exhibited by all the algorithms except the logistic regression. The influence of the solids in the acoustic spectrum indeed does not allow the system to recognise the correct gas-liquid regime. This represents a limit to the flexibility of the geometrical based algorithms (SVM and k-NN) and the decision tree that clearly do not succeed in correlating characteristic features in the biphasic case with corresponding ones in the three-phase case. The logistic regression, instead, is able to present performances similar to the ones obtained in the previous two cases. The reason is related to the different nature of this algorithm: in each case a probability of belonging of the instance to the three different cases is calculated independently. Although all these probabilities

decrease, the correct one outranks the others and therefore the system is able to correctly predict the gas-liquid condition.

Table 3.6 – Overall accuracy and weighted F1-score for the different algorithms in gas-solid-liquid regime prediction using the algorithms trained in the gas-liquid condition.

Algorithm	Logistic regr.	Fine Tree	Medium Tree	Linear SVM	Quad. SVM	Cubic SVM	Fine KNN	Medium KNN	Coarse KNN
Overall accuracy (%)	90.8	32.4	42.3	33.0	34.4	27.3	49.1	51.2	29.8
Weighted F1-score	0.928	0.496	0.539	0.431	0.459	0.438	0.631	0.583	0.390

Figure 3.9 reports the parity plot for the best case (logistic regression) and does not show any particular clustered dataset presenting fallacious behaviour. Amongst the processed data 91.2% are correctly recognised by the ML.
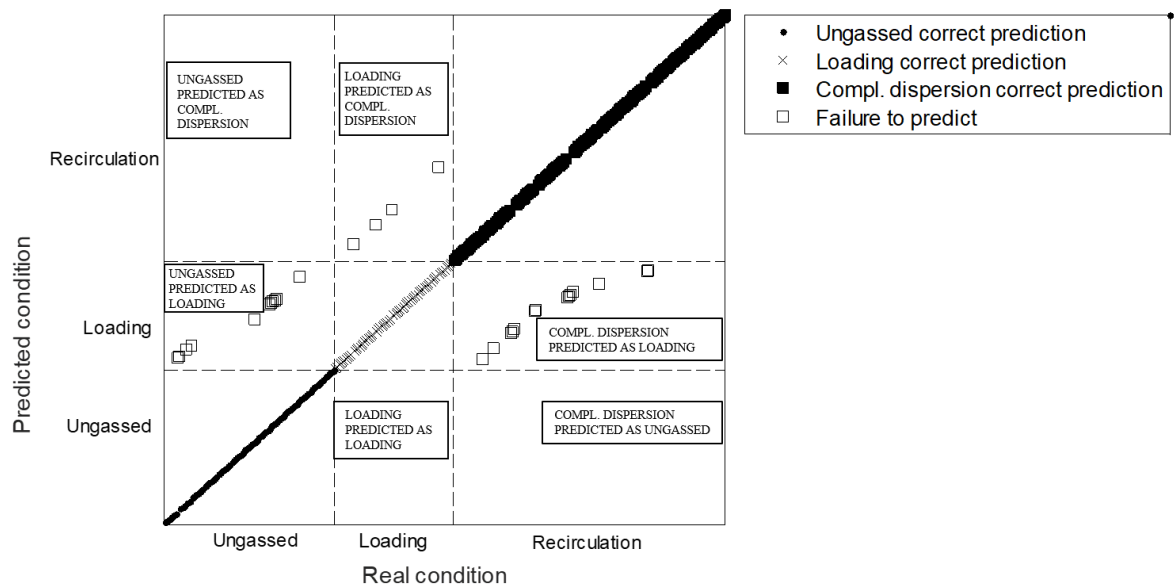
Figure 3.9 – Parity plot reporting logistic regression results in classifying the different signals in the gas-solid-liquid test using the gas-liquid trained algorithms. The points on the bisector are

correctly predicted, contrariwise the prediction is incorrect for the points off the bisector.

The logistic regression, already well-performing in the other cases, demonstrates higher flexibility than the other machine learning algorithms investigated in this study. This can be certainly related to the system used and the choice of data-processing algorithm remains an important issue to be addressed. Deviations from ideal conditions is an every-day challenge on process plants and the ability to adapt to non-forecasted conditions is a critical characteristic for an implementable measurement technique.

3.4   <u>Conclusions</u>

In this work, Acoustic Emission was used in combination with machine learning algorithms, to identify gas-liquid mixing conditions in a stirred tank. The machine was trained to recognise ungassed, loading and completely dispersed conditions using a training dataset, consisting in the acoustic spectrum acquired at the different regimes in two-phase (gas-liquid) and three-phase (gas-solid-liquid) stirred tank. The training procedure was repeated ten times for each algorithm by varying the data points in the leaning dataset. Average results show that with appropriate training, some of the investigated algorithms (SVM with quadratic and cubic kernel and logistic regression) were able to correctly recognise the regimes corresponding to the tested spectra with accuracy higher than 90%.

The system was then challenged to make prediction on the gas sparging regime in the three-phase runs while using the learning gained in the bi-phasic condition to evaluate flexibility of the method in dynamic conditions (as for example in precipitation batch processes). Most of the algorithms did not successfully address this task, presenting accuracy in some cases significantly lower than 50%; however logistic regression, above all, was the one that is able to perform at the same level as for previous tests (>90%).

The conducted study aimed to investigate AE as a potential diagnostic and condition monitoring technique for fluid mixing applications in combination with the use of machine learning algorithms and proposes a methodology to evaluate the most appropriate algorithms. Although amongst the wide range of algorithms available in the literature, only some were taken into consideration, from this investigation it is possible to infer that a combined use of AE and ML could represent a powerful tool for monitoring two-phase and three-phase mixing regimes in situ with high potential of real time application.

3.5 <u>Nomenclature</u>

D	Impeller diameter, m
Fl	Flow number
Fr	Froude number
g	Standard acceleration due to gravity, m s^{-2}
N	Impeller rotational speed, rps
n	Number of features
Q_g	Volumetric gas flow rate, m^3 s^{-1}
B	Baffles length, m
T	Tank diameter
H	Liquid level
P	Precision
R	Recall
V	Volume of the tank, m^3
v_s	Superficial velocity of the gas, m s^{-1}
X	Percentage mass ratio of solids to liquid in suspension

4.

Assessing blending of non-Newtonian fluids in static mixers using PLIF and ERT

Blending of fluids with complex rheology is a challenging task, often difficult to monitor. In this work, PLIF and ERT have been used simultaneously to evaluate the mixing performance of 6 elements KM static mixer for the blending of non-Newtonian fluids of dissimilar rheologies in the laminar regime. The areal distribution method was used to obtain quantitative information from the ERT tomograms and the PLIF images. Comparison of the ERT and PLIF results demonstrates the ability of ERT to detect mixing performance in cases of poor mixing within the resolution of the measurement, though the accuracy decreases as the condition of perfect mixing is approached. ERT, thus, has the potential to detect poor mixing within the confines of its resolution limit and the required conductivity contrast, providing potential rapid at-line measurement for industrial practitioners.

This chapter is published in the Chemical Engineering & Technology journal (Forte et al., 2019a):

The conducted work has been a close collaboration between the authors. The laboratory work has been carried out by Andrea Albano. The data processing and writing was led by Giuseppe Forte.

4.1   Introduction

Non-Newtonian fluids are widespread in industrial processes, for example in the manufacture of home and personal care products, foods and chemicals. Amongst other unit operations, mixing and blending of complex fluids remains a significant process challenge (Connelly and Kokini, 2007; Prakash et al., 1999). Although this operation is often executed in stirred tanks, the industry-driven benefits of moving towards continuous processing suggests a solution involving static mixers. Such devices consist of metallic inserts installed within pipes and applications also include chemical reactions and heat transfer (Paul et al., 2004). Static mixers promote chaotic advection within the flow (Alvarez et al., 1998; Hobbs and Muzzio, 1997; Saatdjian et al., 2012; Wunsch and Bohme, 2000) which contributes significantly to mixing in the laminar regime, considering the difficulty to reach turbulence for non-Newtonian fluids without excessive amount of power input (Aref, 1984; Le Guer and El Omari, 2012). The flow deformation given by the mixing elements causes the formation of striations and as a result the interfacial surface area is increased, improving the diffusion rate at low Reynolds number (Hobbs and Muzzio, 1997).

Many literature studies have been made of the flow in motionless mixers, employing optical methods as Planar Laser Induced Fluorescence (PLIF) (Alberini et al., 2014a; Arratia and Muzzio, 2004; Faes and Glasmacher, 2008; Ramsay et al., 2016), Particle Image Velocimetry (PIV) (Pianko-Oprych et al., 2009; Stobiac et al., 2014; Szalai et al., 2004) or decolorization measurement techniques (Chandra and Kale, 1992; Li et al., 1997). The application of the reported methods requires both the fluid and the pipelines to be transparent, therefore they are not implementable for opaque fluids. An alternative non-invasive technique applicable for opaque media, Positron Emission Particle Tracking (PEPT), employs the Lagrangian tracking of the 3-D position of a positron emitting tracer particle within the fluid to reconstruct its velocity flow field over time (Edwards et al., 2009) and has been applied both for studies on stirred vessels (Barigou, 2004) and static mixers (Rafiee et al., 2011) for Newtonian and non-Newtonian fluids. Alternatively, to measure the concentration distribution, PET (Positron Emission Tracking) can be used where the position and concentration of a radiotracer is monitored in time (Bell, 2015).

Amongst the many geometries commercially available, Kenics® KM static mixers (Chemineer, USA) are commonly used for academic investigations due to their simple geometry (Avalosse and Crochet, 1997; Rahmani et al., 2005; Rauline et al., 2000; Regner et al., 2006; Wageningen et al., 2004). Some works describe numerical simulations of the mixing performance of non-Newtonian fluids in SMX® (Sulzer) geometry (Peryt-Stawiarska, 2014; Wunsch and Bohme, 2000). However, apart from these few studies, the research focus by means of numerical simulation has remained on blending of non-Newtonian fluids in stirred vessels, with the use of different approaches such as Computational Fluid Dynamics including Direct Numerical Simulation (DNS) of the Navier-Stokes equations (Zalc et al., 2002).

The industry driver for continuous processing, is concomitant with the requirement for appropriate Process Analytical Technology (PAT) to enable real-time product quality assurance and control (Uendey et al., 2010). In the context of this paper, the development of in situ measurement techniques represents a critical step towards this. Furthermore, traditional approaches to the development of new formulated liquid products are laboratory scale oriented with little or even no attention given to formulation "manufacturability". This frequently results in not only longer and costlier time to scale up but also increased production costs.

A number of measurement techniques have been applied for monitoring fluid characteristics in inline flows. Nuclear Magnetic Resonance (NMR) (Blythe et al., 2017) and ultrasonics (Pfund et al., 2006) were applied to estimate rheological parameters of non-Newtonian fluids (aqueous solutions of Carbopol 940 and Carbopol EZ-1 respectively) in pipelines in real time, while micro-PIV was applied in determining the velocity profile of both non-Newtonian and Newtonian fluids in laminar regime (Fu et al., 2016).

Electrical Resistance Tomography (ERT), amongst other techniques, offers the advantages of being non-invasive, low-cost, robust and with a high temporal resolution; it is thus an interesting candidate technique in this context for measurement of the phase distribution within liquid continuous mixtures (Pakzad et al., 2008; Wang et al., 1999). Jegatheeswaran et al. (Jegatheeswaran et al., 2018) uses ERT to validate CFD simulations of the blending of two non-Newtonian fluids flowing in SMX static mixers. The same technique has been used for measuring velocity profiles of shampoo in pipelines (Ren et al., 2017) and to evaluate mixing of industrial pulp in static mixers (Yenjaichon et al., 2011). Recent applications of ERT in pipe flows have demonstrated potential for in-line rheometry measurements (ERR) (Machin et al., 2018).

In this paper, we describe the use of ERT to determine the distribution of two non-Newtonian fluids of dissimilar rheology at the outlet of a Kenics KM static mixer in the laminar regime. The measurements are made at the mixer outlet using a two-plane circular array. The ERT measurements are compared with measurements of the mixing distribution collected simultaneously using Planar Laser Induced Fluorescence (PLIF), a proven method in this application. Both ERT and PLIF data are compared quantitatively using the areal distribution method developed by Alberini et al. (Alberini et al., 2014b).

4.2   Materials and methods

Aqueous solutions of carboxymethylcellulose (CMC) and Carbopol 940 were chosen as the model of non-Newtonian fluids, whose flow rheology can be well represented by the power law and Herschel Bulkley constitutive laws respectively. The fluids are chosen with the reported properties (Table 4.1) as they well replicate the properties of JM washcoats employed in the catalyst converters manufacturing. Flow curves were obtained and fitted to the constitutive models using a rheometer (TA Instruments, model: Discovery HR-1) equipped with a 40 mm 4° cone and plate geometry and associated software: the data are shown in Table 4.1.

Table 4.1 – Fluid rheology parameters and electrical conductivity. PL stands for Power Law, while HB identifies a Herschel-Bulkley rheology model.

Fluids	Mass composition	Behaviour	τ_0 [Pa]	K [Pa/s^n]	n [−]	Conductivity [mS cm^{-1}]
PL	0.5% w/w sodium Carboxymethyl Cellulose 99.5% w/w water	Power Law	-	0.49	0.59	1.142
HB1	0.1% w/w Carbopol 99.9% w/w water	Herschel-Bulkley	0.85	0.40	0.58	0.271
HB2	0.2% Carbopol 99.8% w/w water	Herschel-Bulkley	10.27	7.45	0.38	0.456

Figure 4.1 shows the rig schematic. The flow to the mixer was delivered by an Albany rotary gear pump controlled using an inverter control WEG (model CF208). The secondary flow, doped with fluorescent dye (Rhodamine 6G) with a concentration of 0.04 mg l^{-1} (concentration was selected within the linear range of greyscale versus dye concentration), was introduced using a Cole-Parmer Micropump (GB-P35). The injection pipe (with internal diameter of 7.6 mm) was placed in the centre of the main pipe as close as possible to the static mixer. The experiments, reported in Table 4.2, were conducted at isokinetic condition between main flow (MF) and secondary flow (SF): the two fluids were fed at the same superficial velocity, u_S, hence the ratio between the two volumetric flows was equal to the ratio between main and injection pipe sections (MF/SF≈10). The Kenics KM mixer unit had an internal diameter of 25.4 mm (1") and length of 220 mm (L/D= 9) and was equipped with 6 mixing elements.
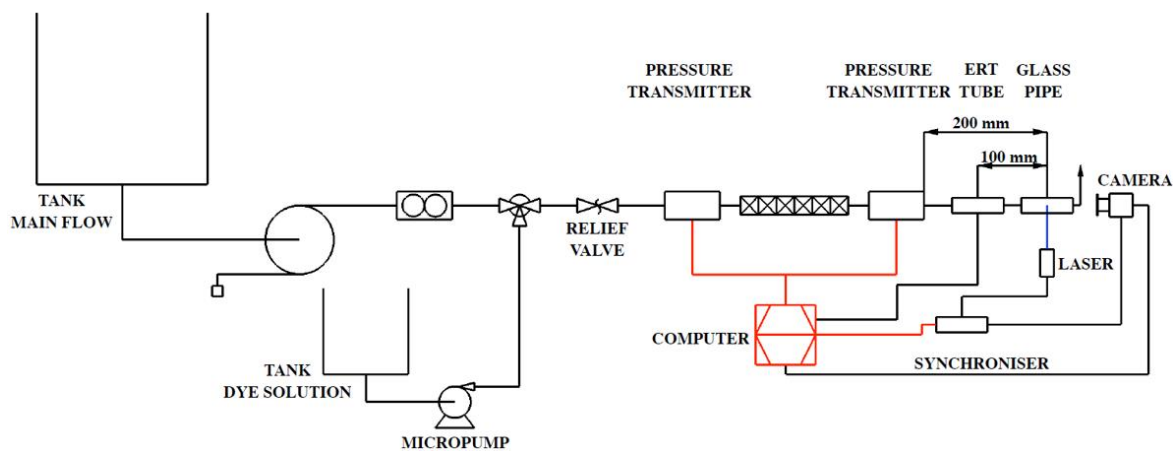
Figure 4.1 – Schematic of the experimental rig (adapted from (Alberini et al., 2014a)). The main fluid is fed through a centrifuge pump and the flow measured with a flowmeter. After the injection of the secondary fluid, the mixture is fed to the static mixers. The pressure drop is measured using pressure transmitter. The mixed fluid goes then through the ERT measurement system and is measured using PLIF before being discharged.

The mixing unit was followed by a planar circular ERT sensor consisting of 16 electrodes. The ERT sensor was connected to a V5R data acquisition system (Industrial Tomography

Systems plc, UK) that controlled electrical excitation and measurement collection. The ERT plane was located 100 mm after the mixer outlet, while the PLIF measurement plane was located at 200 mm from the end of the mixing zone; the two measurement planes were separated by 100 mm.

The terminal part of the pipeline was equipped with a Tee piece designed with a glass window inserted at its end corner through which PLIF measurements are made (the capture procedure may be found in Alberini et al.(Alberini et al., 2014a).

A range of superficial velocities, u_S, was investigated to identify the accuracy of ERT measurements once the contrast, in term of conductivity, between the injected (secondary) and the main flow is decreased. The list of experiment and flow conditions is shown in Table 4.2. Within the range of investigated velocities, the values of Re, calculated using the methodology used by Alberini et al. (2014a), were in the range 25-220 which suggest the system was always running in laminar regime ($Re \ll 2000$). The inlet absolute difference in conductivity (no addition of salt), $\Delta c = |c_{MF} - c_{SF}|$, between the main flow (MF) and the secondary flow (SF) is also reported in Table 4.2, since it is the principal parameter which affects the ERT measurement.

Table 4.2 – List of experiment and flow conditions. The properties of the involved fluids for Main Flow (MF) and Secondary Flow (SF) are reported in Table 4.1.

Experiment	MF	SF	Δc (mS cm^{-1})	u_S (m s^{-1})
I	HB1	PL	0.871	0.20 | 0.27 | 0.34 | 0.40 | 0.47
II	HB2	PL	0.686	0.20 | 0.27 | 0.34 | 0.40 | 0.47
III	HB1	HB2	0.185	| 0.27 | 0.34 | 0.40 | 0.47

4.2.1 Calibration and Post Processing

The ERT system was calibrated prior to the experiment, which consisted of taking a baseline reference frame. For each experiment, the reference was captured with continuous phase at each flow rate after reaching a steady flow condition. The V5R automatically sets the conductivity of the reference measurements equal to unity, thus the changes occurring after the injection are relative and not absolute. The V5R system employs a sample frequency of 125 Hz: for each run a sample of 1000 frames was analysed. The data obtained were processed using the Toolsuite V7.4 software (ITS Ltd.) in order to reconstruct conductivity tomograms. Since ERT is a soft-field technique, the reconstruction problem is not trivial and several algorithms have been developed to generate conductivity tomograms from the raw data, both iterative and non-iterative (Yang and Peng, 2003). Commonly, in the latter category, the Linear Back Projection (LBP) method or one of its variants is used (Noser, Tikhonov reconstruction algorithms) (Wei et al., 2015). In this work the modified standard back projection (MSBP) algorithm implemented in the V5r software was used. Furthermore, for simplicity, only the tomograms obtained in the second plane are used for comparison with PLIF.

The areal method (Alberini et al., 2014b) requires an initial calibration step to be applied in evaluating mixing performance. In this step, the values of C_{inf} and G_{inf} are identified for all the mixtures, as the value of conductivity and greyscale respectively reached at the condition of perfect mixing. Since ERT and PLIF have a different basis of measurement, two dimensionless parameters, X_C and X_G, are introduced to allow comparison of the measured mixing performance between them. A dimensionless relative conductivity X_C can be defined for each pixel as:

$$X_C = (C_i - C_0)/(C_{inf} - C_0) \qquad \textbf{(4.1)}$$

Where C_i is the relative conductivity of the i-th pixel of the tomogram, C_{inf} is the relative conductivity achieved at perfect mixing and C_0 is the reference conductivity of the pixel before the injection, equal to 1 in condition of single phase. Analogously, a dimensionless greyscale X_G is defined:

$$X_G = (G_i - G_0)/(G_{inf} - G_0) \qquad \textbf{(4.2)}$$

Where G_i is the grey scale value of the i-th pixel of the PLIF image, G_{inf} is the grey scale value reached at perfect mixing found in the calibration step, and G_0 is the reference status of the pixel before the injection. The grey scale values of "pure" (100% secondary flow fluids) fluids have been measured resulting in 92 and 250 for PL and HB2 respectively at fixed Rhodamine 6G concentration of 0.04 mg l^{-1}. The measurement is carried out by utilising the camera and averaging the pixel values within a set of 30 images.

In the calibration procedure, both greyscale values and conductivity of the mixtures were measured at different volume fraction x_{SF} values of the secondary flow in the main flow in the interval of interest. Pre-fully-mixed solutions with volume fractions x_{SF} of the secondary flow between 0.02 and 0.10 (which is the maximum volume ratio obtained in the system), were fed

to the system and ERT and PLIF measurements were captured simultaneously. It was noticed that the effect of flow velocity on both measurements (in case of fully premixed solutions) is negligible. The results of the calibration for the relative conductivity and the greyscale values, to obtain C_{inf} and G_{inf}, are reported for the three mixtures in Table 4.3.

Table 4.3 – Relative conductivity, C$_{inf}$, and greyscale, G$_{inf}$, values of the mixture of primary and secondary fluids at different volume fraction of secondary fluids for each pair of fluids employed in the different experiments: I (PL in HB1), II (PL in HB2), and III (HB2 in HB1). The combination of fluids for each experiment are described in Table 4.2 and their flow and rheological properties in Table 4.1.

Experiment I		Experiment II		Experiment III	
x_{pl} in HB1	C_{inf}	x_{pl} in HB2	C_{inf}	x_{hb2} in HB1	C_{inf}
0.02	1.08	0.02	1.06	0.02	0.99
0.04	1.12	0.04	1.10	0.04	0.98
0.06	1.18	0.06	1.13	0.06	0.97
0.08	1.27	0.08	1.15	0.08	0.96
0.1	1.35	0.1	1.18	0.1	0.95
x_{pl} in HB1	G_{inf}	x_{pl} in HB2	G_{inf}	x_{hb2} in HB1	G_{inf}
0.02	120	0.02	247	0.02	247
0.04	119	0.04	243	0.04	245
0.06	119	0.06	240	0.06	242
0.08	118	0.08	237	0.08	239
0.1	118	0.1	234	0.1	237

4.3   <u>Results</u>

The two imaging techniques employed have a substantial difference in spatial resolution: whilst PLIF is able to capture high resolution pictures (2048×2048 pixels), ERT yields relatively low-resolution tomograms (20×20 pixels) which cannot be expected to resolve striations of fluid that are often present when mixing complex rheology fluids. The first step of the conducted study consists in evaluating the effect of downscaling PLIF images from full resolution to a reduced resolution, of the same order of magnitude of ERT tomograms (32×32 pixels). The applied downsizing algorithm allows a reduction scaled by powers of 2, therefore from the starting resolution of $2^{11}\times2^{11}$ pixels, a resolution of $2^{5}\times2^{5}$ pixels is obtained, reasonably close to the ERT tomogram resolution, to draw significant comparison. Subsequently, full size PLIF images and ERT tomograms are directly compared on evaluating achieved mixing performance.

4.3.1 PLIF image analysis by varying resolution

Downscaled PLIF (32×32) images are obtained using the Lanczos kernel downsizing method (Komzsik, 2003) and compared to original full size PLIF images. The objective is to gather whether at low resolution it is possible to characterize mixing performance and assess the loss of information in downscaling PLIF images. An example of the resulting images is shown in Figure 4.2, as a function of flow rate.
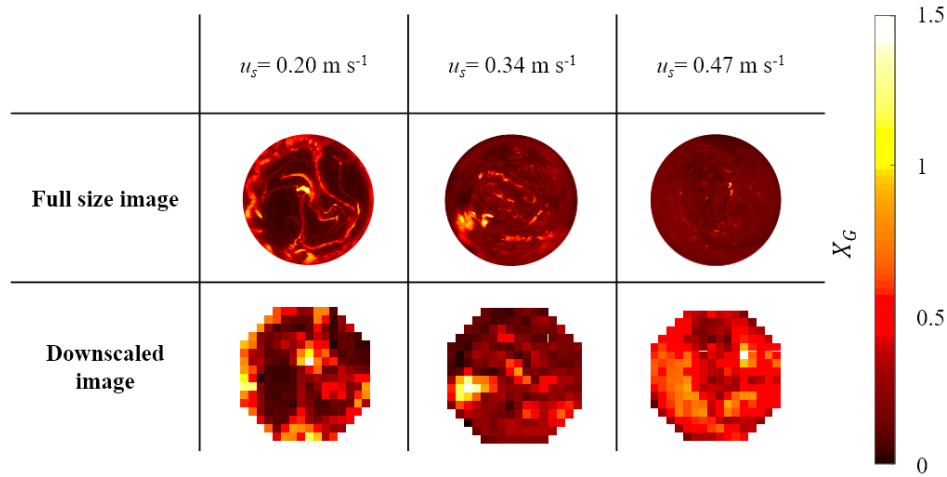
Figure 4.2 – Full size and downscaled PLIF images at different superficial velocities for experiment I. The visual comparison exemplifies the loss of resolution. Details of the experiment and involved fluid properties are reported in Table 4.2 and Table 4.1.

In Figure 4.2, the thick white striations represent the unmixed secondary flow and the dark areas the main flow. The images show a substantial increase in homogeneity as the flow rate is increased with the dark regions observable at low superficial velocity (of 0.20 m s^{-1}) at the full-scale images, reducing and the white regions becoming less intense at higher velocity. In an analogous way, the white and black pixels observed in Figure 4.2 for the downscaled images at low superficial velocity progressively disappear as u_S increases (as observable for $u_S = 0.47$ m s^{-1}, where the image shows improvements in terms of mixing performance).

Although it is possible to appreciate by eye how the downscaling decreases the quality of the images, this transformation does not translate in significant loss of information from a point of view of mixing performance detection capability. In fact, by applying the areal fraction method, it is possible to compare the mixing performance detected by the full resolution pictures and the downscaled images in Figure 4.3.
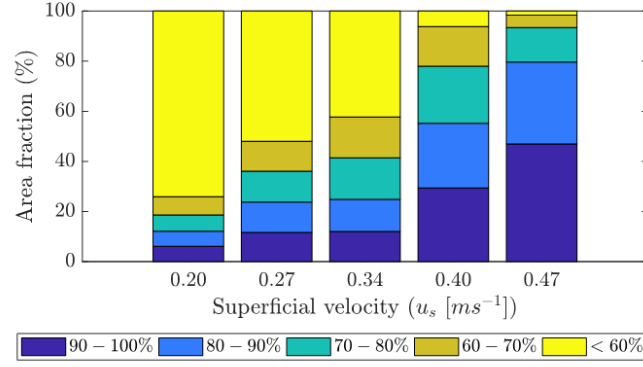
(a)
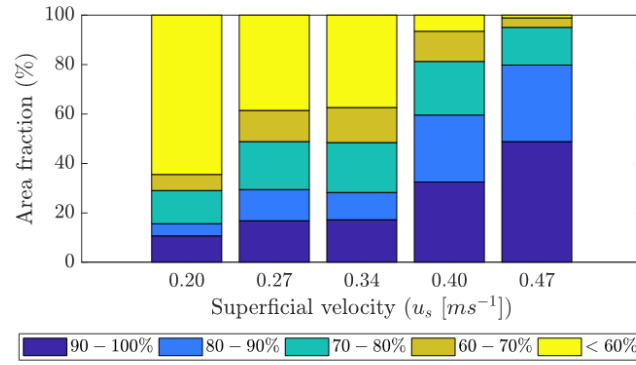
(b)
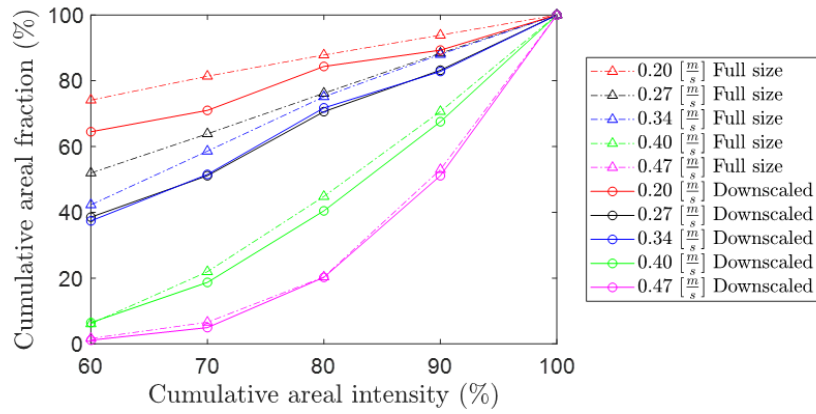
(c)

Figure 4.3 – Areal fraction performance for full resolution images (a) and downscaled images (b); cumulative distributions of areal intensity (c). Although, not clear from the images shown in Figure 4.2, the areal fraction analysis highlights the parity of performance in detecting the mixing performance. The distribution of cumulative areal fraction shows that the performance detection improves at higher flowrate.

In Figure 4.3(a, b), the area fraction histograms are shown for selected superficial velocities. The mixing performance trends are similar for the two set of data (high resolution in Figure 4.3(a) and low resolution in Figure 4.3(b)). This suggests that the resolution can affect the overall results but not drastically as it could be expected (see Figure 4.3(c) for the comparison).

The loss of information in this transformation is not significant particularly at high superficial velocity, where the mixing behaviour of the system is equally depicted by the 32×32 and the 2048×2048 images. This analysis demonstrates how in case of optical methods, although higher resolution guarantees a higher level of insight and information at meso and micro scale, it is still possible to gather information on general mixing performance with low resolution images. In the following sections, PLIF is used to evaluate the capability of ERT to describe mixing performance in the pipeline; as in this work, PLIF is used as a validation for ERT, full resolution PLIF images are used for comparison.

4.3.2 ERT-PLIF comparison

4.3.2.1 Experiment I

Fluids HB1 and PL have similar rheological parameters in terms of consistency index (K) 0.40 and 0.49 and power index (n) 0.58 and 0.59 respectively. The main difference is the presence of a yield stress in HB1. For this set of experiments, different superficial velocities (u_S) were used as given in Table 4.2 and samples of raw PLIF images and ERT tomograms obtained are shown in Figure 4.4.

	$u_s = 0.20$ m s^{-1}	$u_s = 0.34$ m s^{-1}	$u_s = 0.47$ m s^{-1}
PLIF image			
ERT image			
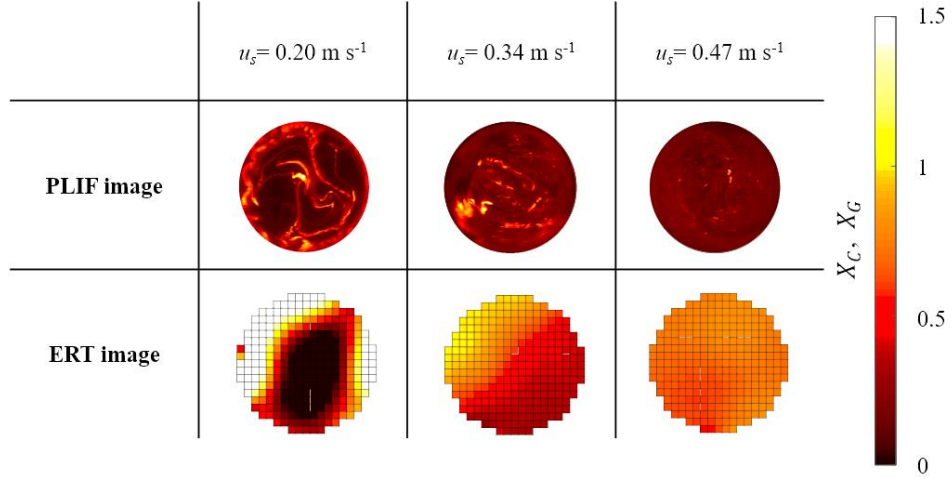
Figure 4.4 – Full size PLIF and ERT images at different superficial velocities for experiment I (Table 4.2) images the distinction between the two phases is clear, the ERT captures smooth change in colour especially at high superficial velocities.

It should be noted that there is a difference in orientation between the tomogram and the PLIF images since the high conductivity zones do not correspond to the same location in the PLIF images. This is thought due to residual rotational flow following the KM mixer elements which slowly dissipates after the mixer outlet. As expected, the resolution of the ERT is inferior to the PLIF, yet the contrast in the image is sufficient to identify an unmixed state. In both sets of images, it is possible to appreciate how the uniformity in colour increases as the superficial velocity is increased and better blending is achieved. The areal distribution analysis together with the cumulative plot is shown for both PLIF and ERT measurements for all values of u_S in Figure 4.5.
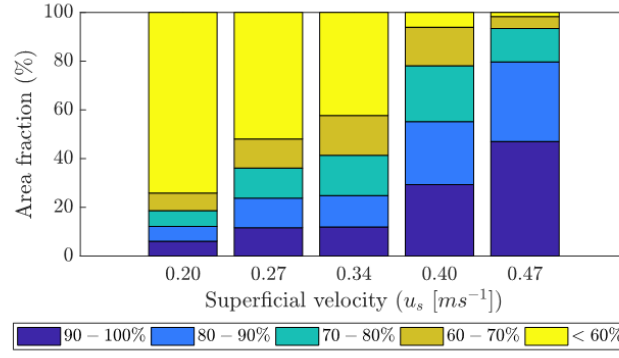
(a)
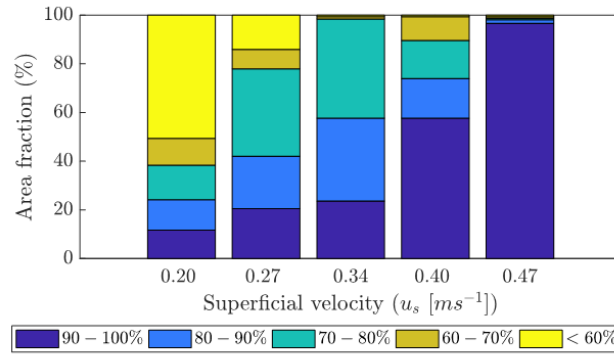
(b)
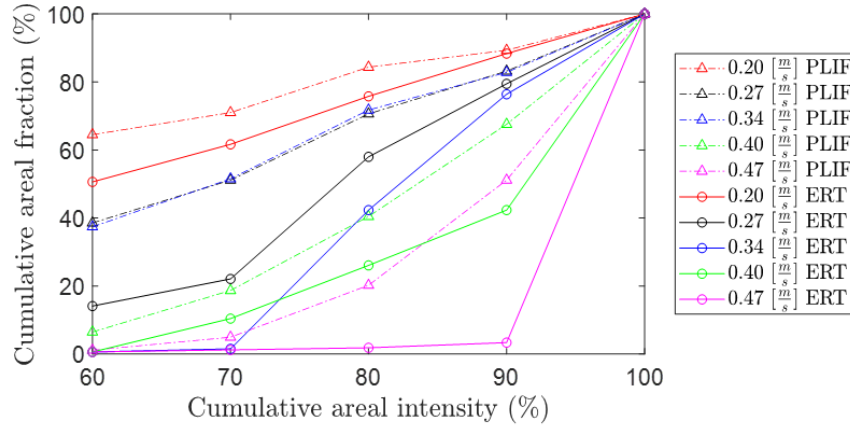
(c)

Figure 4.5 – Discrete areal intensity distribution from PLIF (a) and ERT (b) for all values of u$_S$ and cumulative distributions of areal intensity comparison (c) for experiment I (Table 4.1). The ERT and PLIF show similar profiles at low speed, while ERT cannot guarantee the same detection performance as PLIF.

As expected, the results do not overlap perfectly due to the different principle and resolution between the two techniques and ERT performs poorly as the mixing improves beyond the resolution of the measurement and the striations become too thin to be detected. However, for the first four investigated values of u_S, the observed trend of mixing performance is similar. This is taken to extremes at higher speeds, where ERT tomograms (Figure 4.4) overestimate the mixing performance, probably also due to the low contrast between the conductivities of the two mixing fluids, which is a consequence of the reconstructive algorithm.

4.3.2.2 Experiment II

With the objective to investigate worse mixing performance, a higher concentration of Carbopol 940 was used in the main flow (fluid HB2). The used fluids are reported in Table 4.2. As a consequence, the yield stress and the consistency index ($K_{HB2}/K_{HB1}\sim20$) values of the secondary fluid, employed in experiment II (PL), are higher. A few examples of PLIF and ERT images are showed in Figure 4.6. From previous findings (Alberini et al., 2014a), increasing the viscous properties would be expected to cause a drastic reduction in mixing performance and this is indeed observed - the increase of yield stress entails the formation of lumps as shown in Figure 4.6.
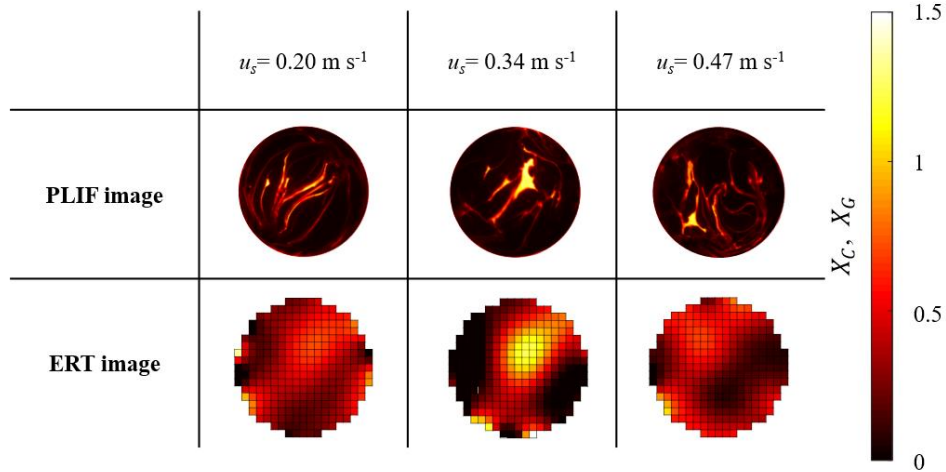
Figure 4.6 – Full size PLIF and ERT images at different superficial velocities for experiment II. Because of the high resistance to mixing of the used fluids (Table 4.2 and Table 4.1) the secondary flow is well visible for PLIF as well as for ERT tomograms.

Both from ERT tomograms and PLIF images it is difficult to qualitatively observe evolutions in mixing performance at higher speed; particularly looking at PLIF images it can be argued that at u_S between 0.27 m s^{-1} and 0.47 m s^{-1} the blending does not improve. Despite the ERT tomograms in Figure 4.6 are qualitatively well representing the PLIF image, the quantitative agreement shown in the cumulative distribution plot (Figure 4.7) is not so.

Although, in this case, the ERT is shown to significantly over predict the mixing performance in absolute terms. However, in a correct manner, it does not predict an improvement in mixing performance as the superficial velocity is increased. As observed for PLIF, particularly in the high mixing performance categories (90-100 and 80-90%) the system does not record any significant difference between the runs, as shown by the coinciding last three points of the cumulative areal fraction (Figure 4.7), meaning that in this case the increase in speed does not significantly improve mixing. This suggests that ERT may be used as a relative measure more than as absolute measurement.
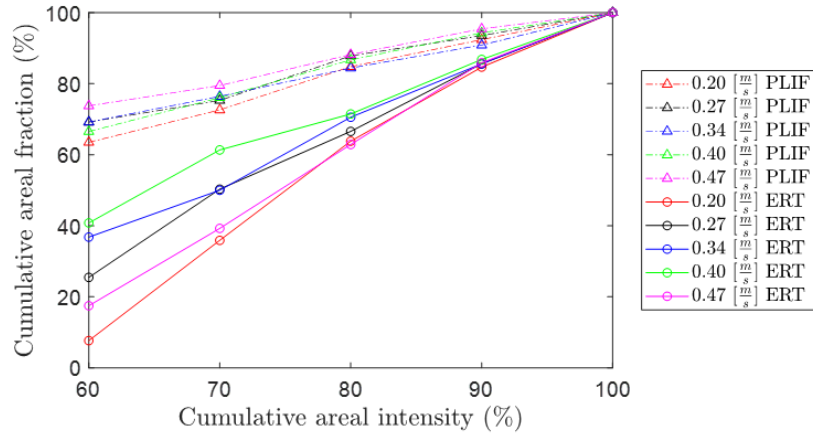
Figure 4.7 – Cumulative distributions of areal intensity for experiment II (Table 4.2). ERT is not able to characterise mixing performance as PLIF.

4.3.2.3 Experiment III

In this experiment (fluids reported in Table 4.2), the difference in conductivity was set to a lower value to further challenge the ERT technique. Moreover, at the same time, the level of achieved final mixing is reduced using fluids HB1 and HB2 as the main and secondary flows respectively. In Figure 4.8 both instantaneous PLIF images and ERT tomograms are shown for comparison at different superficial velocities.
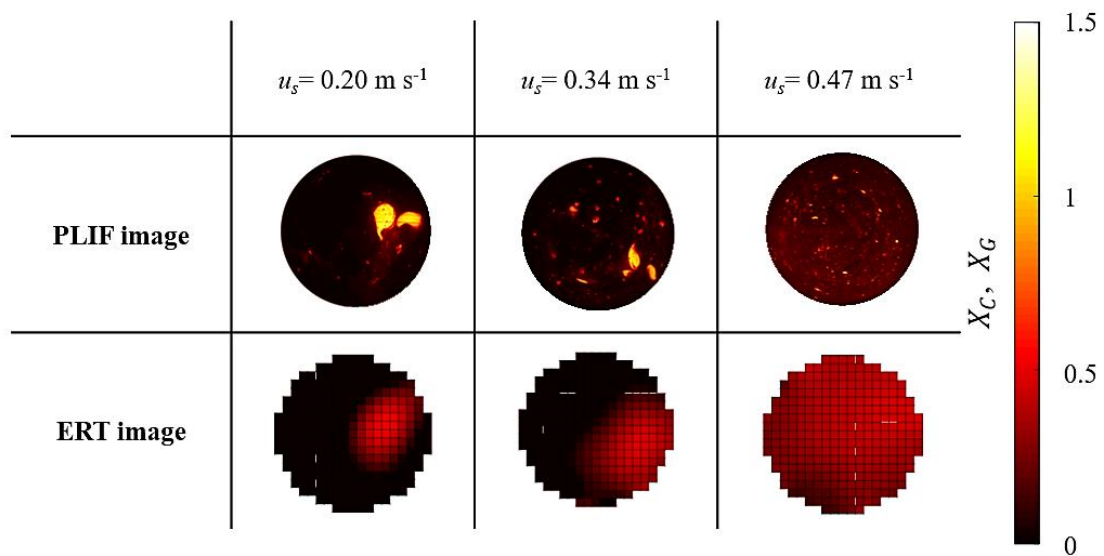
Figure 4.8 – Full size PLIF and ERT images at different superficial velocities for experiment III (Table 4.2). ERT tomograms do not show the same level of detail of PLIF. The reason being, the low size of the secondary fluid areas as well as the low conductivity difference used for this experiment.

From PLIF images it is possible to infer that from an unmixed condition at low speeds the system moves towards better blending performance above u_S equal to 0.4 m s^{-1}. The decreased conductivity contrast results in a smaller colour contrast between the secondary and the main phase in ERT tomograms although a higher level of uniformity is achieved at higher speeds.

Looking at areal fraction analysis (Figure 4.9), it emerges how ERT is able to estimate the unmixed condition at low speed despite the low conductivity contrast. ERT performance still follows observed trends for PLIF, highlighting the same inflection for mixing performance at the speed of 0.27 m s^{-1}. Although, an overestimation is still observed at high speed, particularly for the category of 70-80% mixing, while in this case ERT does not overestimate the highest mixing condition (80-90% and 90-100%) commonly the targeted condition in mixing processes.
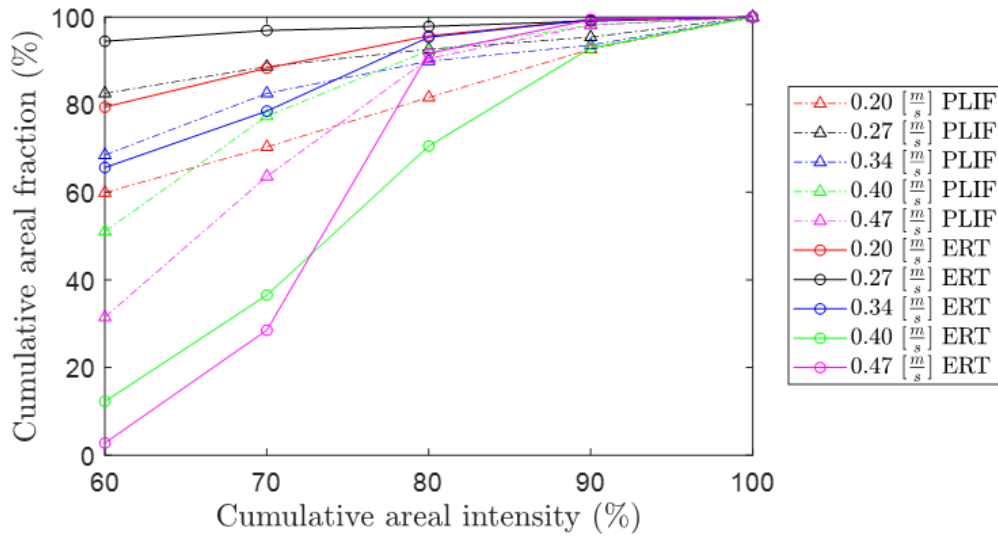
Figure 4.9 – Cumulative distributions of areal intensity for experiment III (Table 4.2). The higher consistency between ERT and PLIF is obtained at low superficial velocities.

Increasing the speed (above 0.27 m s^{-1}), and as a consequence the number of lumps of unmixed injected material, the divergence between PLIF and ERT data increases consistently. This is an issue which is partly due to the reconstruction algorithm (Linear Back Projection, LBP) and partly to the measurement resolution. In fact, LBP approximates a non-linear problem with a linear hypothesis, instead the low resolution characterising the technique limits the size of lumps that can be detected. Clearly, from the tomograms at low speed (at 0.20 m s^{-1}, 0.27 m s^{-1} and 0.34 m s^{-1}), the lumps, or the agglomerations of lumps, can be detected. However, at higher speed ERT fails in detecting them. In the present study, an additional obstacle is represented by the use of small conductivity contrast between the employed phases, which however does not seem to affect significantly the measurement in condition of poor mixing. Additional examples of tomograms are reported in appendix A.

4.4   Conclusions

In this work, the ability of ERT to assess the mixing performance of non-Newtonian fluids in static mixer has been investigated. The same methodology, developed in previous works (Alberini et al., 2014b, 2014a) is used for both PLIF images and ERT tomograms. Three experiments using different fluids with different initial contrast in conductivity have been employed. PLIF has been used to validate the data obtained in terms of qualitative and quantitative analysis. With the proposed method, ERT can be used as a relative measurement (measuring how much the mixing improved relative to the other runs at different superficial velocities) but not as an absolute one, as it could be expected, due to its limitations such as resolution and reconstructive algorithm smoothing. However, the relative trends show high level of agreement with PLIF results in particular to identify conditions of poor mixing (generally for all experimental runs below 0.34 m s^{-1}). This is not the case once the level of mixing increases (generally for all experimental runs above 0.34 m s^{-1}). The tested conditions were inherently challenging for the ERT, considering the employed small conductivity contrast (down to 0.1 mS cm^{-1}), however the lowest observed performance was (commonly to all experiments) obtained when the dimension of the striations/lumps is below the measurement resolution, regardless of the conductivity difference between the mixed phases.

4.5   Nomenclature

C_i Relative conductivity of the i-th pixel in the ERT tomogram, mS cm^{-1}

C_{inf} Relative conductivity of the mixture reached at perfect mixing, mS cm^{-1}

C_0 Relative conductivity of the main fluid prior the injection of secondary fluid, mS cm^{-1}

Δc   Difference in relative conductivity, mS cm^{-1}

G_i Greyscale value of the i-th pixel in the PLIF image

G_{inf} Greyscale value of the mixture reached at perfect mixing

G_0 Greyscale of the main fluid prior the injection of secondary fluid

Re Reynolds number

u_S Superficial velocity, m s^{-1}

X_C Dimensionless relative conductivity

X_G Dimensionless greyscale

x_i Volume fraction of the secondary phase i in the primary phase

5.

Using a Freeman FT4 rheometer and Electrical Capacitance Tomography to assess powder blending

The blending (or otherwise) of two powders of different physical properties (particle size, density, basic flowability) and contrasting electrical permittivity was studied in a Freeman FT4 rheometer. Two initial arrangements were used: one with the heavier, smaller powder on the top that would be expected to mix readily; and the other, the inverse, that would be expected to be resistant to the axial blending mechanism prevalent in the FT4. The torque and thus flow energy were tracked through 30 cycles of the FT4 impeller passing into and back out of the powder layer. In one case, the FT4 data were seen to evolve towards a steady state comparatively quickly, while, in the other, relatively little change in the basic flow energy was observed. The change in the first case is attributed to mixing of the powder and the lack of change in the latter case to the absence of mixing.

Simultaneous ECT measurements using a two-plane sensing arrangement were taken. The reconstructed tomograms and the basic average permittivity data show clearly the mixing in the first case and the absence of blending for the latter. This confirms not only the sensitivity of powder flowability measurements to segregation of component powders, but also the potential of ECT as a measurement tool for powder mixing and segregation studies.

This chapter is published in the Powder Technology journal in the following paper (Forte et al., 2018):

The conducted work has been a collaboration between the authors. The laboratory work was carried out by Giuseppe Forte and Michele Marigo. All the experiments and data processing related to powder characterisation were carried out by Michele Marigo. All the experiments and data processing related to ECT were carried out by Giuseppe Forte.

5.1   Introduction

Powder mixing is a ubiquitous process in many manufacturing industries spanning chemicals, pharmaceuticals, food, personal care and powder metallurgy. In some of these industries powder mixing is a critical process, as the homogeneity of ingredients can be imperative for the functionality and quality of the final products. In the pharmaceutical industry, for example, inhomogeneity leads to tablet-to-tablet non-uniformity of the dosage of the active ingredient in medicines. Unfortunately, trying to mix two dissimilar powders (*e.g.* light and heavy or small and large particles) can lead to an opposite outcome, *i.e.*, more efforts and energy in mixing may actually result in greater de-mixing, more commonly known as segregation (Ottino and Khakhar, 2000). Poor mixing processes are characterised by segregation, which consists of the separation of particles due to differences of physical properties (Seville et al., 2012). Typical factors that can lead to segregation are: differences in particle size, shape, density, surface roughness, forces of attraction and friction (Weinekötter and Gericke, 2013). Differences in these properties have also an effect on powder flow rheological behaviour (Shinohara, 1997). Typically, the three principal mechanisms for segregations are (1) trajectory segregation (different travelling distance between particles with

different sizes), (2) percolation segregation (small particles moving through the powder voidage created by powder bed dilation) and (3) vibration segregation (small particles filling powder bed gaps created by vibration) (Williams, 1976).

Understanding of the mixing and segregation mechanisms as well as the behaviour of the powder mixture is vital in many manufacturing processes for high quality products. To this end, many different mixing systems and material systems have been investigated using both experiments and Discrete Element Method (DEM) numerical simulations in the past several decades. The DEM is a single particle-based approach which is based on definitions of Newton's motion equations. It has been extensively used to study powder mixing (Arratia et al., 2006; Marigo et al., 2012; Moakher et al., 2000; Zhou et al., 2004). In DEM simulations, the motion for all the single particles is tracked and analysed, hence this technique can provide the much-needed insight into the mechanisms governing particle flow (Marigo and Stitt, 2015). However, reliable quantitative and validation studies are still challenging for state-of-the-art DEM simulations (Coetzee and Els, 2009; Coetzee et al., 2017; González-Montellano et al., 2011; Grima and Wypych, 2011). DEM simulations have been used to demonstrate the effect of powder mixing and the corresponding variation in flow energy for bimodal size particles with increasing size ratios in a FT4 Freeman powder rheometer (Yan et al., 2016). The Freeman FT4 powder rheometer (Freeman Technology, Malvern, UK), a bladed mixer-like powder-flow tester, is widely used in industry, mainly in the pharmaceutical sector, to characterise powder flow properties by measuring the resistance (force and torque) encountered by the rotating blade when penetrating the powder bed (Freeman, 2007). Flow energy, which is calculated from the measured force and torque, reflects the flowability of the powders. The dynamic nature of the test can promote particle mixing or segregation during the test procedure as results of particle properties differences.

The FT4 has been proposed as a potential tool to compare and rank the segregation tendency for particulate materials with distinct differences in flow energy of each component. Yan et al. (Yan et al., 2016) demonstrated the potential of using a FT4 Freeman powder rheometer to assess the mixing and segregation (de-mixing) process for populations of particles with different size ratios and flow properties as a result of the selected DEM input frictional parameters. DEM simulations were utilised to demonstrate the mixing and segregation in a Freeman FT4 powder rheometer, using binary mixtures with varied particle size ratio and volume fraction. It was shown, in Figure 5.1, that the change in flow energy associated with segregation and mixing, and their kinetics, depends on the particle DEM frictional contact properties and particle size ratios (SR). The DEM simulations on the Freeman FT4 rheometer, showed the flow energy changes during the test cycles as particles with different size ratios were being mixed or segregated. It was shown that, for a binary mixture of particles, the flow energy decreases as the material is being mixed by the action of the blade.
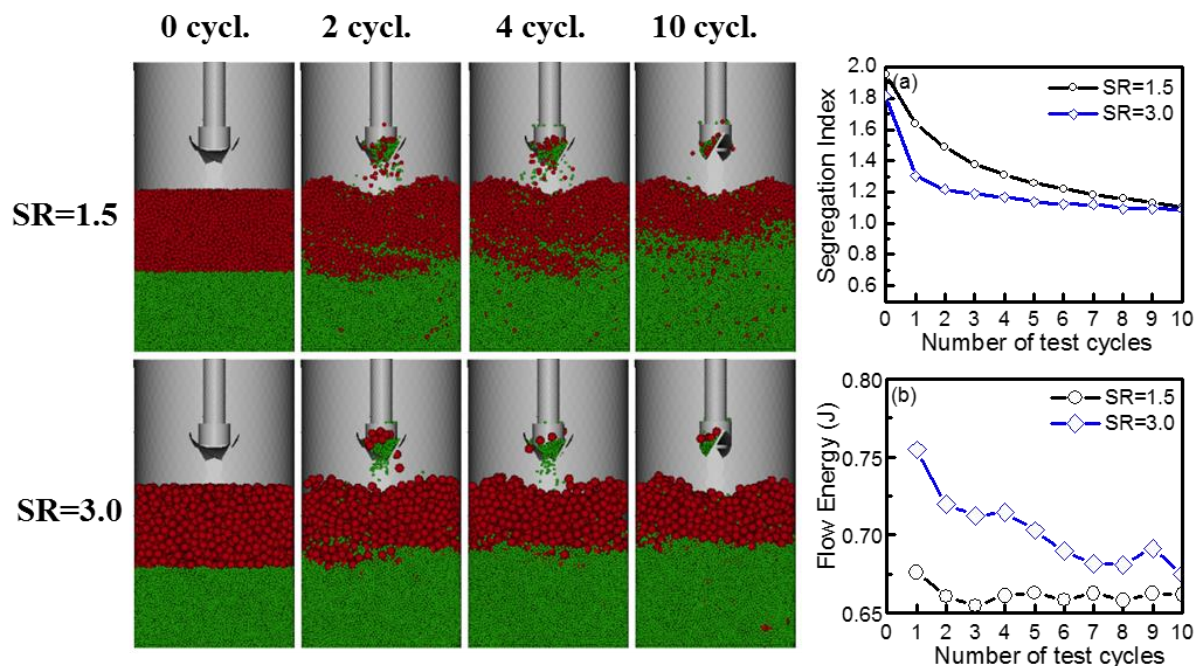
Figure 5.1 – DEM simulations of binary powder mixing in FT4: (left) the DEM simulations snapshots; (right) segregation index (a) and flowability energy (b) as functions of rotations of the impeller (Yan et al., 2016) at different size ratio (SR).

Moreover, the DEM simulations highlighted the formation of a dilated region (low number of particle contacts) behind the blade, while the ones in the front are being compressed (Yan et al., 2016). This indicates the formation of dilated areas where segregation can occur due to sifting segregation mechanisms. These mechanisms can occur as results of localised shearing, creating local dilatancy where the smaller particles can segregate, by the percolation mechanism, falling through the gaps generated between the larger particles (Remy et al., 2011).

In this context, developments in characterisation techniques for powder mixing studies will be beneficial to a better understanding of powder mixing and its industrial applications. Furthermore, better measurement approaches are required to take a step forward in validating the DEM modelling technique for mixing applications. Traditional characterisation techniques, such as sampling involving representative volume extraction using a thief probe in powder samples (Bridgwater, 1995) and slicing powder bed solidified using binder (Muzzio et al., 1997) are invasive and are conducted post experiment. The thief probe method can be problematic as the disturbance can damage the structure of packing, and particles along the sampling path are also collected by the probe. Alternatively, optically based Particle Image Velocimetry (PIV) (Conway et al., 2005) enables a 2D visualisation of the flow patterns within granular materials or at the powder bed surface. In recent years, advances in non-optical techniques have made non-invasive and in-situ characterisation of mixing of granular materials possible. The literature now includes many studies on powder mixing using Positron Emission Particle Tracking (PEPT) (Kuo et al., 2005; Marigo et al., 2013), X-ray tomography (Chester et al., 1999; Liu et al., 2013; Yang and Fu, 2004), and nuclear Magnetic Resonance Imaging (MRI) (Armstrong, 2011; Nakagawa et al., 1997; Porion et al., 2004;

Sederman and Gladden, 2001; Sommier et al., 2001). However, these characterisation techniques are costly and not easily available.

Electrical Capacitance Tomography (ECT) has been used for studies of solid concentration in gas-solid or liquid-solid mixtures (Rautenbach et al., 2013; Zhu et al., 2003) to assess segregation in fluidized bed (Rautenbach et al., 2013) and to monitor granulation (Rimpiläinen et al., 2011). This technique has several advantages including no radiation, low cost, high time resolution, and tolerance to high pressure and high temperature. Furthermore, its non-invasive nature makes it suitable for those processes in which contamination represents a potential issue. ECT exploits the difference in permittivity of inhomogeneous materials within a vessel (or pipeline) to reconstruct, through specific algorithms, the internal permittivity (and thus phase or material) distribution as cross-sectional images. The first research into the use of capacitance measures to reconstruct tomographic images for process applications dates back to the 1980s at the University of Manchester (Wang et al., 2010a). An ECT system is composed of a sensor cage with electrode plates, a Data Acquisition System (DAS) that controls and acquire the measured data by translating the electrode charge measurement into pixel values composing the tomogram. Being a soft-field tomographic technique, where the field lines are affected by the composition of the measurement zone, ECT produces images at a relative low resolution (Marashdeh and Teixeira, 2004). Despite this, it has been used in several applications involving particles, including circulating fluidized beds, fluidized bubbling beds, trickle beds and pneumatic conveying (Hamidipour et al., 2009; Jaworski and Dyakowski, 2001a; Liu et al., 2005; Makkawi and Wright, 2002; Rimpiläinen et al., 2012). Initial work in applying electrical capacitance measures for powder mixing was carried by Ehrhardt et al. (2005) in which a two-electrode electrical capacitance sensor has been used to detect the change in permittivity of different powder mixtures

measured to assess different grades of homogeneity. Work carried out by Rimpilainen et al. (2011), applied the capacitance tomographic technique to image powder mixing. A single plane ECT sensor has been applied in combination with Finite Element Method (FEM) to investigate radial mixing in a high-shear mixer and in a granulator, showing that the ECT technique could effectively give useful information on powder processes.

In this study, ECT has been used to study powder mixing in the FT4 powder by correlating tomographic data and images with the change in mixing obtained from the FT4. The changes in powder flow were compared to the permittivity changes captured by ECT. Two commercially available powder materials (mannitol and zeolite), each with different permittivity were used in the experiments; the difference in permittivity allowing for discrimination between the powders by ECT. The two powders were fully characterised in terms of powder physical properties (particle shape, skeletal density and morphology) and bulk flow properties.

5.2   FT4 rheometer and ECT set-up

The Freeman FT4 powder rheometer, Figure 5.2 (a) and (b) measures the powder flow response by measuring the resistance for a rotating blade penetrating a powder bed (Freeman, 2007). The dynamic nature of the test could promote particle segregation or mixing for blends with a significant difference in single particle properties. In this study, potential particle mixing and segregation and their effect on flow energy has been investigated using the change in flow energy and the change on the overall powder bed electrical permittivity. Figure 5.2 (c) and (d) shows the experimental set-up indicating the blade principle (measured for the penetration force F and rotational torque resistance T) and the modified set-up including the Electrical Capacitance Tomography (ECT) electrodes.
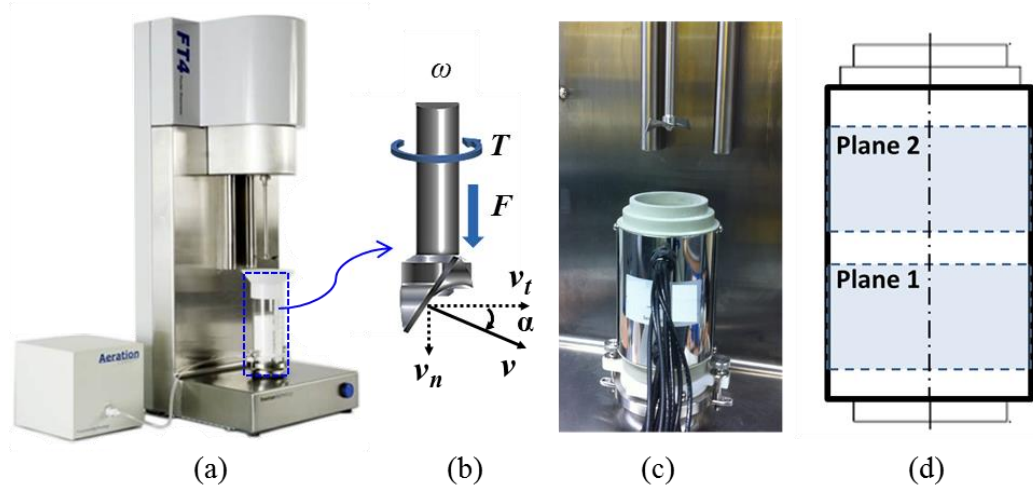
Figure 5.2 – Freeman FT4 Powder Rheometer instrument (a), measurements from the blade: *T* – torque (Nm), *F* - axial force (N), v_t - rotational velocity (m s^{-1}), v_n - axial velocity (m s^{-1}), *v* – tip speed (m s^{-1}), *α* - helix angle (in rad) (b), ECT axial probes installed on a specially made FT4 vessel (c), schematic for the two axial plane ECT probe (d) (in bold the actual volume occupied by powders).

The flow energy is calculated only during these cycles as the integral of the energy gradient throughout the depth of the blade in the powder bed using Eq. (5.1):

$$E = \int_0^h \left(\frac{T}{R\tan\alpha} + F\right)dh \tag{5.1}$$

where the *T* is the torque on the blade, *F* the vertical axial force determined experimentally, *R* the radius of the blade (m), *α* the helix angle (°), with tan*α* equal to the ratio of axial velocity to rotational velocity; *h* the penetration depth of the blade within the particle bed.

Figure 5.2 (c) and (d) shows a picture and a schematic for the ECT probe installed on the purpose built 50 mm diameter plastic sensor cylinder. The ECT instrument used for the work was the commercially available 'm3c' instrument manufactured by Industrial Tomography Systems Ltd. (ITS), Manchester, UK, with a 24-channel input array allowing up to 24 electrodes from a sensor to be connected to the instrument. For the current investigation, a

two-plane sensor, with internal diameter of 50 mm with 8 electrodes per plane, was manufactured by ITS and used with the instrument.

For the purpose of these experiments, the two planes simultaneously recorded tomographic data for each frame and the trend of planar averaged permittivity was used to compare the two planes to determine the axial mixing or segregation of the two powders. The sensor consists of two parts – a polyethylene (PE) inner cylindrical tube and the electrode assembly. The tube was designed specifically to fit the Freeman Rheometer as the couplings to connect the sensor the base of the FT4 were required to be part of the sensor. The electrode assembly consists of 16 copper electrodes 30 mm long, with thin copper strips (7 mm) at the top and bottom of it to prevent permittivity distributions outside the sensor affecting charge measurements. The two planes were divided by a grounded band 10 mm long and the distance between the electrode assembly and the outside earthed screen was 1 mm. The small dimension of the sensor allowed the authors to disregard the distortion caused by the fringe effect (Wang et al., 2007). Nevertheless, the sensor has been designed with relatively long electrodes and with guard electrodes, in order to minimize the distortion caused by not uniformity of the electric field in axial direction (Sun et al., 2015).

The ECT method relies upon the tomographic principle; a known potential is sequentially applied to an electrode within the ring assembly and the resultant induced charge measured at each electrode around the ring; the process is then repeated energizing the following element on the ring. The ECT sensor was connected to the DAS instrument using an individual earthed co-axial cable for each electrode and connectors between the cables and instrument.

The measurement strategy of ECT requires the acquisition of reference frames prior to starting the measurement. The ECT instrument is able to measure the relative changes in permittivity from a starting condition and in a well-defined window of permittivity, therefore,

the measurement strategy requires the acquisition of reference frames prior to measurement. High and low reference frames are required for calibration and normalization. The low reference frame was taken by filling the sensor with the powder having the lowest permittivity (mannitol) while the high permittivity reference frame was taken using the powder with the highest relative permittivity (zeolite). The "ITS Toolsuite" software used for reconstructing the images offers two possible algorithms: linear back projection (LBP) and high dielectric reconstruction (HDR). The latter is generally used for systems in which one of the phases has particularly high permittivity (e.g. water), therefore the chosen reconstruction algorithm was LBP. Although the problem of extracting the electrical permittivity distribution from the peripheral capacitance measurements is non-linear, the use of this method is the most widely applied due to its low computational cost and its relative simplicity when the required image quality is not particularly high (Yang and Peng, 2003). In this study, the focus is kept on the average permittivity changes across the planes during the FT4 cycles disregarding the phase distribution variations across the tomogram, therefore in this case LBP is considered to give an acceptable information quality.

The powders were filled in the mixing FT4- ECT set-up utilizing two filling patterns: one which mixes (1st system: mannitol at the bottom 2nd system: mannitol at the top) and another which does not mix (2nd system: zeolite at the bottom and mannitol at the top). The changes in powder flow were tracked over time, while the FT4 blade was moving in and out the tests cylinders to assess the change in powder bed associated to mixing.

Figure 5.3 shows the two filling patterns (with 50% in volume for each powder fractions) as the following cases:

Case 1, 2 and 3 (to assess repeatability):

- Mannitol at the bottom (low permittivity)

- Zeolite at the top (high permittivity)

Case 4, 5 and 6 (to assess repeatability):

- Zeolite at the bottom (high permittivity)

- Mannitol at the top (low permittivity)
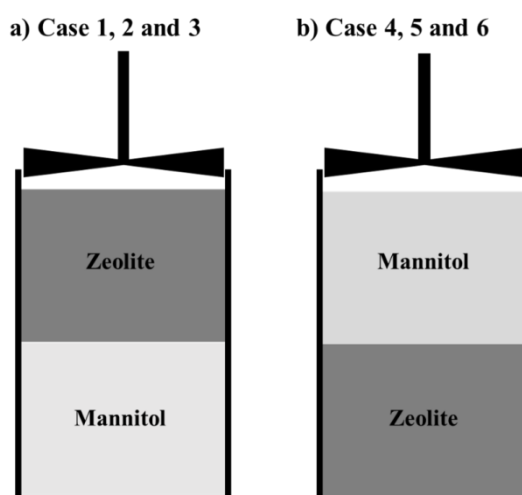
Figure 5.3 – Filling patterns for the four cases studied in this work. Powder details are reported in Section 5.3.

The powder mixing procedure consisted of applying a sequence of 30 cycles to the initial pattern showed in Figure 5.3. Every cycle consisted of a down test (Helix angle -5°, Tip Speed -100 mm/s), during which the energy and the torque at the blade was measured by the FT4, and a conditioning cycle up at a lower tip speed (Helix angle -5°, Tip Speed 60 mm/s). At the end of each cycle the mixing was paused, with the blade outside the chamber, to allow ECT data to be collected. The capacitance measurement strategy involves the application of

an electric field which requires the absence of metallic or external parts within the sensing region. Therefore, in order to collect unbiased data, 20 frames for each plane were collected at the conclusion of every cycle at a sampling rate of 10 frames per second. The frames were then averaged per plane and trend of relative permittivity with mixing cycles was observed. A summary of the measurement and mixing strategy is reported in Table 5.1.

Table 5.1 – Test and condition steps including the blade paused outside the vessel. Each step was repeated 30 times.

Test step	Blade action	Description
Test 1	Helix angle -5°, Tip Seed -100 mm/s, Direction Down	Total flow energy calculated using force and torque during this cycle
Conditioning 1	Helix angle -5°, Tip Speed 60 mm/s, Direction Up	
Blade stop 1	Pause	Pause for 5 seconds outside the vessels for ECT tomogram capture
Test 2	Helix angle -5°, Tip Seed -100 mm/s, Direction Down	Total flow energy calculated using force and torque during this cycle
Conditioning 2	Helix angle -5°, Tip Speed 60 mm/s, Direction Up	
Blade stop 2	Pause	Pause for 5 seconds outside the vessels for ECT tomogram capture
.....		
.....		
.....		
Test 30	Helix angle -5°, Tip Seed -100/s, Direction Down	Total flow energy calculated using force and torque during this cycle
Conditioning 30	Helix angle -5°, Tip Speed 60/s, Direction Up	
Blade stop 30	Pause	Pause for 5 seconds outside the vessels for ECT tomogram capture

5.3   <u>Powder materials characterization methods</u>

The two powders used in these experiments were Mannitol Pearlitol 200 SD (Roquette, UK) and Zeolite commercial spray dried (JM, USA). The materials, used in different JM applications were accurately chosen among different available products for their properties, (both electrical, porosity and density). Although, Mannitol and the used Zeolite are not currently mixed in JM production processes, they were selected among JM most used powders as test case to demonstrate capability of ECT to monitor powder blending. Both powders were characterised with regards to their physical (particle size, particle shape, particle skeletal density) and bulk flow properties, which are the main properties that influence the mixing behavior resulting in a variation of the total flow energy and captured by the ECT.

5.3.1 Powder physical properties: size, morphology and skeletal density

Single particles physical properties, particle size distributions (Sympatec Qicpic dry using dispersing method with 0.5 bar pressure) and particle skeletal density (using Micromeritics 1340 Helium Pycnometer according to ASTM method D6761-02) were measured and are reported in Table 5.2.

Table 5.2 – Summary for PSD (Sympatec Qicpic, 0.5 bar dry) and particle porosity (He pycnometer).

Size	Mannitol	Zeolite
d_{10} [μm]	129.1	76.1
d_{50} [μm]	174.4	134
d_{90} [μm]	247.3	200.5
Span	0.68	0.93
Skeletal density [g/cm^3]	1.461	2.3917

The results for the particle morphology are shown in Figure 5.4. Particle morphology was assessed by scanning electron microscopy (SEM) showing a much higher sphericity for the Zeolite when compared to the Mannitol. The high sphericity was confirmed by the Sympatec Qicpic measurement (including 3 repeats). However, the technique did not quantify the difference in sphericity between the two samples as it can be noticed from the SEM images.
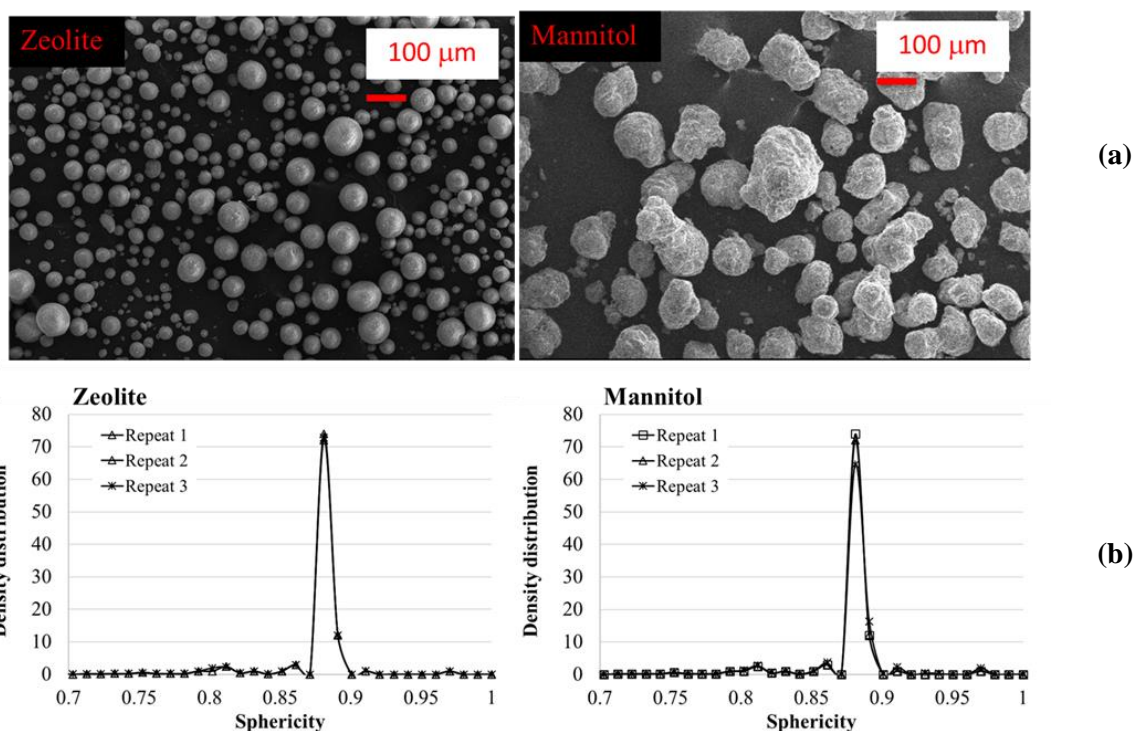
Figure 5.4 – SEM images for Zeolite and Mannitol[1] (a) Shape distribution from Sympatec Qicpic including 3 repeats showing the high particle sphericity (b).

5.3.2 Powder flow bulk properties: Brookfield shear cell flow function and Freeman rheometer stability test

Powder bulk flowability properties, such as cohesion and bulk density, are important properties that would affect powder mixing. Flowability for a bulk powder material depends on many factors, such as particle size, shape, size distribution, packing, density, surface properties as well as processing conditions like moisture content, temperature, humidity, electric charge and the applied shear/stress. In this work, the flowability for the Mannitol and Zeolite was assessed directly by determination of the yield locus and the resulting flow function (*ffc*) and bulk density, using a Brookfield PFT ring tester (Brookfield, UK).

---

[1]SEM analysis was carried out by JM analytics lab

A sample of the powder bulk solid specimen is repetitively loaded vertically by a normal stress (consolidation) and shear deformation is applied by a moving cell with a constant velocity. The result of this load is a horizontal shear stress (Carr and Walker, 1968; Jenike, 1961) that allows to determine the yield locus (the limit at which the bulk material fails and starts to flow) as a relationship between the measured shear force and the applied normal loads. The yield locus and corresponding Mohr's circles can be used to predict how easily a particulate material would flow under those conditions by defining the flow function (*ff*c) (Jenike, 1964).

Figure 5.5(a) shows the very good flowability for the two considered powders, as for both the flow function *ffc* lies in the "free flowing" region. The error bars represented by the standard error are smaller than the symbols utilised in the plot, concluding that the measurements showed high repeatability. The excellent flow properties are the result of low cohesion, fairly large size and narrow range of particle size distribution and the particle near spherical morphology.
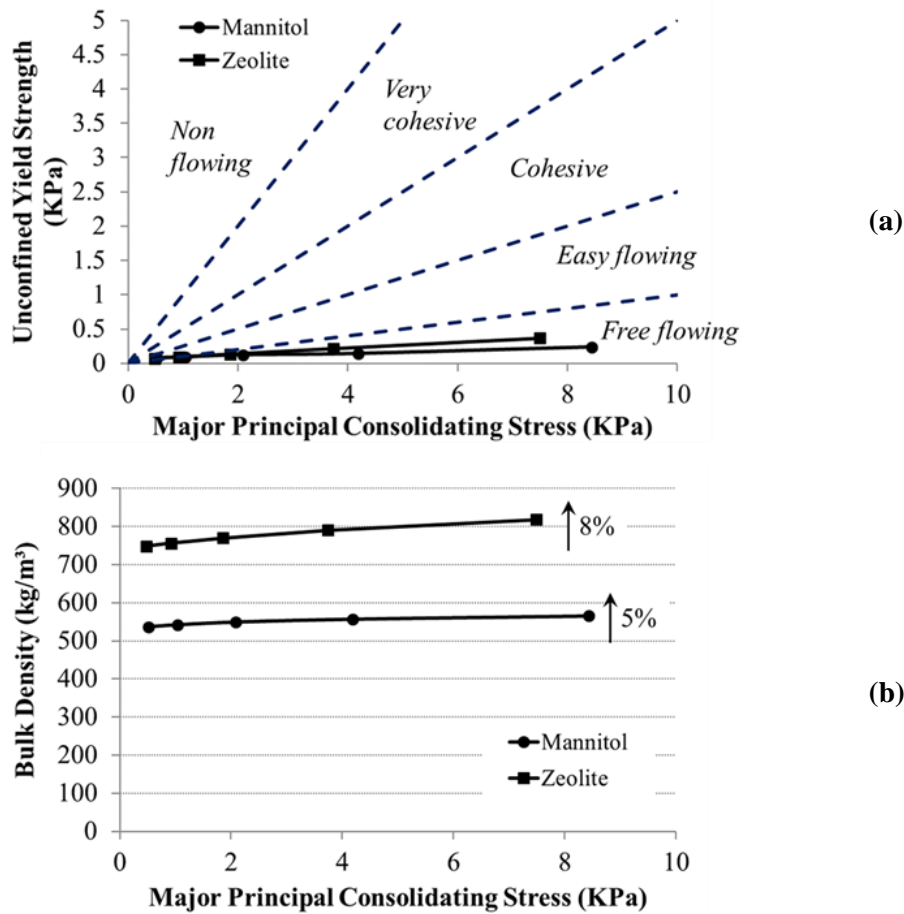
Figure 5.5 – Zeolite unconfined yield strength σ_c versus major principal consolidation stress σ_1 and flow function ffc (a). Bulk density over a range of Major Principal Consolidating Stresses (b). The two powders are characterised by different bulk densities, both showing a relative small increase % when increasing the applied major principal consolidating stress

The bulk densities determined by shear cell measurement (Figure 5.5 (b)) are much lower than the skeletal density of the material measured by helium pycnometry as the latter excludes the micro and nano porosities of the particles and the voidage between the packed particles. From the plot (Figure 5.5) it is possible to notice that the bulk density for the Zeolite (between 750 and 820 kg/m^3) is much higher than the one for mannitol powder Zeolite (between 520 and 580 kg/m^3). The measurements were highly repeatable with a standard error equals to 1.5 kg/m^3. Moreover, it is interesting to note in Figure 5.6 (b) the approximate 5% (Mannitol)

and 8% (Zeolite) increase of bulk density as a function of major principal consolidation stress; this highlights the low compressibility of the two powders. As a result of this which is an additional indicator of good flowability, the powder FT4 Freeman rheometer tests should be highly stable as the powder bed should not compress extensively under the low stress delivered by the blade action. The FT4 Freeman powder flow rheometer was also used by employing the manufacturer stability test to determine the stability under dynamic flow nature of the material. This test procedure includes the repetition of 10 consecutive tests. The first 7 are conducted at the same tip speed (100 mm/sec) followed by the remaining 3 tests conducted at decreasing tip speeds (70 mm/s, 40 mm/s and 10 mm/s). This test is employed to assess the dynamic flow differences between the two powders and their stability. A series of test parameters can be defined to characterise the powder behaviour under these testing conditions as follows:

- Basic Flowability Energy (BFE)= Energy test 7 [mJ];

- Conditioned Bulk Density (CBD) = split mass/split volume [kg/m^3];

- Specific Energy (SE)= (Up Energy cycle 6+ Up Energy cycle 7)/(2 x split mass) [mJ/g];

- Stability Index (SI)= Energy test 7/Energy test 1;

- Flow Index Rate (FIR) = Energy test 11/Energy test 8.

As reported in Figure 5.6, the stability tests, including 3 repeats, match the expectation of high stability for both the powders. Therefore, the possible change of powder flowability during the mixing cycles should not be associated with an increase of solid fraction, which is shown above to be highly unlikely, but rather with the effect of powder mixing or

segregation. Moreover, it can be stated that the flowability is not rate dependents and, as a consequence of this, the blade speed would only have an influence on the rate of mixing and little if any influence on the flowability of the powders.
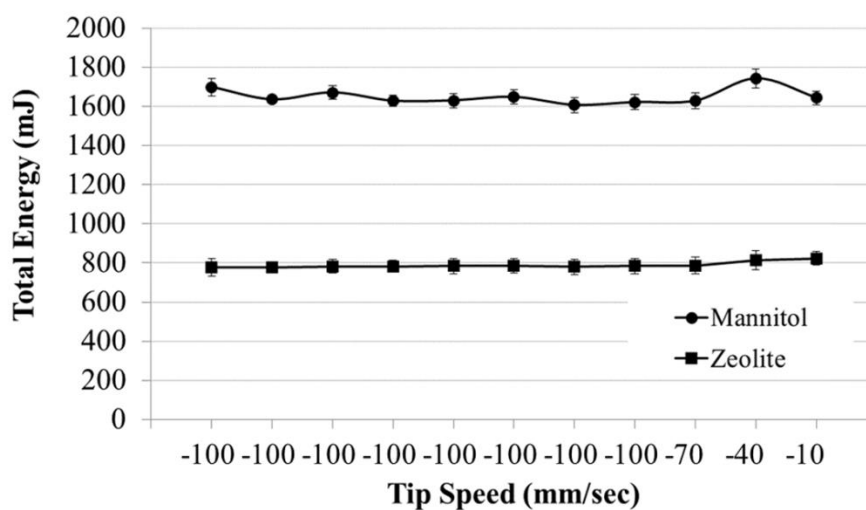
Figure 5.6 – FT4 Freeman standard stability test. Error bars represent the standard error from 3 repeats showing the high stability for the tested powders.
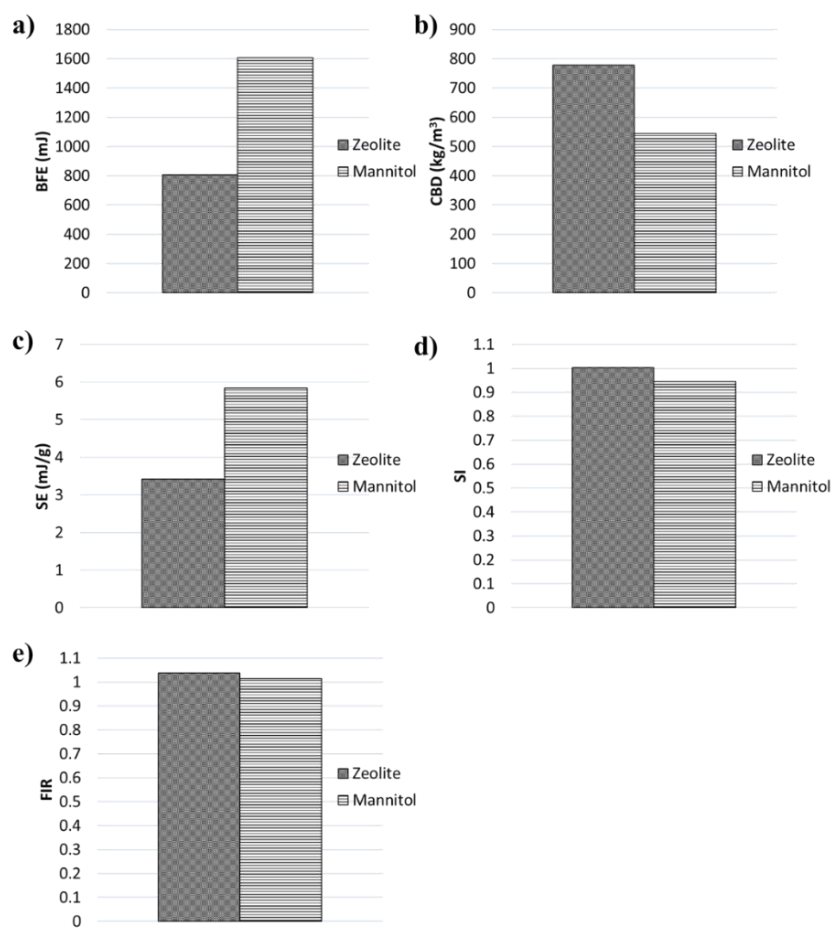
Figure 5.7 – Stability test parameters: (a): Basic Flowability Energy (BFE), (b) Conditioned Bulk Density (CBD), (c) Specific Energy (SE), d) Stability Index (SI), (e) Flow Index Rate (FIR). The standard errors from 3 repeats are not represented in this plot as too small.

In Table 5.3, a summary for the comparison between the data for the two powders, measured by FT4 Freeman powder rheometer, are reported, including the errors from the repeats showing the high repeatability for the measurements. Among other properties, the SI indicates the stable nature of the two powders and the overall higher bulk density for the zeolite materials can be noticed.

Table 5.3 – Summary for powder flow characterization for Mannitol and Zeolite. Standard error for the 3 repeats is shown in brackets.

	Mannitol	**Zeolite**
BFE [mJ]	1606.77 (39.81)	805.77 (13.76)
CBD [kg/m^3]	543.50 (2.75)	777.19 (2.21)
SE [mJ/g]	5.84 (0.06)	3.42 (0.05)
SI	0.95 (0.007)	1.00 (0.004)
FIR	1.01 (0.006)	1.04 (0.005)

The difference in flow energies between the two powders can be explained by the effect of their size distribution, shapes and skeletal density. The mannitol has higher flow energy than the zeolite which is attributed to particle mechanical interlocking resulting from the higher surface roughness and irregular shape as showed from the SEM images in Figure 5.4. The zeolite powder has particles with higher sphericity, lower particle size span, resulting to a higher bulk density. These properties directly affect the mixing ability of the two different powders and it is the effect upon overall bulk mixing that can be observed using ECT.

5.4   Results

For each test case the following procedure was followed:

1) Calibration: the cylinder was fully filled with mannitol and the ECT low reference frame was collected. The chamber was then emptied, cleaned and refilled with zeolite powder to take the ECT high reference frame;

2) Setting the test: the cylinder was filled with 50% in volume of powder 1 creating the bottom layer; the powder 2 was then added to fill the remaining 50% volume;

3) Taking 20 frames at the condition 0;

4) Initiating the repeating test steps;

    a) The blade penetration force and torque were continuously recorded;

    b) The ECT frames (20) were captured when blade has exited the powder bed;

5) Continuing to run the test step to completion, 30 test steps (as indicated in Figure 5.4).

A set of 6 experiments was conducted. The first three tests with Mannitol at the bottom and Zeolite at the top (case 1, 2 and 3). In the second three experiments (case 4, 5 and 6) the inversed filling was considered (Zeolite at the bottom and Mannitol at the top).

The ECT calibration step allows the system to set the boundary of the operational electrical permittivity range. In the tomograms (which report the reconstructed normalised permittivity in the cross-section) a value of 0 is assigned to the low permittivity material and a value of 1 to the high permittivity one. At the starting condition, the electrode plane corresponding to the mannitol (low dielectric constant) will record an average permittivity close to 0 and the electrode plane corresponding to the zeolite layer, an average permittivity value of 1. By inducing powder movement, the impeller will cause the migration of powder from top to bottom and vice versa causing the initial recorded values to become closer. The stress input by the blade onto the powder bed could cause an increase in compaction and influence the average electrical permittivity of the material. The trend of average normalised permittivity is reported in section 5.4.1.

Sections 5.4.2 and 5.4.3 report the results from the FT4 and ECT of the powder mixing studies. In the experimental data, a different behavior is observed for the two cases. In the first three repetitions the two powders were gradually mixed eventually achieving relative state of being well mixed at cycle 27. The second configuration, with zeolite at the bottom and mannitol at the top, does not behave similarly to the first one showing a significant resistance to reaching a state of being well mixed. These behaviors were clearly observed in the ECT tomograms and average conductivity.

5.4.1 Electrical Capacitance Tomography (ECT) validation

Electrical properties of powders are typically affected by the bulk density. The effect of the blade and shaft motion across the powder bed could affect the average permittivity, hence the acquired data during the experimental cycles. To investigate this effect, validation runs were conducted applying the FT4 and the ECT to single material type loading pattern (only one powder type per repeats in the measuring vessel). A number of 10 cycles (the first 10 cycles from the test procedure description from Figure 4) have been applied. The sensor was totally filled with the zeolite powder and the ECT data were recorded as each of the FT4 cycle was completed; the same was then repeated for the mannitol powder. A total of three repetitions per test case were repeated in Figure 5.8.
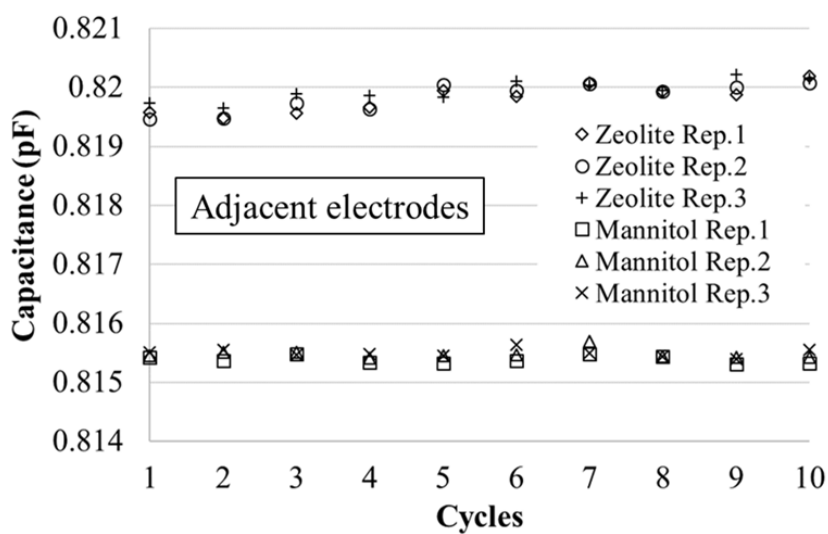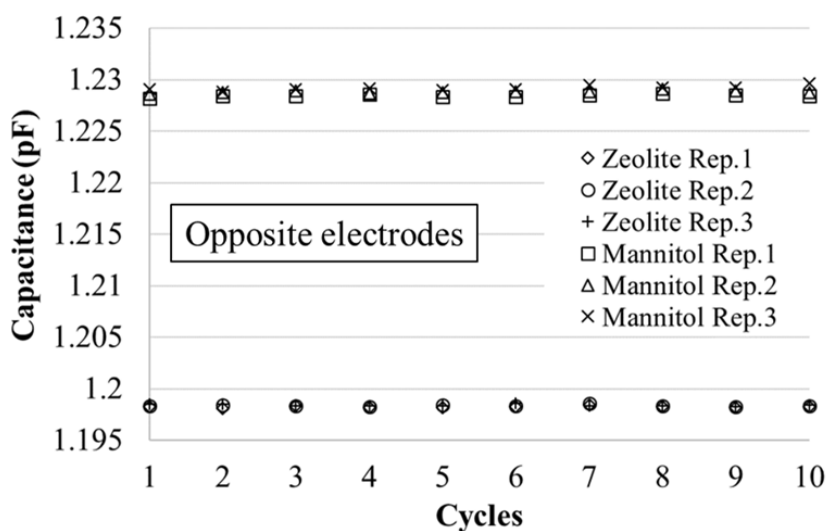
Figure 5.8 - Raw capacitance data versus FT4 cycle runs for one pair of electrodes in adjacent (a) and opposite (b) position for both powders. The capacitance does not change when the powder bed is sheared under repeated cycles.

The recorded raw capacitance for two adjacent and two opposite electrodes is reported for the two cases and the three repetitions. In Figure 5.8, one of the planes is reported for simplicity. It is possible to appreciate that, during the trial, the capacitance measurements at these electrodes over each cycle are not significantly affected. It can be stated that there is not a

major effect in the change in bulk density leading to an insignificant effect on the electrical property of the powder bed.

5.4.2 FT4 Freeman rheometer powder flow total energy results

The total flow energy was determined after each test cycle from the FT4 data using Eq. (1). Figure 5.9 shows that for Cases 1, 2 and 3 the flow energy is changing, presumed to be a consequence of the materials mixing, whereas for Cases 4, 5 and 6 the flow energy is only slightly changed, and the materials may thus be presumed not to be effectively mixing.
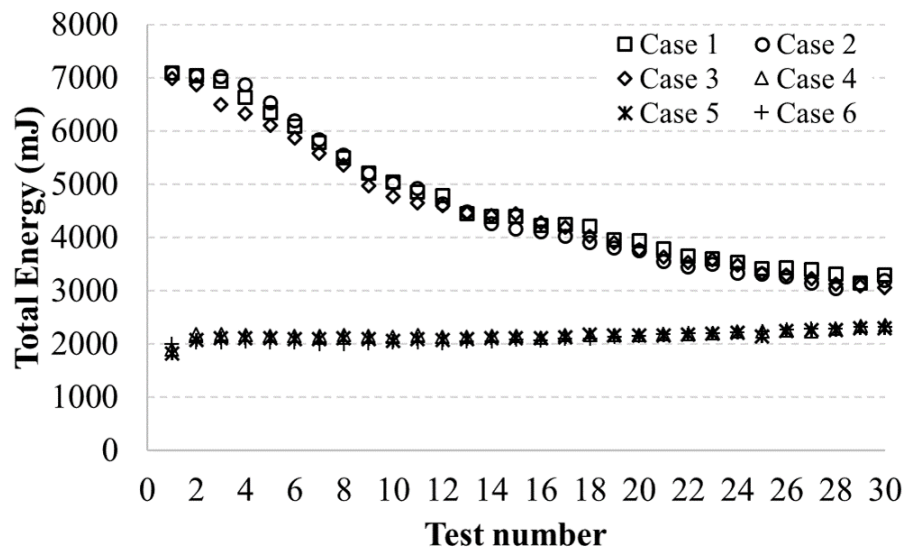

Figure 5.9 – Flowability change, measured as total energy, as function of test step number. The total energy is calculated from Eq. (5.1) using measurements obtained from the FT4.

The change in total energy in the first case is significant across all the cycles as there is a reduction of more than 50% from the 1st to the 30th cycle. The mixing that occurs as a result of the impeller agitation has a significant effect on the data recorded by the rheometer. In general terms, this should be considered when using the FT4 to characterize the flowability of powder mixtures. The degree of homogeneity of the mixture has a significant impact on the measured energy over a prolonged number of test cycles.

5.4.3 ECT results

The FT4 data indicate significant differences in the BFE response for the two different initial loading patterns, which based on the powder flow assessments, can reasonably be ascribed to mixing or the lack of it. The ECT data will now be presented, showing that this is indeed the case.

The ECT results too, expressed as relative permittivity as a function of progression of the FT4 cycles, show different responses in the two cases as shown in Figure 5.10 and 5.11 below.
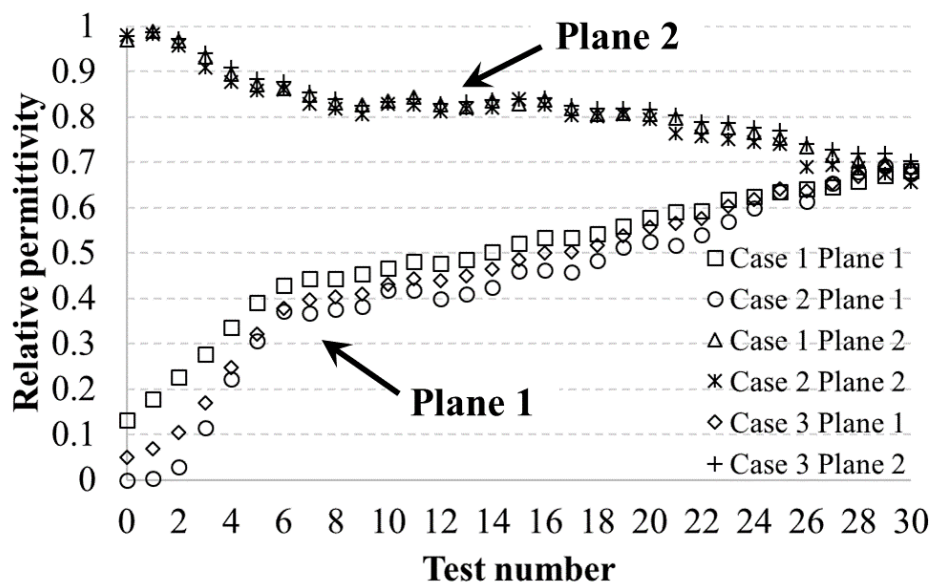

Figure 5.10 – Case 1, 2 and 3 (three repeats): mannitol at the bottom (Plane 1) and zeolite at the Top (Plane 2). The relative permittivity between the two planes becomes closer as the powder samples are mixing.

In Case 1, 2 and 3 (essentially repeats), in agreement with the energy plot from the FT4 data, the dispersion of powder is strongly dynamic; at each run of the blade through the powder bed, the relative average permittivity changes significantly. This shows that the blade induces powder mixing as with the progression of the cycles, the two measurement planes reach the same permittivity, as it would be expected in cases of good mixing. The convergence at the same value of the two planes in the two cases indicates that a high grade of homogeneity was

reached by Cycle 27 and conserved through until Cycle 30. The final value attained depends on the different dielectric constants of the two powders, their mass fraction and the bed voidage present within the sensor (mixing rule). That the same final value is measured for Cases 1, 2 and 3 demonstrates the high repeatability of the FT4 tests. The initial deviation from 0 of the initial value, in Case 1 and 3, of Plane 1 could be attributed to an induced higher packing of the mannitol in the initial filling of the cylinder.

The results of Cases 4, 5 and 6 (essentially repeats of the loading pattern expected to resist mixing) are presented in Figure 5.11.
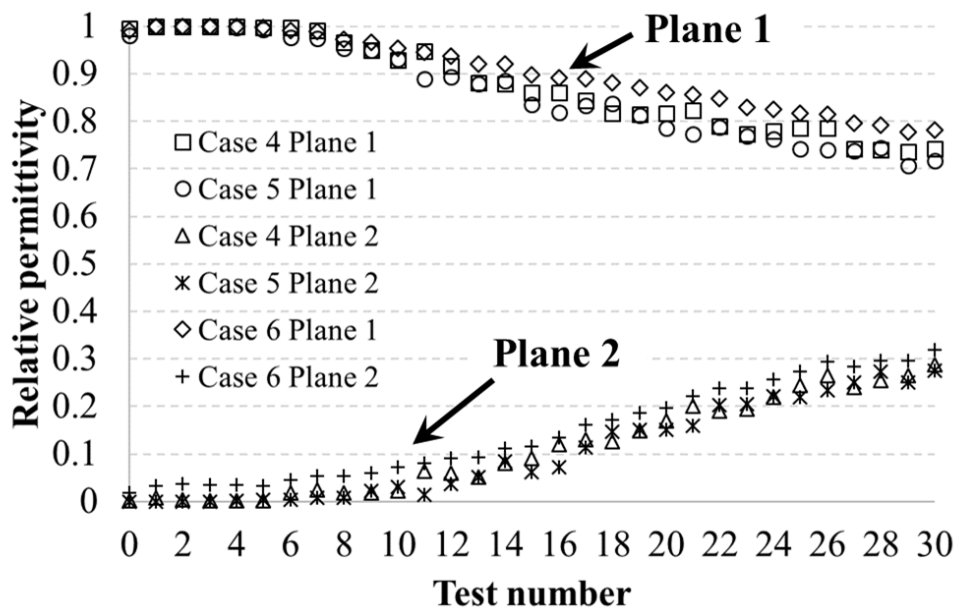

Figure 5.11 – Case 4, Case 5 and Case 6 (three repeats): Mannitol at top (Plane 2) and zeolite at the Bottom (Plane 1). The relative permittivity between the two planes change only slightly as the powder samples mixing is minimal.

In case 4,5 and 6 a different behavior is observed when compared to case 1,2 and 3 as at the end of the 30th cycles, the relative permittivity of the two planes remained far apart. In the first 10 cycles the variation is negligible, denoting a high resistance to blending of the two powders. A similar behavior was noted in the energy plot where the condition seemed not to vary much from the initial condition. The ECT data register a converging trend later in the

experiments, but notably later than observed in Cases 1, 2 and 3 and indicating a significantly lower rate of mixing. This loading configuration case, thus, can be identified as an example of poor mixing, attested by the persistent difference in permittivity of the two planes to the end of the experiments.

In Figure 5.12 a series of sample tomograms is shown for Cases 2 and 5. The initial condition and the tomograms for the two planes are shown for every 5 cycles. The difference in the two cases is evident: while in Case 2 the tomograms for the two planes reach high similarity in Case 4 the final condition shows differences and thus a clear condition of non-homogeneity.
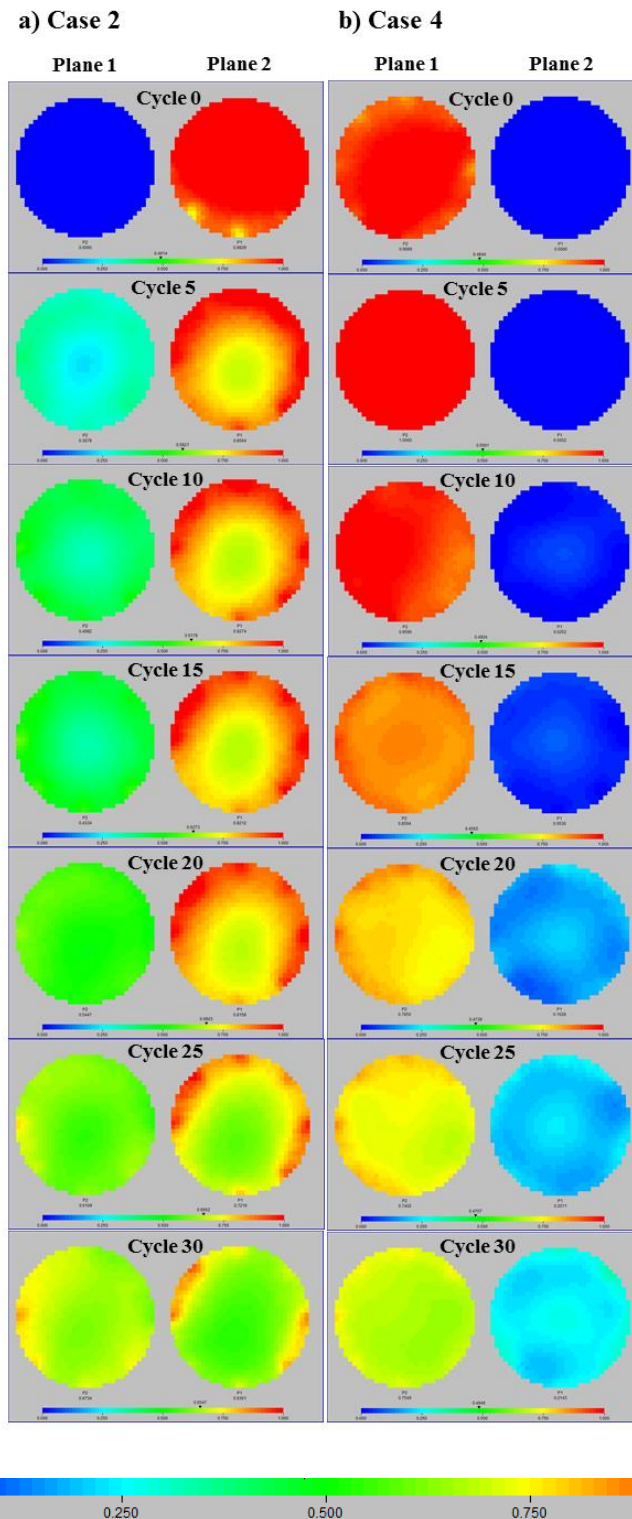
Figure 5.12 – ECT Permittivity plots after each test cycle: case 2 and case 5. The two cases show the (a) powder mixing – Case 2 and (b) powder not mixing – Case 5. The reported scale is in relative electrical permittivity, where 0 corresponds to the pure low permittivity phase (mannitol) and 1 to the pure high permittivity phase (zeolite).

5.5   Conclusions

Mixing of two powders of differing electrical permittivity (Mannitol Pearlitol 200 SD (Roquette, UK) and Zeolite (JM, USA) was experimentally measured using flow energy and torque measurements from a Freeman FT4 and imaged using Electrical Capacitance Tomography. Particle blending for continuously sheared flows was investigated and the capability of ECT to describe the distinct segregation and mixing dynamics of two particle species in a dynamically heterogenic process was demonstrated. The two powders were loaded in two separate layers, and then "mixed" using the FT4 Freeman rheometer. The final achieved conditions were different depending on the initial configuration: when the (denser) mannitol was placed at the bottom of the sensor and the zeolite on top, the system reached the homogeneity condition within the 30 cycles, while in the second case with the initial powder disposition inverted, at the end of the 30th cycle the well mixed condition was not achieved. This phenomenon was observed in the total energy measurement from the FT4 which showed little or no evolution, while it presented a rapid decrease in case 1 where the initial axial powder density and particle size profile favoured mixing. Two very different conditions were thus reached using the same materials in the two reciprocal cases; the reasons for this lying in the properties of the powders. The higher density and most of all the smaller particle size of the zeolite guaranteed the particle migration towards the bottom and the bigger particles to move towards the top for particle scale dynamics during segregation of a bi-disperse mixture under oscillatory shear, a well-known phenomenon of granular segregation also described as Brazil nut effect (Rosato et al., 1987; van der Vaart et al., 2015). In the opposite case the powder migration was less accentuated for the same reason although the blade movement induces a small but not negligible increase in mixing.

The different physical behaviour of the two initial conditions was well represented by ECT measurement; both the tomograms and averaged relative permittivity were able to clearly visualize this behaviour and keep track in real time of the mixing evolution validating the assumption of relating powder flow changes as function of mixing and segregation. Given the non-intrusive nature and high temporal resolution of the ECT technique, it can be concluded that further studies in applying this technique for mixing of powders with different permittivity would be beneficial to identify segregation phenomenon and investigate powder mixing in different conditions.

5.6 <u>Nomenclature</u>

F	Axial force, N
h	Penetration depth, m
T	Torque, Nm
R	Blade radius, m
v	Tip speed, ms^{-1}
v_n	Axial velocity, ms^{-1}
v_t	Rotational velocity, $m\ s^{-1}$
α	Helix angle, rad
ε_r	Relative permittivity
ε	Electrical permittivity, $F\ m^{-1}$

6.
Use of 3D Electrical Capacitance Tomography for interface detection

3D-ECT has been applied for detecting interphases in cases of solid-liquid and liquid-gas conditions. The reconstructed tomograms have been binary gated to image the volume occupied by the different phases.

In the solid-liquid case, plastic phantoms were immersed in glycerol and imaged using ECT. Two methods were applied to quantify the imaging error, with the volumetric approach resulting more robust and practical in comparison to the voxel-by-voxel method.

In the case of gas-liquid, ECT was used to image the horizontal interphase between a liquid (glycerol or IPA) and air. Traditionally a thresholding method is used to identify the boundaries between phases. In this work, an alternative approach, the gradient method, is investigated. Such method looks at the point of inflection of the axial voxel profile as the point of boundary between air and liquid. Differently from the thresholding, this method does not require a priori information. Tests were conducted varying the level of liquid (glycerol, IPA) within the chamber evaluating the achieved accuracy.

6.1   Introduction

Processes involving multiphase flow are ubiquitous within the chemical, pharmaceutical, food and agricultural industries (Mosorov, 2015). The ability to detect real-time changes and phase interactions quickly and accurately has been one of the main targets for the development of innovative measurement techniques (Ismail et al., 2005; Yao and Takei, 2017). The potential of electrical tomography has been recognised and it has been developed as a research tool with the goal of delivering *in-situ* and real time measurements (Xie et al., 1995). In particular, Electrical Capacitance Tomography (ECT) has the resolution to deal with high-speeds within multiphase flows whilst its non-invasive nature represents a desirable feature for applications on process plants (Wang et al., 2010b). ECT detects the difference in permittivity of the material within a sensor or a pipe to reconstruct, through specific algorithms, the phase distribution and it gives as output an image representative of the system. The first research in investigating the use of capacitance measurements to reconstruct tomographic images for process applications dates back to the 1980's at the University of Manchester (C. G. Xie et al., 1992). Since then, the system has evolved, keeping the original measurement principle composed of a sensor with electrode plates, a data acquisition system (DAS) and an algorithm that translates the voltage measurements into pixel values to form the tomogram. The sensor is comprised of a sequence of metal electrodes (copper or copper alloys) arranged in a ring shape in one or more planes. An additional ring of guard electrodes on both side of the sensing region prevents any external loss or interference (Wang et al., 2010a). The electrodes are integrated into the wall of a circular cross-section, usually shielded with a plastic thin film as isolation from the process. The capacitance measurements are in the order of magnitude of pico-farads, therefore each electrode is individually connected to the DAS unit using co-axial cables. This design prevents the charge saturation that could occur in case of a grouped cables connection to the unit. Traditionally the

electrodes have a rectangular curved shape, however, works in the literature report different conical and planar designs made to fit specific geometries or to target different resolution requirements (Peng et al., 2005; Tholin-Chittenden and Soleimani, 2017; Wang et al., 2010b). In Figure 6.1 a schematic representation of an ECT system is shown.
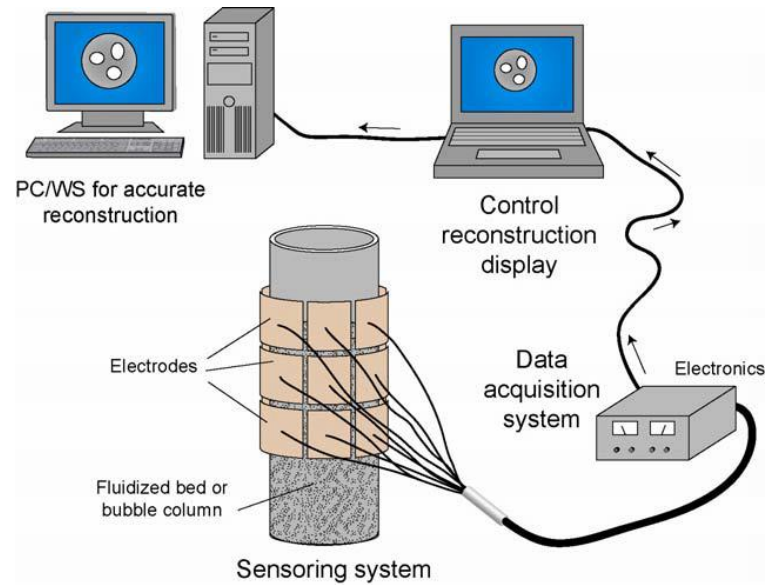

Figure 6.1 – Schematic representation of an ECT system (Wang et al., 2010a). The system is composed of a sensor with three planes, a Data acquisition system connected to a control display and a PC for applying the reconstructing algorithm

The ECT technique works by applying sequentially a known voltage to each electrode and measuring the resulting charge at each remaining electrode to then compute the inter-electrode capacitance; a sketch of a horizontal section of an ECT system is reported in Figure 6.2.
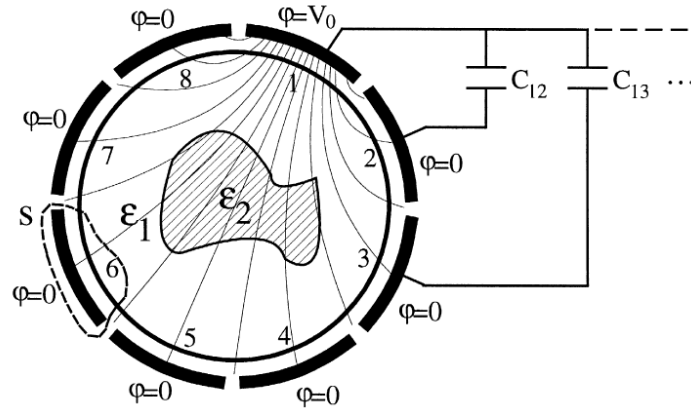
Figure 6.2 – Schematic representation of the ECT measurement principle with a sensor composed of 8 electrodes (Dyakowski et al., 2000). Electrode 1 is energized with a voltage V and the other sensing electrodes are used as receivers. The induced capacitance on each of them constitutes the ECT measurement.

ECT has been used in several applications, including circulating fluidised beds (Jaworski and Dyakowski, 2001b), fluidised bubbling beds (Warsito and Fan, 2005a), trickle beds (A. Wang et al., 2014) pneumatic conveying (Azzopardi et al., 2008; Rao et al., 2001) and drying (Chaplin et al., 2005; Rimpilainen et al., 2012) While its advantages include the aforementioned fast time response and its non-invasive nature, the main limitation of this technology is the low spatial resolution, particularly when compared to hard-field techniques. In tomography, a penetrating wave is used to image a section of an object; if the interaction between the used wave and the system does not alter the energy field, the technique is called hard-field whereas if the energy field is affected by the material present in the sensor, the algorithms of reconstruction become significantly more complex (Wang, 2015). Electrical tomography lies in the latter category, called soft-field tomography. The electric field distribution within the sensor varies according to a non-linear relationship between the material distribution and the capacitance measured on the sensing electrodes at the boundary of the sensor (Wahab et al., 2015).

Although in the literature many works have been carried out describing the application of ECT in 2D (York, 2001), the full potential of the technique has not yet been achieved. Recent works (Clark et al., 2016a; Liao et al., 2015; Aining Wang et al., 2014) have been applying ECT to reconstruct three-dimensional spatial information. Initial approaches have been concerned with the linear interpolation of 2D tomograms collected on single planes with no inter-plane information. For this reason, it has been identified as pseudo-3D tomography. Full 3D-ECT data has been recently become commercially available and applied at a laboratory scale using phantoms and to monitor the process of drying granules used in the pharmaceutical industry (Rimpilainen et al., 2012).

The algorithm employed to reconstruct the pixel values from the voltage measurement has a fundamental role in determining the accuracy of the method. So far, for 3D-ECT, given the complexity of the spatial distribution, the Linear Back Projection (LBP) algorithm or its variants (*e.g.* Tikhonov regularisation) have been employed. Possible alternatives are Neural-Network Multi-Criterion Optimisation (NN-MOIRT) algorithm along with some iterative back projection techniques (Warsito and Fan, 2003). To evaluate the limitations of the technique and identify improvements, 3D-ECT has been compared with other imaging techniques (Chandrasekera et al., 2012; Warsito and Fan, 2005b) to investigate the accuracy of the reconstruction given by different algorithms. Enhancing the reconstruction algorithm is critical for increasing the potential of the technique; especially the improvement of single step methods that enable responses to be determined on the timescale of the process. Such methods could be used in active process control.

The objective of this work is to determine the accuracy of 3D ECT in imaging plastic (PolyMethyl Methacrylate PMMA) phantoms immersed in glycerol; and in precisely detecting the interface between liquid (glycerol and Isopropyl alcohol IPA) and air. The

choice of glycerol and PMMA phantoms is made on the basis of previous work carried out by Clark (et al., 2016b.) in 2D, while the choice of IPA is made based on the electrical permittivity of this material, similar to a wet catalytic converter. The main aim is to develop a data processing methodology for phase boundaries recognition and to investigate an alternative gating method to the classic thresholding approach to identify the interface between the phases composing the system. This would overcome the current need of *a priori* information needed, as the threshold value (between 0-1).

The final goal is to extend the approach to the industrially relevant application of substrate coating, described in Chapter 7. The technique has been evaluated at laboratory and pilot scale before conducting an extensive "on plant" campaign to test suitability, accuracy and robustness of the technology together with the method. A methodology that allows the acquired tomograms to be processed and interrogated to obtain critical information about the process has been developed. The intention is to provide a robust technique that, due to the fast-response and safe nature of the technology, can allow in situ and real time application on plant.

6.2   Theory

The measurement principle of ECT involves sequential excitation of the electrodes in the sensor ring, using each individual electrode in turn as a voltage source and the remaining electrodes as receivers, until a complete array of independent measurements for each electrode pair is generated. For a 24-electrode sensor, this results in 276 independent measurements according to equation (6.1).

$$N = \frac{M(M-1)}{2} \qquad\qquad \textbf{(6.1)}$$

Where N is the number of measurements and M the number of the electrodes belonging to the sensor. Image resolution, often identified as the main downside of ECT (Tapp et al., 2003), is a function of both the measurement resolution, i.e. the number of measurements acquired across the sensing region, and the geometrical settings of the used reconstruction algorithm.

The choice of electrode number and dimension and the overall diameter of the ring have an effect on the measurement resolution and accuracy. Ye et al. (2014) compared different ring sizes (10 20 and 30 mm) suggesting that the increase in sensor diameter reduces resolution and signal to noise ratio. Li and Holland (2015) used FEM modelling to optimise the aspect ratio (length/width) of electrodes for 3D applications and found that sensitivity to noise is optimised for values lower than 1. Many alternative sensor geometries were investigated by Wang et al. (Wang et al., 2010b), including pipe angle bends, t-shape vessels and half cylinders, demonstrating the flexibility and applicability of the technique for a number of various operations.

The aforementioned low spatial resolution, common across all electrical tomography modalities is counter-balanced by a fast temporal resolution. Available commercial ECT kits are capable to acquire data at a frequency of 200 Hz (Dyakowski et al., 1997; Jeanmeure et al., 2002) in contrast with X-ray tomography which is capable of acquiring approximately one frame every two seconds (Warsito and Fan, 2005a).

Focusing on the physical basis of the technique, the equation that describes the relationship between the permittivity, potential and charge distributions across the sensor is Poisson equation:

$$\nabla \varepsilon(x, y, z) \nabla \varphi(x, y, z) = -\rho(x, y, z) \qquad \textbf{(6.2)}$$

where $\varepsilon(x, y, z)$ is the permittivity distribution, $\nabla\varphi(x, y, z)$ is the potential distribution of the electric field and $\rho(x, y, z)$ is the charge density. For each individual measurement a capacitance C is obtained, which is a function of the permittivity distribution, the potential distribution and the imposed voltage (ΔV) as given in (6.3).

$$C = -\frac{1}{\Delta V} \int \int_{\Gamma} \varepsilon(x, y, z)\, \nabla\varphi\left(x, y, \varepsilon(x, y, z)\right) d\Gamma \qquad \textbf{(6.3)}$$

This equation describes the capacitance over the area Γ of one electrode and is also known as the forward problem (Yang and Peng, 2003). Thus, equation (6.3) states that the capacitance between the different electrode combinations can be considered as a function of permittivity distribution:

$$C = f(\varepsilon) \qquad \textbf{(6.4)}$$

As a consequence, it is possible to state that perturbations in the permittivity distribution will have effect on the capacitance which can be expressed as:

$$\Delta C = \frac{df}{d\varepsilon}\Delta\varepsilon + O((\Delta\varepsilon)^2) \qquad \textbf{(6.5)}$$

Where $\frac{df}{d\varepsilon}$ is also known as the sensitivity of the capacitance versus the permittivity and the second addendum represents variation of higher order terms. This term can be neglected as in ECT applications $\Delta\varepsilon$ is usually small (Ye et al., 2014), therefore the expression is:

$$\Delta C = s\Delta\varepsilon \qquad \textbf{(6.6)}$$

Where $s = \frac{df}{d\varepsilon}$ is the sensitivity of the capacitance to changes in permittivity. This equation, also known as the forward problem, can be generally handled with three approaches (Warsito et al., 2007):

151

- linearization techniques (Huang et al., 1989; Marashdeh and Teixeira, 2004; C. Xie et al., 1992)

- computational finite-element method (Bayford et al., 2001);

- analytical methods (Anderson et al., 1995).

The first option is generally the preferred one as analytical methods are only applicable for very simple geometries and the computational methods require impractically long computational times (Warsito et al., 2007). Linearization methods provide relatively fast and simple solutions, but they are affected by smoothing, that can be improved through iteration in the reconstruction process. These methods are also called sensitivity methods and to generate an image they discretise the domain into voxels (three-dimensional pixels). In this domain, the equation (6.6) is written as:

$$C = SG \tag{6.7}$$

Where C is a N-dimensional vector, G is the image-describing vector composed of N_V elements (or voxels) and S is the sensitivity Jacobian matrix of dimension $N \times N_V$. The sensitivity matrix can be obtained between electrodes i and j based on the potential distribution, expressed as:

$$S_{i,j}(x,y,z) = -\int_{p(x,y,z)} \frac{E_i(x,y,z)}{V_i} \cdot \frac{E_j}{V_j} dx \, dy \, dz \tag{6.8}$$

Where $E_i(x,y,z)$ is the potential distribution when an excitation voltage V_i is applied to electrode i while the other electrodes j are grounded, and $p(x,y,z)$ is the volume of the pixel at (x,y,z) (Li and Yang, 2008).

The ECT system normally undergoes a calibration step, because as described in eq. (6.6) it is the change in permittivity which is important, not the absolute value. The calibration is executed by acquiring two measurements of capacitance at the highest and the lowest permittivity condition, respectively called C_{low} and C_{high}. All measured capacitances $C_{i,j}$ are then normalised with respect to the corresponding calibrated values $C_{i,j_{low}}$ and $C_{i,j_{high}}$:

$$C_{i,j}^n = \frac{C_{i,j} - C_{i,j_{low}}}{C_{i,j_{high}} - C_{i,j_{low}}}$$
(6.9)

The discretised forward problem then becomes:

$$\lambda = SG$$
(6.10)

Where λ is the N-dimensional normalised capacitance array. However, ECT algorithms need to solve the so-called inverse problem:

$$G = S^{-1}\lambda ,$$
(6.11)

in order to obtain the voxel values across the whole tomogram in relationship to the sensitivity matrix S and the measured capacitance values. If S was invertible this problem would be easily solved, however in this case the inverse of S does not exist, making of the inverse problem an ill-posed mathematical problem (Warsito et al., 2007).

Among a number of algorithms used to numerically solve this problem, the Linear Back Projection (LBP) is the most common. It imposes:

$$S^{-1} = S^T.$$
(6.12)

Physically, the array S^T can be considered as a mapping relating the capacitance vector space to the permittivity vector. Therefore, it is possible to calculate $\hat{G}$ the approximate solution of equation (6.11) as:

$$\hat{G} = \frac{S^T \lambda}{S^T u}, \qquad\qquad (6.13)$$

where u is the identity vector.

The accuracy obtained using LBP is often low, but it is still widely used for online applications for the fast response and simplicity (Yang and Peng, 2003). LBP has been utilised in many applications in industry, such as fluidised bed drying (Rimpilainen et al., 2012), pneumatic conveying (Azzopardi et al., 2008) and bubble columns (Al-Masry et al., 2010). LBP works have been also extensively applied for phantoms and multiphase boundary recognition (Clark et al., 2016b; Warsito and Fan, 2005a). A variant of LBP includes the Tikhonov regularisation (Tikhonov and Arsenin, 1977). The Tikhonov method is a general regularisation mathematical tool that has been extended to ECT for solving image reconstruction (Lionheart, 2001; Peng et al., 2000). Based on its regularisation procedure the solution to equation (6.11) is expressed as:

$$\hat{G} = (S^T S + \mu I)^{-1} S^T \lambda, \qquad\qquad (6.14)$$

where I is the identity matrix, and μ is the regularisation parameter defined positive (Yang and Peng, 2003). This parameter influences the accuracy of the model: a small value gives good approximation to the initial problem, but it is more prone to errors, while, at the opposite, a larger value increases the committed approximation error avoiding the recurrence of data error. At present, although studies have investigated the parameter choice for ERT application, the value of μ in reconstructing ECT tomograms is chosen arbitrarily.

Other reconstruction algorithms reported in the literature includes single step methods as Newton One Step Error Reconstruction (NOSER) and other iterative reconstruction methods such as Landweber (Stephenson et al., 2008; Yorkey et al., 1987), iterative Tikhonov (Lee et al., 2006) and Newton-Raphson (Hansen, 1998). Iterative reconstruction strategies achieve higher accuracy for tomographic images, however, often the processing and computing time significantly increase reducing the possibilities of real-time application (Matusiak et al., 2010).

In this work, LBP and Tikhonov regularisation are the only reconstruction algorithms investigated, as the work aims to evaluate potential for inline implementation of the technique and cannot afford high reconstruction time. However, the current study does not exclude the possibility, as research in industrial process tomography advances, that different algorithms can substitute the current methods available in the commercial devices or that improved computational power could allow iterative algorithms to sensibly reduce reconstruction time.

6.3   Materials and Methods

The components of an electrical tomography device are:

- Sensor: a series of electrodes, arranged in different layouts according to the application;

- Data Acquisition System (DAS): the process unit that controls the electrical input and acquires the voltage measured at the electrodes;

- Computer: it represents the interface between the user and the DAS. It is also used to run reconstruction algorithms and to generate the tomograms.

The sensor used in this work has 24 electrodes disposed in 3 planes. It has an internal diameter of 147 mm and the height of the sensing region is 121 mm (the total sensor height is

267 mm). Each electrode had a length of 36 mm and width of 56 mm (*L/W*=0.64). The main dimensions of the sensor are reported in Figure 6.3.
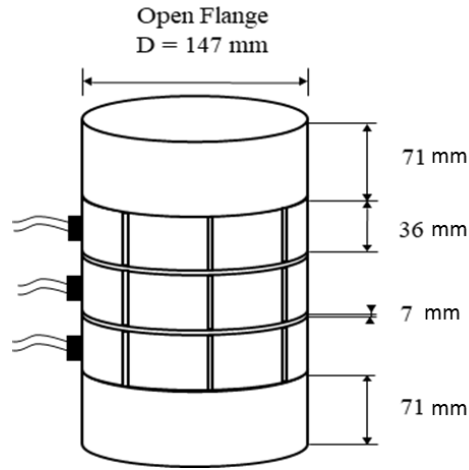
Figure 6.3 – Schematic of the used 3D ECT sensor. It is composed by three planes of 8 electrodes. Each electrode is individually connected to the DAS.

Above and below the top and bottom planes, there are guard electrodes (not reported in Figure 6.3) that isolate the sensing region from external disturbances. The electrodes are not in direct contact with the process, but they are implanted into a plastic (dielectric) wall. Each electrode is connected singularly to the DAS through co-axial cables. The DAS used in this work is a m3c (24 channels) manufactured by Industrial Tomography Systems (ITS Ltd., Manchester UK). The DAS applied a voltage of 18 V alternated current based sine wave with a frequency of 1 MHz. The resulting acquired voltage matrixes were fed to the ITS Reconstruction Toolsuite software to apply the reconstruction algorithms and obtain the 3D tomogram composed of 32×32×32 voxels. Such tomograms are described with a 3D matrix composed of 32,768 voxels (32^3) that is then post processed in MATLAB®. However, the produced cubic matrix is manipulated to remove the squares at the edge and take into consideration only the cylindrical shape representing the internal area of the sensor; the resulting number of

meaningful voxels is 25,984. An example of a tomogram with description of voxel dimensions is shown in Figure 6.4.
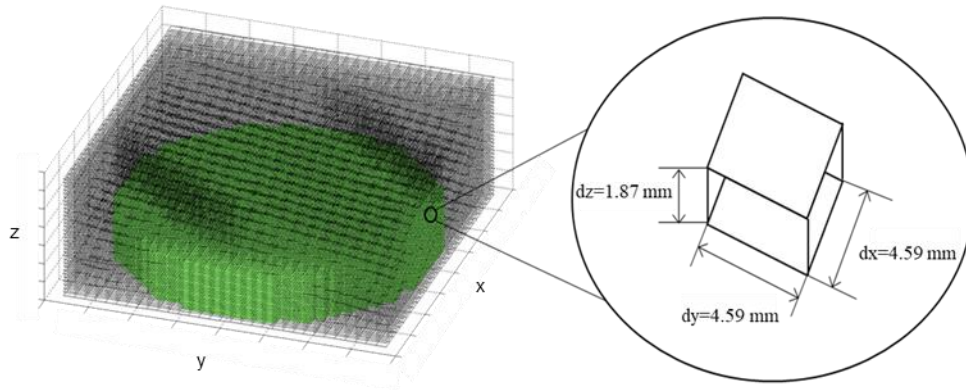
Figure 6.4 – 3D scheme of a tomogram with voxels size used in this work. On the left a three-dimensional grid shows how the volume is discretized; on the left the single voxel size.

All the single voxels composing the tomogram have a value comprised between 0 and 1 accordingly to the previously carried out calibration step. What is often required is the location of the interface in a multiphase system; therefore, the image is then binary gated to identify two separate phases. The general way this is done is to use a threshold value to assign the individual voxels to one phase or the other (in case of a bi-phasic system) (Qin et al., 2006). An alternative method, called the gradient method, used to identify a horizontal interface is described and proposed in paragraph 6.3.2.

6.3.1 Solid liquid interface

In this experiment, the methodology and data processing applied is an extension of Clark's work in 2D (Clark et al., 2016b): plastic phantoms of different shapes are immersed in glycerol and different methods are used to evaluate the accuracy of the generated 3D tomogram. The PMMA phantoms used were a cylinder with a diameter of 50 mm and a square prism with a width of 50 mm. Both phantoms had a height covering the whole of the sensing region. The measurement principle is based on the gradient in permittivity between

the liquid phase (glycerol has a relative permittivity equal to 40) and the solids (relative permittivity of 2.3). The acquisition is done at 2 frames per second where each frame is the result of 10 averaged complete measurement acquired voltages. This is a standard setting of the ITS Multi-Modality Tomography Configurator (MMTC) software applied with the objective of having a stable signal. The acquired frames were then converted into 3D tomograms using ITS Reconstruction Toolsuite software using the LBP algorithm.

Each phantom was placed at the centre of the sensor and held in position using a clamp. Figure 6.5 shows a planar view of the phantom placement in the ECT chamber.
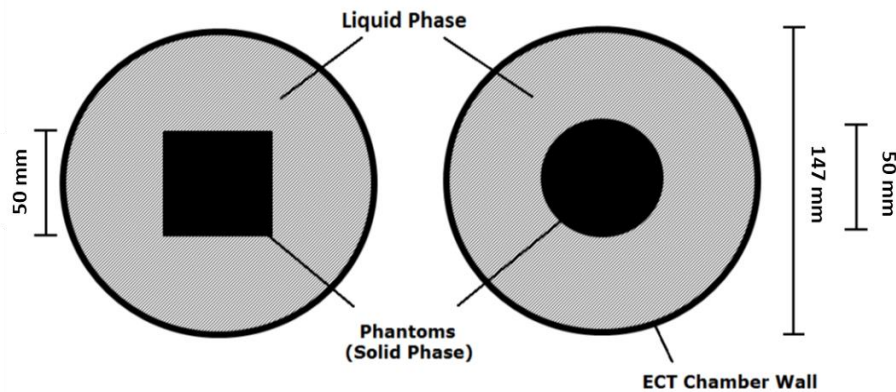
Figure 6.5 – Planar view of the phantom location within the ECT cage (adapted from (Clark et al., 2016b)). The two phantoms are placed in the centre of the sensor.

In order to allow computation of the error in the reconstructed image, for both cases, a digitised reference is built, representing the ideal results that could be obtained with the resolution of the technique. By doing this, a first error, called digitisation error is introduced (0.5% and 5% respectively for the cylinder and the prism, on a volumetric basis). However, the overall error computed subsequently will disregard the digitisation error, taking as a term of comparison the generated reference 3D images reported in Figure 6.6.

(a)

(b)
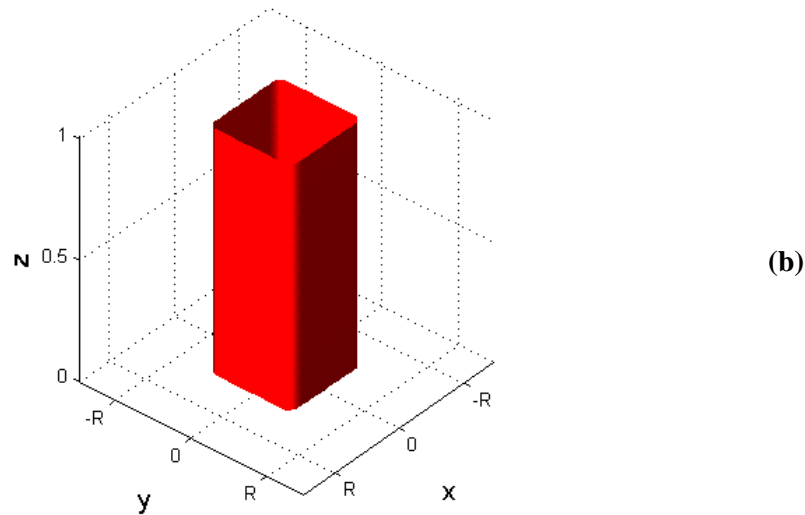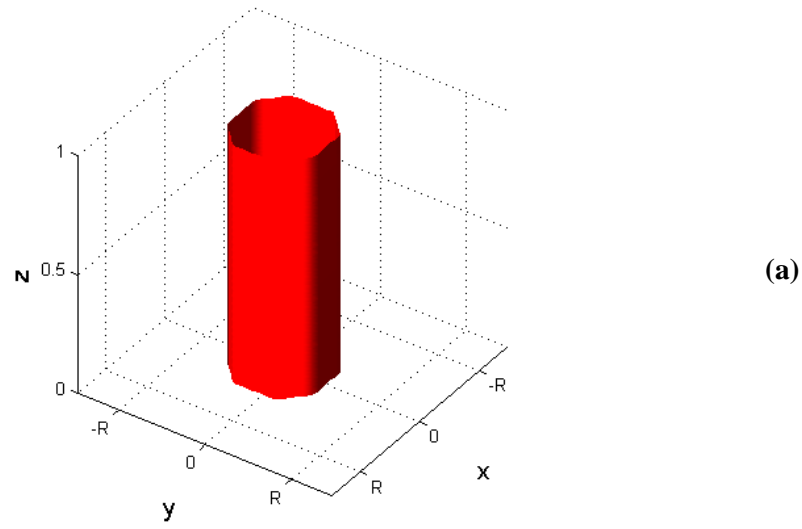
Figure 6.6 – Reference images for the cylinder (a) and the square prism (b). The reference images are built for constituting a mean of comparison for experimental data.

In Figure 6.6, the red surface identifies the interface between the phantoms and the liquid phase. These images constitute the terms of comparison for the thresholded binary gated tomograms. Different values of threshold were used, and two approaches of computing error were introduced to evaluate the optimum thresholding that minimises the error:

- Voxel-by-voxel error, e_{VbV}

- Volumetric error, e_V

The voxel-by-voxel approach (equivalent to pixel-by-pixel but in 3D) compares one by one the corresponding voxels in the theoretical and experimental images; it is described by equation (6.15) (Clark et al., 2016).

$$e_{VbV} = \frac{1}{N} \sum_{i=1}^{N_t} \left| (\vartheta_{image}^{(i)} - \vartheta_{real}^{(i)}) \right|, \tag{6.15}$$

where e_{VbV} is the image calculated using the voxel-by-voxel method, N_t is the total number of voxels with value lower than the threshold, $\vartheta_{image}^{(i)}$ is the reconstructed value of the i-th voxel and $\vartheta_{real}^{(i)}$ is the theoretical expected value of the same voxel. This approach is the traditional method used in similar applications (Kuzeljevic, 2010) but requires a level of information not always available in imaging experiments. Indeed, because the method compares the values of individual voxels, this implies that each of their theoretical values is known. This is a limitation for any industrial tomographic application, as methods with such level of *a priori* knowledge are not flexible and have low chances of being implemented. A different method, known as the areal method, was introduced by Alberini et al. (Alberini et al., 2014b) for studies on blending of non-Newtonian fluids in pipelines using Planar Laser Induced Fluorescence (PLIF) (detailed description in Chapter 4), and adapted by Clark (Clark et al., 2016b) for ECT. This approach compares the area occupied by the imaged object in the tomogram with the known area that is covered by the object. In this work, the areal approach is extended to the third dimension, hence being renamed as the volumetric approach. The extension consists of comparison of the difference in volume occupied by the imaged object in the tomogram with the built reference; it is described by the following equations (6.16-17)

$$V_{image} = V_C \frac{\sum \vartheta_{image}}{N} \Big|_{\vartheta_{image} < t} \qquad \text{(6.16)}$$

$$e_V = \frac{|V_{image} - V_{phantom}|}{V_{phantom}} \qquad \text{(6.17)}$$

Where e_V is the volumetric error, $\beta_{phantom}$ is the phantom reference volume, β_{image} is the object reconstructed volume in the tomogram computed in (6.16) as a portion of the volume of the chamber, β_C, occupied by the number of voxels ϑ_{image} with values lower than the threshold t in relation to the total number of voxels N describing the chamber.

Both e_{VbV} and e_V are dependant on the threshold value t and are used to identify what is the best threshold value to be used to represent appropriately the phantom.

6.3.2 Liquid gas horizontal interface

Interesting applications for ECT involve dynamic changes in moisture content in the axial direction. Such operations include substrate coating (described in Chapter 7), drying but also fluidised bed and trickle beds sharing the same cylindrical symmetry. In this trial, the ECT chamber was filled with liquid at different heights and the volumetric error approach is used to evaluate accuracy of the ECT reconstruction. The experiment was repeated with two different materials (the reported property is at ambient temperature of 20°C):

- Glycerol (ε_r=40) (Clark et al., 2016b);

- Iso-propanol IPA (ε_r=18.6) (Shell, 2016).

In both cases, the initial liquid level was set to $z = 0$ (at the bottom of the sensing region) and small volumes of liquid corresponding to increments in level of 5 mm were added. In both cases a glass beaker with diameter equal to 143 mm was used for liquid containment and to

avoid the contact with the walls. Furthermore, the additions were carefully done using a small rod in order to avoid splashing on the walls during the additions. The use of a beaker separating the liquid from the sensor wall was chosen for mimicking the applications described in Chapter 7. Although an air gap between sample and walls can reduce the penetration of the electric field within the object, this is a necessary condition for in-line implementation of the technology. It is essential to avoid contacts between sensor and the parts and the tolerance of robot placement needs to be taken into account. Furthermore, during the IPA experiment, the chamber was covered to reduce loss for evaporation as much as possible.

Assuming that the interphase between gas and liquid would be perpendicular to the axis of the sensor, it is possible to evaluate an alternative strategy to the thresholding approach for detection of the interface using ECT. Figure 6.7(a) shows the case of a horizontal interface in the case of glycerol-air. At the bottom of the tomogram, the red voxels (corresponding to values of 1) represent the liquid (high permittivity) while the blue voxels (corresponding to values of 0) are representative of the air phase (low permittivity). A gradient method has been utilised for binary gating the tomogram: each individual column of voxels in the tomogram was interrogated in the z direction as shown in Figure 6.7(a) in order to find the point of inflection of the voxel value. The process is repeated for each column of the 3D matrix describing the tomogram. Figure 6.7(b) shows the value for each of the 32 voxels in one column of the matrix in the z direction parallel to the axis of the sensor.

(a)

(b)
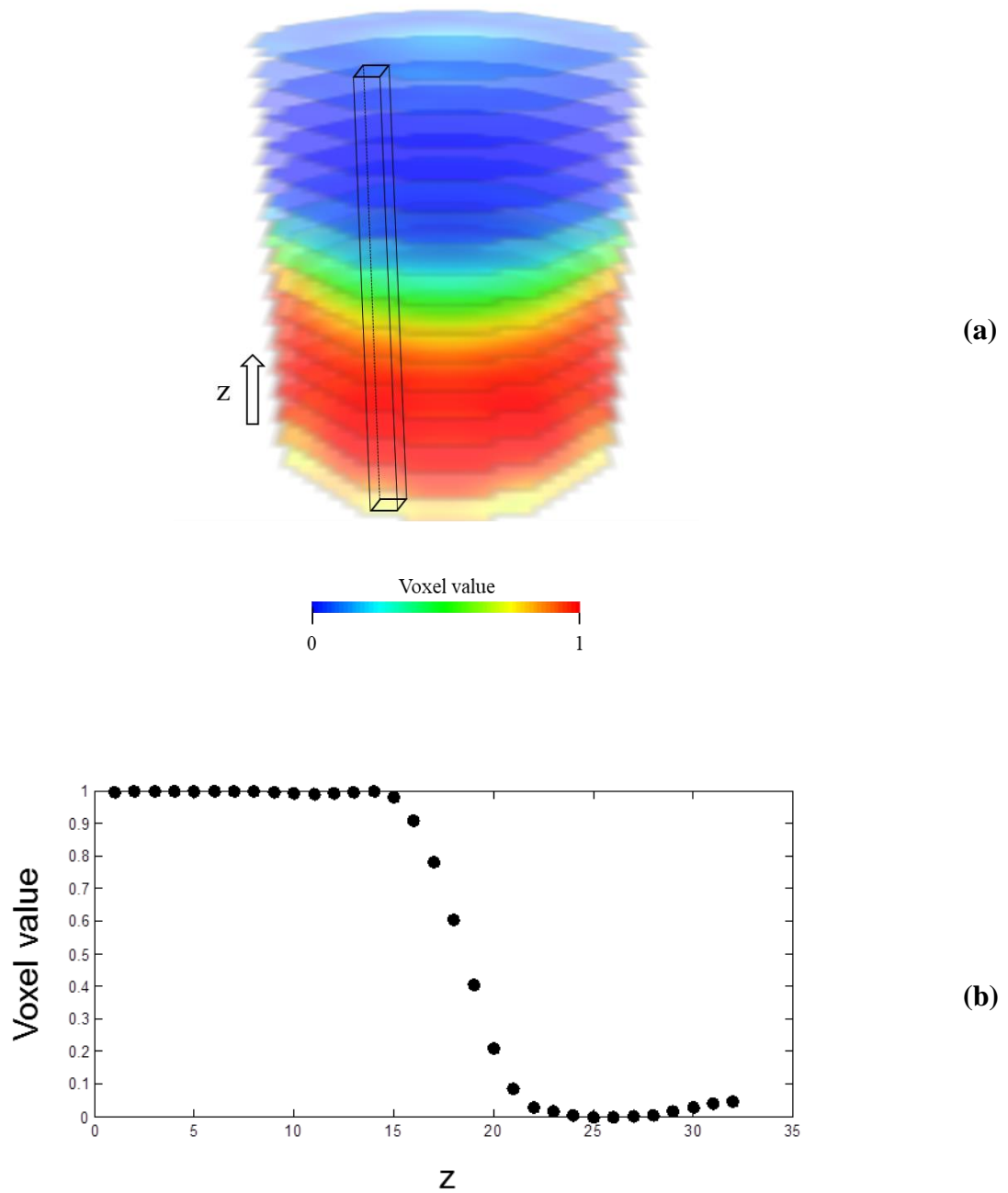
Figure 6.7 – Schematic of a 3D tomogram with the detail of one vertical (z direction) column of voxels (a): the liquid, having the higher relative permittivity, is identified by the red zone at the bottom; the color varies to blue when moving towards the top where the gas phase (low permittivity) is located; the voxel value profile along z direction for the highlighted column (b).

In the profile reported in Figure 6.7(b) the gating is done at z =18.5, therefore a value of 1, which identifies the high permittivity region, is assigned to the first 18 voxels and a value of 0 (low permittivity phase) is assigned to the remaining 14.

6.4   Results and discussion

6.4.1 Plastic phantom experiment

In this trial, the aim is to investigate a method to identify the correct thresholding value to image the plastic PMMA phantoms in glycerol.   Prior to taking the measurements, a calibration is carried out; the high reference frame was taken by filling the ECT chamber with the material having the highest permittivity, glycerol (ε_r = 40); air (ε_r = 1) was used as low reference. To choose the optimal threshold value t, both e_{VbV} and e_V were calculated by varying t. The obtained error plots are reported in Figure 6.8.
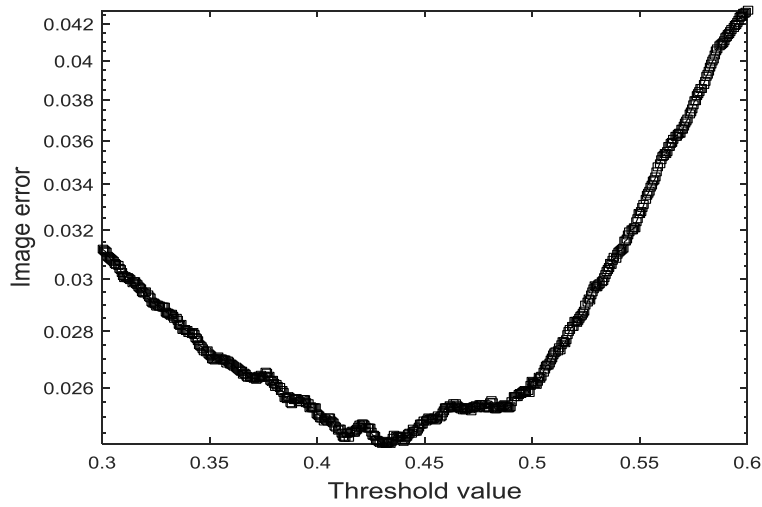
(a)
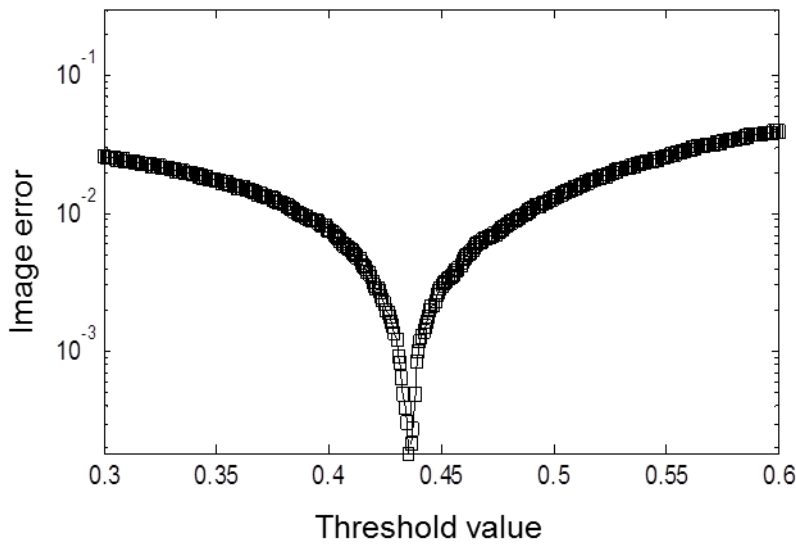
(b)

Figure 6.8 – Error plots using the voxel-by-voxel (a) and the volumetric (b) methods for the cylinder phantom. In (a) the identification of the minimum by applying the v-b-v method is less immediate than in (b) where the volumetric method is proposed.

The plots for the two approaches are in slightly different format: the second is plotted with a logarithmic scale to facilitate easier the identification of the minimum. The value of absolute error varies depending on the different definition of the two approaches, while the voxel-by-voxel (v-b-v) method achieves a minimum error of 2.5%, the volumetric method instead gives

significantly lower error value (0.02%). The significant result, beside the magnitude of the error, is the conclusion that both approaches give similar optimal threshold values *t* (identified by the minimum in the two plots) which are 0.437 for the v-b-v and 0.441 for the volumetric method. An immediate way of qualitatively visualising the results is by comparison of the binary gated tomograms obtained choosing the two optimal threshold values. In Figure 6.9(a) they are imaged together with the reference body.
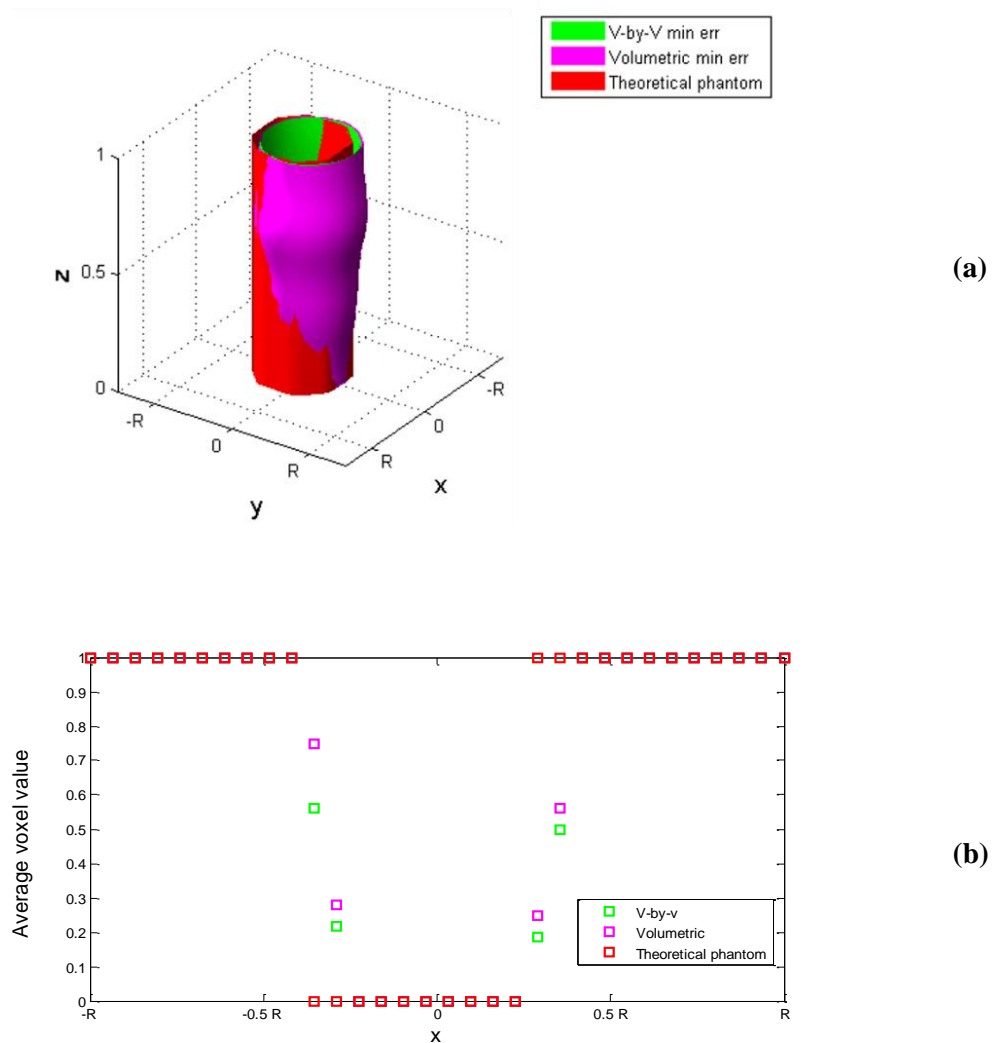
Figure 6.9 – Reconstructed iso-surface images and theoretical image for the cylinder phantom (a); axial averaged voxel value comparison between the three images across x direction for y=0 (b).

166

In Figure 6.9(a) three different coloured surfaces are imaged which represent the imaged interface between the plastic cylinder and the liquid. The reconstructed tomograms using the two different approaches to identify the threshold value, depicted green for the voxel-by-voxel approach and magenta for the volumetric approach, almost exactly overlap. The value indicated by the volumetric method is slightly higher than the one obtained with the voxel-by-voxel approach therefore the magenta surface covers the green one. In Figure 6.9(b), the voxels are averaged over z and then the obtained value is plotted, at $y = 0$, along x. For x close to R or $-R$, the obtained value (1) is the same for the three profiles and it identifies the glycerol phase. When x approaches $0.4\,R$, the voxel value for the reference varies steeply from 1 to 0, while the profiles for the voxel-by-voxel and volumetric obtained tomograms is smoother, with the latter having always the highest value. This is the reason why in the showed tomogram its surface covers the voxel-by-voxel image. Furthermore, comparing the two reconstructed tomograms with the red reference body (and the profiles), it is also clear that the phantom was slightly off-centred although all measures were taken to place it as centrally as possible. This is the cause for the higher value obtained for the error (e_{VbV}) when comparing the individual voxels, a small displacement can end up in a high number of voxels not corresponding to their expected value, instead the volumetric approach (which minimises e_V) relaxes this aspect giving less importance to the placement of the phantom and more to the actual volume occupied by it.

In similar fashion, the results obtained, using the square prism as phantom, are shown in Figure 6.10.
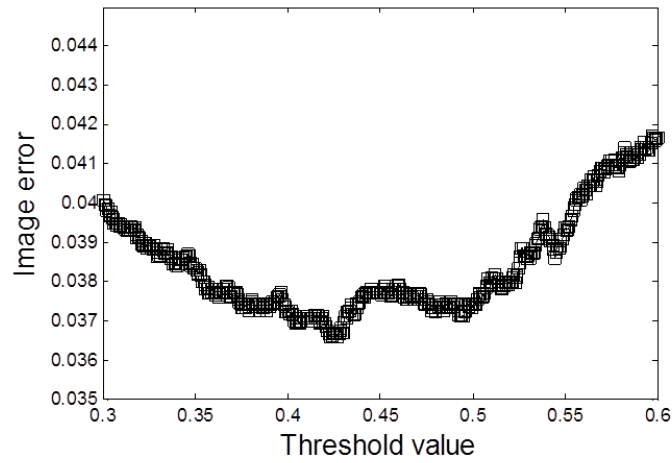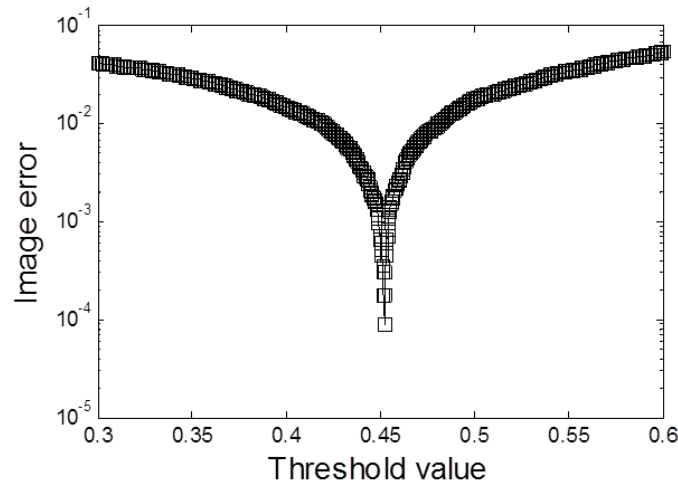
Figure 6.10 – Error plots using the voxel-by-voxel (b) and the volumetric (c) methods for the square prism.

As noted for the cylinder case above, the two techniques identify similar threshold values (0.427 for v-b-v and 0.451 for volumetric method). In the case of the square (angular) shape, it is challenging to reproduce the detail involved using an electric field (Martinez Olmos et al., 2011; Olmos et al., 2012). Nevertheless, the voxel-by-voxel error of 3.67% can be considered comparable with the one obtained with the cylindrical shape (2.5%), as well as the volumetric

error, in the order of 10^{-4}. In Figure 6.11 the comparison between the reconstructed tomograms and the reference square prism is reported.

(a)

(b)
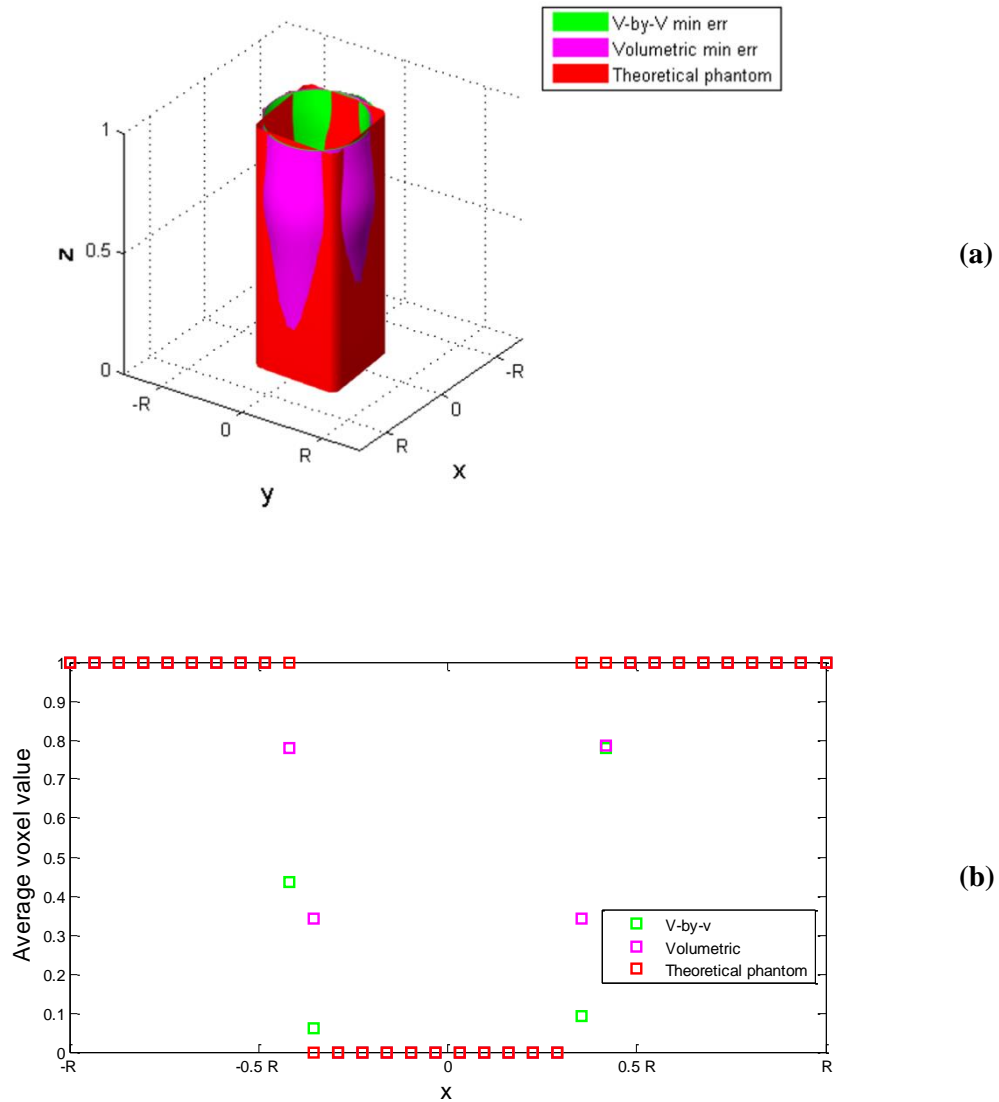
Figure 6.11 – Reconstructed iso-surface images and theoretical image for the square prism phantom (a); axial averaged voxel value comparison between the three images across x direction for y=0 (b).

In this case, the phantom reconstruction is concentric with the reference body, although, it is not possible to recognize the prism squared shape from the reconstructed tomograms. The edgy shape of the phantom cannot be resolved by the ECT reconstruction algorithm. The

169

profiles reported in Figure 6.11(b) show a higher concentricity and at the same time a higher distance for the voxel values of the two approaches at a given x, compared with Figure 6.9(b), due to a slighter higher difference between the two threshold values.

Furthermore, in all the iso-surface plots shown above, it can be noted how the diameter of the reconstructed object is higher at the top while decreasing towards the bottom. This can be related to the difference in sensitivity of the electrodes or to uneven sensitivity of the technique across the entirety of the sensor. This will be more thoroughly discussed in the next sections. A first example to visualise this flaw, characterizing the technique, can be seen in Figure 6.12, where one of the phantoms is located next to the sensor wall.
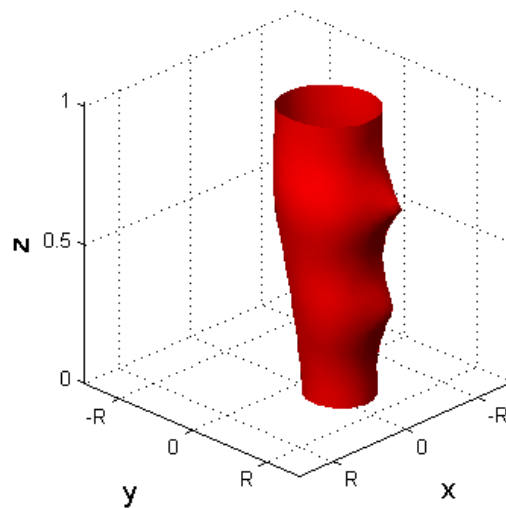
Figure 6.12 – Reconstructed iso-surface images for a cylinder phantom positioned next to the wall.

In this condition, reconstructed using the optimum threshold value found for the cylinder phantom above, it is possible to observe that the uneven diameter across the axis of the phantom is still visible, together with artefacts present at $z = 0.33$ and $z = 0.66$. Such locations correspond to the gaps between the electrode planes which is identified as one of the

positions within the chamber suffering of higher reconstruction error, as identified also by other researchers (Li and Holland, 2015).

Conclusions

From the above study, it can be argued that the volumetric method could be used as an accurate method to evaluate error and, therefore, to choose the optimal threshold value. The v-b-v method requires knowledge of both the shape of the phantom and its location in the sensor with high precision. This is not a significant concern in laboratory controlled experiments, but it could be more problematic to overcome in industrial applications. The volumetric approach requires knowing only the number of voxels occupied by the phantom and not their position. Therefore, this approach is the one utilised to evaluate the error committed in locating the horizontal interface between liquid and gas in the next section.

The ECT technique was able to image phantoms in glycerol with error of the order of 2-4%; although this value could be considered high if compared to hard-field techniques it is in line with literature observations (Clark, 2016; Li and Holland, 2015). The main limitations observed are related to the variability of the accuracy across the volume of the chamber. It has been observed that, axially, there is an uneven evaluation of the reconstructed phantom, due most probably to difference sensitivity of the electrode planes; this was already observed by Clark in 2D (Clark, 2016). An additional weakness is observed in the interplane zones, which are obvious when observing Figure 6.12; this area constitutes a particular point where performance of ECT inflects. In the radial direction, a good symmetry is observed when the phantoms were placed in the middle of the cage. However, when placing the phantom off-centre and close to the wall, the obtained tomogram is highly non-symmetric, revealing a limitation of the technique to accurately imaging objects in the proximity of the wall; it is therefore desirable to have the object not in contact with the wall.

6.4.2 Liquid-gas horizontal interface

This experiment aims to investigate the accuracy of ECT in imaging a horizontal interface between a liquid and air and to assess the capabilities of a threshold-free approach. This approach, the gradient method, is then tested for imaging the intermediate steps of coating detection in the automotive catalyst production in Chapter 7.

The sensor was filled with glycerol at different heights and the error in imaging the liquid volume using ECT was evaluated. Initially, the repeatability of the axial profile was tested to assess whether the application of the gradient method would give a reliable answer when applied to different frames. In Figure 6.13, an average voxel value profile for each of the 32 planes in the tomograms is plotted, varying the number of used frames for a chamber filled with glycerol at a relative height of $z = 0.28$.
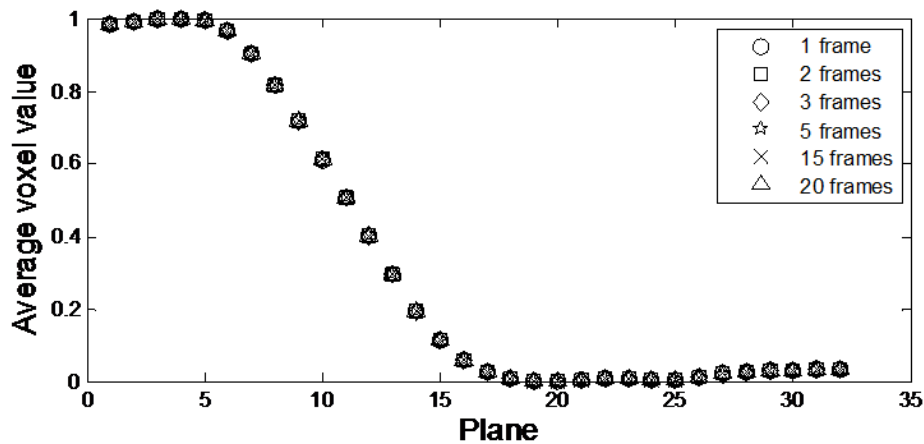
Figure 6.13 – Average voxel value across z direction with variable number of processed frames. The voxel value is reported for the 32 planes in the tomograms, varying the number of used frames for a level of glycerol equal to $z = 0.28$.

The obtained profile (with error bars of the order of dimension of the used symbols) does not change by varying the number of processed frames, therefore a single frame under controlled conditions can be considered representative of the object.

The thresholding and the gradient (or differential) method were initially compared using glycerol at different fill heights. The obtained performance in terms of volumetric error are comparable. As an example, the v-b-v error is reported in Figure 6.14 where the two filling levels (50% and 82%) are shown. Whilst the first method can produce a plot that describes the error trend depending on the chosen threshold value, the second method gives in output a single number, obtained by averaging the dosing length calculated for each voxel column.
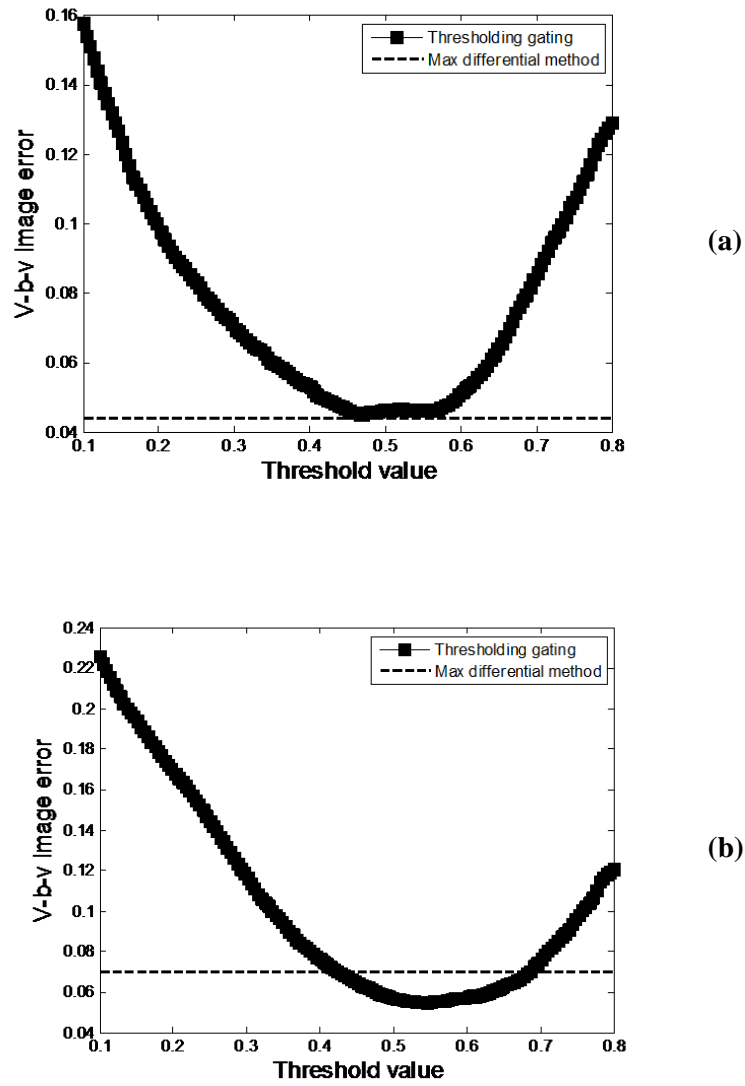
Figure 6.14 – Error plots comparison for 50% (a) and 86% (b) filling level. The error for the thresholding gating and the max differential measurement method is calculated eq. (6.15).

The results show that the errors induced by the two approaches are comparable. In the first case shown in Figure 6.14(a) (50%) the error committed by using the differential method is lower than the one obtained by using the thresholding, while, in the second case (Figure 6.14(b)) the latter is more accurate for a wide range of threshold values. However, the gradient method has the huge advantage that it does not need any *a priori* information (such

as the optimised gating threshold value) and its algorithm is not dependant on the involved materials.

As discussed in previous sections, the reconstruction algorithms play a significant role in determining the accuracy of the technique. In Figure 6.15, the results obtained by utilising LBP and Tikhonov methods (by varying the regularisation parameter ($\mu_1 = 10^{-10}$, $\mu_2 = 10^{-11}$, $\mu_3 = 10^{-12}$) for reconstructing the 3D matrix are compared for the case of glycerol.
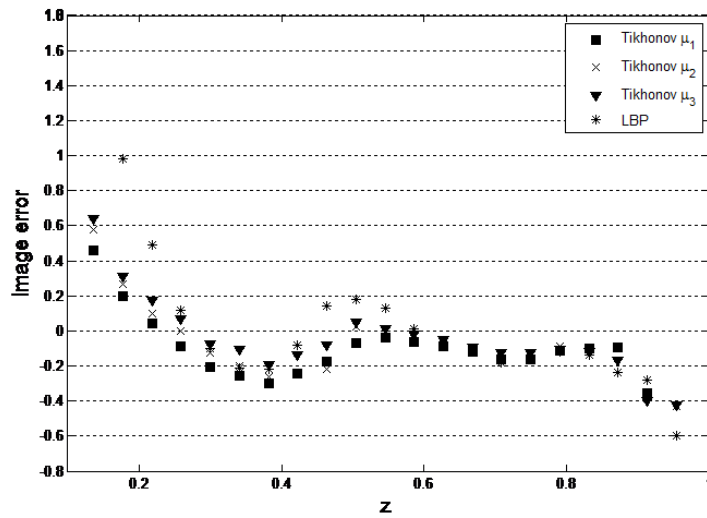
Figure 6.15 – Error plot at different relative height (z) in the sensor varying the reconstruction algorithm ion the case of glycerol.

The computed error in Figure 6.15 is the volumetric error, showing an overall relative error to compare with the average height calculated using the different reconstruction algorithms. None of the four algorithms are able to achieve good performance when the interface is located below $z = 0.18$ and above $z = 0.92$. For the Tikhonov reconstruction, the best profile is achieved with μ_3, which constrains the error to +-20% in the region comprised between $z=0.2$ and $z=0.9$. This is still quite similar to the error for the LBP method, therefore an ultimate decision cannot be made on the basis of this plot to identify which algorithm

175

possesses the highest accuracy. It has to be mentioned that, in the reconstructed images, the LBP method tends to produce more curved surfaces, overestimated at the boundaries and underestimated in the middle; this can be observed in the reported tomograms in Figure 6.16.
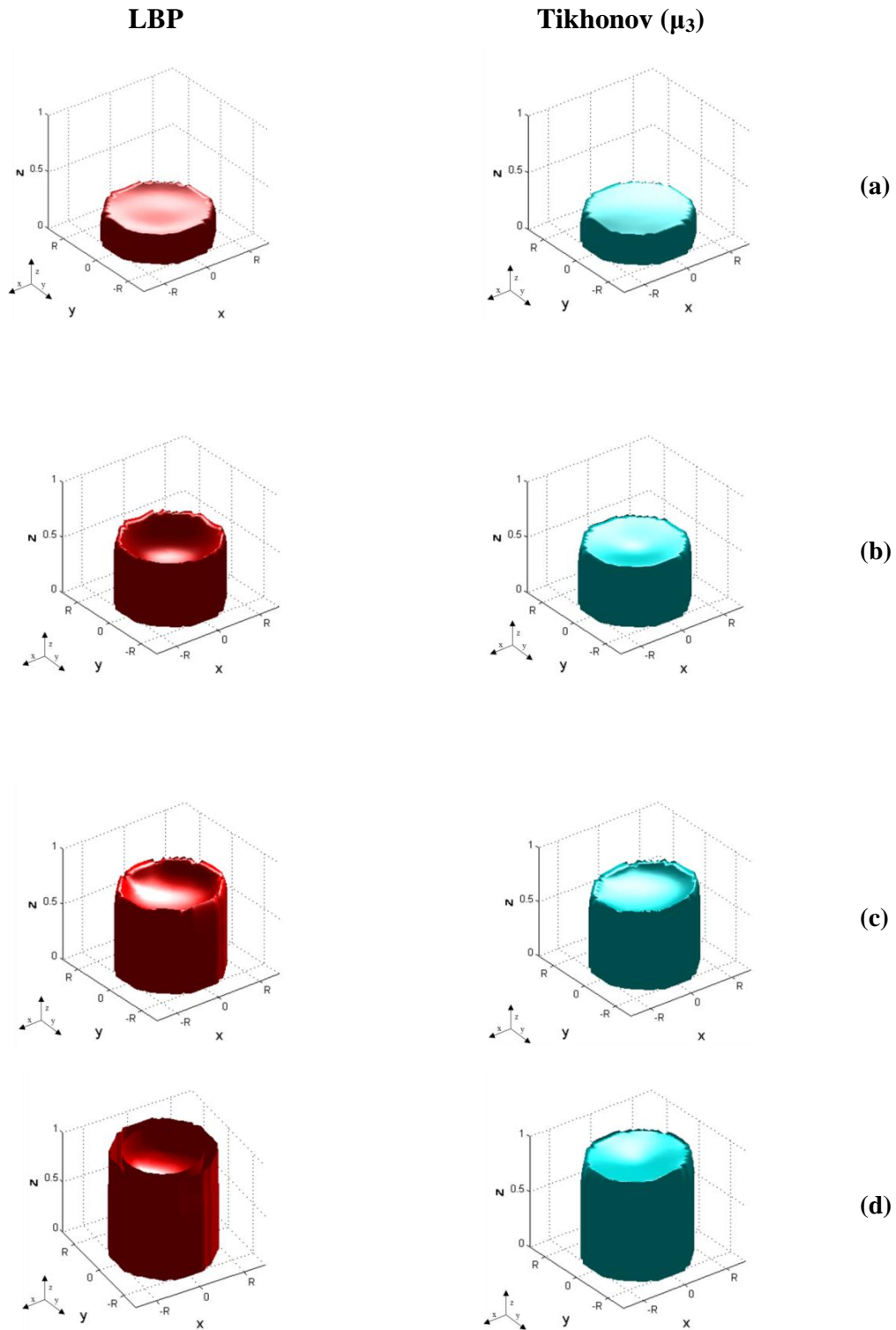
Figure 6.16 – Example of tomograms in the case of glycerol-air reconstructed with LBP (in red) and μ3 Tikhonov regularisation with μ = μ3 (in cyan) for different relative filling levels: 0.2 (a), 0.5 (b), 0.7 (c) and 0.9 (e). Images in picture are taken as example from Figure 6.15. They are shown as an exemplification of the obtained surface profile. Tikhonov regularization method shows flatter profile compared to LBP.

Although the difference between the two reconstruction methods is not significant in terms of dosing length, the Tikhonov method visually shows flatter interface compared to the LBP reconstruction method. A variable that is indicative of this behaviour is the standard deviation, reported in Figure 6.17. The standard deviation is calculated amongst the different heights computed for each column of the matrix. This method allows the variability of obtained heights across the columns to be visualised.
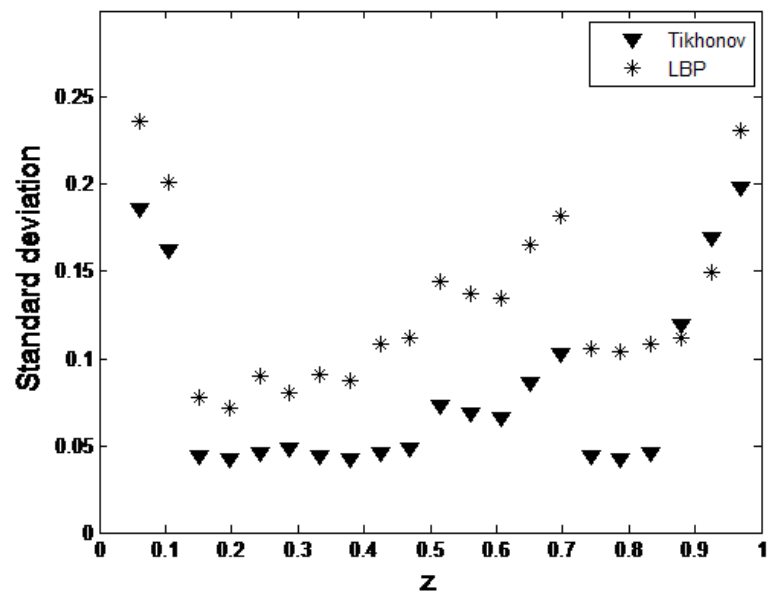
Figure 6.17 – Standard deviation at different relative filling levels of glycerol in the sensor for the Tikhonov and LBP reconstruction methods. The standard deviation is used as a mean to analyse differences in flatness obtained by using the two methods. Tikhonov reconstructed images presents in most cases the lowest value, suggesting this method is able to picture better flat profiles.

As shown in Figure 6.17, the LBP presents a higher standard deviation 90% of the time, sometimes more than double with respect to the Tikhonov reconstruction, therefore the latter has been chosen to resolve the inverse problem and generate the matrices to facilitate the analysis carried out in the next sections.

As stated above, a critical aspect for the use of ECT in the envisaged applications is the accuracy of the measured interface axial location. This has, therefore, been explored systematically using the glycerol-generated phantom horizontal interface. In Figure 6.18, the sensitivity of the technique is investigated varying the position of the liquid-gas interface both for glycerol and IPA, comparing two binary gating methods.

(a)

(b)
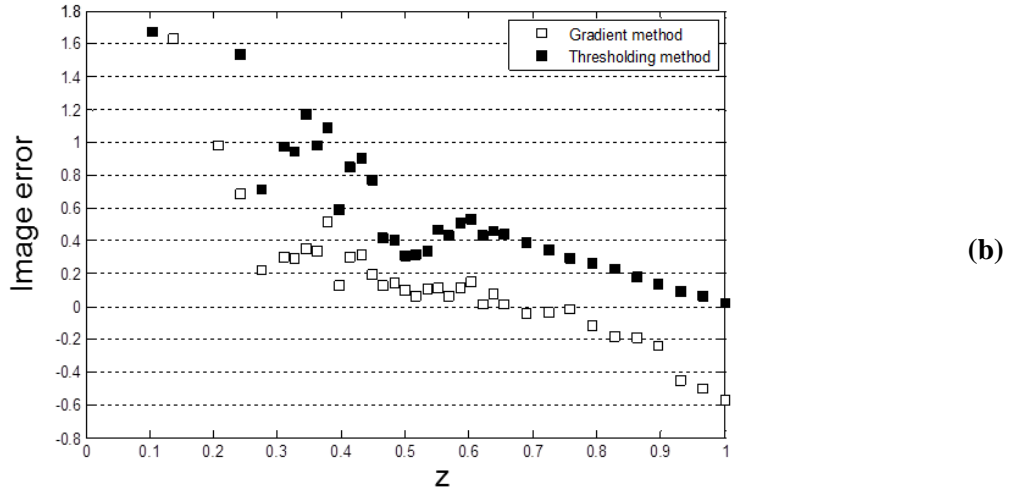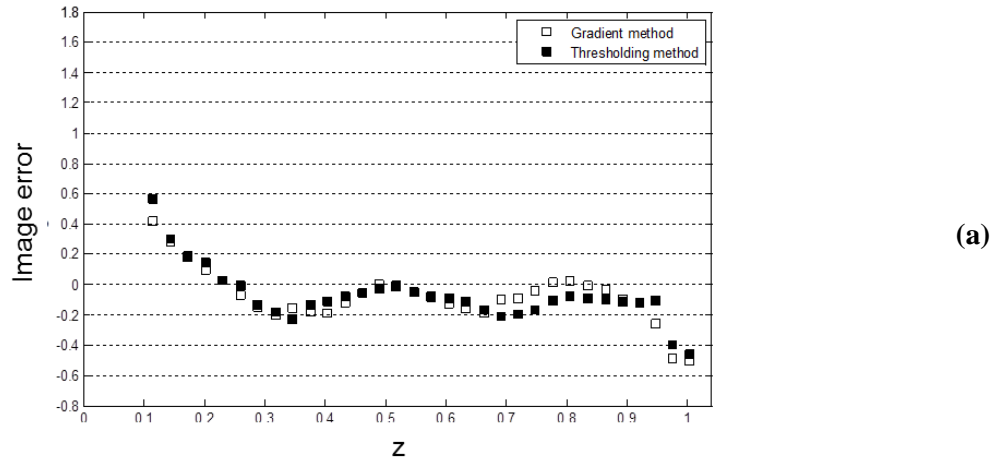
Figure 6.18 – Image error expressed as volumetric error eq. (6.17) comparison among the two different binary gating methods for glycerol (a) and IPA (b) at different interface height (z).

In Figure 6.18, the two methods are compared in imaging the volume occupied by the liquid (glycerol and IPA) in a two-phase case, where the second phase is air. The interface is moved along the axis z and in both cases when z is small or large, corresponding to a small volume or a large volume of contained liquid respectively, the accuracy is poor. The performances improve when the location of the interface is $0.4 < z < 0.6$, corresponding to the middle electrode plane. In this position, the error is close to 0, although differences are noted both by varying the material and the binary gating method.

It is clear that with the glycerol-air system, ECT achieves lower error; this is due to the fact that the relative permittivity between the two substances is 40 compared to the permittivity ratio of the IPA-air system, which is equal to ~18. In the second case, the error is magnified especially at the edges of the sensor. Furthermore, the two curves obtained in Figure 6.18(b) exhibit a higher offset, with the performance obtained with the gradient method overcoming the one obtained with the thresholding. This increased overestimation is connected to the reduced permittivity difference, but also to the method itself; indeed, while the gradient method finds only one interface for each of the voxel columns, the thresholding is also more subject to disturbances in the reconstruction that may cause artefacts far from the interface. This is highlighted by the comparison in Figure 6.19.

(a)

(b)
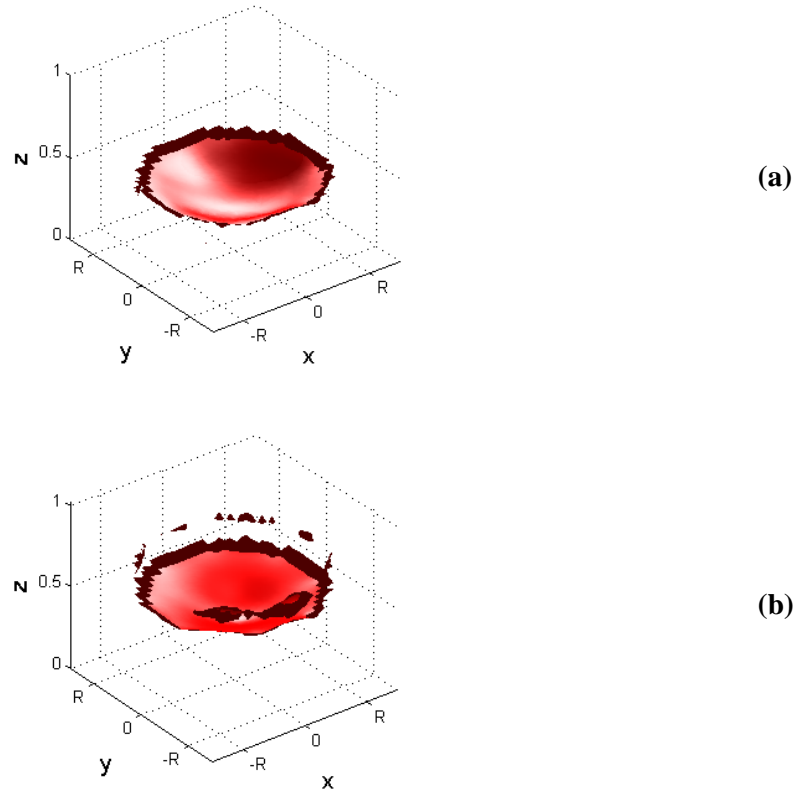
Figure 6.19 – Comparison of two interfaces detected with the thresholding approach. While for case (a) there are not artefacts altering the performance of ECT, in case (b) instead unexpected zones of high permittivity are located above the interface.

In Figure 6.19 the interface between glycerol and water is imaged, with glycerol being located from the red surface downwards. The images are shown to highlight how in the case of $z=0.6$ (Figure 6.19(b)) the presence of artefacts towards the top of the figure present a noisy image that is far from the reality. In both cases it is also shown how the surface has a concentric defect, with a concave shape. This behaviour is believed due to the limitation in penetration exhibited by the technique. The presence of such artefact poses an additional problem for the application of thresholding that increases the error.

In Figure 6.20, examples of tomograms obtained with the two binary gating methods are shown.
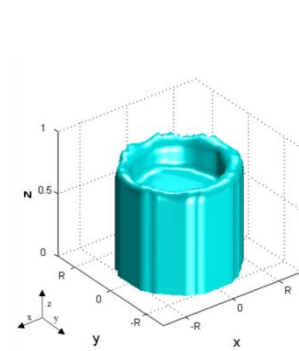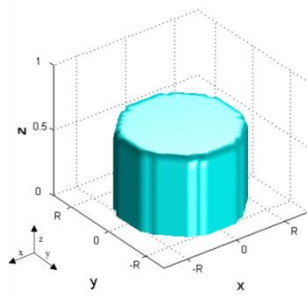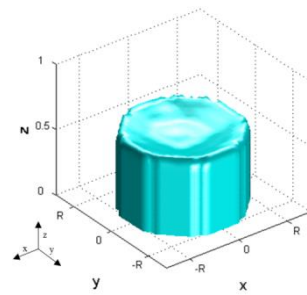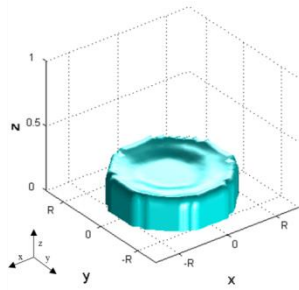
Gradient method　　　　**Thresholding method**
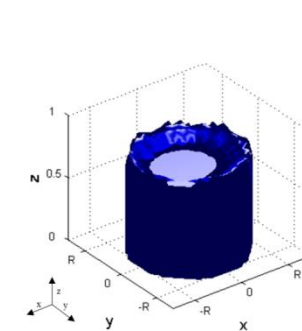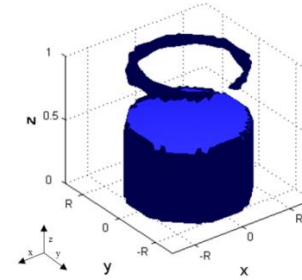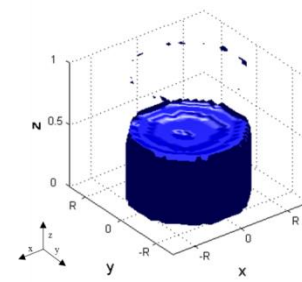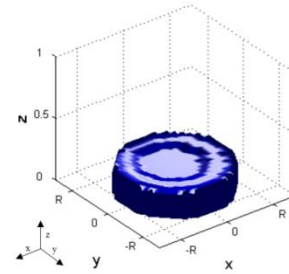
(a): level 0.12

(b): level 0.45

(c): level 0.65

(d): level 0.75

182
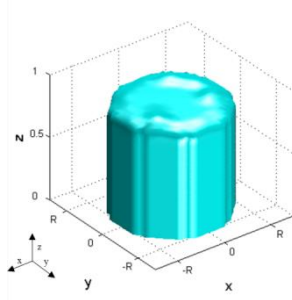
Gradient method   **Thresholding method**
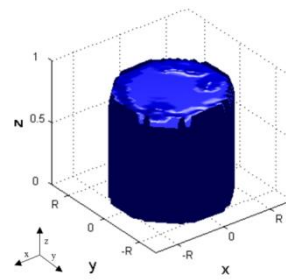
(e): level 0.88

Figure 6.20 – Example of tomograms binary gated using the gradient method (in cyan) and the thresholding method (in blue) for different relative glycerol filling levels: 0.12 (a), 0.45 (b), 0.65 (c) 0.75 (d) and 0.88 (e).

The tomograms reported in Figure 6.20 show an example of binary gated image of glycerol at different heights:

- At low z (Figure 6.20(a)), both tomograms overestimate the level showing a concave surface; the quantity of liquid is small, therefore the dielectric properties of the system is very close to air, hence, the generated signal is small, amplifying the error

- At intermediate z (Figure 6.20(b) and (c)) the interface is rather flat, especially at z=0.65 when the second plane of electrode is fully covered. This is the optimum condition where the error is a minimum for the gradient method. As discussed before the binary gating can present problem of artefacts at the top where zones of high permittivity are detected and gated as glycerol regions.

- When the level is in the interplane zone (Figure 6.20(d)), it is possible to observe a significant decrease of performance with both tomograms having a steep interface, very high at the edges and at a significant lower level in the middle of the tomogram. This is the condition at which the worst performance is shown.

- At high z (Figure 6.20(e)) the performance of ECT improves again, until z=0.95 above which the system fails in identifying an interface between the two phases.

Conclusions

The sensitivity of ECT technique in imaging a horizontal interface between liquid and gas at different relative height in the sensor was examined. It is observed that the techniques work poorly when the sensor is full of one of the two materials whilst it gives good accuracy when the 50% ratio is approached. It is also observed that when the interface is located between electrode planes, particularly uneven shapes are reconstructed. The application of the gradient method outperformed the traditional thresholding at intermediate filling levels, where artefacts presented unexpected high permittivity areas in the top part of the sensor. The conducted experiments suggest ECT can be applied for horizontal interface detection only when the interface is located away from the far ends of the sensor. The interplane gaps are shown to be error prone zones which could be reduced by designing a sensor with minimum interplane gap. These recommendations are used for designing sensors and experiments in Chapter 7.

6.5 <u>Overall Conclusions</u>

3D ECT has been investigated as tomographic technique to image a biphasic interface (solid-liquid and liquid-gas). A method developed by Alberini (Alberini et al., 2014b) and applied to ECT by Clark (Clark et al., 2016b), to identify the optimised threshold value in the case of plastic phantoms immersed in liquid in 2D, has been extended and applied in the three-dimensional case. The areal method (renamed as volumetric method) was assessed to be a valuable approach to evaluate performance of the technique with less information in place compared to the voxel by voxel approach.

The same method for evaluating imaging error was then used to describe the ECT performance in imaging a horizontal interface between a dielectric liquid (glycerol or IPA) and air. Two single-step linear reconstruction methods were compared: LBP and Tikhonov regularisation, with the latter being also tuned in respect to the regularisation parameter μ. An image error analysis was conducted that indicated the methods have a similar accuracy. The Tikhonov method with $\mu=10^{-12}$ was observed to achieve the better results in term of accuracy in filling level and standard deviation was used as a measure of "flatness" of the interface.

A gradient method was developed as an alternative to the thresholding approach which requires the *a priori* knowledge of an optimum threshold value to be used for binary gating. The gradient method already used in other tomographic techniques (X-ray (Shashishekhar, 2015)) has demonstrated good performance in locating the interface with some observed limitations. It achieves good performance (low error) when the interface is located at a relative axial height higher than $z = 0.2$ and lower than $z = 0.8$. It has been observed that when one of the two phases was covering less than half of the first electrode plane, the system would struggle to differentiate this condition from the monophasic condition. The accuracy of the detection is also subject to the location of the liquid level in respect to the electrode planes: when this was located between electrode planes, an inflection in performance was observed.

Recommendations address both operations and sensor design: when possible the horizontal interface should be placed within the middle plane electrode and outside the interplane gap.

6.6   <u>Nomenclature</u>

$C_{i,j}^n$	Normalised capacitance
N_V	Number of voxels
e_V	Volumetric error

e_{VbV}	Voxel by voxel error
C	Capacitance, F
R	Radius, m
V	Voltage, V
W	Electrode width, m
E	Potential distribution, V
G	Vector of voxel values
L	Electrode length, m
M	Number of the electrodes
N	Number of measurements
S	Sensitivity Jacobian matrix
i , j	Indexes identifying couples of electrodes
p	Pixel volume, m^3
s	Capacitance sensitivity, m
t	Threshold value
u	Identity vector
x, y, z	Geometrical coordinates, m

Greek letters

β_C	Volume of the chamber, m^3
β_{image}	Volume of the imaged phantom, m^3
$\beta_{phantom}$	Volume of the real phantom, m^3
$\vartheta_{image}^{(i)}$	Imaged voxel value
$\vartheta_{real}^{(i)}$	Real voxel value
Γ	Electrode area, m^2
ε_r	Relative permittivity
ρ	Charge density, C m^{-3}
φ	Electric potential, V
β	Volume, m^3
ε	Electrical permittivity, F m^{-1}
λ	Vector of normalised capacitance
μ	Tikhonov regularisation parameter

7.

Electrical Capacitance Tomography for Clean Air Dosing Length On-line Measurement

The Catalytic converter manufacturing is a complex multi-steps process. Depositing washcoat over the honeycomb substrates is one of the involved unit operations, also known as coating. Improving the monitoring of this operation is identified as a point of improvement within the process for JM Clean Air business.

3D Electrical Capacitance Tomography was tested for coating depth detection on a Clean Air production line. ECT is an attractive potential replacement or support for the current X-ray system with its expected ability to monitor every part with near real time output as well as anticipated significantly lower cost. A statistically valid number of cordierite half coated monoliths were tested (50 Flow Through parts and 18 Gasoline Particulate Filters). The items were collected from the line straight after the coating process and scanned with the 3D ECT sensor and then with the X-Ray machines (3DX-ray) used on plants. The obtained 3D ECT images were compared with X-Ray scans in order to evaluate the performance of the new technology against the existing application. 3D-ECT repeatability, sensitivity to ambient noise and accuracy were investigated.

The work reported in this chapter has been conducted with the help and support of engineers and operators from Johnson Matthey Clean Air and Technology Centre. The reported work has been filed as internal JM reports.

7.1 Introduction

Johnson Matthey is one of the market-leading providers of catalysts for automotive emissions control. A catalytic converter is an exhaust emission control device which reduces the concentration of toxic substances and pollutants in the gas flow leaving an internal combustion engine. The catalyst consists of a high surface area honeycomb substrate that constitutes the surface area over which the washcoat, the catalyst carrier, is deposited (Cooper, 1983). The washcoat is used to suspend the active catalyst and is composed of a slurry containing an inorganic support and platinum group metals (PGMs) including Platinum, Palladium, Rhodium (Cooper, 1983). Once the washcoat has been deposited, the support is dried and calcined and the washcoat layer becomes well-adhered to the support. In use, the exhaust gases pass over this surface and redox reactions promoted by the active catalyst breaks down the pollutants before the gases are released into the environment.

Figure 7.1 – Monoliths handled by a robot on the production line (Global Info Reports, 2018).

Catalytic converters are installed on many types of vehicles and depending on the type of engine, size of the vehicle and regulation, the catalyst formulation, support and substrate material may vary. The substrates can be made from different materials (examples are reported in Figure 7.2):

- Metal: metallic foil substrates are made of an Iron-Chromium-Aluminium alloy (e.g. FeCr alloy) and are usually manufactured in small batches for applications where a low back-pressure is required for high performance (Litto et al., 2016), for example for sports cars.

- Ceramic: generally Cordierite (a magnesium iron aluminium cyclosilicate), Silicon Carbide (SiC) or Aluminium Titanate (AT). These are characterized by low weight, high resistance to temperature and thermal shock and ease of manufacture (Heck et al., 2001).
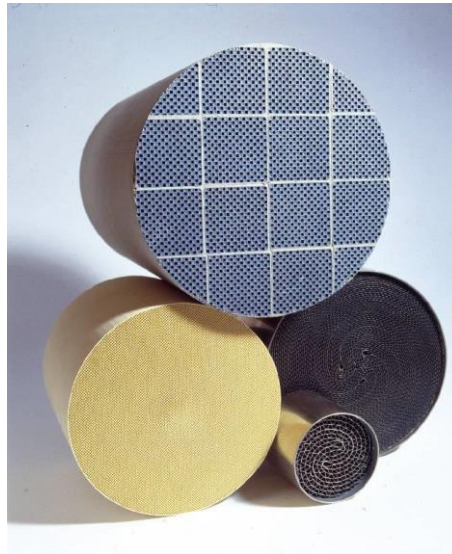
Figure 7.2 – Ceramic SiC (top), ceramic flow through (bottom left) and two metallic (front and right) catalyst monoliths (Johnson Matthey, 2018).

Catalytic converters have a different operating strategy depending on whether the channels are blocked at one end (filter) or if the gas is free to run straight through the honeycomb

(through flow). The former solution is usually adopted for Diesel engines, where such blocked cells entrap particulates avoiding the emission of solid products of combustion. The gas is instead transported through the membrane to adjacent channels having open ends that allow gas to discharge into the atmosphere. Although these particulate filters are traditionally used for diesel engines (diesel particulate filters DPF), their application is being extended to gasoline direct injection engines (Gasoline Particulate filters GPF) (Johnson Matthey, 2017b).

Currently flow through (FT) monoliths are the most used solution in gasoline engines. In such devices, the gas is free to flow from the inlet to the outlet of the channel without encountering any physical barrier.

The manufacture of these items is a complex multi-step process involving compounds of different nature and structure. The chemistry and engineering concerning catalyst production are strictly dependent upon the customer requirements, the type of fuel, the final installation of the item and environmental emission limits.

The washcoat is prepared through sequential processes of powder incorporation, milling, blending of the active components and rheology modification and is then used to coat the substrates. During the coating step, the washcoat is firstly placed on top of the monolith (its rheology characteristics are chosen to prevent seepage into the channels) and then drawn through the channels by applying a specific vacuum (between 15 and 50 kPa) on the other end of the monolith. The negative pressure causes the washcoat to move down through the part, and the yield stress and complex rheology of the fluid (well described by a Herschel-Bulkley model) allows it to deposit as a thin layer on the wall. When the pressure gradient reaches the equilibrium, the flow stops and a certain percentage of the monolith length, called dose length, is covered by the solid/liquid suspension. The process, then, involves drying and turning upside down the item to repeat the same procedure onto the other side. The part is

then dried a second time and sent to the calcination process. A block diagram of the process is given in Figure 7.3 (a).
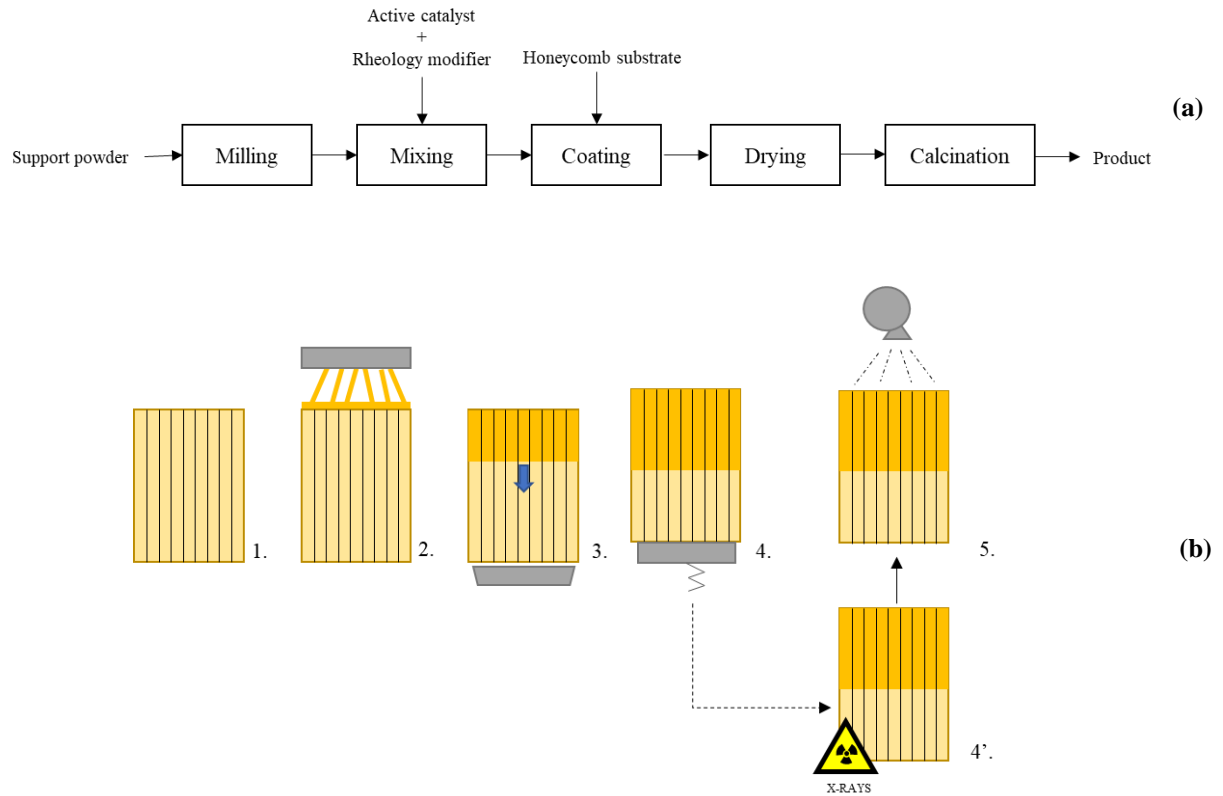
Figure 7.3 – Block diagram representing the catalyst converter production process (a). And a pictorial representation of the coating process on the line (b): a bare substrate is placed on the coating bench by a robot (1), then a controlled quantity of washcoat is placed on top (2) and pulled through the channels applying a vacuum from the bottom of the part (3); the part is then weighed (4) and is dryied with hot air (5). Some parts are sampled before drying for X-ray measurements of the dosing length (4') and if respecting specification are fed to drying. At the end of the first pass the parts are flipped upside down and the same process is repeated for the second end of the substrate.

Figure 7.3(b) describes the process substrates undergo during the coating stage. Although it is represented as a line, the process is executed on a round table which allows the parts to move from one stage to the other (Figure 7.4).
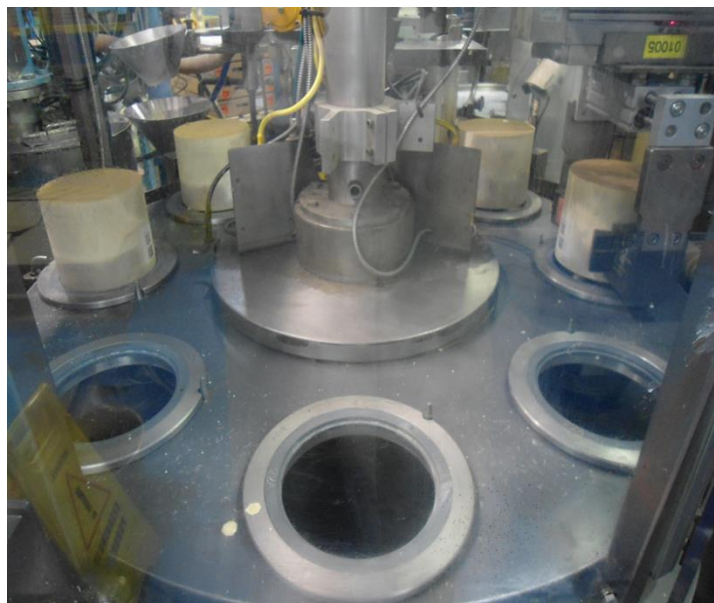
Figure 7.4. – Picture of the round table on the FastCat plant. The parts are moved by rotating the table. This ensures the minimum robot handling of the parts to avoid physical damage of the parts.

The aforementioned process is the traditional process for "Flow-through" monoliths. Although the filter manufacturing requires, sometime, different steps, the overall process does not deviate significantly from the Flow-through production flow. The coating process is a delicate stage and requires the maximum possible precision; an overlap between the two coatings would represent a waste of expensive PGM and therefore of money (Kaspar et al., 2003). However, the presence of a gap between the two coating layers would make the catalyst less effective and possibly result in the exit gas being out of specification. In Figure 7.5, the possible cases occurring after the coating application are reported.
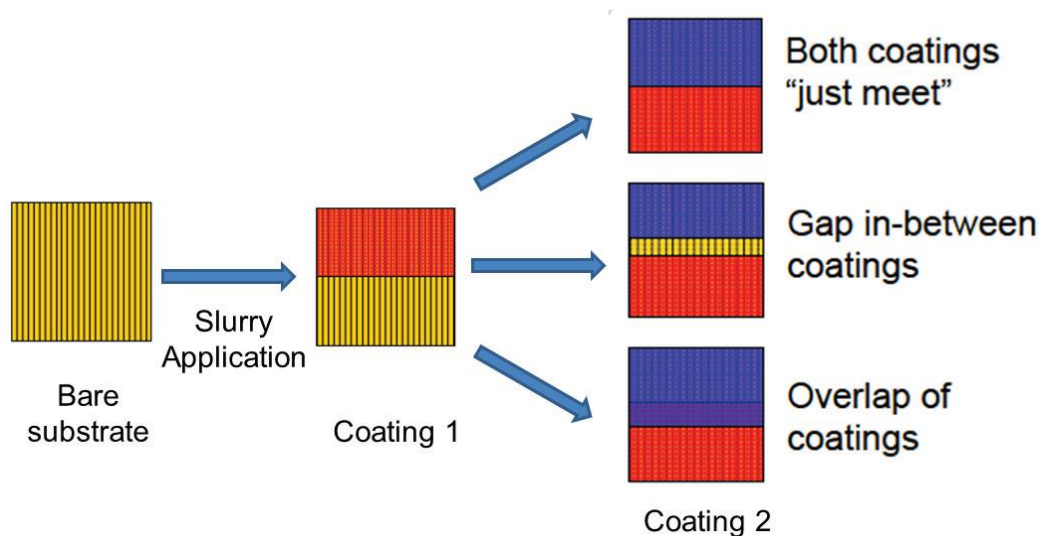
Figure 7.5 – Catalytic converter coating possible outcomes (Shashishekhar and Veselitza, 2017). After the second coating is applied the outcome can result in a perfect condition where the two coatings just meet, a second condition where there is a gap between the two coatings, and a third where there is an overlap between the two layers.

The aim of the manufacturing process is to achieve the smaller possible overlap to meet the customer criteria of no gap between the two coating layers. It is key to be able to visualise both dosings to assess the quality of the product. The used parameter is the dosing length, defined as the average depth of the monolith covered by the washcoat. Although it is not possible to achieve a completely uniform and flat profile, internally this parameter is identified with one single number that is used to make a decision on whether the part meets the specification. The dosing length is usually expressed in millimetres or as a percentage of the total substrate length. For most parts is between 50 and 60% of the part length.

The nature of the final product makes this parameter difficult to monitor online and without disruptive tests. The method implemented on plant to measure the dose length currently involves the use of X-ray projected images. A detailed description of how X-ray tomography is applied for coating applications for catalytic converters is reported by Shashishekhar and

Veselitza (2017). This method, although recognised as very reliable, currently requires the parts to be removed from the line to be measured in a shielded X-ray machine, hence, it is not suitable for inline implementation. In addition, the time required for the scan, and the results to be accessible, is over one order of magnitude larger than the cycle time. It is not possible to monitor 100% of the substrates without slowing down significantly the production. Although constituting a quality control for monitoring of the process, dose length measurements are also requirements of customers, therefore being necessary measures included in contracts.

X-ray equipment is expensive to buy and maintain and their high-energy nature also requires special health and safety measures to be put in place.

The above-mentioned considerations constituted reasons for seeking for an alternative technique that could either substitute or support dosing length in situ measurements for 100% of the produced items. Such an additional control measure, potentially identified as Electrical Capacitance Tomography, would constitute an additional feature that Johnson Matthey could offer to customers, increasing their confidence of quality of the products and potentially representing a strategic advantage over competitors.

7.1.1 X-ray system

X-rays are widely used in medical applications and, in similar fashion, can provide a high-resolution image in industrial applications (Abdullah et al., 2010). This high spatial resolution technique generates projection images on the basis of differences in density within the scanned item. Such mechanisms applies well to the half coated monolith in which, the coated part has a high loading of high density material (Shashishekhar, 2015). Currently, the measurement does not happen on the line after the coating. Rather, the item is withdrawn

from the coating line and moved in a shielded machine in which it is scanned with X-rays as shown in Figure 7.6.
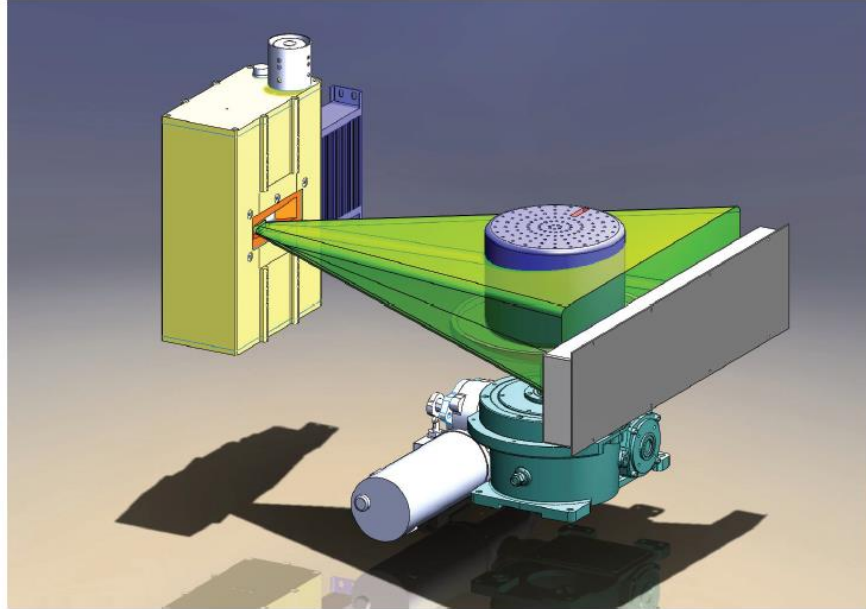
Figure 7.6 Schematic of X-ray measurement process (Shashishekhar and Veselitza, 2017). The X-ray generator on the left is the radiation source, the sample is placed over a sample drive unit and on the right the X-ray detector contains the photodiodes that capture the resulting X-ray radiation.

The monolith is placed on a platform between the X-ray source and the detector array. The X-ray CT system is composed by:

- An X-ray generator, typically of 150 kV intensity (180 to 640 W) equipped with a beamer to direct x-ray towards the part (3DX-RAY ltd. UK, 2017).

- Sample drive unit, consisting of a platform where the part is placed.

- X-ray detector: assembled into the scanner and consisting of a collimator and photodiode arrays.

As the generated X-rays pass through the part, absorption and scattering occur causing attenuation in the signal. The attenuation through a homogeneous material is described by the Beer-Lambert law (Izumi et al., 1993):

$$I = I_0^{-\omega\chi} \, ,$$

(7.1)

Where I is the intensity measured at the detector, I_0 is the emitted initial intensity, χ is the distance of travelling and ω is the linear attenuation coefficient specific to the material. In practical applications though, as in this case, the object is composed by different phases and materials, therefore the equation becomes:

$$I = \int I_0^{-p\chi} (E)dE \, ,$$

(7.2)

with E being the X-ray energy and p being the projection function defined as:

$$p(x) = \sum_{i=1}^{n} \omega_i \chi_i$$

(7.3)

Where ω_i and x_i are the attenuation coefficient and the linear extent of the i-th material present along the path respectively. However, for practical applications (Abdullah et al., 2010), the dependence of the intensity on the X-ray energy is not accounted for and therefore the expression becomes:

$$I = I_0^{-p\chi}$$

(7.4)

Generally, I_0 at the detector is measured running a blank test, used as a calibration for the part measurement. This is to take into account the off-centre angle of the cone beam. X-ray tomography, being a hard-field technique, allows the achievement of high spatial resolutions, however, the linearity allows the X-ray to this is true when the thickness of crossed material is constant (the centre of the part). Studies in the literature report an observed biasing effect on

the edge of cylindrical object when imaged with planar X-rays. Amongst others, the beam hardening effect (Ketcham and Carlson, 2001) gives to the obtained images a gradient of brightness, from the centre of the object towards the edge, without real physical changes in the material distribution. This effect can be the cause of odd profile observed in the periphery of X-ray images, in internal JM studies.

An example of the raw X-ray projection for a half-coated (one pass) monolith is shown in Figure 7.7.

Figure 7.7 – X-ray projected image of a monolith. At the top, the black pixels identify the region where the high density washcoat is deposited. At the bottom, the grey pixels show the uncoated area.

On the basis of these, the plant operator evaluates the quality of the coating and decides if it meets the specification required or if it has to be rejected (some examples of rejects are shown in Figure 7.8).
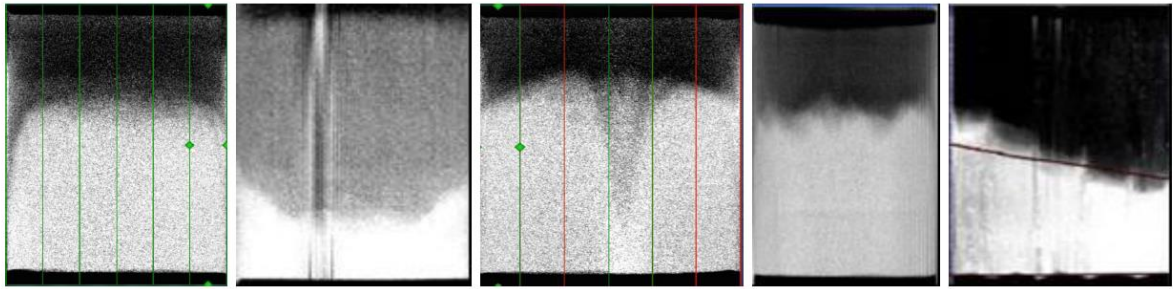
Figure 7.8 – Example of rejects. All of the shown examples do not present a flat profile within specifications.

The evaluation of coating depth (or length) is calculated by the software that divides the substrate image in 4 vertical regions (Figure 7.9) and computes an average density profile for each of them.
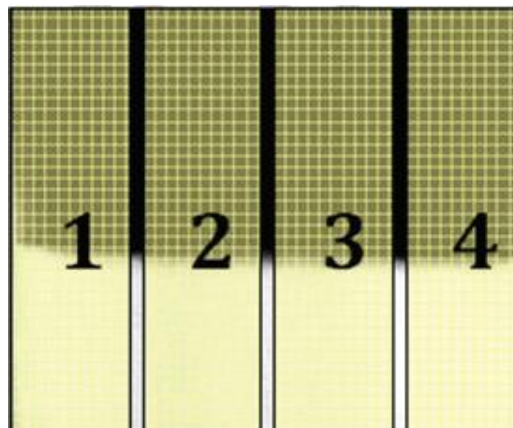
Figure 7.9 – Schematic of X-ray computational strategy. The X-ray resulting scan is divided in 4 vertical sections that are individually interrogated to identify the coating profile.

The final dosing length is determined to be at the point of inflection of the average density curve (Young et al., 2009), in the case reported in figure it is identified as X_{mid} at the 91st pixel of the image.
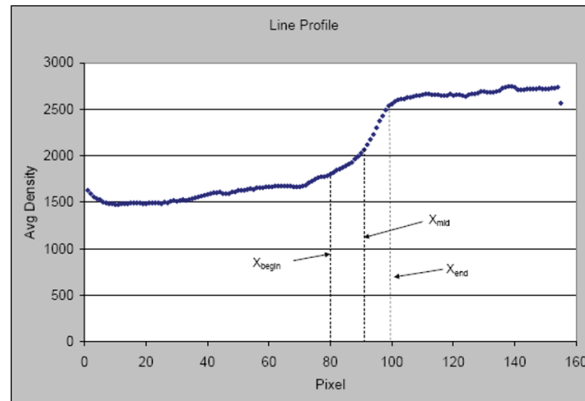
Xmid = pixel 91
Total part length = 155 pixels
Coating Depth % = 91/155 = 58.7%

Figure 7.10 – Example of X-ray coating profile (Shashishekhar and Veselitza, 2017). The average density goes from low values (1500 of the arbitrary scale) to high values (2700); this corresponds to the transition between the dry part and the coated part respectively. X_{mid} is identified as the point of inflection of the curve, hence the interface between dry and coated.

The X-ray measurement for dosing length is the common approved solution amongst JM production line managers and operators as well as for automotive OEM customers. As shown in Figure 7.8-9, the resolution of the obtained scan is very high and the difference between the high density zone at the top and the low density area at the bottom is clearly demarked, but this is not always the case. It is indeed observed that, especially in the case of the second dose, some images are unclear, and this can lead to large quantities of quarantined products of uncertain quality. An example of a snapshot from the operating software is reported in Figure 7.11 with the substrate imaged lying down on one side.
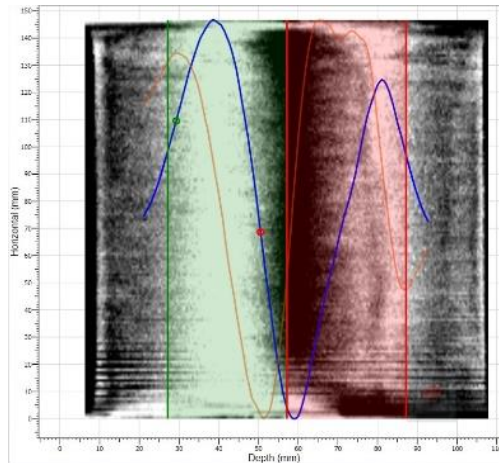
Figure 7.11 – Example of a snapshot from the 3DX-RAY scanning software of a second pass monolith. The monolith is placed lying down on one side. If on the first pass (right to left) the dosing length is in specification (green), on the other side the second pass results in a fail (red).

In this case, (Figure 7.11), the overlap between the two doses represents an issue for the identification of the dosing length: the first dose was executed from the right to the left, whilst the second (the one object of the analysis) was executed in the opposite direction. Because of the overlap, it is difficult for the software, hence for the operator, to identify the second dosing length. This uncertainty, observed on a number of Gasoline Particulate Filters (GPF) products, represents one of the limits of the technique. It is hoped that this issue will be overcome using ECT as the measurement is based on the difference in permittivity between the wet and dry part, and thus it is not influenced by the presence of the previous deposited (dry) layer of washcoat.

Furthermore, given the time required, in the case of X-ray, to remove the item from the line and scan it, the method cannot be used to test every single item (in general one part in 18 is measured), therefore, for each item not meeting the specifications, a certain number of unmeasured monoliths are taken off the line (typically 35). This can result in a high number

of rejects and down time, therefore consisting in a high cost in terms of time and resources beside the high cost of the X-ray equipment itself.

For these reasons, 3D-ECT is being investigated to provide a cheaper, faster (potential for QA) and lower energy measurement technique. The resolution and accuracy have been investigated, along with the implementation issues of installing it on plant. In this chapter, experiments from one of the two on plant campaigns are reported. The trials were carried out on Clean Air production plants in Royston and Macedonia and had as objectives:

- Obtaining a statistically significant dataset to compare 3D-ECT technique with X-ray;

- Assessing 3D-ECT capabilities for inline implementation;

- Evaluating advantages and limitations of the technique.

7.2   Material and Methods

7.2.1 Substrates

To evaluate the capability of ECT to be applied on different materials, different ceramic substrates have been tested.   Three ceramics (cordierite, AT and SiC) have been tested; however this work was carried out specifically for cordierite substrates, which represent the most common product (Williams, 2001).

Metallic substrates have not been tested since they are conductive, therefore their relative permittivity is considered to be infinite because conduction will always prevail on polarisation for a conductive medium (Lorrain et al., 1988).   Floating metals have been studied before using ECT by Zhang and Soleimani (2015) and models have been built to identify the location of a metal rod in a sensor.   However, although the authors have been able to identify

the location of the rod in the sensor, it was impossible to have an insight within the object because of the Faraday cage effect.

The tests have been carried out in different locations (laboratory, production lines) and with varying size of the monoliths depending on the available product. The reported results are carried out on cordierite parts with diameter of 143.76 mm and different heights and coating.

- For feasibility and defect detection (Section 7.3.1) the parts had a height of 152.4 mm and the coating was carried out with a PGM based washcoat DF751P (containing TOSOH AZM4 zeolite, Palladium nitrate, Sasol Dispersible Boehmite (Disperal), water, nitric acid and natrosol® thickener). The test was carried out at the Technology Centre in Royston (UK). In Figure 7.12 a picture of the ECT settings by the coating bench is shown.

- For the repeatability study (Section 7.3.2) the parts had a height of 152.4 mm and the coating was carried out using silica-stabilised alumina slurry (S5/155 Silica Alumina 5%SiO2, 95%Al2O3).

- For the plant campaign test the trials were run in FastCat plant, Royston on two different supports:

  o Flow through (FT) cordierite parts (50 parts scanned) with height of 127 mm and washcoat formulation JM842 (PGM based). The applied coating is a second pass, meaning that the deposited layer was placed over an existing dry (but active) coating. The coating depth specification was 63.5-88.5 mm (50-70%).

o Gasoline Particulate Filters (GPF) cordierite parts (18 parts scanned) with height of 127 mm and first pass washcoat. Formulation (PGM based) and target depth specification was undisclosed.

Figure 7.12 – Picture of the ECT equipment installed on the coating bench in the Tech Centre in Royston.

The quantity and composition of washcoat used for each part varied depending on the coated parts, the batch and the plant needs. The mass of washcoat varied between 430 and 670 g and the vacuum applied for pulling it through the honeycomb was in the range between -30 and -59 kPa.

7.2.2 ECT system

The ECT general set-up is described in section 6.2; for these experiments, the same setup in terms of DAS (m3c ITS Ltd.) and software (MMTC ITS Ltd.) was used. However, for geometrical reasons, in this study a range of different sensors, all having three planes of 8 electrodes each as for Figure 7.13, were used:

- *Sensor A*: having a sensing height H of 122 mm, an electrode height h of 36 mm and an interplane gap g of 7 mm was used. It had a diameter of 147 mm. Sensor A was used for feasibility and defects detection trials in section 7.3.1 and also deployed for the study carried out in Chapter 6.

- *Sensor B*: having a sensing height H of 90 mm, an electrode height h of 29 mm, interplane gap g of 1.5 mm and a diameter D of 186.2 mm. This sensor was used for the repeatability test in section 7.3.2.

- *Sensor C*: deployed in the tests conducted on plant (section 7.3.3) had a diameter D of 149 mm and a sensing H height of 60 mm (with electrode height h of 19 mm and interplane gap g of 1.5 mm).
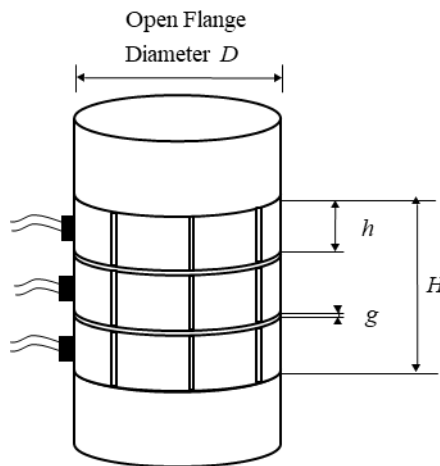
Figure 7.13 – General scheme of a 3-electrode plane equipped ECT sensor: H is the sensing height, h is the electrode length, g is the interplane gap and D is the open flange diameter.

It has to be noted that the sensing region did not cover the total monolith volume for any case. This is to ensure that only the substrate would be included within the sensing region (no air or support platform) and also because the intention is to focus the measurement towards the

target dosing length which is normally located in the region between 40 and 70% of the relative height of the monolith.

For all the conducted experiments, the calibration step was taken using a bare substrate as the low permittivity reference and a fully coated monolith as the high permittivity reference. Fully coated is defined as a monolith having a wet freshly coated layer that covers the totality of the sensing region. Practically, this was obtained by increasing the amount of washcoat deposited and the vacuum pressure to ensure the minimum length was reached. This was checked using X-ray scans. The images were reconstructed using the Tikhonov regularisation as for Chapter 6 and, unless otherwise stated, the gradient method was used for evaluating the interface location.

7.2.3 X-ray

X-ray scans were used as a term of comparison to evaluate the performance of ECT. The scans were obtained using an industrial MDXi X-ray cabinet system by 3DX-RAY Ltd. (Loughborough, UK). The machine is equipped with a photodiode array as a detector and a 150 kV/1.2 mA X-ray generator of, capable of emitting up to 640 W of power. The system is shown in Figure 7.14.

Figure 7.14 – Picture of a MDXi industrial X-ray system (3DX-RAY ltd., 2017b).

The parts are generally placed in the shielded chamber where the measurement takes place. The monitor shows to the operator the outcome of the measurement.

In this study, the images were further processed offline to extract the dosing length from the greyscale X-ray images. In the software this value is named as decision data and it is a greyscale value comprised between 1 (white colour) and 0 (black). In Figure 7.15, an example of X-ray scans obtained for FT and GPF and the resulting profiles.
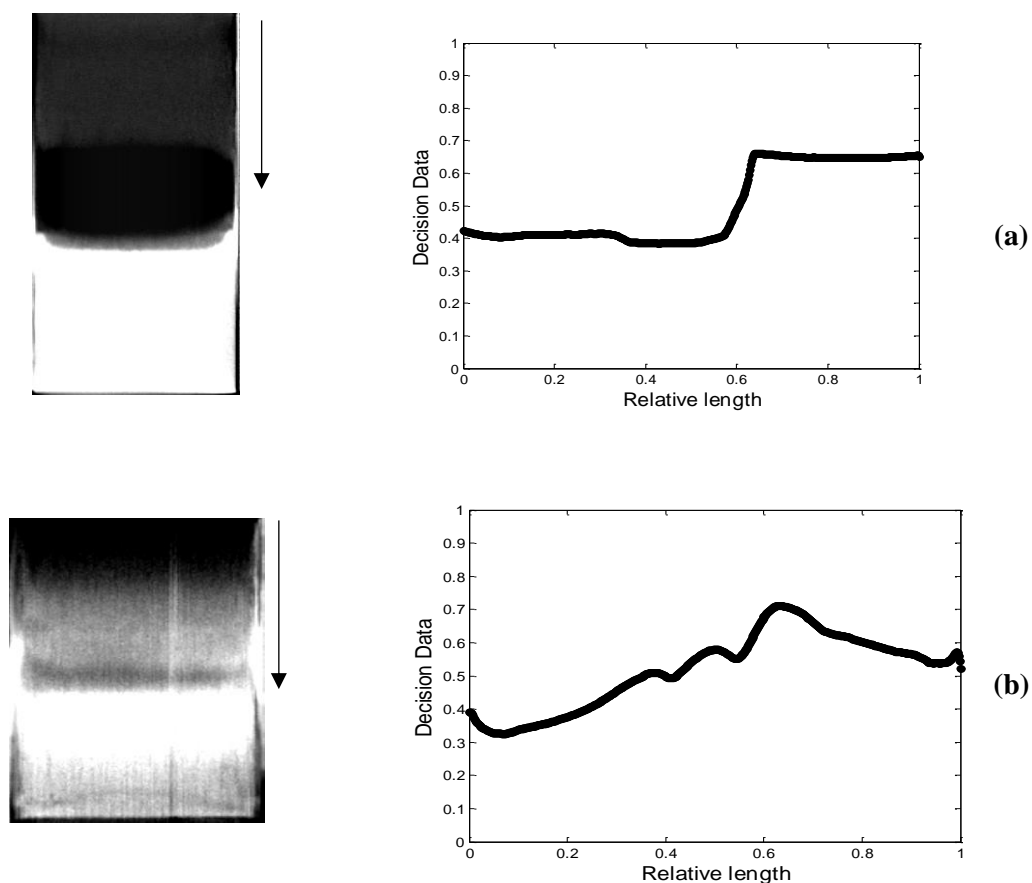
Figure 7.15 – X-ray raw image and decision data plot for FT (a) and GPF (b). The plots on the right are obtained by averaging the greyscale value for each of the horizontal pixel rows of the corresponding images on the left.

The images were processed using a MATLAB script to identify the inflection point of the decision data curve. Generally, the obtained results were found to be reliable when the X-ray images present a well-defined profile, as in the case of FT where the curve is monotonic in the region of interest. On the contrary, the data for GPF produced a non-monotonic profile; this constitutes an issue for the use of the X-ray technology, which is currently under study within Johnson Matthey. However, given the small batch analysed in this study, the obtained results from the MATLAB® processing were visually checked to ensure no artefact could affect the results.

207

7.2.4 Plant trials

Plant trials were conducted at line 1 FastCat, Clean Air production plant in Royston. The ECT unit was placed beside the rotary table as shown in Figure 7.16.

Figure 7.16 – ECT installed by line 1 in FastCat.

The monoliths were taken off the line after the coating, before they were fed to the drying zone. In order to obtain the highest data quality, it is necessary to scan the parts before the moisture starts leaving the item.

Each processed part was scanned using ECT ten times and then X-ray scanned using the MDXi machine available on plant. While X-ray machines scan 100% of the length of the monolith, the used ECT sensor covers only a portion of it. For the used sensor B, the ECT sensing region height is 60 mm, therefore, 47.3% of the monolith height is scanned by the ECT (between 36.4% and 83.7% from the top of the monolith). The reason for this relies on the relative dimension between the available sensors and the coated parts (the bigger sensor available would have been oversized for the processed batch). In practical terms, each part was placed on a flat support and the sensor was manually lowered onto it. A designed cross-

sectional area change in proximity of the end of the sensor (a little step) acted as a limit and allows correct positioning.

7.2.5 Graphical User Interface

For the post processing and the application of the gradient method a provisional Graphical user interface (GUI) has been created in MATLAB® to facilitate the user producing the information on dosing length location and give an idea of how an online implementation interface would look like at a glance (Figure 7.17).
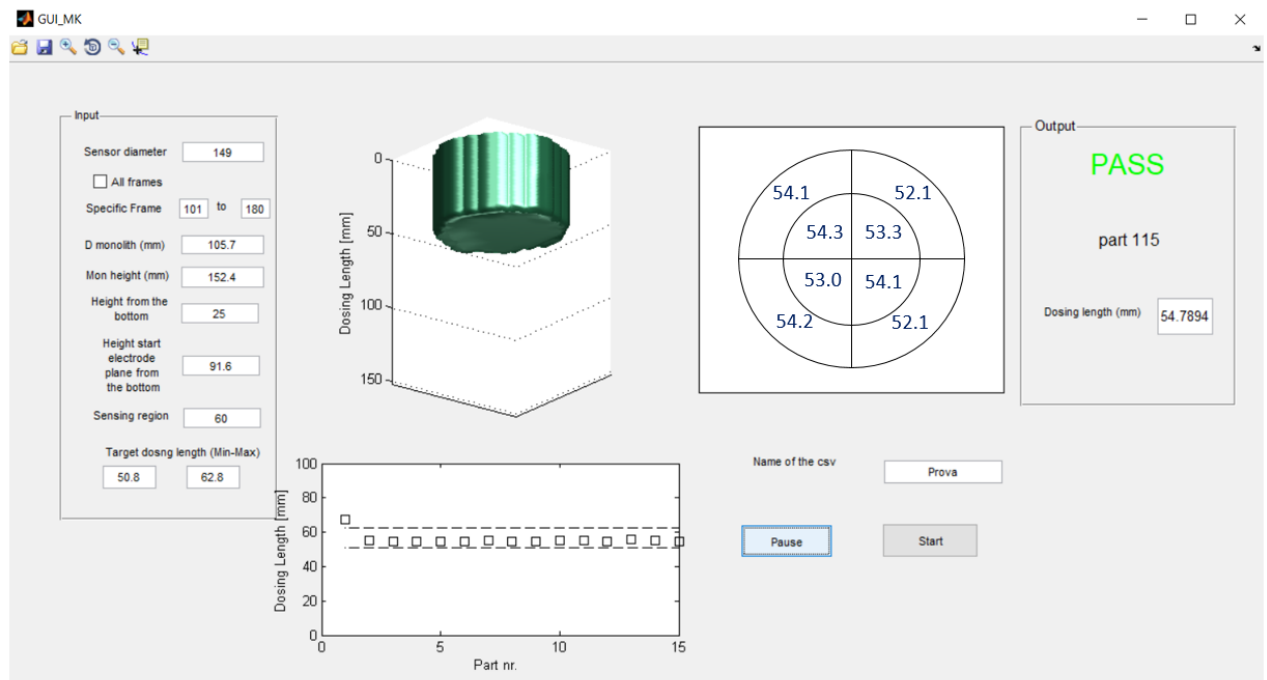
Figure 7.17 – Picture of the GUI developed in MATLAB. On the left the user can provide input parameters; in the middle, a reconstruction of the tomogram for visual inspection at the top with the dosing length plot is reported, at the bottom a plot for comparing with historical values. On the right, the catalytic converter dose length is reported for circular sectors. On the far right, the system flaga the examined part as pass/fail and gives the overall dose length in mm.

Pressing the start button, the ECT file is uploaded and the indicated frames are processed, with a time scale of less than a second per image. On the left-hand side input parameters are inserted, including the size and position of the items, the design dimension of the sensor and

the target dose length. In the middle of the figure, on top, a tomogram shows the interface profile, with the green solid representing the deposited wet washcoat on the substrate. Below it, the dose length of the current frame is plotted together with previous analysed tomograms. On the circular picture on the right, the section is divided in 8 regions and for each region the measured dose length is reported. On the right, a PASS\FAIL word is displayed depending if the global dosing length is within specification. Underneath, there is the identification number of the part together with the measured global dose length. Start and Pause buttons activate and stop the processing, while the name tag is used to produce the spreadsheet containing the results.

7.3   <u>Results</u>

The most used substrate within JM production sites is cordierite. The ECT technique was initially tested and developed for such substrates, but, considering the added value to the production line, it has also been tested for AT and SiC. However, the obtained results for AT and SiC do not reach comparable accuracy to the cordierite substrates. This is due to their electrical properties: permittivity being too high in the case of AT and the anisotropic nature of SiC substrates, presenting concrete vertical slices within its structure, influences the electrical properties and the absorption of washcoat during the coating. Therefore, in this chapter, only data obtained for cordierite monoliths are reported.

This section is structured in three parts. The first (Section 7.3.1) reports initial findings regarding the capabilities of ECT to detect the dose length and in particular to be able to identify anomalies in the coating. The second section (7.3.2) is focused on the evaluation of the repeatability and robustness of the technique. The third part (7.3.3) reports of a data acquisition campaign conducted at the Johnson Matthey Clean Air plant in Royston and had as an objective to evaluate response of ECT in a production environment and to gather a

statistically significant dataset. All the parts tested were cross-referenced to X-ray measurements.

7.3.1 Defect detection

Initial tests on applying 3D-ECT for dosing length detection were conducted in the Tech Centre in Royston. Sensor A was used with a sensing height of 122 mm. The main objective was to assess whether 3D-ECT could recognize flat profiles and deliberately flawed coating profiles. ECT results were actively compared with X-Ray scans. In Figure 7.18, some images obtained with 3D ECT and X-ray are shown for visual comparison.

<div align="center">

3D-ECT   **X-ray**

</div>

(a)

(b)

(c)

(d)
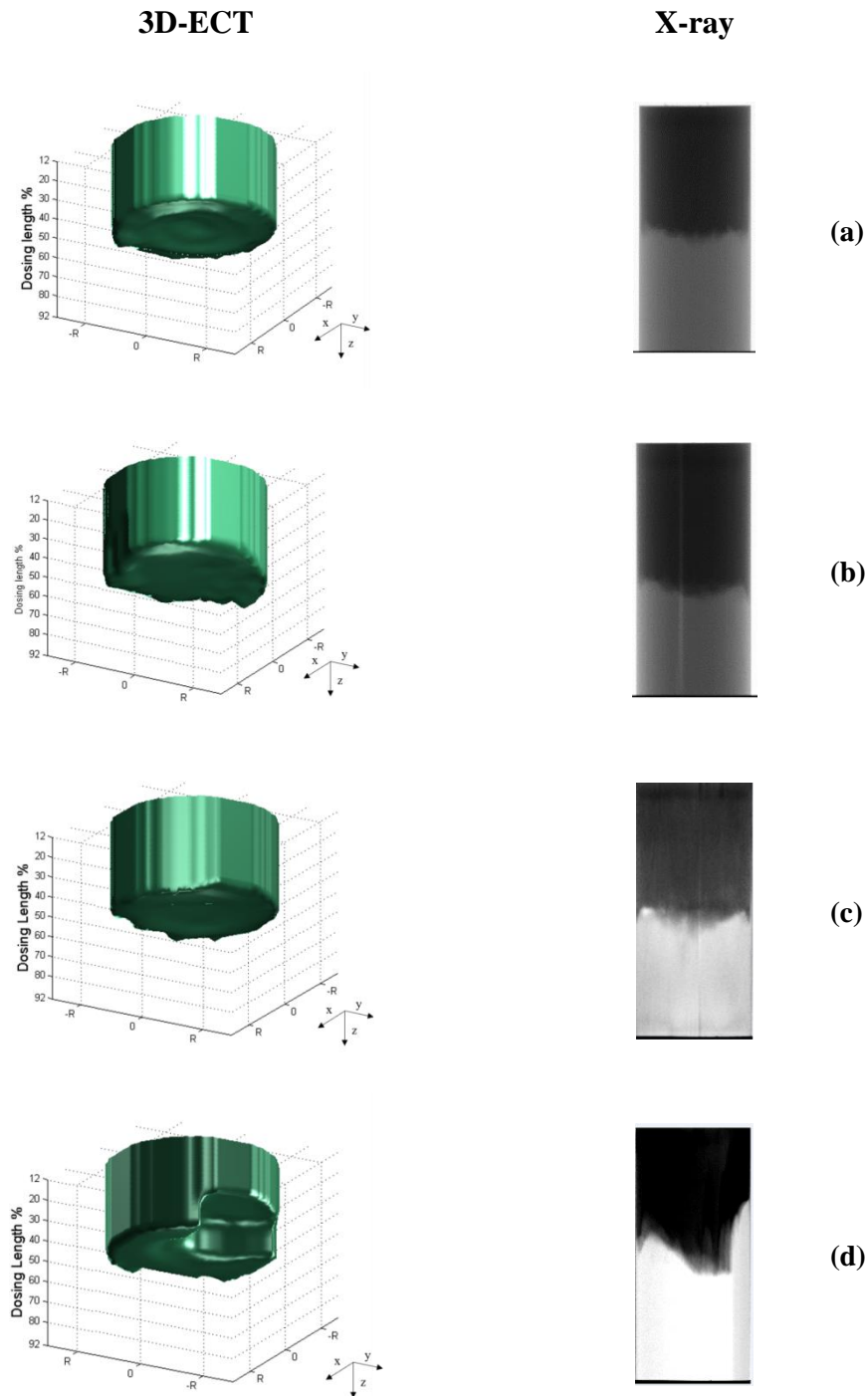
Figure 7.18 – Defect detection example images. On the left column the 3D ECT tomograms and on the right the corresponding X-ray profile. Case (a) and (b) represent first dose profiles in specification; case (c) is a second pass dose; case (d) is a purposely side flawed dosing.

Figure 7.18(a) shows scan of a part having an ideal good profile presenting a good match between X-ray and ECT both visually and within limits in terms of dosing length (54% and

58% respectively). In similar fashion, in Figure 7.18(b), images and detected dosing length also correspond well (59% for X-ray and 57% for ECT), with a slightly longer dose on the right side of the part, visible in both images. In case (c), the monolith, after being coated on one side and dried, was coated on the opposite end, to simulate a second pass coating and challenge the ECT to detect the coating depth. Figure 7.18 (c) shows that the presence of the first coating does not alter the ECT measurement. Although the contrast for the X-ray measurement is decreased, it is still possible to evaluate the length.

Case (d) shows a flawed profile containing an eccentric non-symmetrical defect which is detected by both the techniques with an appreciable similarity. In this case, the orientation of the part in the X-ray is critical: the same defect could be missed if the part is rotated to a different position, as shown in Figure 7.19 in which the same item is rotated by 90°.

Figure 7.19 – X-ray scan for item n° 14 rotated by 90°.

In Figure 7.19 the shape of the defect is not as clear, although to an expert eye the dosing quality does not respect the standards in some manner. A less evident eccentric defect could be easily missed with a 2D scan if not oriented in the right way, leading to a product out of specification.

This initial trial has demonstrated the capability of ECT to detect coating depth within substrate. From the images shown in Figure 7.18, ECT has potential to measure dosing length and capture possible defects in the intermediate coating steps in for cordierite monoliths.

7.3.2 Repeatability tests

Repeatability tests were conducted at lab scale on cordierite monoliths (diameter of 143.7 mm) coated with alumina slurry. In this section, the repeatability tests are described and discussed as well as introducing a key aspect of the coating measurement, known as capillary creeping.

A coated part was firstly scanned with the X-ray and then measured with the ECT. The part was placed into the cage to acquire 30 frames and then taken out. It was then placed again in the cage for a new measurement. This process was repeated five times. Afterwards, the part was rotated 90 degrees (named as rotation 2) and five analogous measurements were taken. At the end of the measurement, the part was scanned again with the X-ray. This process had the objective to evaluate how robust the technique is to perturbations caused by manual placement. In Table 7.1, the dosing length is reported both for the gradient method and the thresholding method along with the standard deviation.

Table 7.1 – Dosing length and standard deviation obtained for the repeatability tests using both the gradient and the thresholding methods for the first orientation named rotation 1 and the 90 degrees rotation named as rotation 2.

	Description	Gradient method		Thresholding method	
		Dosing length (mm)	Standard deviation (mm)	Dosing length (mm)	Standard deviation (mm)
Rotation 1	Start	78.55	0.231	79.79	0.4669
	Re-placed 1	77.76	0.158	81.82	0.489
	Re-placed 2	77.93	0.167	83.08	0.609
	Re-placed 3	78.84	0.192	82.41	0.253
	Re-placed 4	77.75	0.237	84.92	0.481
	Re-placed 5	78.28	0.247	84.71	0.536
Rotation 2	Start	76.15	0.660	88.57	0.0283
	Re-placed 1	75.35	0.391	90.79	0.390
	Re-placed 2	76.07	0.481	90.51	0.495
	Re-placed 3	75.09	0.327	92.61	0.251
	Re-placed 4	74.86	0.241	93.88	0.343
	Re-placed 5	75.21	0.282	94.58	0.219

The table shows that comparison of the dosing length obtained with the gradient and thresholding method gives different trends. For the former, the results for rotation 1 and 2 show differences of approximately 2 mm and there is not a clear trend. The same cannot be said for the latter, which instead sees an increasing trend as shown in Figure 7.20.
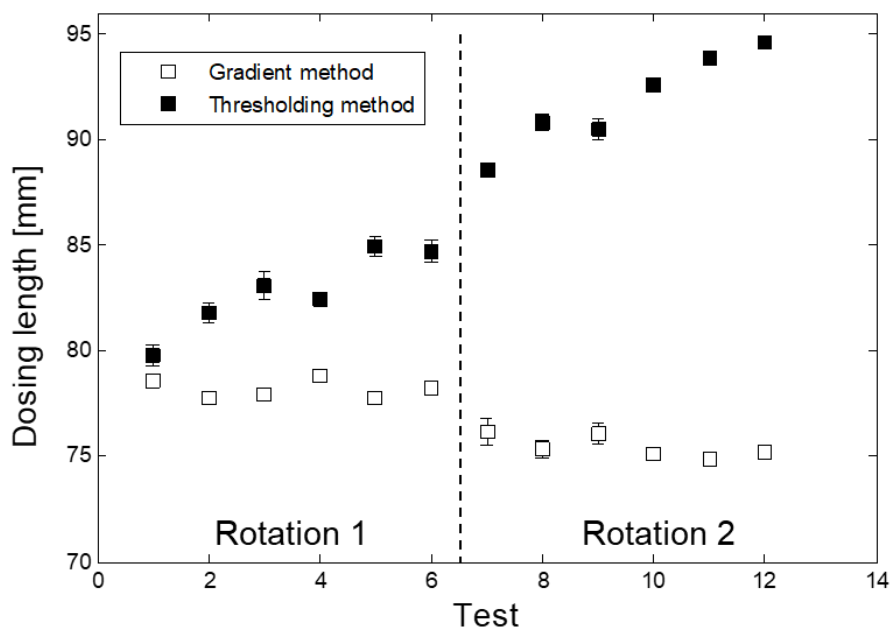
Figure 7.20 – Dosing length obtained for the repeatability test using the gradient method and the thresholding method. Data are reported in Table 7.1.

The thresholding method detects an increase in dosing length which is due to the gradual movement of the wet interface through the monolith during the measurement. This effect, also known as *wicking* or *capillary creeping,* has been observed before by JM and it is also visible through X-ray scans before and after the ECT measurement (Figure 7.22).

	Rotation 1	**Rotation 2**
Before ECT		
Post ECT		
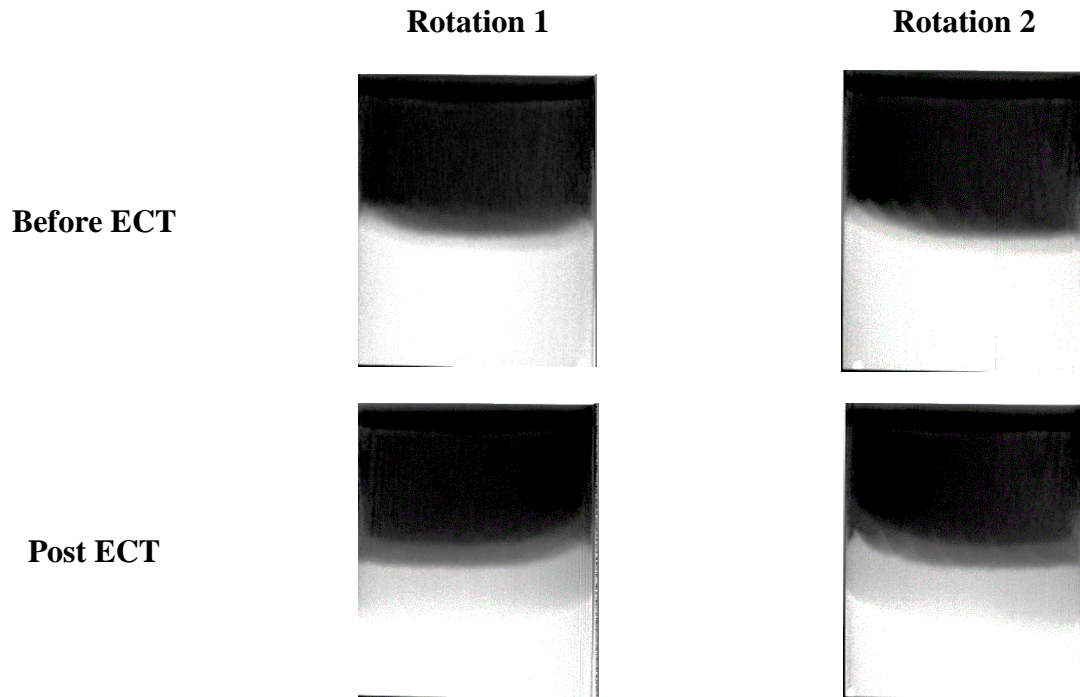
Figure 7.21 – X-ray scans for two rotations before and after ECT measurements. The second measurement is executed a few minutes after the first scan.

The X-ray scans in Figure 7.21 show a region shaded in grey between the black and white regions, indicating the presence of a separate interface caused by moisture movement along the monolith due to capillary forces. Since capacitance measurements are influenced by the moisture content, this ingress would be detected, however, only the threshold method captures this phenomenon. The reason lies in the different mechanism behind the algorithm. The gradient location is not necessarily modified by the moisture movement; on the contrary, by keeping the thresholding value fixed, the number of voxels higher than that value increases as water travels down the monolith. This effect is explained by Figure 7.22 (a), in which the voxel value profile is plotted along the dimensionless length of the sensor z (where $z=0$ identifies the bottom of the sensor, while z=1 the top of the sensing region).
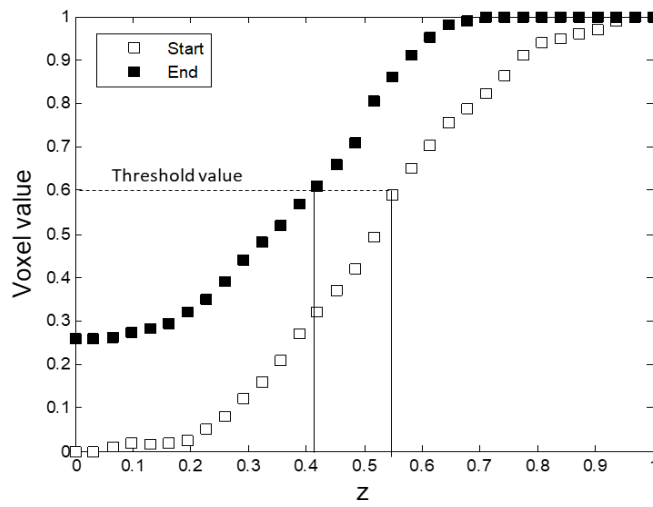
(a)
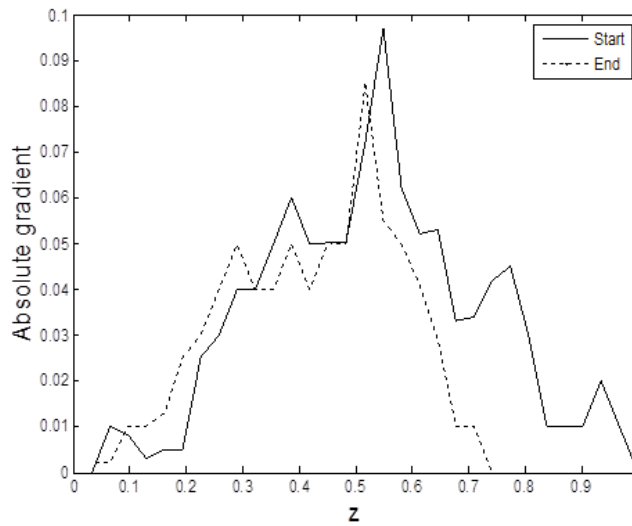
(b)

Figure 7.22 – Voxel value profile for the repeatability test at the start and at the end of the trial (a). The wicking phenomenon causes the profile to vary over time. The absolute gradient (b) profile has a less evident change over the same period of time.

Figure 7.22(a) shows how the profile shifts towards lower z as the moisture travels down between the start and the end of the ECT measurement. This shift, together with the fixed threshold value, causes the interface to be detected further down in the ECT cage, at lower z. The gradient method is less sensitive to this effect, as shown in Figure 7.22(b), where the

absolute gradient is reported for the voxel value, the maximum does not significantly move from the initial location. This characteristic of the method makes it more robust in respect to timing of the measurement: in cases of blockage of production lines ECT would still be able to detect the location of the initial interface up to a limit. Indeed, it is possible to observe a flattening of the profile, therefore it is expected to fail if left for enough time. To test this time limit, one part was left into the cage overnight (approximately 16 hours) after coating. The obtained results are shown in Figure 7.23.
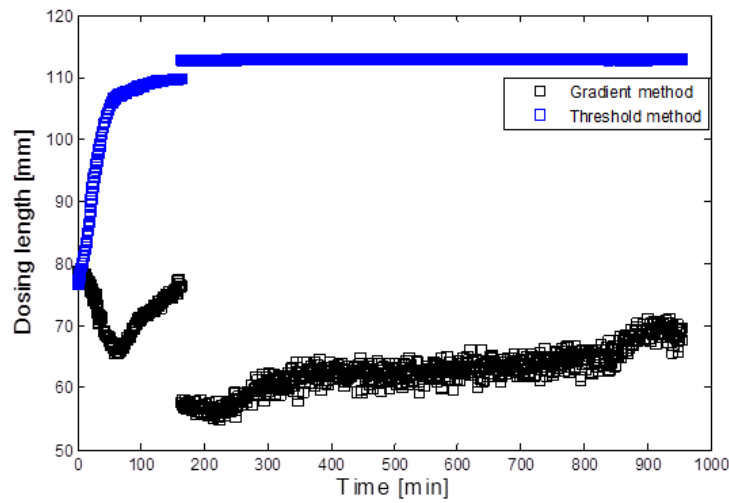
(a)
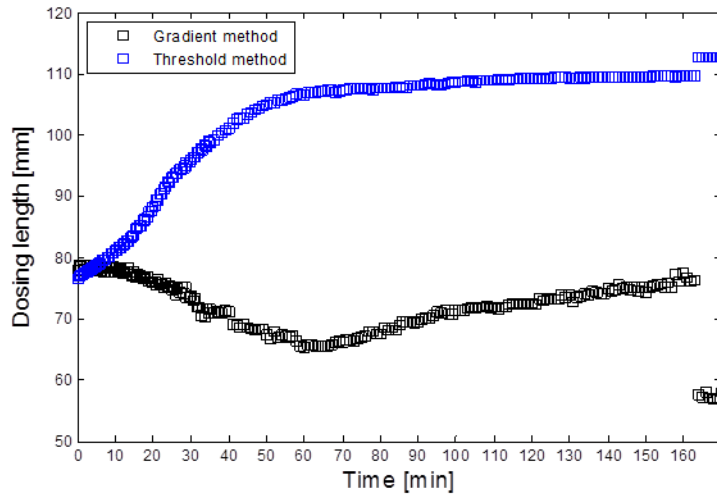
(b)

Figure 7.23 – Dosing length using the gardient and the thresholding method for the whole overnight period (a) and a zoom on the first 165 min (b).

In Figure 7.23 (a) the dosing length is reported for the whole period of 16 hours. Although at the beginning, the two algorithms start from the same dosing, they follow different trends. The dosing length measured by the thresholding method increases over time until it reaches 110 mm, where the sensor region ends and therefore the measured part of the monolith is all wet. The gradient method follows a different path: the dosing length decreases at first, and

then increases until a discontinuity is registered when the moisture travels out of the field of view of the sensor. As predicted, the gradient method fails as the voxel value profile flattens as shown in the example in Figure 7.22(a). Figure 7.23(b) zooms into the first 165 minutes, which is approximately the time required to the capillary creeping to cover the sensing region. For the first ten minutes the gradient method presents a stable measurement of approximately 77.89 mm, while in the same time window the thresholding dosing length increases from a starting length of 76.64 mm to 81.5 mm. Therefore, as observed before, while the threshold value is useful to follow the moisture creeping towards the dry end of the monolith, the gradient approach instead remains more stable for the first minutes, while becoming unreliable as the time between coating and measurement increases.

7.3.3 Plant tests

The tests run on the FastCat production lines in Royston employed ECT and X-ray measurements of both FT and GPF monoliths. In this section, results obtained by the two techniques are compared. Within the ECT results section, prior to the start of the measurement, a study on the stability of the calibration step is carried out. This initial analysis aims to evaluate how the referencing step is influenced by the surrounding "noisy" environment as a production plant. Subsequently, a large sample of monoliths was tested.

ECT results

Reference variability

The quality of the ECT measurement is strongly influenced by the calibration. The calibration, executed on a bare substrate and a fully coated monolith, is also function of environmental variables as humidity and temperature. It could be influenced by other external factors, for example the presence of electromagnetic fields, not uncommon seen the large

electrical and mechanical equipment present on plants. It is important to assess whether during a batch, these variables would cause major oscillation on the measured voltages.

For this reason, a reference library was collected in addition to the usual online reference file. The reference library consisted of two sets of 5 calibration files, taken before starting the online measurement trial and at the end of the day. For each frame, 276 voltages measurements are acquired by the ECT according to the Equation (6.1).

In Figure 7.24 the voltage measurements for the 5 reference files are shown for the low permittivity calibration point (a) and the high permittivity calibration (b).

(a)

(b)
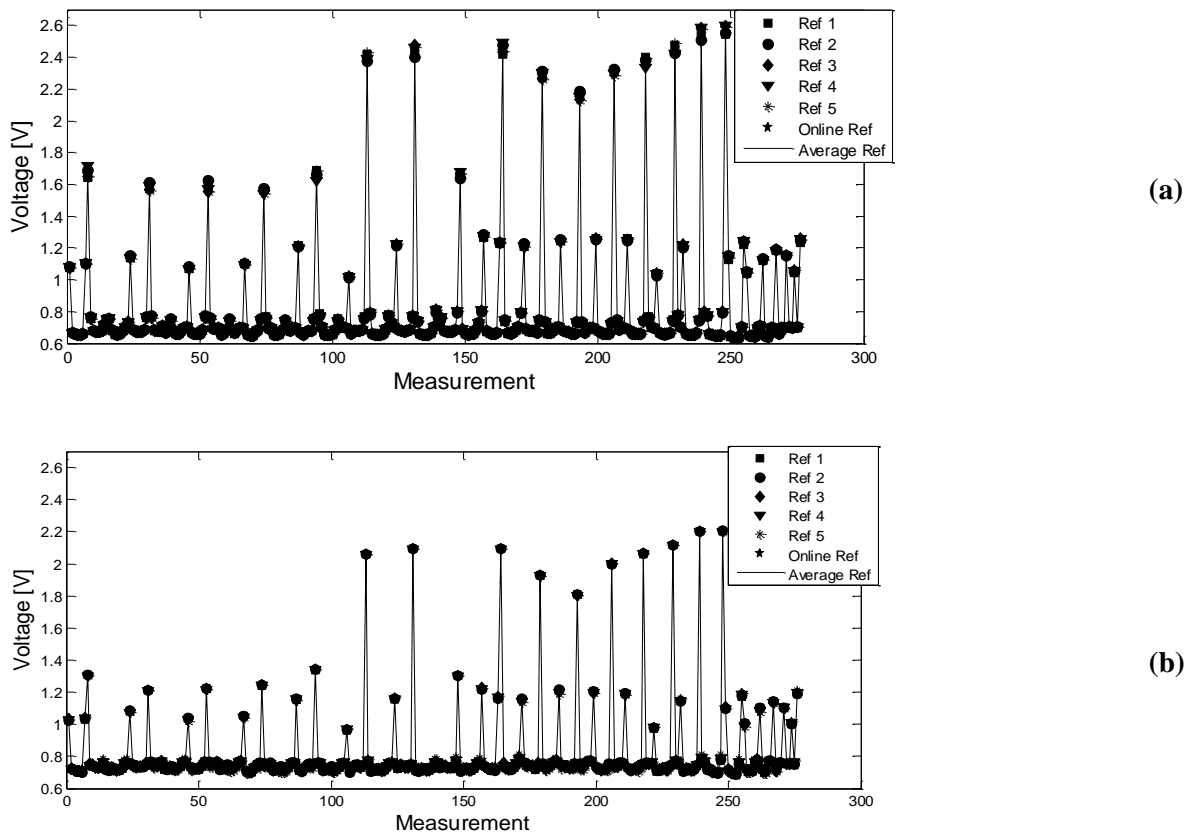
Figure 7.24 – Reference voltage measurement comparison for the low permittivity (a) and high permittivity (b) calibration for five reference dataset, the online reference and their average.

The measured voltages overlap well with each other demonstrating low variability on the calibration. In particular, for the high reference frame, the standard deviation between the five runs is very low, in the order of 10^{-6} V. This is due to the fact that the high permittivity reference is taken on a wet part; the high content of moisture makes it less affected by environmental noise (e.g. handling, air humidity). The latter seems to have a slightly higher influence on the low reference frame (dry part). In this case the standard deviation is in the order of 10^{-3}.

A similar is effect is observed when compared the files obtained at the start and at the end of the day as shown in Figure 7.25.

(a)

(b)
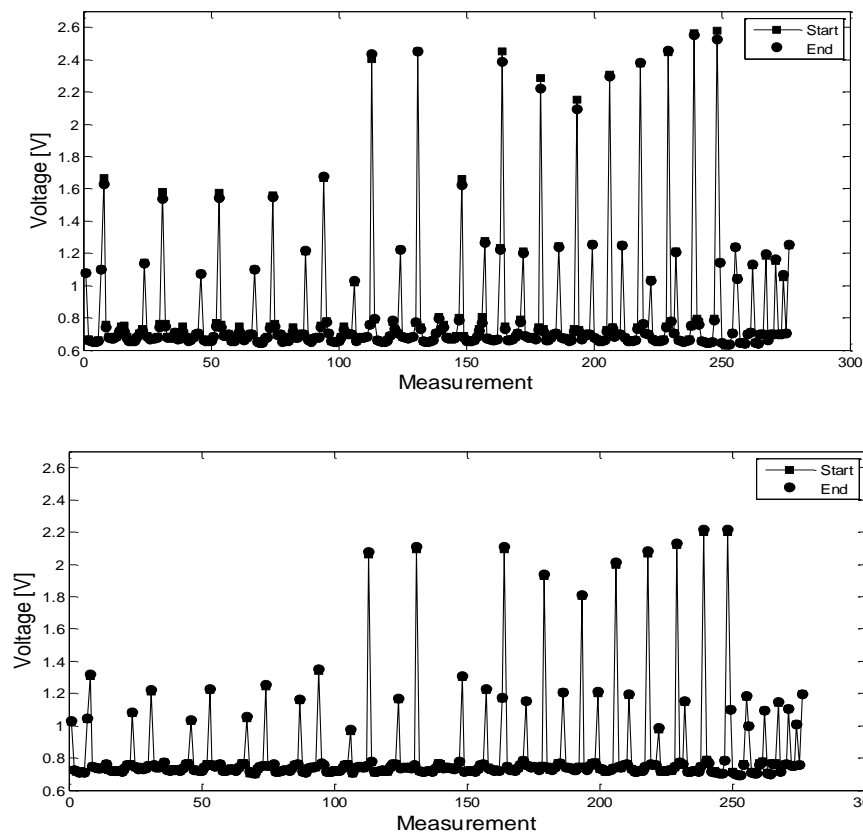
Figure 7.25 – Average voltage measurement comparison Start-End of the trial for low (a) and high (b) permittivity calibration for the online reference file.

The absolute values shown in Figure 7.24 and 7.25 express generally good repeatability of the calibration process, however, do not give information about the influence of those oscillations on the outcome of the trial (e.g. dosing length). This is investigated in Figure 7.26. Three of the reference frames for both sets, the total average and the online reference are used for reconstructing the 3D tomograms. The gradient method was then applied to extract the dosing length for each of them.

(a)

(b)
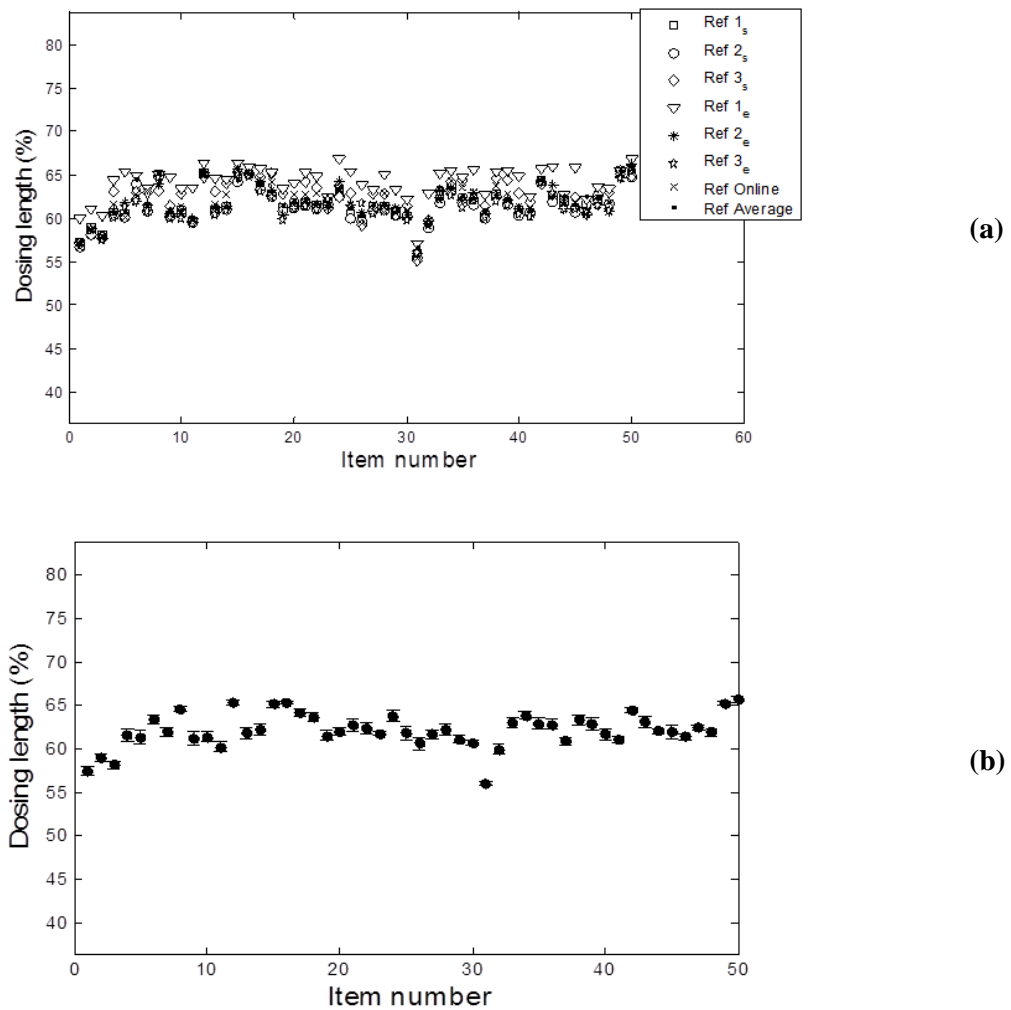
Figure 7.26 – Comparison of dosing length (%) results calculated using 3D ECT with different calibration files taken at the start (s) and end (e) of the trials, the one taken online, and the average reference (a). Average of dosing length (%) calculated with different references with standard deviation bars (b).

A small effect on the inferred dosing length is observed by varying the reference file and re-calculating the reconstruction. This effect is mainly due to the variability in the low reference frame, although from Figure 7.26(b) it is clear that swapping the references does not affect significantly the predicted dosing length. The current low bias may be reduced with automation; the absolute value of the registered signal is low and cables movement caused by manual handling contribute to the variability. Furthermore, the low reference calibration is the easiest to realize as it does not require any processing of the part. From the above it may thus be stated that the observed variations have little influence on the measurement outcome.

Online measurements

In this section, the ECT images are reconstructed using the online reference file. In the first instance, the dosing length was calculated for each of the ten frames taken for each part and the results in dosing length and standard deviation are presented in Figure 7.27.
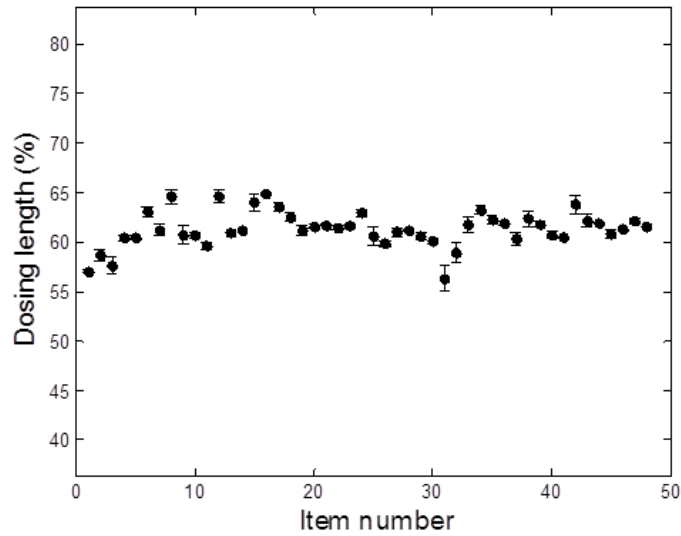
(a)
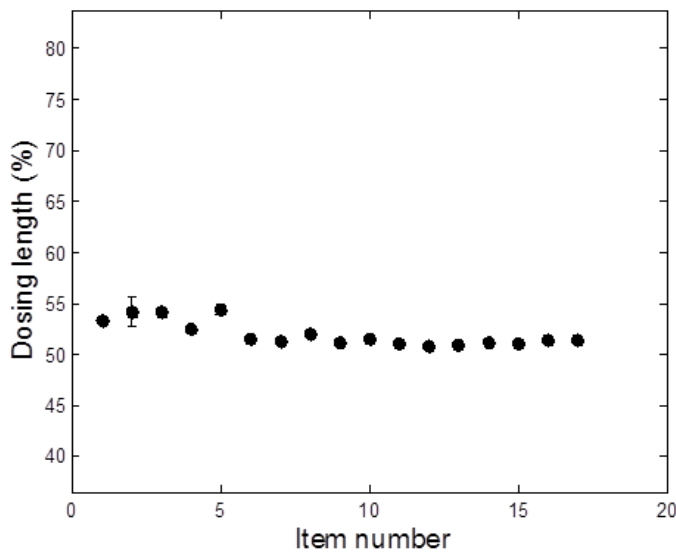
(b)

Figure 7.27 – Averaged height evaluated frame by frame for FT (a) and GPF (b) parts. The dosing length measured using ECT is calculated by applying the gradient method. The error bars show the standard deviation characterising the 30 averaged frames.

The repeatability in detecting the dosing length is very high for both substrates, and is exceptionally high for the GPF, with the exception of the single item n° 2 that presents higher variability within the 10 frames, probably due to the presence of washcoat on the external of the part. This indicates that in eventual online practice only a single measurement is required.

In both trials, a few parts were also scanned twice, at different angles. After scanning the part for the first time, this was turned by 90° and replaced within the sensor for the second scan. The results are showed in Figure 7.28 for both substrates.

(a)

(b)
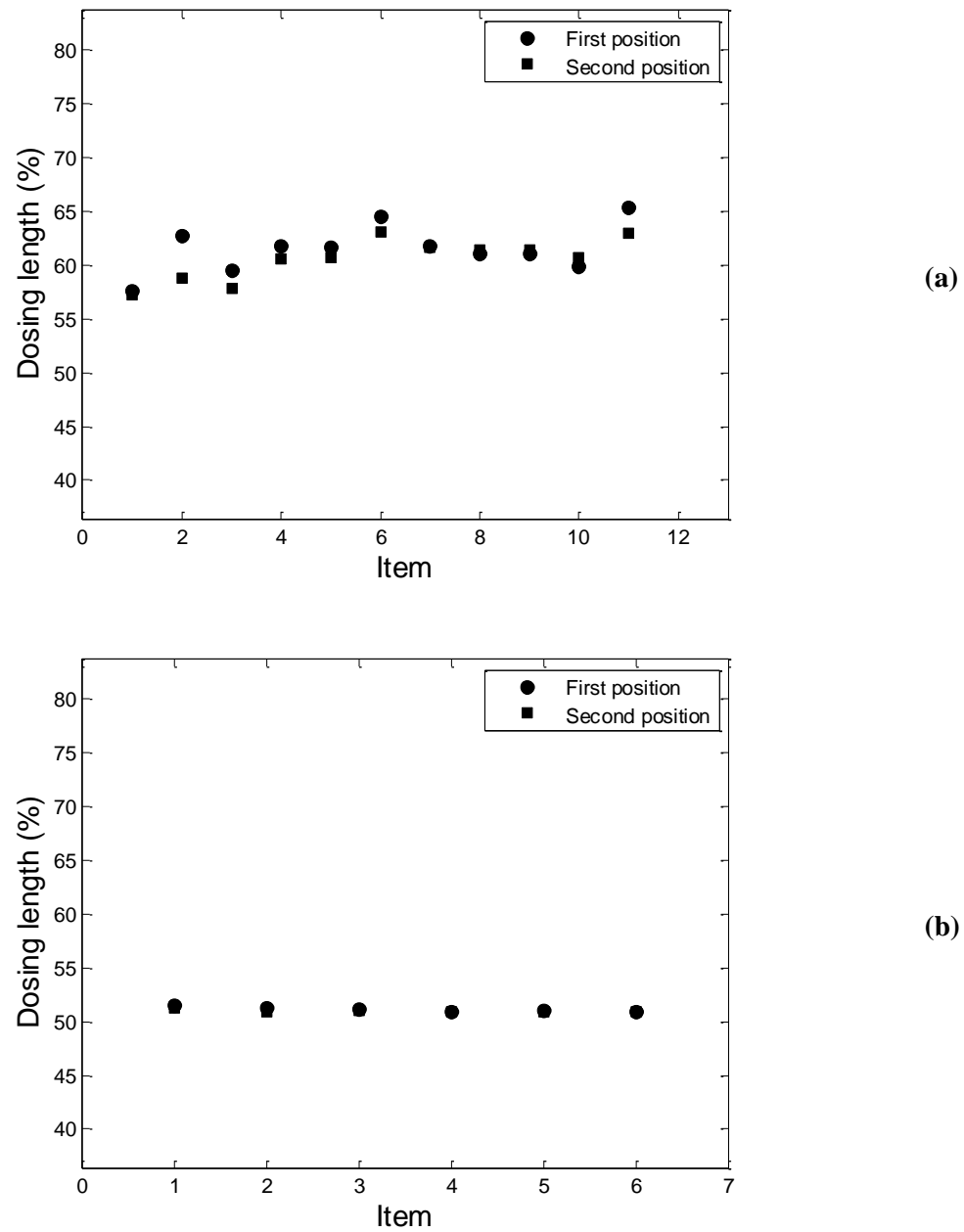
Figure 7.28 – Dosing length comparison of rotated parts for FT (a) and GPF (b) for selected items.

In the first case 7.28(a), there is a slight, although detectable, change in the measured dosing length at different angles, highlighting a certain impact of manual handling on the

measurement. The two scans were taken in sequence; therefore, it is unlikely that creeping effect could be affecting the data between the two scans. The observed effect on FT is not present on the GPF parts where no change is observed when rotating the parts.

X-ray vs ECT comparison

This section is divided in three parts:

- Dosing length comparison, where the ECT predicted dose length and the X-ray measurement, obtained by the software, are compared;

- Flatness comparison, where the regularity of the interface shape is compared between ECT and X-ray. For this measurement, the X-ray scans are post-processed using the same algorithm applied to the ECT to extract the same parameter.

- Images comparison, where the obtained tomograms and scans are visually compared.

Dosing length comparison

X-ray data directly obtained from the software as an output parameter were compared with ECT (processed with the gradient method), in Figure 7.29, where the specifications limits are highlighted for FT, while not disclosed for the GPF batch. The axis limits are chosen to match the sensing region length of the ECT sensor.
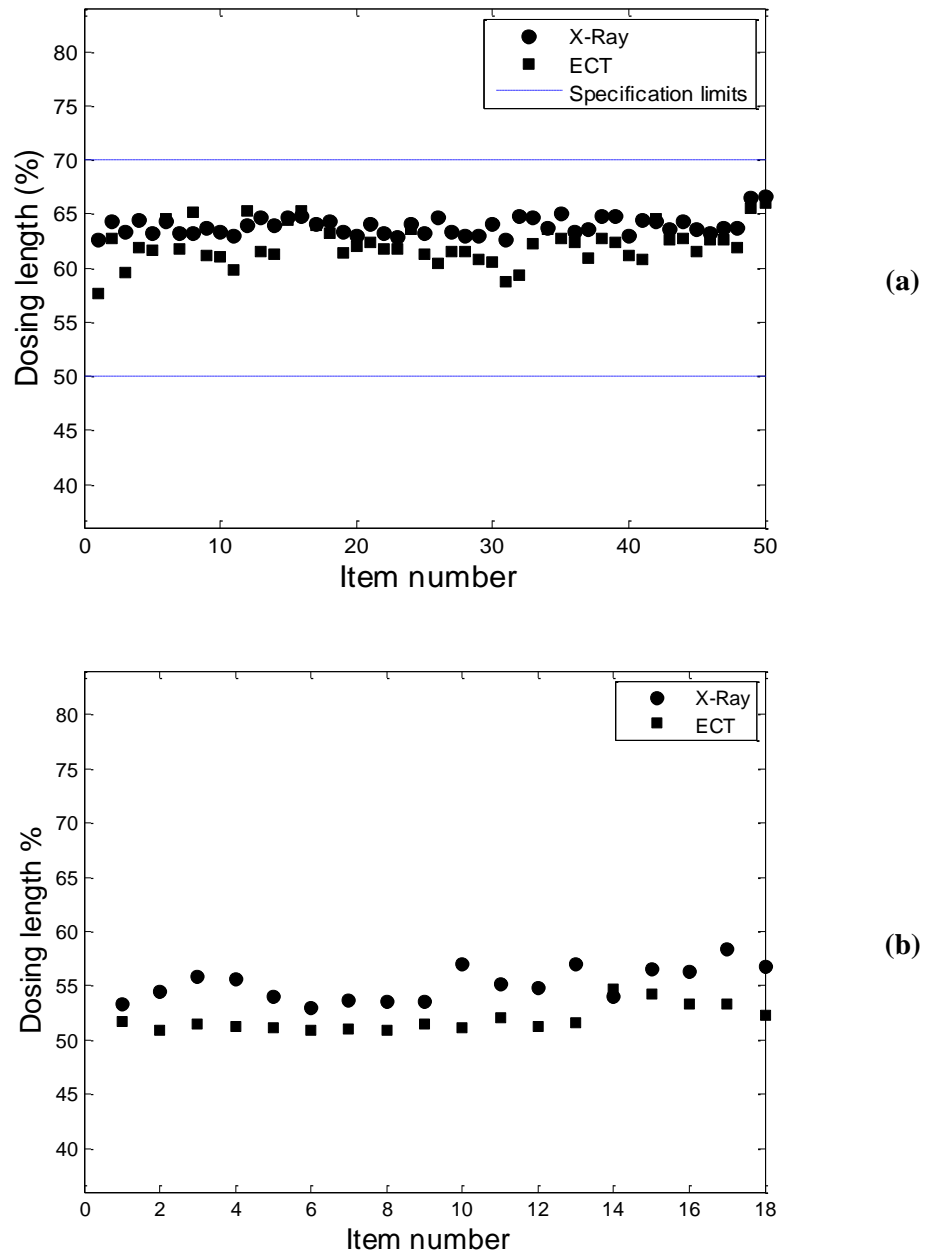
Figure 7.29 – Comparison of dosing length between X-ray and ECT for FT (a) and GPF (b). The same ECT dataset shown in Figure 7.26 are compared with X-ray data.

In the case of FT, all the analysed items are within the specification limits of the batch, according to both techniques. In Figure 7.29 it is noticeable how ECT data lead, most of the time, to a shorter dosing length measurement than the X-ray. The reasons for this offset may be due to the order by which the measurements were taken: ECT scans were taken first and in

the second place the parts were manually taken to X-ray machines, not located by the line. On some occasions, a few parts were removed from the line, scanned using the ECT in sequence and then taken to the X-ray machines. As observed in §7.3.2 this may cause the wicking to take place, therefore increasing the detected dosing length.

Figure 7.29 suggests there is a small but detectable difference between the dosing lengths as measured by the two methods: ECT tends to indicate a shorter length than X-ray. Whether this offset is random or systematic is analysed in Figure 7.30 where a probability density function of the error is plotted. The definition of the error is described in Equation (7.5).

$$Relative\ error = \frac{L_{ECT} - L_{Xray}}{L_{Xray}} \qquad (7.5)$$

In these graphs the dosing length predicted by the ECT is compared to the X-ray, the accredited and applied measurement technique on plant. This comparison highlights the difference of the length calculated by the two techniques.
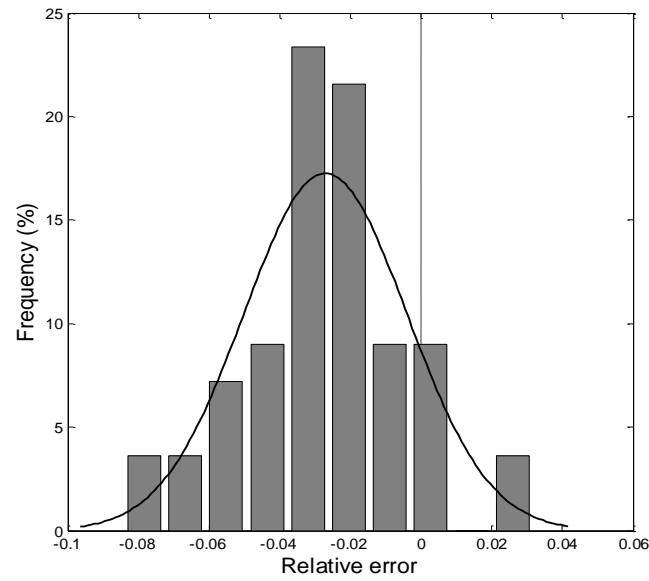
(a)
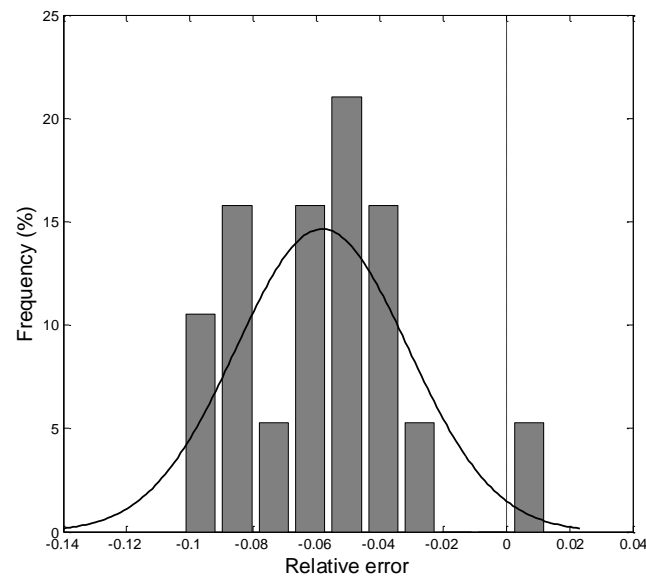
(b)

Figure 7.30 – Probability density function of the relative error as for (7.5) for FT (a) and GPF (b).

In Figure 7.30 both plots show how the probability density function of the error can be well approximated by a Gaussian distribution. This assumption is verified in Figure 7.31, in which a normal probability plot is drawn. The assumption of normal distribution is considered valid when the points aligned with good approximation on a straight line (Chambers, J., 1983).
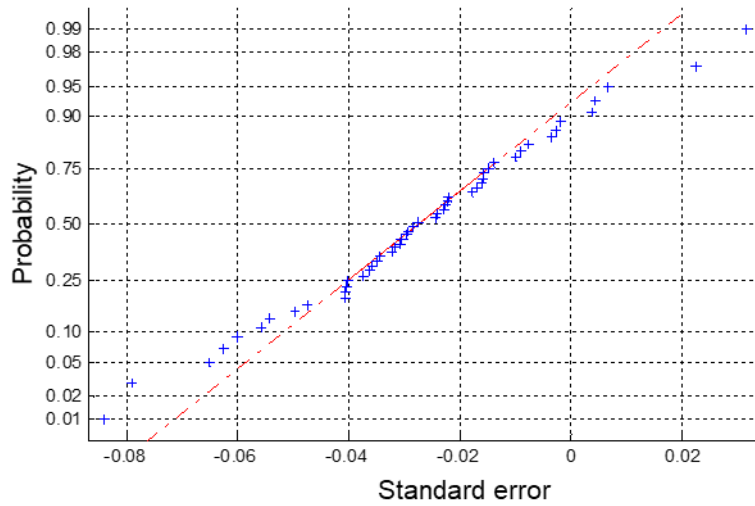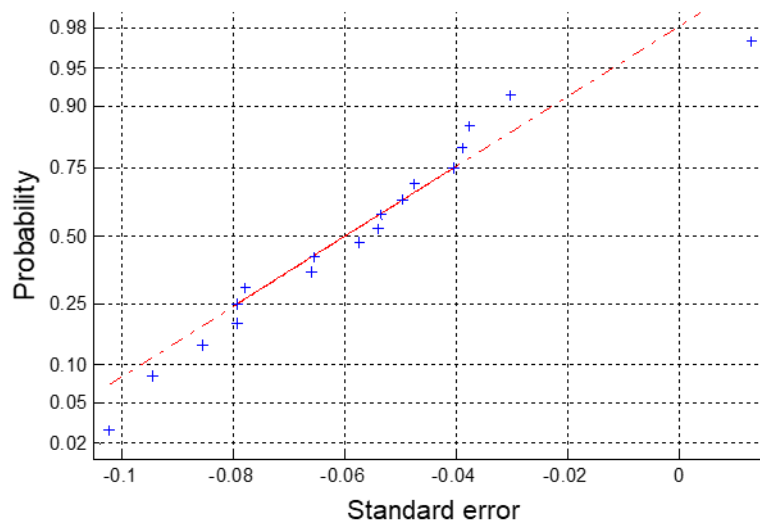
Figure 7.31 – Normal probability plot for FT (a) and GPF (b) in reference to the Gaussian curves reported in Figure 7.30.

The normal distribution assumption is a powerful tool from the data analysis point of view because the offset can be recognized as systematic and therefore predictable. In Table 7.2 the standard deviations and means of the two data sets are summarised.

Table 7.2. Mean and standard deviation for the Gaussian curve drawn in Figure 7.30, representative of the relative error between X-ray and ECT images as for (7.5).

Case	Mean	Standard deviation
FT	-0.0271	0.0229
GPF	-0.0581	0.0264

In the FT case the observed offset is very small ($< 2.8\%$ or approximately equal to the standard deviation) between ECT and X-ray dosing lengths. This value could be used as an offset parameter or correction factor to the ECT predicted dosing length with high confidence (given by the low standard deviation); it will lead to increased correspondence of the ECT and X-ray dosing length detection.

The detected value for GPF is higher in absolute value, but this may be due to the difficulty of the detecting dosing length from the X-ray data with precision, or most likely to a higher effect of capillary creep of the dosing front in filters than FT, caused by different pore dimensions. The standard deviation is consistent with this hypothesis as it is almost identical to the FT case, suggesting that the obtained measurements are characterised by the same high level of consistency.

Flatness comparison

In this section, 3D ECT and X-Ray images are processed and compared in terms of flatness of the interface. The MDXi software gives in output only a value for the dosing length, therefore, for this comparison, the image data processing developed for ECT is applied to the X-Ray images. Each column of pixels is interrogated, and the interface is located on the local maximum gradient. In this way, the two techniques are compared under the same data

interrogation methodology. Figure 7.32 shows how the gated images look before and after applying this binary gating method.
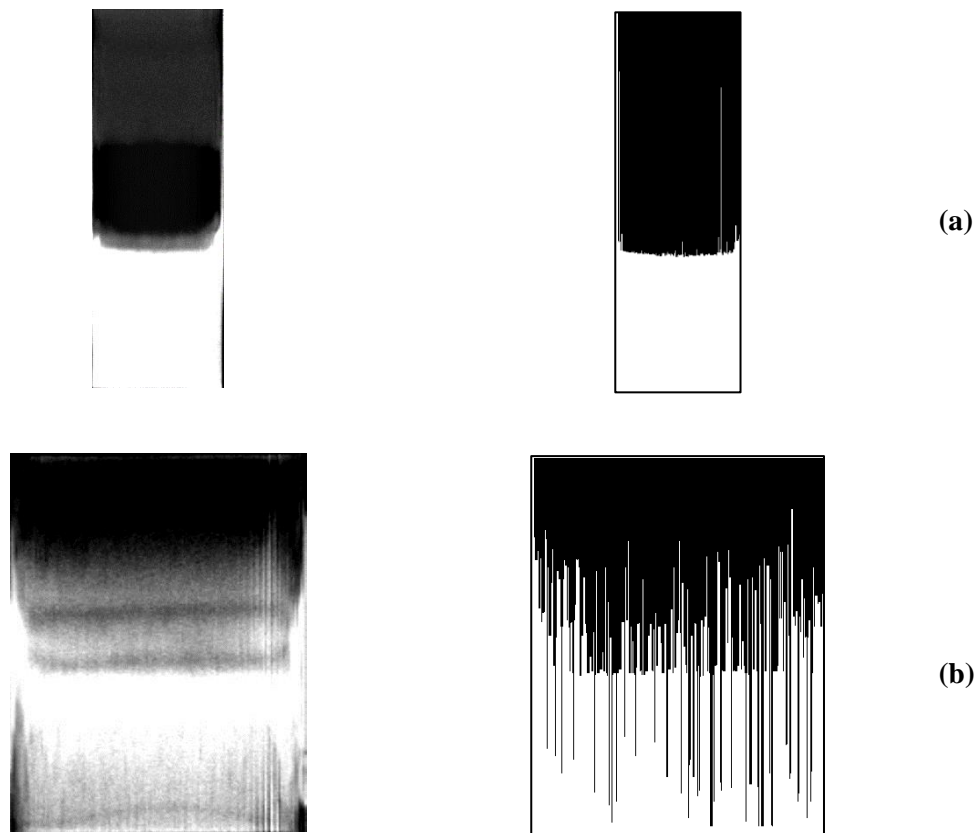
Figure 7.32 – Raw X-ray images (left) and binary gated images after applying binary gating column-by-column using the maximum gradient approach (right) for FT (a) and GPF (b).

The results of this process highlight the high quality of X-Ray images obtained for the FT parts when compared with the GPF scans that present a more scattered profile.

The obtained images are used to evaluate the dosing length of the parts and in Figure 7.33 they are shown against the one obtained with ECT, with error bars representing the standard deviation of the detected heights for each column of pixels (or voxels in the case of ECT).
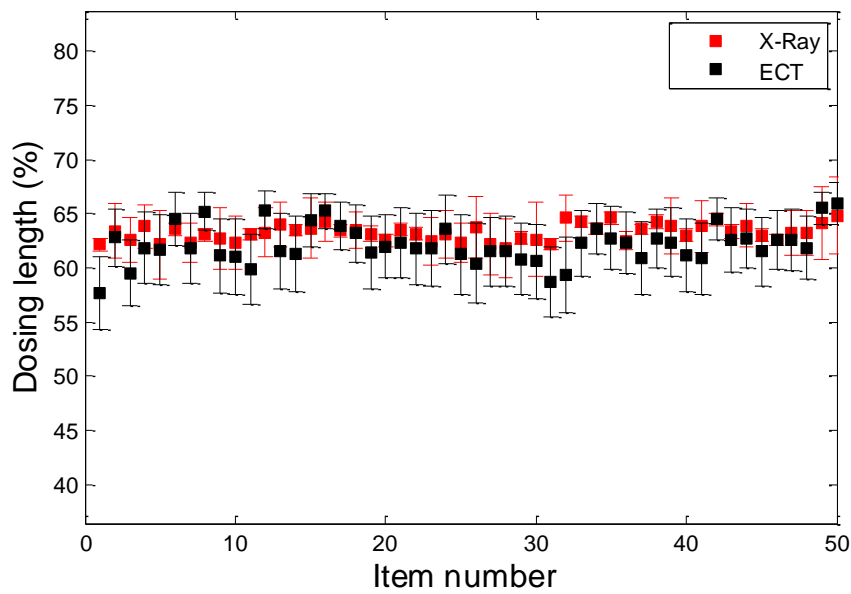
(a)
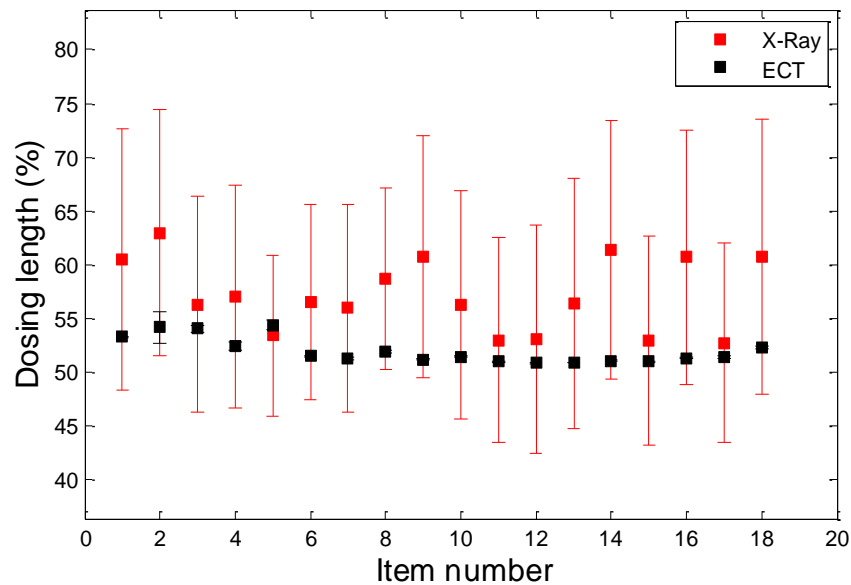
(b)

Figure 7.33 – Dosing length comparison between X-ray and ECT applying the gradient gating method with error bars (expressing dosing length variability across the image) for FT (a) and GPF (b).

The error bars plotted along with the dosing length for X-Ray in the FT case express how flat and sharp the interface is: the errors are small. For FT, the ECT images present slightly higher but comparable values of curvature to X-ray ones as it can be noted observing the relative length of error bars in Figure 7.33(a). In the case of GPF (Figure 7.33(b)), instead, ECT

exhibits a smaller standard deviation compared to X-ray, hence, a flatter surface. This was observed above in Figure 7.32(a) were the GPF binary gated image showed a strongly uneven profile, caused by the low contrast in the raw image.

Images comparison

In the following Tables (7.3, 7.4) some of the ECT and X-ray images are visually compared. Reported images are sampled tomograms from figure 7.29 where the numerical comparison is carried. All images are included in Appendix C.

Table 7.3. **X-Ray vs. 3D ECT (using gradient method) images for FT parts. Reported tomograms are a pictorial representation of the data in Figure 7.29 (a). The comparison shows the different kind of images obtainable by X-ray and ECT.**
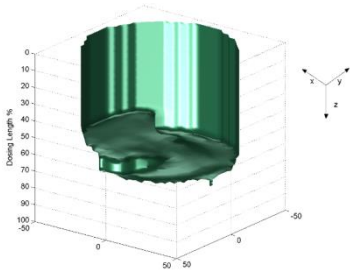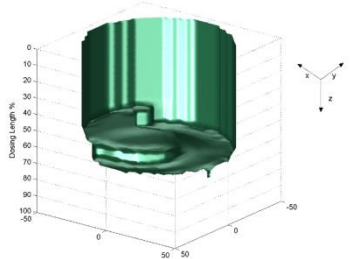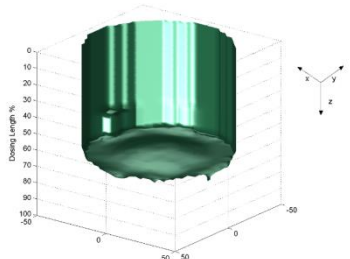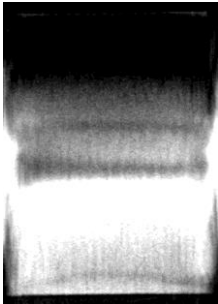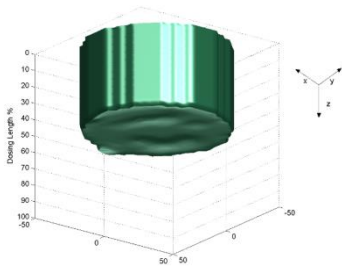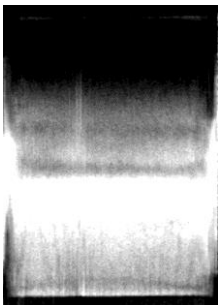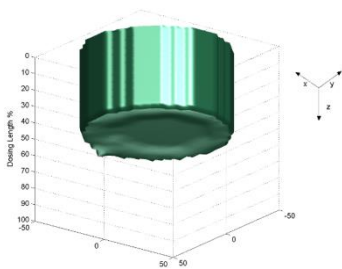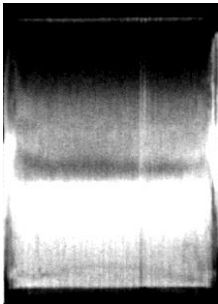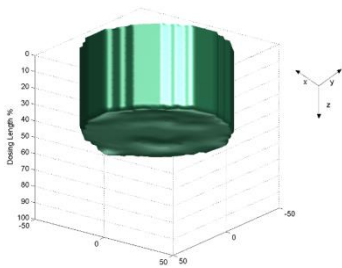
Item nr.	X-Ray		ECT	
	Image	Dosing (%)	3D image	Dosing (%)
10		63.3		61.1
20		62.9		62.0
50		66.6		65.9

Table 7.4. X-Ray vs. 3D ECT images for GPF parts. Reported tomograms are a pictorial representation of the data in Figure 7.29 (b). The comparison shows the different kind of images obtainable by X-ray and ECT.

Item nr.	X-Ray		ECT	
	Image	Dosing (%)	3D image	Dosing (%)
6		57		51.6
15		55.6		51.2
18		53.3		51.7

Tables 7.3 and 7.4 visually and numerically compare the dosing length evaluated by the two different techniques on the same parts. In the FT case (Table 7.3) X-Ray images show mostly flat profiles; defects seem to be concentrated towards the periphery of the parts, where the coating length is noticeably lower. Although this can be due to the beam hardening effect (Ketcham and Carlson, 2001) causing artefacts at the periphery of the item. 3D ECT does not present in all cases symmetric profiles (Appendix C), rather else it discloses less flat profiles. The situation reverses when looking at Table 7.4 where the X-Ray images are difficult to interpret and present a less clear interface between the coated and uncoated sections. In this case, 3D ECT images show flat profiles generally with no visible defect on the coating profile.

Overall, the obtained images allow to state that there is a very good match between the X-ray existing technique and 3D ECT. Further improvements on the latter can be achieved other than with automation, therefore acting on SNR, also with little modification in the existing reconstruction protocol.

7.4   <u>Conclusions</u>

3D Electrical Capacitance Tomography was tested as a potential measurement technique in real time for coating depth detection on a Clean Air production line. ECT is an attractive potential replacement for the current X-ray system with its expected ability to monitor every part with near real time output as well as anticipated significantly lower cost. The data processing described in Chapter 6 was used to evaluate the dosing length and a GUI was created to demonstrate ease of visualisation and data extrapolation for plant applications.

This work had a first step conducted at lab scale in which ECT has been challenged in detecting defects in the dosing length and compared with X-ray, showing capability to

visualise common failures in the coating process. Although X-ray has a higher spatial resolution, the advantage of ECT in comparison with X-ray is the fast time response but also the possibility to cover a three-dimensional space rather than a planar projection.

The technique was then tested for repeatability. Limitations about the time between the coating application and the measurement were identified. The gradient approach was found more stable for measurements carried out in a time frame of approximately 10 minutes, while the thresholding approach is affected by the diffusion of moisture (wicking) along the part. Although this represents an issue for on-plant application, this method could be used to study the dynamic of wicking. For the purpose of comparing ECT with the X-ray technique, though, the gradient approach was used.

A number of cordierite half coated monoliths have been tested (50 Flow Through parts and 18 Gasoline Particulate Filters) on the FastCat Clean Air (JM) production plant in Royston. The items were collected from the line after the coating process and scanned both with the 3D ECT and with the X-Ray machines (3DX-ray) used on plants. 3D-ECT repeatability, sensitivity to ambient noise and external factors were also investigated. The comparison with X-Ray shows high grade of accuracy of ECT technique which can produce reliable dosing length 3D information by taking one frame in a time window of 0.1-0.2 s. Dosing length and curvature data show similar results for FT parts in which X-Ray exhibits flatter and sharper interfaces. For GPF parts ECT seems to produce higher quality images and less curved profiles. Specification limits were only known for FT parts and all the processed parts fall into the limits and would result in a pass. ECT was proven to be usable in plant environment and to give 3D reliable information regarding the coating length. This study confirms the reliability of 3D ECT as a measurement technique that produces measurement values comparable to the X-ray technique.

7.4.1 Recommendations

The analysed dataset offers a statistical relevant comparison between the two techniques. The fast-time response, 3D visualization, lower cost and lower magnitude of energy involved in the measurements represent a set of possible desirable improvements to existing technology. Specifically, the following are recommended to move the technique towards commercial exploitation

- Tests for Clean Air to date have all used 5.66" (143.8 mm) substrates. Smaller substrates have been tested, but not rigorously. Sensor cages for representative smaller and larger substrates should be used for validation tests.

- The reliability of the hardware (purchased from Industrial Tomography Systems Ltd, Manchester UK) should be assessed for in-line process application. The device is robust for "research use" but may require up-grading for plant application and required reliability.

- Improvements in the reconstruction and data processing are achievable through collaboration with tomographic system supplier; it is believed this will lead to increased performance.

- There are clear concepts on how to integrate the measurement into a coating line, and the use of robotics to present the part to the sensor cage. Prototypes will be required to demonstrate this.

7.5 <u>Nomenclature</u>

e_V Volumetric error

D   Sensor diameter, m

g Interplane gap, m

H Sensing height, m

h   Electrode height, m

E x-ray energy, eV

I X-ray intensity

N Number of measurements

p Projection function

x, y, z Geometrical coordinates, m

ε Electrical permittivity, F m^{-1}

χ Distance of travel, m

ω Linear attenuation coefficient, m^{-1}

8.
Overall conclusions

The research in this thesis investigates the use of inline measurement techniques such as electrical tomography and acoustic emission for real time in-situ monitoring of multiphase manufacturing processes. The industry-driven objective of the work was to improve knowledge and capabilities in measurement and control within JM. It is indeed essential that better monitoring tools are deployed in the next few years to put into practice the smart manufacturing concept. The present work has looked at innovative applications of existing measurement techniques, aiming to develop data processing approaches to extract useful quantitative information. The spectrum of investigated combinations of technique in process operations is wide, including "wet" and "dry" conditions. This gives further proof of the wide set of scenarios present in the modern factories and the huge room for improvement in the area.

This work has led to journal publications and conference presentations as well as to plant trials and business driven studies, both of which demonstrate the impact achieved by the conducted work.

8.1   <u>Conclusions Overview</u>

Modern factories are evolving to embody the smart manufacturing concept. Data are gaining more and more importance, and their availability in real time is a requirement for guaranteeing product quality, reducing waste to a minimum and maximising yields. This need has been the driver for the research presented in this thesis.

A variety of in situ measurement techniques have been investigated with the broad aim of increasing the expertise within Johnson Matthey and to offer possible solutions in the process measurement and control field. The investigated measurement techniques are characterised by their non-destructive, non-intrusive nature together with their fast-response and low-cost attributes. The use of electrical tomography and acoustic emission in the chemical industry, however, has been limited so far, because of their complex nature and their still evolving capabilities in solving manufacturing related issues. Together with dealing with understanding the physics of the measurement, and processing the detected response, an additional challenge is to evaluate the transferral of the techniques from a laboratory to a plant environment. It is also critical to develop a clear and easy to use tool for supporting decision making (from operators or machines). This thesis aims, therefore, to provide both an overview of fundamental theory behind the analysed measurement techniques and investigate their response, bearing in mind the final goal of inline implementation.

In Chapter 1, an introduction describes the context that provides the foundation of this thesis. Together with a brief description of Industry 4.0, an overview of the most common in situ measurement techniques and their applications is given. The focus is kept on the investigated techniques: Electrical Resistance Tomography, Electrical Capacitance Tomography and Acoustic Emission. JM divisions are described to emphasise the wide range of formulated products and intermediates dealt with. The structure of this thesis and the overall and specific

objectives are described. In addition, publications resulting from this work are reported. Each of the experimental chapters describes in detail the theory behind the used techniques and its specific aim.

In this final chapter, the findings and overall conclusions of the conducted research are summarised, and future steps are discussed.

8.2 **Reflection on thesis aims**

(1) Increase JM expertise in the field of process tomography and in-line measurement methods to extract plant relevant information in a broad range of applications.

The conducted work investigated electrical tomography and acoustic emission techniques that had previously found little industrial application within the Company, the exception being previous EngD studies.

ERT was used for Gas-Liquid applications and liquid blending studies. It has proven a powerful technique to evaluate gas-holdup in multiphase stirred tanks and level of mixing in cases of non-Newtonian fluid in pipelines. The obtained results on fundamental studies, aroused interest within Clean Air, Efficient Natural Resources and Health business units.

ECT has constituted object of studies especially for coating applications, being able to obtain dosing length information in a faster way than the current practise on plant (X-ray tomography). Furthermore, ECT has been used for evaluating powder segregation in an FT4 Freeman Rheometer chamber, constituting an extension of the ECT applications in a notoriously challenging condition to monitor.

Acoustic Emission has been generally used in the literature for structural and civil engineering tasks but has the potential to gather useful information also in chemical plants. It was used in combination with machine learning algorithms on a well-known unit operation, already object of study of this thesis, of gas-liquid mixing. The use of a single non-invasive inexpensive sensor achieved high level of accuracy in identifying gas-liquid mixing regimes, constituting an encouraging first step towards the use of AE in similar applications.

(2) Develop data processing approaches for extracting key parameters to support decision making on plant.

Electrical tomography and AE are well-known to be data rich techniques. Whereas process tomography gives in output a tomographic image, AE offers a broadband acoustic spectrum; in both cases the information may be not so easy to read. In this thesis, the focus towards the in-line implementation has also interested the data processing and the output of the used techniques.

ERT using the linear probe was considered at first a qualitative technique, capable of producing "nice pictures" but limited when it came to extract quantitative studies. The use of Maxwell law in the case of multiphase mixing (Chapter 2) demonstrated instead that it is possible to extract gas-hold up values at different mixing regimes. The axial profiles also give insight into the axial distribution of gas within the tank.

In the case of liquid-liquid blending in pipelines, the use of the Areal method (Chapter 4), in different fashion, allowed to evaluate the mixing performance, although, highlighting limitations related to the resolution of the technique.

ECT was extensively tested with phantoms for implementing a data processing method that could satisfy the needs of immediate response and ease of reading. In the case of dual planar ECT for powder mixing, the average normalised permittivity was used to monitor powder blending/segregation in comparison with the total energy obtained by the FT4 rheometer.

For the catalytic converter application, a gradient method was developed to extract the dose length achieved during the coating operation. This approach, in contrast to the traditional thresholding method, does not need a priori information and it was firstly tested on glycerol (or IPA) – air interphases before being applied on industrially relevant products. A GUI was also implemented, as part of this study, to showcase a decision-making tool achievable by using ECT for such applications.

AE was tested on gas-liquid mixing, with the objective to identify the different mixing regimes within the agitated vessel. For achieving this information, a range of machine learning classification algorithms were tested. The study identified the Support Vector Machine as the best performing method. Although the Acoustic spectrum has multiple features the output of the measurement was thought to give a single parameter identifying the mixing condition.

(3) Extending work done at laboratory scale to industrial environment to demonstrate capabilities and opportunities of implementation.

Although a few tests were run using ERT and AE on bigger scales, this point is concerned in particular with the application of ECT for the coating process, a critical step in the manufacturing of automotive catalytic converters. The three-dimensional tomographic technique was tested on JM production plants both in Royston (UK) and North Macedonia

(MK) for both Flow-through monoliths and Gasoline Particulate filters. The results obtained by using the ECT were comparable with the ones observed by the X-ray scanner, the current quality control method in production. As an outcome of this study, ECT is now being investigated internally as a potential supporting technique alongside X-ray, because of its potential to monitor 100% of the produced parts.

8.3   Discussion on business case

The background for the business case of this thesis was explained in Chapter 1. Contextually, it was outlined that, whilst the techniques and methods covered in this thesis targeted specific applications, the project aimed to enhance the research in the PAT field within JM. This was achieved, through a wide number of collaborations entertained across different business units within the company. Broadly, the knowledge within the company on the investigated methods has improved, as well as the opportunity to meet some of the monitoring and control needs.

The use of ERT was not new to JM. Previous studies (Clark, 2016; Oguh, 2012) had looked at this technique to monitor multiphase mixing within precious metal refining processes. The conducted work extended the previous steps and increased confidence that quantitative information characterising the system could be extracted using ERT in stirred tanks. This work not only looked at the traditional batch mixing processes, but also demonstrated, although with some limitations, the opportunity to use ERT for continuous mixing processes in pipelines. This perspective put ERT in a continuously evolving light that, besides the above mentioned metal refining processes, can be of interest for bioreactors (fermenters) and battery material production processes, respectively within Health and New Market divisions.

Unlike ERT, the 3-D ECT was in a less advanced state at the start of the project. The technique constituted object of previous study within JM (Clark, 2016), but only in the traditional bi-dimensional fashion and on fundamental development, without directly involving formulation process studies. Contextually with the start of this work, the technique was upgraded to 3-D by the manufacturer, and the opportunity to target the catalytic converter production was identified. The technique was tested on phantoms and data processing approaches were developed before conducting in situ experiments on process intermediates. Thanks to these tests, opportunities for improving the techniques were identified. At the same time, JM was given an additional tool to be exploited in terms of improving and potentiate the monitoring capabilities on catalytic converters production.

The use of Acoustic Emission had not found, prior this study, particular interest within the company. Aside the utilisation of this technique, also the use of machine learning tools was not investigated before in relation to the measurement and control field. The conducted work looked at empowering the AE data processing with advanced statistical and AI tools. Although the specific case study is interesting for the Health sector and precious metal refining, the combination of such computer science tools with measurement techniques represent an opportunity for the whole strive towards the smart manufacturing realisation.

8.4   Future work

One of the outcomes of the conducted work is the increased interest within the company in the measurement and control field. A further EngD project has been funded and together with two new research engineers will form a Measurement and Control core science group within JM. Furthermore, JM is empowering its IT to support research and development in the field. This shows that the digitisation process is taking place and that more multidisciplinary work needs to be done to progress in this direction.

In regard to the fundamental work that could be beneficial for the company in the short term, a number of future work points are hereby outlined:

1) Implementation of 3-D ECT on plant – the conducted work has demonstrated the capabilities of the electrical tomographic techniques in terms of speed and accuracy of dosing length detection. Nonetheless, for progressing with the industrialisation of the method, work needs to be carried out in collaboration between the company and the supplier ITS Ltd. In its current state, the 3-D-ECT apparatus is a research toolbox, not robust enough for guaranteeing the reliability required on a production site. It is, therefore, recommended that JM collaborates with the supplier for upgrading the instrumentation hardware as well as tailoring the digital response to the required quality and measurement standards. Whether this collaboration will take place is a strategic decision belonging to the Clean Air business unit.

2) Scale-up study using ERT on multiphase systems – at the end of this work, a number of different scales linear probes have been designed and manufactured. ERT has already been tested using the traditional circular cage sensor geometry at large scales, although always remaining purely an investigation tool with no chances of actual industrial deployment. The objective of a scale up study using the linear probe geometry is to make use of the developed study and data processing at plant scale.

3) Acoustic emission tests on bigger scale – similarly to the previous point, the objective is to empower industrial plants with inline suitable techniques. To this end, it is necessary to conduct tests at larger scale in controlled conditions to

identify opportunities and limitations offered by the development method involving AE for multiphase mixing

4) Combining AE and ERT using ML – as discussed in the Chapter 1 of this work, Industry 4.0 means also combining information from different sources for creating holistic models that can represent the physical systems. In this case, ERT and AE were used to monitor the same unit operation. This can constitute a stimulating opportunity to combine two data rich measurement techniques with AI algorithms to improve real time monitoring.

5) AE for powder processing – during this work, a few tests were run applying AE (using the same apparatus described in Chapter 3) for monitoring processes involving powders. The preliminary observations reveal potential for the technique to monitor milling processes, as a condition monitoring tool but also for end point detection. Another interesting process to monitor would be granulation, for which there is already some work in the literature (Whitaker et al., 2000) suggesting suitability of the method.

9.
References

Abdullah, B., 2017. Evaluation of gas–liquid mass transfer in gas-induced stirred tank reactor using electrical resistance tomography. Journal of Chemical Technology & Biotechnology 92, 2123–2133. https://doi.org/10.1002/jctb.5220

Abdullah, J., Mohd, S., Shari, R., Hassan, H., Mahmood, A.A., 2010. X-Ray Computed Tomography for Visualising Inner Structures of Industrial Materials (No. INIS-MY--2012-108). International Nuclear Information System, Bangi, Malaysia.

Acres, G.J.K., Harrison, B., 2004. The Development of Catalysts for Emission Control from Motor Vehicles: Early Research at Johnson Matthey. Topics in Catalysis 28, 3–11. https://doi.org/10.1023/B:TOCA.0000024329.85506.94

Addali, A., Al-lababidi, S., Yeung, H., Mba, D., Khan, F., 2010. Acoustic Emission and Gas-Phase Measurements in Two-Phase Flow. Proceedings of the Institution of Mechanical Engineers, Part E: Journal of Process Mechanical Engineering 224, 281–290. https://doi.org/10.1243/09544089JPME359

Alberini, F., Simmons, M.J.H., Ingram, A., Stitt, E.H., 2014a. Use of an areal distribution of mixing intensity to describe blending of non-newtonian fluids in a kenics KM static mixer using PLIF. AIChE Journal 60, 332–342. https://doi.org/10.1002/aic.14237

Alberini, F., Simmons, M.J.H., Ingram, A., Stitt, E.H., 2014b. Assessment of different methods of analysis to characterise the mixing of shear-thinning fluids in a Kenics KM static mixer using PLIF. Chemical Engineering Science 112, 152–169. https://doi.org/10.1016/j.ces.2014.03.022

Alcalà, M., Blanco, M., Bautista, M., González, J.M., 2010. On-line monitoring of a granulation process by NIR spectroscopy. J Pharm Sci 99, 336–345. https://doi.org/10.1002/jps.21818

Aldrich, C., Theron, D.A., 2000. Acoustic estimation of the particle size distributions of sulphide ores in a laboratory ball mill. J. S. Afr. Inst. Min. Metall. 100, 243–248.

Ali Othman, N., Takei, M., 2015. 24 - Application of tomography in microreactors, in: Wang, M. (Ed.), Industrial Tomography. Woodhead Publishing, pp. 667–692. https://doi.org/10.1016/B978-1-78242-118-4.00024-1

Allied Market Research, 2018. Automotive Catalyst Market Size & Share, Industry Forecast [WWW Document]. URL https://www.alliedmarketresearch.com/automotive-catalyst-market (accessed 6.28.19).

Al-Masry, W.A., Ali, E.M., Alshebeili, S.A., Mousa, F.M., 2010. Non-invasive imaging of shallow bubble columns using electrical capacitance tomography. Journal of Saudi Chemical Society 14, 269–280. https://doi.org/10.1016/j.jscs.2010.02.022

Al-Masry, W.A., Ali, E.M., Aqeel, Y.M., 2005. Determination of Bubble Characteristics in Bubble Columns Using Statistical Analysis of Acoustic Sound Measurements. Chemical Engineering Research and Design 83, 1196–1207. https://doi.org/10.1205/cherd.05014

Al-Salemi, B., Ayob, M., Noah, S.A.M., 2018. Feature ranking for enhancing boosting-based multi-label text categorization. Expert Systems with Applications 113, 531–543. https://doi.org/10.1016/j.eswa.2018.07.024

Alvarez, M.M., Muzzio, F.J., Cerbelli, S., Adrover, A., Giona, M., 1998. Self-similar spatiotemporal structure of intermaterial boundaries in chaotic flows. Phys. Rev. Lett. 81, 3395–3398. https://doi.org/10.1103/PhysRevLett.81.3395

Anderson, D.K., Tozer, R.C., Freeston, I.L., 1995. Analytic solution of the forward problem for induced current electrical impedance tomography systems. IEE Proceedings - Science, Measurement and Technology 142, 425–432. https://doi.org/10.1049/ip-smt:19952133

Apte, C., Damerau, F., Weiss, S., 1994. Automated Learning of Decision Rules for Text Categorization. ACM Trans. Inf. Syst. 12, 233–251. https://doi.org/10.1145/183422.183423

Aref, H., 1984. Stirring by Chaotic Advection. J. Fluid Mech. 143, 1–21. https://doi.org/10.1017/S0022112084001233

Armor, J.N., 2011. A history of industrial catalysis. Catalysis Today, Special issue on Industrial Catalysis 163, 3–9. https://doi.org/10.1016/j.cattod.2009.11.019

Armstrong, B., 2011. The study of pharmaceutical powder mixing through improved flow property characterisation and tomographic imaging of blend content uniformity. University of Birmingham.

Arratia, P.E., Duong, N., Muzzio, F.J., Godbole, P., Reynolds, S., 2006. A study of the mixing and segregation mechanisms in the Bohle Tote blender via DEM simulations. Powder Technology 164, 50–57. https://doi.org/10.1016/j.powtec.2006.01.018

Arratia, P.E., Muzzio, F.J., 2004. Planar Laser-Induced Fluorescence Method for Analysis of Mixing in Laminar Flows. Industrial & Engineering Chemistry Research 43, 6557–6568. https://doi.org/10.1021/ie049838b

Avalosse, T., Crochet, M.J., 1997. Finite-element simulation of mixing: 2. Three-dimensional flow through a kenics mixer. AIChE Journal 43, 588–597. https://doi.org/10.1002/aic.690430304

Azzopardi, B.J., Jackson, K., Robinson, J.P., Kaji, R., Byars, M., Hunt, A., 2008. Fluctuations in dense phase pneumatic conveying of pulverised coal measured using electrical capacitance tomography. Chemical Engineering Science 9, 2548–2558. https://doi.org/10.1016/j.ces.2008.02.013

Banares-Alcantara, R., Venkatasubramanian, V., Westerberg, A.W., Rychener, M.D., 1985. Knowledge-based expert systems: an emerging technology for CAD in chemical engineering. Chem. Eng. Prog. 9, 127–142.

Bañares-Alcántara, R., Westerberg, A.W., Ko, E.I., Rychener, M.D., 1987. Decade—A hybrid expert system for catalyst selection—I. Expert system consideration. Computers & Chemical Engineering 11, 265–277. https://doi.org/10.1016/0098-1354(87)85008-1

Bao, Y.Y., Hao, Z.G., Gao, Z.M., Shi, L.T., Smith, J.M., Thorpe, R.B., 2006. Gas dispersion and solid suspension in a three-phase stirred tank with multiple impellers. Chem. Eng. Commun. 193, 801–825. https://doi.org/10.1080/00986440500267261

Barigou, M., 2004. Particle Tracking in Opaque Mixing Systems: An Overview of the Capabilities of PET and PEPT. Chemical Engineering Research and Design 82, 1258–1267. https://doi.org/10.1205/cerd.82.9.1258.44160

Barrios Sosa, A.C., Williamson, R.T., Conway, R., Shankar, A., Sumpter, R., Cleary, T., 2011. A Safe and Efficient Synthetic Route to a 2,5-Dimethyl-1-aryl-1H-imidazole Intermediate. Org. Process Res. Dev. 15, 449–454. https://doi.org/10.1021/op100335q

Bayford, R.H., Gibson, A., Tizzard, A., Tidswell, T., Holder, D.S., 2001. Solving the forward problem in electrical impedance tomography for the human head using IDEAS (integrated design engineering analysis software), a finite element modelling tool. Physiol. Meas. 22, 55–64. https://doi.org/10.1088/0967-3334/22/1/308

Bell, S.D., 2015. The Development of Radioactive Gas Imaging for the Study of Chemical Flow Processes. University of Birmingham, Birmingham.

Bender, R., Kuss, O., 2010. Methods to calculate relative risks, risk differences, and numbers needed to treat from logistic regression. J Clin Epidemiol 63, 7–8. https://doi.org/10.1016/j.jclinepi.2009.07.007

Berthold, J., Imkamp, D., 2013. Looking at the future of manufacturing metrology: roadmap document of the German VDI/VDE Society for Measurement and Automatic Control. Journal of Sensors and Sensor Systems 2, 1–7. https://doi.org/10.5194/jsss-2-1-2013

Blythe, T.W., Sederman, A.J., Stitt, E.H., York, A.P.E., Gladden, L.F., 2017. PFG NMR and Bayesian analysis to characterise non-Newtonian fluids. J. Magn. Reson. 274, 103–114. https://doi.org/10.1016/j.jmr.2016.11.003

Bolton, G.T., 2006. A Review of Linear Electrical Tomography Probes for Monitoring the Behaviour of Multiphase Mixing Processes. Presented at the 12th European Conference on Mixing, Bologna.

Bolton, G.T., Qiu, C.H., Wang, M., 2002. A Novel Electrical Tomography Sensor for Monitoring the Phase Distribution in Industrial Reactors, in: 7th UK Conference on Mixing. Bradford.

Boyd, J.W.R., Varley, J., 2001. The uses of passive measurement of acoustic emissions from chemical engineering processes. Chem. Eng. Sci. 56, 1749–1767. https://doi.org/10.1016/S0009-2509(00)00540-6

Bragg Sir, W., H., 1921. The world of sound. Bell, London.

Brecher, C., Klocke, F., Schmitt, R., Schuh, G., Aachener Werkzeugmaschinen-Kolloquium, RWTH Aachen, Fraunhofer-Institut für Produktionstechnologie IPT (Eds.), 2014. Integrative Produktion: Industrie 4.0 - Aachener Perspektiven, Berichte aus Ingenieurwissenschaften. Shaker, Aachen.

Bridgwater, J., 1995. Particle technology. Chemical Engineering Science, Frontiers of Chemical Engineering Science 50, 4081–4089. https://doi.org/10.1016/0009-2509(95)00225-1

Brittain, H.G., 2006. UV/VIS Reflectance Spectroscopy [WWW Document]. Spectroscopy of Pharmaceutical Solids. https://doi.org/10.1201/9780849361333-7

Caesarendra, W., Widodo, A., Yang, B.-S., 2010. Application of relevance vector machine and logistic regression for machine degradation assessment. Mechanical Systems and Signal Processing 24, 1161–1171. https://doi.org/10.1016/j.ymssp.2009.10.011

Carletti, C., Montante, G., De Blasio, C., Paglianti, A., 2016. Liquid mixing dynamics in slurry stirred tanks based on electrical resistance tomography. Chem. Eng. Sci. 152, 478–487. https://doi.org/10.1016/j.ces.2016.06.044

Carletti, C., Montante, G., Westerlund, T., Paglianti, A., 2014. Analysis of solid concentration distribution in dense solid–liquid stirred tanks by electrical resistance tomography. Chemical Engineering Science 119, 53–64. https://doi.org/10.1016/j.ces.2014.07.049

Carr, J.F., Walker, D.M., 1968. An annular shear cell for granular materials. Powder Technology 1, 369–373. https://doi.org/10.1016/0032-5910(68)80019-1

Cents, A.H.G., Brilmant, D.W.F., Versteeg, G.F., 2005. Ultrasonic investigation of hydrodynamics and mass transfer in a gas-liquid(-liquid) stirred

vessel. International Journal of Chemical Reactor Engineering 3. https://doi.org/10.2202/1542-6580.1164

Cervera-Padrell, A.E., Nielsen, J.P., Jønch Pedersen, M., Müller Christensen, K., Mortensen, A.R., Skovby, T., Dam-Johansen, K., Kiil, S., Gernaey, K.V., 2012. Monitoring and Control of a Continuous Grignard Reaction for the Synthesis of an Active Pharmaceutical Ingredient Intermediate Using Inline NIR spectroscopy. Org. Process Res. Dev. 16, 901–914. https://doi.org/10.1021/op2002563

Chablani, L., Taylor, M.K., Mehrotra, A., Rameas, P., Stagner, W.C., 2011. Inline Real-Time Near-Infrared Granule Moisture Measurements of a Continuous Granulation–Drying–Milling Process. AAPS PharmSciTech 12, 1050–1055. https://doi.org/10.1208/s12249-011-9669-z

Chambers, J., C.W., Kleiner B, Tukey P., 1983. Graphical Methods for Data Analysis, 1st ed, Chapman and Hall/CRC. New York.

Chanda, A., Daly, A.M., Foley, D.A., LaPack, M.A., Mukherjee, S., Orr, J.D., Reid, G.L., Thompson, D.R., Ward, H.W., 2015. Industry Perspectives on Process Analytical Technology: Tools and Applications in API Devlopment. Org. Process Res. Dev. 19, 63–83. https://doi.org/10.1021/op400358b

Chandra, K.G., Kale, D.D., 1992. Pressure-drop for laminar-flow of viscoelastic fluids in static mixers. Chemical Engineering Science 47, 2097–2100.

Chandrasekera, T.C., Wang, A., Holland, D.J., Marashdeh, Q., Pore, M., Wang, F., Sederman, A.J., Fan, L.S., Gladden, L.F., Dennis, J.S., 2012. A comparison of magnetic resonance imaging and electrical capacitance tomography: An air jet through a bed of particles. Powder Technol. 227, 86–95. https://doi.org/10.1016/j.powtec.2012.03.005

Chaouki, J., Larachi, F., Dudukovic, M.P., 1997. Non-Invasive Monitoring of Multiphase Flows, 1st ed. Elsevier Science.

Chaplin, G., Pugsley, T., Lee, L. van der, Kantzas, A., Winters, C., 2005. The dynamic calibration of an electrical capacitance tomography sensor applied to the fluidized bed drying of pharmaceutical granule. Meas. Sci. Technol. 16, 1281–1290. https://doi.org/10.1088/0957-0233/16/6/007

Chapman, C.M., Nienow, A.W., Cooke, M., Middleton, J. C., 1983b. Particle-gas-liquid mixing in stirred vessels. Part IV: Mass transfer and final conclusions. Chem. Eng. Res. Des. 61, 182–185.

Chen, B., J., Chen, X.F., Li, B., 2011. Reliability estimation for cutting tool based on logistic regression model. Chinese journal of Mechanical Engineering 47, 158–164.

Chen, J.W., Kemoun, A., Al-Dahhan, M.H., Dudukovic, M.P., Lee, D.J., Fan, L.S., 1999. Comparative hydrodynamics study in a bubble column using computer-automated radioactive particle tracking (CARPT)/computed tomography (CT) and particle image velocimetry (PIV). Chem. Eng. Sci. 54, 2199–2207. https://doi.org/10.1016/S0009-2509(98)00349-2

Chester, A.W., Kowalski, J.A., Coles, M.E., Muegge, E.L., Muzzio, F.J., Brone, D., 1999. Mixing dynamics in catalyst impregnation in double-cone blenders. Powder Technology 102, 85–94. https://doi.org/10.1016/S0032-5910(98)00193-4

Chung, K.H.K., Simmons, M.J.H., Barigou, M., 2009. Local gas and liquid phase velocity measurement in a miniature stirred vessel using PIV combined with a new image processing algorithm. Experimental Thermal and Fluid Science 33, 743–753. https://doi.org/10.1016/j.expthermflusci.2009.01.010

Clark, P.J., 2016. Towards in-situ characterisation of formulated products. University of Birmingham.

Clark, P.J., Forte, G., Simmons, M.J.H., Stitt, E.H., 2016a. Towards 3D-Electrical Capacitance Tomography for Interface Detection. Johnson Matthey Technology Review 60, 164–175. https://doi.org/10.1595/205651316X691537

Clark, P.J., Tsoligkas, A.N., Simmons, M.J.H., Robbins, P.T., Stitt, E.H., 2016b. A comparison of methods for in situ discrimination of imaged phase boundaries using electrical capacitance tomography. Meas. Sci. Technol. 27, 025401. https://doi.org/10.1088/0957-0233/27/2/025401

Coates, J.P., 2010. Infrared Spectroscopy for Process Analytical Applications, in: Process Analytical Technology. John Wiley & Sons, Ltd, pp. 157–194. https://doi.org/10.1002/9780470689592.ch6

Coetzee, C.J., Els, D.N.J., 2009. Calibration of Discrete Element Parameters and the Modelling of Silo Discharge and Bucket Filling. Comput. Electron. Agric. 65, 198–212. https://doi.org/10.1016/j.compag.2008.10.002

Coetzee, R.A., Mwesigye, A., Huan, Z., 2017. Optimal slope angle selection of an evacuated tube collector for domestic solar water heating. 1 28, 104–119. https://doi.org/10.17159/2413-3051/2017/v28i1a1621

Cole, P., Watson, J., 2005. Acoustic Emission for Corrosion Detection. Presented at the Middle East Nondestructive Conference &Exhibition, Bahrain, Manama, p. 7.

Connelly, R.K., Kokini, J.L., 2007. Examination of the mixing ability of single and twin screw mixers using 2D finite element method simulation with particle tracking. Journal of Food Engineering 79, 956–969. https://doi.org/10.1016/j.jfoodeng.2006.03.017

Conway, S.L., Lekhal, A., Khinast, J.G., Glasser, B.J., 2005. Granular flow and segregation in a four-bladed mixer. Chemical Engineering Science 60, 7091–7107. https://doi.org/10.1016/j.ces.2005.03.008

Cooley, J.W., Lewis, P.A.W., Welch, P.D., 1969. The Fast Fourier Transform and Its Applications. IEEE Transactions on Education 12, 27–34. https://doi.org/10.1109/TE.1969.4320436

Cooper, B.J., 1983. Durability of Platinum-Containing Automotive Exhaust Control Catalysts. Johnson Matthey Technology Review 27, 146.

Cover, T., Hart, P., 1967. Nearest neighbor pattern classification. IEEE Transactions on Information Theory 13, 21–27. https://doi.org/10.1109/TIT.1967.1053964

Crouter, A., Briens, L., 2015. Passive acoustic emissions from particulates in a V-blender. Drug Dev. Ind. Pharm. 41, 1809–1818. https://doi.org/10.3109/03639045.2015.1009913

Custom Sensors & Technology [WWW Document], n.d. URL http://www.customsensors.com/ (accessed 7.11.19).

Del Nobile, M.A., Laverse, J., Lampignano, V., Cafarelli, B., Spada, A., 2015. 25 - Applications of tomography in food inspection, in: Wang, M. (Ed.), Industrial Tomography. Woodhead Publishing, pp. 693–712. https://doi.org/10.1016/B978-1-78242-118-4.00025-3

Di Benedetti, M., Loreto, G., Matta, F., Nanni, A., 2013. Acoustic Emission Monitoring of Reinforced Concrete under Accelerated Corrosion. J. Mater. Civ. Eng. 25, 1022–1029. https://doi.org/10.1061/(ASCE)MT.1943-5533.0000647

Dickens, J.E., 2010. Overview of Process Analysis and PAT, in: Process Analytical Technology. John Wiley & Sons, Ltd, pp. 1–15. https://doi.org/10.1002/9780470689592.ch1

Dong, F., Jiang, Z.X., Qiao, X.T., Xu, L.A., 2003. Application of electrical resistance tomography to two-phase pipe flow parameters measurement. Flow Measurement and Instrumentation, Multi Phase Flow Measurement 14, 183–192. https://doi.org/10.1016/S0955-5986(03)00024-4

Dudukovic, M.P., 2000. Opaque multiphase reactors: Experimentation, modeling and troubleshooting. Oil Gas Sci. Technol. 55, 135–158. https://doi.org/10.2516/ogst:2000008

Dyakowski, T., Edwards, R.B., Xie, C.G., Williams, R.A., 1997. Application of capacitance tomography to gas-solid flows. Chemical Engineering Science, Process Tomography 52, 2099–2110. https://doi.org/10.1016/S0009-2509(97)00037-7

Dyakowski, T., Jeanmeure, L.F.C., Jaworski, A.J., 2000. Applications of electrical tomography for gas–solids and liquid–solids flows — a review. Powder Technology 112, 174–192. https://doi.org/10.1016/S0032-5910(00)00292-8

Edwards, I., Axon, S.A., Barigou, M., Stitt, E.H., 2009. Combined Use of PEPT and ERT in the Study of Aluminum Hydroxide Precipitation. Ind. Eng. Chem. Res. 48, 1019–1028. https://doi.org/10.1021/ie8010353

Ehrhardt, N., Montagne, M., Berthiaux, H., Dalloz-Dubrujeaud, B., Gatumel, C., 2005. Assessing the homogeneity of powder mixtures by on-line electrical capacitance. Chemical Engineering and Processing: Process Intensification, Pneumatic Conveying and Handling of Particulate Solids 44, 303–313. https://doi.org/10.1016/j.cep.2004.03.016

Elforjani, M., Shanbr, S., 2018. Prognosis of Bearing Acoustic Emission Signals Using Supervised Machine Learning. IEEE Transactions on Industrial Electronics 65, 5864–5871. https://doi.org/10.1109/TIE.2017.2767551

Esbensen, K.H., Halstensen, M., Tønnesen Lied, T., Saudland, A., Svalestuen, J., de Silva, S., Hope, B., 1998. Acoustic chemometrics—from noise to information. Chemometrics and Intelligent Laboratory Systems 44, 61–76. https://doi.org/10.1016/S0169-7439(98)00114-2

Faes, M., Glasmacher, B., 2008. Measurements of micro- and macromixing in liquid mixtures of reacting components using two-colour laser induced fluorescence. Chemical Engineering Science, Model-Based Experimental Analysis 63, 4649–4655. https://doi.org/10.1016/j.ces.2007.10.036

Ferizi, U., Besser, H., Hysi, P., Jacobs, J., Rajapakse, C.S., Chen, C., Saha, P.K., Honig, S., Chang, G., 2019. Artificial Intelligence Applied to Osteoporosis: A Performance Comparison of Machine Learning Algorithms in Predicting Fragility Fractures From MRI Data. J. Magn. Reson. Imaging 49, 1029–1038. https://doi.org/10.1002/jmri.26280

Fishwick, R.P., Winterbottom, J.M., Parker, D.J., Fan, X.F., Stitt, E.H., 2005. Hydrodynamic measurements of up- and down-pumping pitched-blade turbines in gassed, agitated vessels, using positron emission particle tracking. Ind. Eng. Chem. Res. 44, 6371–6380. https://doi.org/10.1021/ie049191v

Ford, J.J., Heindel, T.J., Jensen, T.C., Drake, J.B., 2008. X-ray computed tomography of a gas-sparged stirred-tank reactor. Chem. Eng. Sci. 63, 2075–2085. https://doi.org/10.1016/j.ces.2008.01.007

Forte, G., Albano, A., Simmons, M.J.H., Stitt, H.E., Brunazzi, E., Alberini, F., 2019a. Assessing Blending of Non-Newtonian Fluids in Static Mixers by Planar Laser-Induced Fluorescence and Electrical Resistance Tomography. Chemical Engineering & Technology 42, 1602–1610. https://doi.org/10.1002/ceat.201800728

Forte, G., Alberini, F., Simmons, M.J.H., Stitt, E.H., 2019b. Measuring gas hold-up in gas–liquid/gas–solid–liquid stirred tanks with an electrical resistance tomography linear probe. AIChE Journal 65, e16586. https://doi.org/10.1002/aic.16586

Forte, G., Clark, P.J., Wale, O., Hall, J.F., Zumaeta, N., Simmons, M.J.H., Stitt, E.H., 2016. Extending the application of electrical resistance tomography using linear probes in fluid mixing diagnosis, in: 8th World Congress on Industrial Process Tomography. Iguassu Falls, Brazil.

Forte, G., Clark, P.J., Yan, Z., Stitt, E.H., Marigo, M., 2018. Using a Freeman FT4 rheometer and Electrical Capacitance Tomography to assess powder blending. Powder Technology, Particulate Product Manufacturing – an In-silico approach 337, 25–35. https://doi.org/10.1016/j.powtec.2017.12.020

Freeman, R., 2007. Measuring the flow properties of consolidated, conditioned and aerated powders — A comparative study using a powder rheometer and a rotational shear cell. Powder Technology, Special Edition from the PSA2005 Conference 174, 25–33. https://doi.org/10.1016/j.powtec.2006.10.016

Fu, T., Carrier, O., Funfschilling, D., Ma, Y., Li, H.Z., 2016. Newtonian and Non-Newtonian Flows in Microchannels: Inline Rheological Characterization. Chem. Eng. Technol. 39, 987–992. https://doi.org/10.1002/ceat.201500620

Gao, Z., Smith, J.M., Müller-Steinhagen, H., 2001. Gas Dispersion in Sparged and Boiling Reactors. Chemical Engineering Research and Design, 4th International Symposium on Mixing in Industrial Processes 79, 973–978. https://doi.org/10.1205/026387601552721523

Global Info Reports, 2018. Global Emission Control Catalyst Market - Growth Opportunities, Regional Insights, Competitive Landscape, Market Trend Analysis, Forecast to 2025 (No. 1071358), Chemicals and Materials.

González-Montellano, C., Ramírez, Á., Gallego, E., Ayuga, F., 2011. Validation and experimental calibration of 3D discrete element models for the simulation of the discharge flow in silos. Chemical engineering science.

Grand View Research, 2019. Catalyst Market Size, Share, Trends, Industry Growth Report 2019-2025.

Gregory, C.H., Appleton, H.B., Lowes, A.P., Whalen, F.C., 1946. Instrumentation & control in the German Chemical industry.

Grima, A.P., Wypych, P.W., 2011. Development and validation of calibration methods for discrete element modelling. Granular Matter 13, 127–132. https://doi.org/10.1007/s10035-010-0197-4

Hakansson, A., 2018. Rotor-Stator Mixers: From Batch to Continuous Mode of Operation-A Review. Processes 6, 32. https://doi.org/10.3390/pr6040032

Halow, J.S., 1997. Chapter 9 - Electrical capacitance imaging of fluidized beds, in: Chaouki, J., Larachi, F., Duduković, M.P. (Eds.), Non-Invasive Monitoring of Multiphase Flows. Elsevier Science B.V., Amsterdam, pp. 263–307. https://doi.org/10.1016/B978-044482521-6/50010-3

Hamidipour, M., Larachi, F., Ring, Z., 2009. Monitoring Filtration in Trickle Beds Using Electrical Capacitance Tomography. Ind. Eng. Chem. Res. 48, 1140–1153. https://doi.org/10.1021/ie800810t

Hamood-ur-Rehman, M., Ein-Mozaffari, F., Dahman, Y., 2013. Dynamic and local gas holdup studies in external loop recirculating airlift reactor with two rolls of fiberglass packing using electrical resistance tomography. Journal of Chemical Technology & Biotechnology 88, 887–896. https://doi.org/10.1002/jctb.3917

Hansen, L.S., Pedersen, S., Durdevic, P., 2019. Multi-Phase Flow Metering in Offshore Oil and Gas Transportation Pipelines: Trends and Perspectives. Sensors 19, 2184. https://doi.org/10.3390/s19092184

Hansen, P., 1998. Rank-Deficient and Discrete Ill-Posed Problems, Mathematical Modeling and Computation. Society for Industrial and Applied Mathematics. https://doi.org/10.1137/1.9780898719697

Harrison, S.T.L., Stevenson, R., Cilliers, J.J., 2012. Assessing solids concentration homogeneity in Rushton-agitated slurry reactors using electrical resistance tomography (ERT). Chem. Eng. Sci. 71, 392–399. https://doi.org/10.1016/j.ces.2011.10.053

Hausman, D.S., Cambron, R.T., Sakr, A., 2005. Application of Raman spectroscopy for on-line monitoring of low dose blend uniformity. Int J Pharm 298, 80–90. https://doi.org/10.1016/j.ijpharm.2005.04.011

Heck, R.M., Gulati, S., Farrauto, R.J., 2001. The application of monoliths for gas phase catalytic reactions. Chemical Engineering Journal, FRONTIERS IN CHEMICAL REACTION ENGINEERING 82, 149–156. https://doi.org/10.1016/S1385-8947(00)00365-X

Hermann, M., Pentek, T., Otto, B., 2016. Design Principles for Industrie 4.0 Scenarios, in: 2016 49th Hawaii International Conference on System Sciences (HICSS). IEEE, Koloa, HI, USA, pp. 3928–3937. https://doi.org/10.1109/HICSS.2016.488

Hilbe, J.M., 2009. Logistic Regression Models, 1st ed. Chapman and Hall CRC Press.

Hobbs, D.M., Muzzio, F.J., 1997. The Kenics static mixer: a three-dimensional chaotic flow. Chem. Eng. J. 67, 153–166. https://doi.org/10.1016/S1385-8947(97)00013-2

Holden, P.J., Wang, M., Mann, R., Dickin, F.J., Edwards, R.B., 1998. Imaging stirred-vessel macromixing using electrical resistance tomography. AIChE Journal 44, 780–790. https://doi.org/10.1002/aic.690440403

Holland, D.J., 2015. 18 - Applications of tomography in bubble column and trickle bed reactors, in: Wang, M. (Ed.), Industrial Tomography. Woodhead Publishing, pp. 477–507. https://doi.org/10.1016/B978-1-78242-118-4.00018-6

Hosseini, S., Patel, D., Ein-Mozaffari, F., Mehrvar, M., 2010. Study of solid–liquid mixing in agitated tanks through electrical resistance tomography. Chemical Engineering Science 65, 1374–1384. https://doi.org/10.1016/j.ces.2009.10.007

Huang, S., Plaskowski, A., Xie, C., Beck, M., 1989. Tomographic Imaging of 2-Component Flow Using Capacitance Sensors. Journal of Physics E-Scientific Instruments 22, 173–177. https://doi.org/10.1088/0022-3735/22/3/009

Imkamp, D., Berthold, J., Heizmann, M., Kniel, K., Manske, E., Peterek, M., Schmitt, R., Seidler, J., Sommer, K.-D., 2016. Challenges and trends in manufacturing measurement technology – the "Industrie 4.0" concept 11.

International Platinum Group Metals Association, 2019. Catalytic Converters [WWW Document]. URL https://ipa-news.com/index/pgm-applications/automotive/catalytic-converters/ (accessed 6.28.19).

Ismail, I., Gamio, J.C., Bukhari, S.F.A., Yang, W.Q., 2005. Tomography for multi-phase flow measurement in the oil industry. Flow Measurement and Instrumentation 2–3, 145–155. https://doi.org/10.1016/j.flowmeasinst.2005.02.017

Izumi, S., Kamata, S., Satoh, K., Miyai, H., 1993. High energy X-ray computed tomography for industrial applications. IEEE Transactions on Nuclear Science 40, 158–161. https://doi.org/10.1109/23.212333

Jamshed, A., Cooke, M., Ren, Z., Rodgers, T.L., 2018. Gas–liquid mixing in dual agitated vessels in the heterogeneous regime. Chemical Engineering Research and Design 133, 55–69. https://doi.org/10.1016/j.cherd.2018.02.034

Jang, J.-R., 1993. ANFIS: adaptive-network-based fuzzy inference system. IEEE Transactions on Systems, Man, and Cybernetics 23, 665–685. https://doi.org/10.1109/21.256541

Jaworski, A.J., Dyakowski, T., 2001a. Application of electrical capacitance tomography for measurement of gas-solids flow characteristics in a pneumatic conveying system. Meas. Sci. Technol. 12, 1109–1119. https://doi.org/10.1088/0957-0233/12/8/317

Jaworski, A.J., Dyakowski, T., 2001b. Application of electrical capacitance tomography for measurement of gas-solids flow characteristics in a pneumatic conveying system. Meas. Sci. Technol. 12, 1109. https://doi.org/10.1088/0957-0233/12/8/317

Jeanmeure, L.F.C., Dyakowski, T., Zimmerman, W.B.J., Clark, W., 2002. Direct flow-pattern identification using electrical capacitance tomography. Experimental Thermal and Fluid Science 26, 763–773. https://doi.org/10.1016/S0894-1777(02)00186-3

Jegatheeswaran, S., Ein-Mozaffari, F., Wu, J., 2018. Process intensification in a chaotic SMX static mixer to achieve an energy-efficient mixing operation of non-newtonian fluids. Chem. Eng. Process. 124, 1–10. https://doi.org/10.1016/j.cep.2017.11.018

Jenike, A.W., 1964. Storage and flow of solids. Bulletin of the Utah Engineering Experiment 123.

Jenike, A.W., 1961. Gravity flow of bulk solids. Bulletin of the Utah Engineering Experiment 108, 1–294.

Jestel, N.L., 2010. Raman Spectroscopy, in: Process Analytical Technology. John Wiley & Sons, Ltd, pp. 195–243. https://doi.org/10.1002/9780470689592.ch7

Jin, H., Yang, S., Wang, M., Williams, R.A., 2007. Measurement of Gas Holdup Profiles in A Gas Liquid Cocurrent Bubble Column Using Electrical Resistance Tomography. AIP Conference Proceedings 914, 869–876. https://doi.org/10.1063/1.2747525

Johnson Matthey, 2019a. Preliminary results for the year ended 31st March 2019 42 [WWW Document]. URL https://matthey.com/news/2019/full-year-results-2018-19 (accessed 7.5.19).

Johnson Matthey, 2019b. Fuel cells | Johnson Matthey [WWW Document]. URL https://matthey.com/markets/automotive/fuel-cells (accessed 7.16.19).

Johnson Matthey, 2018. Annual Report 2018 | Johnson Matthey [WWW Document]. URL https://matthey.com/investors/report-archive/annual-report-2018 (accessed 7.4.19).

Johnson Matthey, 2017a. Celebrating 200 Years of Inspiring Science. [WWW Document] URL https://matthey.com/-/media/files/jm-200-history-book.pdf (accessed 8.2.19).

Johnson Matthey, 2017b. PGM Market Report 53. [WWW Document] URL http://www.platinum.matthey.com/documents/new-item/pgm%20market%20reports/pgm_market_report_may_2017.pdf (accessed 7.5.19)

Kagermann, H., Wahlster, W., Helbig, J., 2013. Recommendations for Implementing the Strategic Initiative INDUSTRIE 4.0 -- Securing the Future of German Manufacturing Industry, National Academy of Science and Engineering, München.

Kantzas, A., 2015. 17 - X-ray tomography of fluidized beds, in: Wang, M. (Ed.), Industrial Tomography. Woodhead Publishing, pp. 451–475. https://doi.org/10.1016/B978-1-78242-118-4.00017-4

Karamizadeh, S., Abdullah, S.M., Halimi, M., Shayan, J., Rajabi, M. j, 2014. Advantage and drawback of support vector machine functionality, in: 2014 International Conference on Computer, Communications, and Control Technology (I4CT). pp. 63–65. https://doi.org/10.1109/I4CT.2014.6914146

Kasat, G.R., Pandit, A.B., 2005. Review on mixing characteristics in solid-liquid and solid-liquid-gas reactor vessels. Can. J. Chem. Eng. 83, 618–643. https://doi.org/10.1002/cjce.5450830403

Kasemsumran, P., Auephanwiriyakul, S., Theera-Umpon, N., 2016. Face recognition using string grammar fuzzy K-nearest neighbor. 2016 8th International Conference on Knowledge and Smart Technology (KST) 55–59. https://doi.org/10.1109/KST.2016.7440531

Kaspar, J., Fornasiero, P., Hickey, N., 2003. Automotive catalytic converters: current status and some perspectives. CATALYSIS TODAY 77, 419–449.

Ketcham, R.A., Carlson, W.D., 2001. Acquisition, optimization and interpretation of X-ray computed tomographic imagery: applications to the geosciences. Computers & Geosciences, 3D reconstruction, modelling & visualization of geological materials 27, 381–400. https://doi.org/10.1016/S0098-3004(00)00116-3

Khalili, F., Jafari Nasr, M.R., Kazemzadeh, A., Ein-Mozaffari, F., 2018. Analysis of gas holdup and bubble behavior in a biopolymer solution inside a bioreactor using tomography and dynamic gas disengagement techniques. Journal of Chemical Technology and Biotechnology 93, 340–349.

Khopkar, A.R., Ranade, V.V., 2008. CFD simulation of gas–liquid stirred vessel: CARPT/CT measurements and CFD simulations. AIChE Journal 52, 1654–1672. https://doi.org/10.1002/aic.10762

Komzsik, L., 2003. The Lanczos Method: Evolution and Application. SIAM.

Kotsiantis, S.B., 2007. Supervised Machine Learning: A Review of Classification Techniques. Informatica 31.

Kouroussis, D., Anastassopoulos, A., Vionis, P., Kolovos, V., 2000. Unsupervised pattern recognition of acoustic emission from full scale testing of a wind turbine blade. Journal of Acoustic Emission 18, 217–223.

Kourunen, J., Kayhko, R., Matula, J., Kayhko, J., Vauhkonen, M., Heikkinen, L.M., 2008. Imaging of mixing of two miscible liquids using electrical impedance tomography and linear impedance sensor. Flow Meas. Instrum. 19, 391–396. https://doi.org/10.1016/j.flowmeasinst.2008.07.002

Kuo, H.P., Knight, P.C., Parker, D.J., Seville, J.P.K., 2005. Solids circulation and axial dispersion of cohesionless particles in a V-mixer. Powder Technology 152, 133–140. https://doi.org/10.1016/j.powtec.2004.12.003

Kusiak, A., 2018. Smart manufacturing. International Journal of Production Research 56, 508–517. https://doi.org/10.1080/00207543.2017.1351644

Kuzeljevic, Z., 2010. Hydrodynamics of Trickle Bed Reactors: Measurements And Modeling. Washington University, St. Louis, USA.

Laakkonen, M., Honkanen, M., Saarenrinne, P., Aittamaa, J., 2005. Local bubble size distributions, gas-liquid interfacial areas and gas holdups in a stirred vessel with particle image velocimetry. Chem. Eng. J. 109, 37–47. https://doi.org/10.1016/j.cej.2005.03.002

Lasi, H., Fettke, P., Kemper, H.-G., Feld, T., Hoffmann, M., 2014. Industry 4.0. Bus Inf Syst Eng 6, 239–242. https://doi.org/10.1007/s12599-014-0334-4

Le Guer, Y., El Omari, K., 2012. Chaotic Advection for Thermal Mixing, in: vanderGiessen, E., Aref, H. (Eds.), Advances in Applied Mechanics, Vol 45. Elsevier Academic Press Inc, San Diego, pp. 189–237.

Lee, B.W., Dudukovic, M.P., 2014. Determination of flow regime and gas holdup in gas-liquid stirred tanks. Chem. Eng. Sci. 109, 264–275. https://doi.org/10.1016/j.ces.2014.01.032

Lee, H.L.T., Boccazzi, P., Gorret, N., Ram, R.J., Sinskey, A.J., 2004. In situ bioprocess monitoring of Escherichia coli bioreactions using Raman spectroscopy. Vibrational Spectroscopy, The 2nd International Conference on Advanced Vibrational Spectroscopy (ICAVS-2) 35, 131–137. https://doi.org/10.1016/j.vibspec.2003.12.015

Lee, S., Lee, S., Kim, Y., Kim, J., Choi, B., Kim, K., 2006. A filtering approach of iterative Tikhonov regularization method in ECT, in: 2006 IEEE SENSORS. Presented at the 2006 IEEE SENSORS, pp. 919–922. https://doi.org/10.1109/ICSENS.2007.355616

Lee, S.L., O'Connor, T.F., Yang, X., Cruz, C.N., Chatterjee, S., Madurawe, R.D., Moore, C.M.V., Yu, L.X., Woodcock, J., 2015. Modernizing Pharmaceutical Manufacturing: from Batch to Continuous Production. J Pharm Innov 10, 191–199. https://doi.org/10.1007/s12247-015-9215-8

Lemke, M., Fernández-Trujillo, R., Löhmannsröbenc, H.-G., 2005. In-situ LIF Analysis of Biological and Petroleum-based Hydraulic Oils on Soil. Sensors 5, 61–69. https://doi.org/10.3390/s5010061

Leugers, M.A., Lipp, E.D., 2006. Raman Spectroscopy in Process Analysis, in: Encyclopedia of Analytical Chemistry. American Cancer Society. https://doi.org/10.1002/9780470027318.a2113

Li, H., Wang, Y., Zhao, P., Zhang, X., Zhou, P., 2015. Cutting tool operational reliability prediction based on acoustic emission and logistic regression model. Journal of Intelligent Manufacturing 26, 923–931. https://doi.org/10.1007/s10845-014-0941-4

Li, H.Z., Fasol, C., Choplin, L., 1997. Pressure Drop of Newtonian and Non-Newtonian Fluids Across a Sulzer SMX Static Mixer. Chemical Engineering Research and Design, Fluid Flow 75, 792–796. https://doi.org/10.1205/026387697524461

Li, J.-K., Humphrey, A.E., 1991. Use of fluorometry for monitoring and control of a bioreactor. Biotechnology and Bioengineering 37, 1043–1049. https://doi.org/10.1002/bit.260371109

Li, W.., Lu, G.W., Huang, L., Gao, H., Du, W.M., 2003. Aspirin Synthesis On-line Measurement by Raman Spectroscopy. Acta Phys.-Chim. Syn. 19, 105–108.

Li, Y., Holland, D.J., 2015. Optimizing the Geometry of Three-Dimensional Electrical Capacitance Tomography Sensors. IEEE Sensors Journal 15, 1567–1574. https://doi.org/10.1109/JSEN.2014.2363901

Li, Y., Yang, W., 2008. Image reconstruction by nonlinear Landweber iteration for complicated distributions. Meas. Sci. Technol. 19, 094014. https://doi.org/10.1088/0957-0233/19/9/094014

Liao, A., Zhou, Q., Zhang, Y., 2015. Application of 3D electrical capacitance tomography in probing anomalous blocks in water. Journal of Applied Geophysics 117, 91–103. https://doi.org/10.1016/j.jappgeo.2015.03.030

Lionheart, W.R.B., 2001. Reconstruction Algorithms for Permittivity and Conductivity Imaging. Proceedings of the 2nd World Congress on Industrial Process Tomography, Hannover, Germany , Wednesday 29th to Friday 31st August 2001 4–11.

Litto, R., Mmbaga, J.P., Hayes, R.E., Plati, S., Blagojevic, V., Subject, P., 2016. Exhaust emissions and fuel economy improvements through thermal performance control in a novel three-way catalytic converter. Can. J. Chem. Eng. 94, 905–912. https://doi.org/10.1002/cjce.22449

Liu, R., Yin, X., Li, H., Shao, Q., York, P., He, Y., Xiao, T., Zhang, J., 2013. Visualization and quantitative profiling of mixing and segregation of granules using synchrotron radiation X-ray microtomography and three dimensional reconstruction.

International Journal of Pharmaceutics 445, 125–133. https://doi.org/10.1016/j.ijpharm.2013.02.010

Liu, S., Chen, Q., Wang, H.G., Jiang, F., Ismail, I., Yang, W.Q., 2005. Electrical capacitance tomography for gas–solids flow measurement for circulating fluidized beds. Flow Measurement and Instrumentation, Tomographic Techniques for Multiphase Flow Measurements 16, 135–144. https://doi.org/10.1016/j.flowmeasinst.2005.02.013

Lorrain, P., Corson, D.R., Lorrain, F., 1988. Electromagnetic fields and waves: including electric circuits, 3rd ed. ed. Freeman, New York.

Ma, Y., Zheng, Z., Xu, L., Liu, X., Wu, Y., 2001. Application of electrical resistance tomography system to monitor gas/liquid two-phase flow in a horizontal pipe. Flow Measurement and Instrumentation 12, 259–265. https://doi.org/10.1016/S0955-5986(01)00026-7

Machin, T.D., Wei, H.-Y., Greenwood, R.W., Simmons, M.J.H., 2018. In-pipe rheology and mixing characterisation using electrical resistance sensing. Chemical Engineering Science 187, 327–341. https://doi.org/10.1016/j.ces.2018.05.017

Maiwald, M., Fischer, H.H., Kim, Y.-K., Hasse, H., 2003. Quantitative on-line high-resolution NMR spectroscopy in process engineering applications. Anal Bioanal Chem 375, 1111–1115. https://doi.org/10.1007/s00216-002-1723-y

Makkawi, Y.T., Wright, P.C., 2002. Fluidization regimes in a conventional fluidized bed characterized by means of electrical capacitance tomography. Chemical Engineering Science 57, 2411–2437. https://doi.org/10.1016/S0009-2509(02)00138-0

Mann, R., Dickin, F.J., Wang, M., Dyakowski, T., Williams, R.A., Edwards, R. B., 1997. Application of Electrical Resistance Tomography to Interrogate Mixing Processes at Plant Scale. Chemical Engineering Science 52, 2087–97. https://doi.org/10.1016/S0009-2509(97)00036-5

Marashdeh, Q., Teixeira, F.L., 2004. Sensitivity matrix calculation for fast 3-D electrical capacitance tomography (ECT) of flow systems (vol 40, pg 1204, 2004). IEEE Trans. Magn. 40, 1972–1972. https://doi.org/10.1109/TMAG.2004.831453

Marigo, M., Cairns, D.L., Davies, M., Ingram, A., Stitt, E.H., 2012. A numerical comparison of mixing efficiencies of solids in a cylindrical vessel subject to a range of motions. Powder Technology 217, 540–547. https://doi.org/10.1016/j.powtec.2011.11.016

Marigo, M., Davies, M., Leadbeater, T., Cairns, D.L., Ingram, A., Stitt, E.H., 2013. Application of Positron Emission Particle Tracking (PEPT) to validate a Discrete Element Method (DEM) model of granular flow and mixing in the Turbula mixer. International Journal of Pharmaceutics 446, 46–58. https://doi.org/10.1016/j.ijpharm.2013.01.030

Marigo, M., Stitt, E.H., 2015. Discrete Element Method (DEM) for Industrial Applications: Comments on Calibration and Validation for the Modelling of Cylindrical Pellets. KONA Powder and Particle Journal 32, 236–252. https://doi.org/10.14356/kona.2015016

Martin, D., 1977. Early warning of bank failure: A logit regression approach. Journal of Banking & Finance 1, 249–276. https://doi.org/10.1016/0378-4266(77)90022-X

Martinez Olmos, A., Castillo, E., Martinez-Marti, F., Morales, D.P., Garcia, A., Banqueri, J., 2011. An Imaging Method for Electrical Capacitance Tomography Based on Projections Multiplication, in: Kyriacou, P.A., O'Riordan, A., McConnell, G. (Eds.), Sensors & Their Applications Xvi. Iop Publishing Ltd, Bristol, p. 012032.

Matusiak, B., da Silva, M.J., Hampel, U., Romanowski, A., 2010. Measurement of Dynamic Liquid Distributions in a Fixed Bed Using Electrical Capacitance Tomography and Capacitance Wire-Mesh Sensor. Ind. Eng. Chem. Res. 49, 2070–2077. https://doi.org/10.1021/ie900988f

Maxwell, J.C., 1881. A Treatise on Electricity and Magnetism, 2nd ed. Clarendon Press.

McKinsey & Company, 2016. The age of analytics: competing in a data-driven world.

Microstrategy, 2018. 2018 Global state of enterprise analytics.

Middleton, J.C., 1997. Gas-Liquid Dispersion and Mixing, in: Mixing in the Process Industries. Butterworth Heinemann, pp. 322–363.

Middleton, J.C., 1992. Chapter 15 - Gas–liquid dispersion and mixing, in: Harnby, N., Edwards, M.F., Nienow, A.W. (Eds.), Mixing in the Process Industries. Butterworth-Heinemann, Oxford, pp. 322–363. https://doi.org/10.1016/B978-075063760-2/50036-6

Middleton, J.C., Smith, J.M., 2003. Gas–Liquid Mixing in Turbulent Systems, in: Handbook of Industrial Mixing: Science and Practice. John Wiley and Sons, pp. 585–638.

Moakher, M., Shinbrot, T., Muzzio, F.J., 2000. Experimentally validated computations of flow, mixing and segregation of non-cohesive grains in 3D tumbling blenders. Powder Technology 109, 58–71. https://doi.org/10.1016/S0032-5910(99)00227-2

Montante, G., Paglianti, A., 2015. Gas hold-up distribution and mixing time in gas-liquid stirred tanks. Chem. Eng. J. 279, 648–658. https://doi.org/10.1016/j.cej.2015.05.058

Mosorov, V., 2015. 19 - Applications of tomography in reaction engineering (mixing process), in: Wang, M. (Ed.), Industrial Tomography, Woodhead Publishing Series in Electronic and Optical Materials. Woodhead Publishing, pp. 509–528. https://doi.org/10.1016/B978-1-78242-118-4.00019-8

Murthy, S.K., 1998. Automatic Construction of Decision Trees from Data: A Multi-Disciplinary Survey. Data Min. Knowl. Discov. 2, 345–389. https://doi.org/10.1023/A:1009744630224

Muzzio, F.J., Robinson, P., Wightman, C., Dean Brone, 1997. Sampling practices in powder blending. International Journal of Pharmaceutics 155, 153–178. https://doi.org/10.1016/S0378-5173(97)04865-5

Nakagawa, M., Altobelli, S.A., Caprihan, A., Fukushima, E., 1997. NMRI study: asial migration of radially segregated core of granular mixtures in a horizontal rotating cylinder. Chemical Engineering Science 52, 4423–4428. https://doi.org/10.1016/S0009-2509(97)00181-4

National Academies of Sciences, E., 2018. Data Science: Opportunities to Transform Chemical Sciences and Engineering: Proceedings of a Workshop—in Brief. https://doi.org/10.17226/25191

Nienow, A.W., Bujalski, W., 2002. Recent Studies on Agitated Three-Phase (Gas–Solid–Liquid) Systems in the Turbulent Regime. Chemical Engineering Research and Design 80, 832–838. https://doi.org/10.1205/026387602321143363

Nienow, A.W., Warmoeskerken, M.M.C.G., Smith, J. M., Konno, M., 1985. On the flooding/loading transition and the complete dispersal condition in aerated vessels agitated by a Rushton-turbine, in: 5th European Conference on Mixing. Wurtsburg, West Germany, pp. 143–154.

Nordon, A., Carella, Y., Gachagan, A., Littlejohn, D., Hayward, G., 2006. Factors affecting broadband acoustic emission measurements of a heterogeneous reaction. The Analyst 131, 323–330. https://doi.org/10.1039/B510922A

Nordon, A., Waddell, R.J.H., Bellamy, L.J., Gachagan, A., McNab, D., Littlejohn, D., Hayward, G., 2004. Monitoring of a heterogeneous reaction by acoustic emission. Analyst 129, 463–467. https://doi.org/10.1039/b402875a

Obregón, L., Quiñones, L., Velázquez, C., 2013. Model predictive control of a fluidized bed dryer with an inline NIR as moisture sensor. Control Engineering Practice 21, 509–517. https://doi.org/10.1016/j.conengprac.2012.11.002

Oguh, U.I., 2012. Multiphase contacting in PGM hydrometallurgy (d_en). University of Birmingham.

Ohtsu, M., 1996. The history and development of acoustic emission in concrete engineering. Mag. Concr. Res. 48, 321–330. https://doi.org/10.1680/macr.1996.48.177.321

Ojeda, C.B., Rojas, F.S., 2009. Process Analytical Chemistry: Applications of Ultraviolet/Visible Spectrometry in Environmental Analysis: An Overview. Applied Spectroscopy Reviews 44, 245–265. https://doi.org/10.1080/05704920902717898

Olmos, A.M., Botella, G., Castillo, E., Morales, D.P., Banqueri, J., Garcia, A., 2012. A reconstruction method for electrical capacitance tomography based on image fusion techniques. Digit. Signal Prog. 22, 885–893. https://doi.org/10.1016/j.dsp.2012.07.002

Ottino, J.M., Khakhar, D.V., 2000. Mixing and Segregation of Granular Materials. Annu. Rev. Fluid Mech. 32, 55–91. https://doi.org/10.1146/annurev.fluid.32.1.55

Ouzineb, K., Hua, H., Jovanovic, R., Dubé, M.A., McKenna, T.F., 2003. Monomer compartmentalisation in miniemulsion polymerisation studied by infrared spectroscopy. Comptes Rendus Chimie 6, 1343–1349. https://doi.org/10.1016/j.crci.2003.10.001

Pakzad, L., Ein-Mozaffari, F., Chan, P., 2008. Using electrical resistance tomography and computational fluid dynamics modelling to study the formation of cavern in the mixing of pseudoplastic fluids possessing yield stress. Chemical Engineering Science 63, 2508–2522. https://doi.org/10.1016/j.ces.2008.02.009

Pakzad, L., Ein-Mozaffari, F., Upreti, S.R., Lohi, A., 2013. Characterisation of the mixing of non-Newtonian fluids with a scaba 6SRGT impeller through ert and CFD. The Canadian Journal of Chemical Engineering 91, 90–100. https://doi.org/10.1002/cjce.21616

Paul, E.L., Atiemo-Obeng, V.A., Kresta, S.M., 2004. Handbook of Industrial Mixing: Science and Practice. John Wiley & Sons.

Peng, L., Merkus, H., Scarlett, B., 2000. Using Regularization Methods for Image Reconstruction of Electrical Capacitance Tomography. Particle & Particle Systems Characterization 17, 96–104. https://doi.org/10.1002/1521-4117(200010)17:3<96::AID-PPSC96>3.0.CO;2-8

Peng, L., Mou, C., Yao, D., Zhang, B., Xiao, D., 2005. Determination of the optimal axial length of the electrode in an electrical capacitance tomography sensor. Flow Measurement and Instrumentation 16, 169–175. https://doi.org/10.1016/j.flowmeasinst.2005.02.015

Peryt-Stawiarska, S., 2014. The CFD analysis of non-Newtonian fluid flow through a SMX static mixer. Przem. Chem. 93, 196–198.

Pfund, D.M., Greenwood, M.S., Bamberger, J.A., Pappas, R.A., 2006. Inline ultrasonic rheometry by pulsed Doppler. Ultrasonics 44, E477–E482. https://doi.org/10.1016/j.ultras.2006.05.027

Pianko-Oprych, P., Nienow, A.W., Barigou, M., 2009. Positron emission particle tracking (PEPT) compared to particle image velocimetry (PIV) for studying the flow generated by a pitched-blade turbine in single phase and multi-phase systems. Chemical Engineering Science 64, 4955–4968. https://doi.org/10.1016/j.ces.2009.08.003

Porion, P., Sommier, N., Faugère, A.-M., Evesque, P., 2004. Dynamics of size segregation and mixing of granular materials in a 3D-blender by NMR imaging investigation. Powder Technology 141, 55–68. https://doi.org/10.1016/j.powtec.2004.02.015

Powers, D.M.W., 2011. Evaluation: From precision, recall and fmeasure to roc, informedness, markedness and correlation. Journal of Machine Learning Technologies 2, 37–63.

Prakash, S., Karwe, M.V., Kokini, J.L., 1999. Measurement of velocity distribution in the Brabender Farinograph as a model mixer, using Laser-Doppler Anemometry. J. Food Process Eng. 22, 435–454. https://doi.org/10.1111/j.1745-4530.1999.tb00498.x

Prasath, V.B.S., Alfeilat, H.A.A., Lasassmeh, O., Hassanat, A.B.A., 2017. Distance and Similarity Measures Effect on the Performance of K-Nearest Neighbor Classifier - A Review. arXiv:1708.04321 [cs].

Primrose, K., 2015. 26 - Application of process tomography in nuclear waste processing, in: Wang, M. (Ed.), Industrial Tomography. Woodhead Publishing, pp. 713–725. https://doi.org/10.1016/B978-1-78242-118-4.00026-5

Qin, M., Chen, D.Y., Wang, L.L., Yu, X.Y., 2006. An Adaptive Threshold Image Reconstruction Algorithm of Oil-Water Two-Phase Flow in Electrical Capacitance Tomography System. J. Phys.: Conf. Ser. 48, 422–426. https://doi.org/10.1088/1742-6596/48/1/080

Rafiee, M., Bakalisa, S., Fryer, P.J., Ingram, A., 2011. Study of laminar mixing in kenics static mixer by using Positron Emission Particle Tracking (PEPT). Procedia Food Science, 11th International Congress on Engineering and Food (ICEF11) 1, 678–684. https://doi.org/10.1016/j.profoo.2011.09.102

Rahmani, R.K., Keith, T.G., Ayasoufi, A., 2005. Numerical Simulation and Mixing Study of Pseudoplastic Fluids in an Industrial Helical Static Mixer. J. Fluids Eng 128, 467–480. https://doi.org/10.1115/1.2174058

Ramsay, J., Simmons, M.J.H., Ingram, A., Stitt, E.H., 2016. Mixing performance of viscoelastic fluids in a Kenics KM in-line static mixer. Chemical

Engineering Research and Design, 10th European Congress of Chemical Engineering 115, 310–324. https://doi.org/10.1016/j.cherd.2016.07.020

Ranade, V., Deshpande, V.R., 1999. Gas–liquid flow in stirred reactors: Trailing vortices and gas accumulation behind impeller blades. CHEM ENG SCI 54, 2305–2315. https://doi.org/10.1016/S0009-2509(98)00301-7

Rao, S.M., Zhu, K., Wang, C.-H., Sundaresan, S., 2001. Electrical Capacitance Tomography Measurements on the Pneumatic Conveying of Solids. Ind. Eng. Chem. Res. 40, 4216–4226. https://doi.org/10.1021/ie0100028

Rashidi, M., 1997. Chapter 15 - Fluorescence imaging techniques: Application to measuring flow and transport in refractive index-matched porous media, in: Chaouki, J., Larachi, F., Duduković, M.P. (Eds.), Non-Invasive Monitoring of Multiphase Flows. Elsevier Science B.V., Amsterdam, pp. 519–580. https://doi.org/10.1016/B978-044482521-6/50016-4

Rauline, D., Le Blévec, J.-M., Bousquet, J., Tanguy, P.A., 2000. A Comparative Assessment of the Performance of the Kenics and SMX Static Mixers. Chemical Engineering Research and Design, Fluid Mixing 78, 389–396. https://doi.org/10.1205/026387600527284

Rautenbach, C., Melaaen, M.C., Halvorsen, B.M., 2013. Possible Identification of Size difference Segregation using Electrical Capacitance Tomography and Statistical Analysis. 15.

Razzak, S.A., Barghi, S., Zhu, J.-X., Mi, Y., 2009. Phase holdup measurement in a gas-liquid-solid circulating fluidized bed (GLSCFB) riser using electrical resistance tomography and optical fibre probe. Chem. Eng. J. 147, 210–218. https://doi.org/10.1016/j.cej.2008.07.022

Regner, M., Östergren, K., Trägårdh, C., 2006. Effects of geometry and flow rate on secondary flow and the mixing process in static mixers—a numerical study. Chemical Engineering Science 61, 6133–6141. https://doi.org/10.1016/j.ces.2006.05.044

Remy, B., Khinast, J.G., Glasser, B.J., 2011. Polydisperse granular flows in a bladed mixer: Experiments and simulations of cohesionless spheres. Chemical Engineering Science 66, 1811–1824. https://doi.org/10.1016/j.ces.2010.12.022

Ren, Z., Kowalski, A., Rodgers, T.L., 2017. Measuring inline velocity profile of shampoo by electrical resistance tomography (ERT). Flow Meas. Instrum. 58, 31–37. https://doi.org/10.1016/j.flowmeasinst.2017.09.013

Rewatkar, V., Joshi, J., 1991. Critical Impeller Speed for Solid Suspension in Mechanically Agitated three phase Reactors .2. Mathematical-Model. Ind. Eng. Chem. Res. 30, 1784–1791. https://doi.org/10.1021/ie00056a014

Ricard, F., Brechtelsbauer, C., Xu, X.Y., Lawrence, C.J., 2005. Monitoring of multiphase pharmaceutical processes using electrical resistance tomography. Chem. Eng. Res. Des. 83, 794–805. https://doi.org/10.1205/cherd.04324

Richardson, D.J., Holdich, R.G., 2001. A Novel and Low Cost Probe for Monitoring Dispersed Solids Concentrations in Liquids. Chemical Engineering Research & Design 83, 569–574. https://doi.org/10.1205/02638760152424343

Rimpiläinen, V., Heikkinen, L.M., Vauhkonen, M., 2012. Moisture distribution and hydrodynamics of wet granules during fluidized-bed drying characterized with volumetric electrical capacitance tomography. Chemical Engineering Science 75, 220–234. https://doi.org/10.1016/j.ces.2012.03.028

Rimpiläinen, V., Poutiainen, S., Heikkinen, L.M., Savolainen, T., Vauhkonen, M., Ketolainen, J., 2011. Electrical capacitance tomography as a monitoring tool for high-shear mixing and granulation. Chemical Engineering Science 66, 4090–4100. https://doi.org/10.1016/j.ces.2011.05.044

Rink, B., Harabagiu, S., Roberts, K., 2011. Automatic extraction of relations between medical concepts in clinical texts. J. Am. Med. Inf. Assoc. 18, 594–600. https://doi.org/10.1136/amiajnl-2011-000153

Rizwan, M., Anderson, D.V., 2014. Using k-Nearest Neighbor and Speaker Ranking for Phoneme Prediction. 2014 13th International Conference on Machine Learning and Applications 383–387. https://doi.org/10.1109/ICMLA.2014.68

Rosato, A., Strandburg, K.J., Prinz, F., Swendsen, R.H., 1987. Why the Brazil nuts are on top: Size segregation of particulate matter by shaking. Phys. Rev. Lett. 58, 1038–1040. https://doi.org/10.1103/PhysRevLett.58.1038

Rozak, P., Zielinski, J., Czop, P., Jablonski, A., Barszcz, T., Mareczek, M., 2018. Supervised Classification Methods in Condition Monitoring of Rolling Element Bearings, in: Timofiejczuk, A., Chaari, F., Zimroz, R., Bartelmus, W., Haddar, M. (Eds.), Advances in Condition Monitoring of Machinery in Non-Stationary Operations, Cmmno 2016. Springer-Verlag Berlin, Berlin.

Rushton, J.H., Bmbinet, J.-J., 1968. Holdup and flooding in air liquid mixing. The Canadian Journal of Chemical Engineering 46, 16–21. https://doi.org/10.1002/cjce.5450460103

Rymarczyk, T., Klosowski, G., 2019. The use of elastic net and neural networks in industrial process tomography. Prz. Elektrotechniczny 95, 59–62. https://doi.org/10.15199/48.2019.05.15

Saatdjian, E., Rodrigo, A.J.S., Mota, J.P.B., 2012. On chaotic advection in a static mixer. Chem. Eng. J. 187, 289–298. https://doi.org/10.1016/j.cej.2012.01.122

Safavian, S.R., Landgrebe, D., 1991. A survey of decision tree classifier methodology. IEEE Transactions on Systems, Man, and Cybernetics 21, 660–674. https://doi.org/10.1109/21.97458

Saltzman, R.S., 2006. Ultraviolet/Visible Spectroscopy in Process Analyses, in: Encyclopedia of Analytical Chemistry. American Cancer Society. https://doi.org/10.1002/9780470027318.a2118

Saravanan, K., Joshi, J.B., 1996. Fractional gas hold-up in gas inducing type of mechanically agitated contactors. The Canadian Journal of Chemical Engineering 74, 16–30. https://doi.org/10.1002/cjce.5450740104

Sardeshpande, M.V., Gupta, S., Ranade, V.V., 2017. Electrical Resistance Tomography for Gas Holdup in a Gas-Liquid Stirred Tank Reactor. Chemical Engineering Science 170, 476–490.

Schmidt, J.A., 2000. Ultraviolet/visible spectroscopy of chromophores in mechanical pulps, in: Encyclopedia of Analytical Chemistry. John Wiley & Sons, pp. 8388–8406.

Schoonheydt, R.A., 2010. UV-VIS-NIR spectroscopy and microscopy of heterogeneous catalysts. Chem. Soc. Rev. 39, 5051–5066. https://doi.org/10.1039/C0CS00080A

Schwab, K., 2016. The Fourth Industrial Revolution. World Economic Forum, Geneva, Switzerland.

Sederman, A.J., Gladden, L.F., 2001. Magnetic resonance imaging as a quantitative probe of gas-liquid distribution and wetting efficiency in trickle-bed reactors. Chem. Eng. Sci. 56, 2615–2628. https://doi.org/10.1016/S0009-2509(00)00513-3

Seville, J.P., Tüzün, U., Clift, R., 2012. Processing of Particulate Solids. Springer Science & Business Media.

Sharifi, M., Young, B., 2013. Electrical Resistance Tomography (ERT) applications to Chemical Engineering. Chemical Engineering Research and Design 91, 1625–1645. https://doi.org/10.1016/j.cherd.2013.05.026

Shashishekhar, N., 2015. Industrial applications of automated X-ray inspection. AIP Conference Proceedings 1650, 534–544. https://doi.org/10.1063/1.4914651

Shashishekhar, N., Veselitza, D., 2017. Automated X-ray quality control of catalytic converters. AIP Conference Proceedings 1806, 130003. https://doi.org/10.1063/1.4974712

Shell, 2016. Shell Chemicals Datasheet: Isopropyl alcohol [WWW Document]. URL https://www.shell.com/business-customers/chemicals/our-products/solvents-

chemical/alcohols/_jcr_content/par/tabbedcontent/tab/textimage.stream/14600230446
37/b0b7ef356c65f2fdd262453bd3eb009011c1bfd0/ipa-s1111-eu.pdf

Shinohara, K., 1997. Fundamental and Rheological Properties of Powders, in: Fayed, M.E., Otten, L. (Eds.), Handbook of Powder Science & Technology. Springer US, Boston, MA, pp. 96–145. https://doi.org/10.1007/978-1-4615-6373-0_4

Smith, J.M., 1991. Simple performance correlations for agitated vessels, in: 7th European Congress on Mixing. Brugge, pp. 233–241.

Smith, J.M., 1985. Dispersion of Gases in Liquids: the hydrodynamics of gas dispersion in low viscosity liquids, in: Ulbrecht, J.J. and Patterson, G.K., Eds. Presented at the Mixing of Liquids by Mechanical Means, Gordon and Breach Science Publishers, New York, pp. 115–126.

Smith, J.M., Warmoeskerken, M.M.C.G., 1985. The dispersion of gases in liquids with turbines, in: 5th European Conference on Mixing. BHRA Fluid Eng., Cranfield, UK, Wurtsburg, West Germany, pp. 115–126.

Sommier, N., Porion, P., Evesque, P., Leclerc, B., Tchoreloff, P., Couarraze, G., 2001. Magnetic resonance imaging investigation of the mixing-segregation process in a pharmaceutical blender. International Journal of Pharmaceutics 222, 243–258. https://doi.org/10.1016/S0378-5173(01)00718-9

Soofi, A.A., Awan, A., 2017. Classification Techniques in Machine Learning: Applications and Issues. Journal of Basic and Applied Sciences 13, 459-465–465.

Soppe, W., Rieffe, H., Weeber, A., 2005. Bulk and surface passivation of silicon solar cells accomplished by silicon nitride deposited on industrial scale by microwave PECVD. Progress in Photovoltaics: Research and Applications 13, 551–569. https://doi.org/10.1002/pip.611

Spellings, M., Glotzer, S.C., 2018. Machine learning for crystal identification and discovery. AIChE Journal 64, 2198–2206. https://doi.org/10.1002/aic.16157

Stamatiou, I.K., Muller, F.L., 2017. Determination of mass transfer resistances of fast reactions in three-phase mechanically agitated slurry reactors. AICHE J. 63, 273–282. https://doi.org/10.1002/aic.15540

Stanley, S.J., Bolton, G.T., 2008. A Review of Recent Electrical Resistance Tomography (ERT) Applications for Wet Particulate Processing. Particle & Particle Systems Characterization 25, 207–215. https://doi.org/10.1002/ppsc.200701126

Stephenson, D.R., Mann, R., York, T.A., 2008. The sensitivity of reconstructed images and process engineering metrics to key choices in practical electrical impedance tomography. Meas. Sci. Technol. 19, 094013. https://doi.org/10.1088/0957-0233/19/9/094013

Stobiac, V., Fradette, L., Tanguy, P.A., Bertrand, F., 2014. Pumping characterisation of the maxblend impeller for Newtonian and strongly non-Newtonian fluids. The Canadian Journal of Chemical Engineering 92, 729–741. https://doi.org/10.1002/cjce.21906

Sun, J., Yang, W., Tian, W., 2015. 3D imaging based on fringe effect of an electrical capacitance tomography sensor. Measurement, 74, 186–199. https://doi.org/10.1016/j.measurement.2015.07.018

Suykens, J. a. K., Vandewalle, J., 1999. Least Squares Support Vector Machine Classifiers. Neural Processing Letters 9, 293–300. https://doi.org/10.1023/A:1018628609742

Szalai, E.S., Arratia, P., Johnson, K., Muzzio, F.J., 2004. Mixing analysis in a tank stirred with Ekato Intermig® impellers. Chemical Engineering Science 59, 3793–3805. https://doi.org/10.1016/j.ces.2003.12.033

Takriff, M.S., Ahmad, A., Rosli, M.I., Jantan, S., 2013. ERT visualization of gas dispersion performance of aerofoil and radial impellers in an agitated vessel. Jurnal Teknologi 64, 75–78. https://doi.org/10.11113/jt.v64.2136

Tan, C., Dong, F., 2015. 16 - Applications of tomography in mineral transportation, in: Wang, M. (Ed.), Industrial Tomography, Woodhead Publishing Series in Electronic and Optical Materials. Woodhead Publishing, pp. 431–450. https://doi.org/10.1016/B978-1-78242-118-4.00016-2

Tapp, H.S., Peyton, A.J., Kemsley, E.K., Wilson, R.H., 2003. Chemical engineering applications of electrical process tomography. Sens. Actuator B-Chem. 92, 17–24. https://doi.org/10.1016/S0925-4005(03)00126-6

Tholin-Chittenden, C., Soleimani, M., 2017. Planar Array Capacitive Imaging Sensor Design Optimization. IEEE Sensors Journal 17, 8059–8071. https://doi.org/10.1109/JSEN.2017.2719579

Tikhonov, A.N., Arsenin, V.Y., 1977. Solutions of ill-posed problems. Winston & Sons, Washington D.C.

Twigg, M.V., 2011. Catalytic control of emissions from cars. Catalysis Today, Special issue on Industrial Catalysis 163, 33–41. https://doi.org/10.1016/j.cattod.2010.12.044

Uendey, C., Ertunc, S., Mistretta, T., Looze, B., 2010. Applied advanced process analytics in biopharmaceutical manufacturing: Challenges and prospects in real-time monitoring and control. J. Process Control 20, 1009–1018. https://doi.org/10.1016/j.jprocont.2010.05.008

Ulissi, Z.W., Tang, M.T., Xiao, J., Liu, X., Torelli, D.A., Karamad, M., Cummins, K., Hahn, C., Lewis, N.S., Jaramillo, T.F., Chan, K., Nørskov, J.K., 2017.

Machine-Learning Methods Enable Exhaustive Searches for Active Bimetallic Facets and Reveal Active Site Motifs for CO2 Reduction. ACS Catal. 7, 6600–6608. https://doi.org/10.1021/acscatal.7b01648

Upstone, S.L., 2013. Ultraviolet/Visible Light Absorption Spectrophotometry in Clinical Chemistry Update based on the original article by Stephen L. Upstone, Encyclopedia of Analytical Chemistry, © 2000, John Wiley & Sons, Ltd., in: Encyclopedia of Analytical Chemistry. American Cancer Society. https://doi.org/10.1002/9780470027318.a0547.pub2

Utomo, M.B., Warsito, W., Sakai, T., Uchida, S., 2001. Analysis of distributions of gas and TiO2 particles in slurry bubble column using ultrasonic computed tomography. Chemical Engineering Science 56, 6073–6079. https://doi.org/10.1016/S0009-2509(01)00228-7

van der Vaart, K., Gajjar, P., Epely-Chauvin, G., Andreini, N., Gray, J.M.N.T., Ancey, C., 2015. Underlying Asymmetry within Particle Size Segregation. Phys. Rev. Lett. 114, 238001. https://doi.org/10.1103/PhysRevLett.114.238001

Van't Riet, K., Smith, J.M., 1975. The trailing vortex system produced by rushton turbine agitators. Chem Eng Sci 30, 1093–1105.

Vapnik, V., 2000. The Nature of Statistical Learning Theory, 2nd ed, Information Science and Statistics. Springer-Verlag, New York.

Veera, P.U., Patwardhan, A.W., Joshi, J.B., 2001. Measurement of Gas Hold-up Profiles in Stirred Tank Reactors by Gamma Ray Attenuation Technique. Chemical Engineering Research and Design 79, 684–688. https://doi.org/10.1205/026387601316971352

Venkatasubramanian, V., 2019. The promise of artificial intelligence in chemical engineering: Is it here, finally? AIChE Journal 65, 466–478. https://doi.org/10.1002/aic.16489

Wageningen, W.F.C. van, Kandhai, D., Mudde, R.F., Akker, H.E.A. van den, 2004. Dynamic flow in a Kenics static mixer: An assessment of various CFD methods. AIChE Journal 50, 1684–1696. https://doi.org/10.1002/aic.10178

Wahab, Y.A., Rahim, R.A., Rahiman, M.H.F., Aw, S.R., Yunus, F.R.M., Goh, C.L., Rahim, H.A., Ling, L.P., 2015. Non-invasive process tomography in chemical mixtures – A review. Sensors and Actuators B: Chemical 210, 602–617. http://dx.doi.org/10.1016/j.snb.2014.12.103

Wahl, P.R., Fruhmann, G., Sacher, S., Straka, G., Sowinski, S., Khinast, J.G., 2014. PAT for tableting: Inline monitoring of API and excipients via NIR spectroscopy. European Journal of Pharmaceutics and Biopharmaceutics 87, 271–278. https://doi.org/10.1016/j.ejpb.2014.03.021

Wang, A., Marashdeh, Q., Fan, L.-S., 2014. ECVT imaging of 3D spiral bubble plume structures in gas-liquid bubble columns. Can. J. Chem. Eng. 92, 2078–2087. https://doi.org/10.1002/cjce.22070

Wang, A., Marashdeh, Q., Motil, B.J., Fan, L.-S., 2014. Electrical capacitance volume tomography for imaging of pulsating flows in a trickle bed. Chem. Eng. Sci. 119, 77–87. https://doi.org/10.1016/j.ces.2014.08.011

Wang, A., Marashdeh, Q., Teixeira, F.L., Fan, L.-S., 2015. 20 - Applications of capacitance tomography in gas–solid fluidized bed systems, in: Wang, M. (Ed.), Industrial Tomography. Woodhead Publishing, pp. 529–549. https://doi.org/10.1016/B978-1-78242-118-4.00020-4

Wang, F., Marashdeh, Q., Fan, L.-S., Warsito, W., 2010a. Electrical Capacitance Volume Tomography: Design and Applications. Sensors 10, 1890–1917. https://doi.org/10.3390/s100301890

Wang, F., Marashdeh, Q., Fan, L.-S., Warsito, W., 2010b. Electrical Capacitance Volume Tomography: Design and Applications. Sensors (Basel) 10, 1890–1917. https://doi.org/10.3390/s100301890

Wang, H., Tang, L., Cao, Z., 2007. An image reconstruction algorithm based on total variation with adaptive mesh refinement for ECT. Flow Meas. and Instrum., 18, 5–6, 262–267. https://doi.org/10.1016/j.flowmeasinst.2007.07.004

Wang, H., Jia, X., Wang, X., Zhou, Z., Wen, J., Zhang, J., 2014. CFD modeling of hydrodynamic characteristics of a gas-liquid two-phase stirred tank. Appl. Math. Model. 38, 63–92. https://doi.org/10.1016/j.apm.2013.05.032

Wang, M., 2015. Industrial Tomography - Science and Applications, 1st ed. Woodhead Publishing Series in Electronic and Optical Materials.

Wang, M., Dickin, F.J., Mann, R., 1999. Electrical Resistance Tomographic Systems for Industrial Applications. Chemical Engineering Communications 175, 49–70. https://doi.org/10.1080/00986449908912139

Wang, M., Dorward, A., Vlaev, D., Mann, R., 2000. Measurements of gas-liquid mixing in a stirred vessel using electrical resistance tomography (ERT). Chem. Eng. J. 77, 93–98.

Warmoeskerken, M.M.C.G., Smith, J.M., 1985. Flooding of disc turbines in gas-liquid dispersions: A new description of the phenomenon. Chemical Engineering Science 40, 2063–2071. https://doi.org/10.1016/0009-2509(85)87023-8

Warmoeskerken, M.M.C.G., van Houwelingen, M. C., Drijlink, J. J., Smith, J. M., 1984. The role of cavity formation in stirred gas-liquid-solid reactors. Chem. Eng. Res. Des. 62, 197–200.

Warsito, W., Fan, L.S., 2005b. Dynamics of spiral bubble plume motion in the entrance region of bubble columns and three-phase fluidized beds using 3D ECT. Chem. Eng. Sci. 60, 6073–6084. https://doi.org/10.1016/j.ces.2005.01.033

Warsito, W., Fan, L.S., 2003. Neural network multi-criteria optimization image reconstruction technique (NN-MOIRT) for linear and non-linear process tomography. Chemical Engineering and Processing: Process Intensification 42, 663–674.

Warsito, W., Marashdeh, Q., Fan, L.-S., 2007. Electrical Capacitance Volume Tomography. IEEE Sensors Journal 7, 525–536.

Weck, M., 2005. Werkzeugmaschinen 1. Springer Berlin Heidelberg, Berlin, Heidelberg. https://doi.org/10.1007/978-3-540-28085-9

Weckenmann, A., Jiang, X., Sommer, K.-D., Neuschaefer-Rube, U., Seewig, J., Shaw, L., Estler, T., 2009. Multisensor data fusion in dimensional metrology. CIRP Annals - Manufacturing Technology 2, 701–721. https://doi.org/10.1016/j.cirp.2009.09.008

Wei, K., Qiu, C., Soleimani, M., Primrose, K., 2015. ITS Reconstruction Tool-Suite: An inverse algorithm package for industrial process tomography. Flow Measurement and Instrumentation, Special issue on Tomography Measurement & Modeling of Multiphase Flows 46, 292–302. https://doi.org/10.1016/j.flowmeasinst.2015.08.001

Weinekötter, R., Gericke, H., 2013. Mixing of Solids. Springer Science & Business Media.

Weinekötter, R., Reh, L., 1995. Continuous Mixing of Fine Particles. Particle & Particle Systems Characterization 12, 46–53. https://doi.org/10.1002/ppsc.19950120108

Whitaker, M., Baker, G.R., Westrup, J., Goulding, P.A., Rudd, D.R., Belchamber, R.M., Collins, M.P., 2000. Application of acoustic emission to the monitoring and end point determination of a high shear granulation process. International Journal of Pharmaceutics 205, 79–91. https://doi.org/10.1016/S0378-5173(00)00479-8

Wietzke, S., Jansen, C., Jördens, C., Krumbholz, N., Vieweg, N., Scheller, M., Shakfa, M.K., Romeike, D., Hochrein, T., Mikulics, M., Koch, M., 2009. Industrial applications of THz systems, in: International Symposium on Photoelectronic Detection and Imaging 2009: Terahertz and High Energy Radiation Detection Technologies and Applications. International Society for Optics and Photonics, p. 738506. https://doi.org/10.1117/12.840991

Williams, J.C., 1976. The segregation of particulate materials. A review. Powder Technology 15, 245–251. https://doi.org/10.1016/0032-5910(76)80053-8

Williams, J.L., 2001. Monolith structures, materials, properties and uses☉. Catalysis Today 34.

Williams, R.A., Jia, X., West, R.M., Wang, M., Cullivan, J.C., Bond, J., Faulks, I., Dyakowski, T., Wang, S.J., Climpson, N., Kostuch, J.A., Payton, D., 1999. Industrial monitoring of hydrocyclone operation using electrical resistance tomography. Minerals Engineering 12, 1245–1252. https://doi.org/10.1016/S0892-6875(99)00109-0

Wu, W.-Z., Zhang, W.-X., 2002. Neighborhood operator systems and approximations. Information Sciences 144, 201–217. https://doi.org/10.1016/S0020-0255(02)00180-9

Wu, X., Kumar, V., Quinlan, J.R., Ghosh, J., Yang, Q., Motoda, H., McLachlan, G.J., Ng, A., Liu, B., Yu, P.S., Zhou, Z.-H., Steinbach, M., Hand, D.J., Steinberg, D., 2008. Top 10 algorithms in data mining. Knowl Inf Syst 14, 1–37. https://doi.org/10.1007/s10115-007-0114-2

Wuest, T., Weimer, D., Irgens, C., Thoben, K.-D., 2016. Machine learning in manufacturing: advantages, challenges, and applications. Production & Manufacturing Research 4, 23–45. https://doi.org/10.1080/21693277.2016.1192517

Wunsch, O., Bohme, G., 2000. Numerical simulation of 3d viscous fluid flow and convective mixing in a static mixer. Arch. Appl. Mech. 70, 91–102. https://doi.org/10.1007/s004199900042

Xie, C., Huang, S., Hoyle, B., Thorn, R., Lenn, C., Snowden, D., Beck, M., 1992. Electrical Capacitance Tomography for Flow Imaging - System Model for Development of Image-Reconstruction Algorithms and Design of Primary Sensors. Iee Proceedings-G Circuits Devices and Systems 139, 89–98. https://doi.org/10.1049/ip-g-2.1992.0015

Xie, C.G., Reinecke, N., Beck, M.S., Mewes, D., Williams, R.A., 1995. Electrical tomography techniques for process engineering applications. The Chemical Engineering Journal and the Biochemical Engineering Journal 56, 127–133. https://doi.org/10.1016/0923-0467(94)02907-5

Xue, Dezhen, Balachandran, P.V., Hogden, J., Theiler, J., Xue, Deqing, Lookman, T., 2016. Accelerated search for materials with targeted properties by adaptive design. Nature Communications 7, 11241. https://doi.org/10.1038/ncomms11241

Yan, J., Koç, M., Lee, J., 2004. A prognostic algorithm for machine performance assessment and its application. Production Planning & Control 15, 796–801. https://doi.org/10.1080/09537280412331309208

Yan, J., Lee, J., 2004. Degradation Assessment and Fault Modes Classification Using Logistic Regression. J. Manuf. Sci. Eng 127, 912–914. https://doi.org/10.1115/1.1962019

Yan, Z., Wilkinson, S.K., Stitt, E.H., Marigo, M., 2016. Investigating mixing and segregation using discrete element modelling (DEM) in the Freeman FT4 rheometer. International Journal of Pharmaceutics 513, 38–48. https://doi.org/10.1016/j.ijpharm.2016.08.065

Yang, C.-Y., Fu, X.-Y., 2004. Development and validation of a material-labeling method for powder process characterization using X-ray computed tomography. Powder Technology 146, 10–19. https://doi.org/10.1016/j.powtec.2004.06.011

Yang, W.Q., Peng, L., 2003. Image reconstruction algorithms for electrical capacitance tomography. Meas. Sci. Technol. 14, R1. https://doi.org/10.1088/0957-0233/14/1/201

Yao, J., Takei, M., 2017. Application of Process Tomography to Multiphase Flow Measurement in Industrial and Biomedical Fields: A Review. IEEE Sens. J. 17, 8196–8205. https://doi.org/10.1109/JSEN.2017.2682929

Yawalkar, A.A., Pangarkar, V.G., Beenackers, A.A.C.M., 2002. Gas hold-up in stirred tank reactors. The Canadian Journal of Chemical Engineering 80, 158–166.

Ye, J., Wang, H., Yang, W., 2014. Characterization of Electrical Capacitance Tomography sensors with different diameter. IEEE Sensors J. 14, 2240–2251. https://doi.org/10.1109/JSEN.2014.2307572

Yenjaichon, W., Pageau, G., Bhole, M., Bennington, C.P.J., Grace, J.R., 2011. Assessment of mixing quality for an industrial pulp mixer using Electrical Resistance Tomography. Can. J. Chem. Eng. 89, 996–1004. https://doi.org/10.1002/cjce.20502

York, T., 2001. Status of electrical tomography in industrial applications. J. Electron. Imaging 10, 608–619. https://doi.org/10.1117/1.1377308

Yorkey, T.J., Webster, J.G., Tompkins, W.J., 1987. Comparing Reconstruction Algorithms for Electrical Impedance Tomography. IEEE Transactions on Biomedical Engineering BME-34, 843–852. https://doi.org/10.1109/TBME.1987.326032

Young, I.T., Gerbramds, J.J., van Vliet, L.J., 2009. Fundamentals of Image Processing, in: Video, Speech and Audio Signal Processing and Associated Standards. CRC Press.

Zainal-Mokhtar, K., Mohamad-Saleh, J., 2013. An Oil Fraction Neural Sensor Developed Using Electrical Capacitance Tomography Sensor Data. Sensors (Basel) 13, 11385–11406. https://doi.org/10.3390/s130911385

Zalc, J.M., Szalai, E.S., Alvarez, M.M., Muzzio, F.J., 2002. Using CFD to understand chaotic mixing in laminar stirred tanks. AIChE Journal 48, 2124–2134. https://doi.org/10.1002/aic.690481004

Zhang, J.L., Mao, M.X., Ye, J.M., Wang, H.G., Yang, W.Q., 2016. Investigation of wetting and drying process in a gas-solid fluidized bed by electrical capacitance tomography and pressure measurement. Powder Technol. 301, 1148–1158. https://doi.org/10.1016/j.powtec.2016.07.069

Zhang, L., Liu, Q., Yang, W., Wei, N., Dong, D., 2013. An Improved K-nearest Neighbor Model for Short-term Traffic Flow Prediction. Procedia - Social and Behavioral Sciences, Intelligent and Integrated Sustainable Multimodal Transportation Systems Proceedings from the 13th COTA International Conference of Transportation Professionals (CICTP2013) 96, 653–662. https://doi.org/10.1016/j.sbspro.2013.08.076

Zhang, M., Soleimani, M., 2015. Imaging floating metals and dielectric objects using electrical capacitance tomography. Measurement 74. https://doi.org/10.1016/j.measurement.2015.07.009

Zhao, W., Buffo, A., Alopaeus, V., Han, B., Louhi-Kultanen, M., 2017. Application of the compartmental model to the gas-liquid precipitation of CO2-Ca(OH)(2) aqueous system in a stirred tank. AICHE J. 63, 378–386. https://doi.org/10.1002/aic.15567

Zhao, W., Han, B., Jakobsson, K., Louhi-Kultanen, M., Alopaeus, V., 2016. Mathematical model of precipitation of magnesium carbonate with carbon dioxide from the magnesium hydroxide slurry. Comput. Chem. Eng. 87, 180–189. https://doi.org/10.1016/j.compchemeng.2016.01.013

Zhou, Y.C., Yu, A.B., Stewart, R.L., Bridgwater, J., 2004. Microdynamic analysis of the particle flow in a cylindrical bladed mixer. Chemical Engineering Science 6, 1343–1364. https://doi.org/10.1016/j.ces.2003.12.023

Zhu, K., Madhusudana Rao, S., Wang, C.-H., Sundaresan, S., 2003. Electrical capacitance tomography measurements on vertical and inclined pneumatic conveying of granular solids. Chemical Engineering Science 58, 4225–4245. https://doi.org/10.1016/S0009-2509(03)00306-3

Zwietering, T., 1958. Suspending of Solid Particles in Liquid by Agitators. Chem. Eng. Sci. 8, 244–253. https://doi.org/10.1016/0009-2509(58)85031-9

3DX-RAY ltd., 2017a. 3D X-ray specification.

3DX-RAY ltd., 2017b. MDXi datasheet.

Appendix A – Chapter 4 supporting information

Chapter number of relevant chapter in thesis: 4

Page numbers of relevant chapter: 99-118

In this appendix, more images of the conducted experiments in chapter 4 are reported for
visualization.
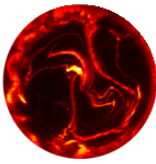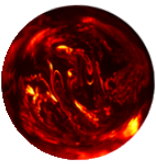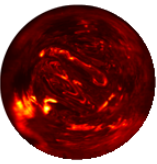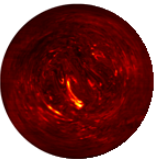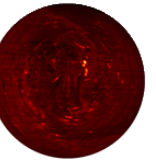
**Figure A.1 - Full size (a-e) and downscaled (f-l) PLIF images at different superficial velocities for
experiment I (Extension of Figure 4.2 of the manuscript).**

Figure A.2 - Full size PLIF (a-e) and ERT (f-l) images at different superficial velocities for experiment I. (Extension of Figure 4.4 of the manuscript).
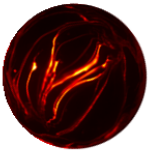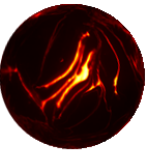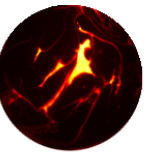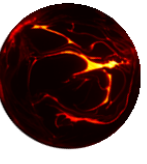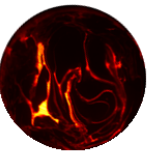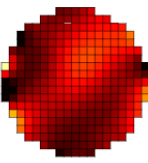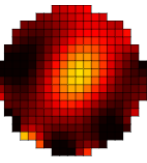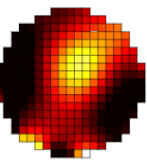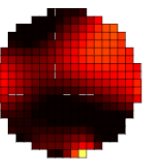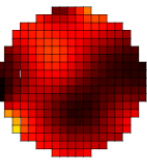
	$u_S = 0.20$ m s^{-1}	$u_S = 0.27$ m s^{-1}	$u_S = 0.34$ m s^{-1}	$u_S = 0.40$ m s^{-1}	$u_S = 0.47$ m s^{-1}
PLIF image	(a)	(b)	(c)	(d)	(e)
ERT image	(f)	(g)	(h)	(i)	(l)
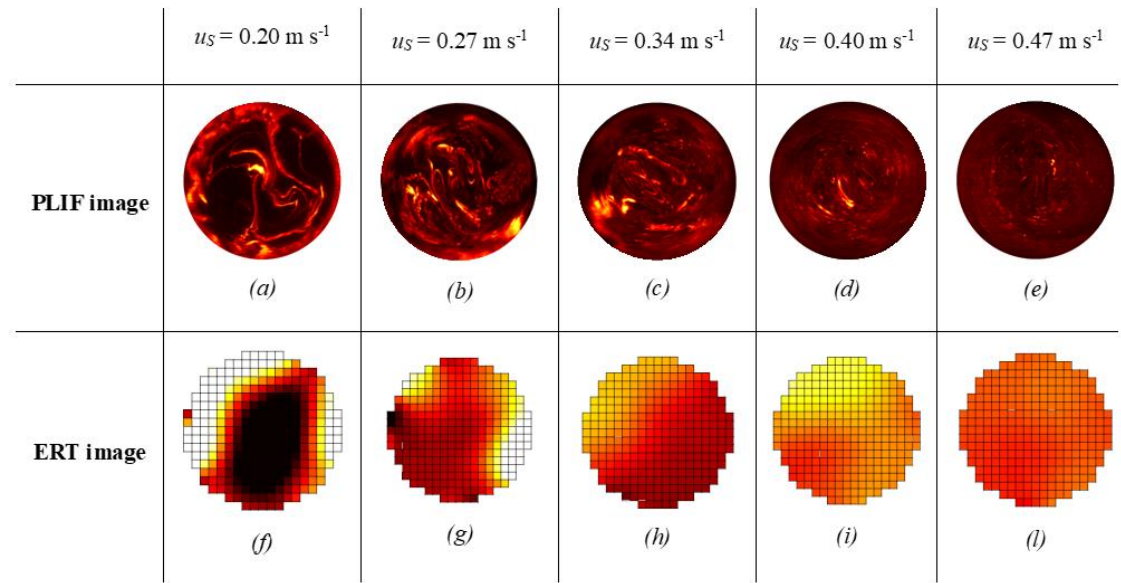
Figure A.3 - Full size PLIF (a-e) and ERT (f-l) images at different superficial velocities for experiment II. (Extension of Figure 4.6 of the manuscript).

	$u_S = 0.20$ m s^{-1}	$u_S = 0.27$ m s^{-1}	$u_S = 0.34$ m s^{-1}	$u_S = 0.40$ m s^{-1}	$u_S = 0.47$ ms^{-1}s
PLIF image	(a)	(b)	(c)	(d)	(e)
ERT image	(f)	(g)	(h)	(i)	(l)

Figure A.4 - Full size PLIF (a-e) and ERT (f-l) images at different superficial velocities for experiment III. (Extension of Figure 8 of the manuscript).

Appendix B – Towards 3D-Electrical Capacitance Tomography for interface detection (Clark et al., 2016a)
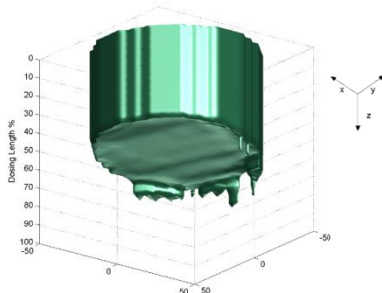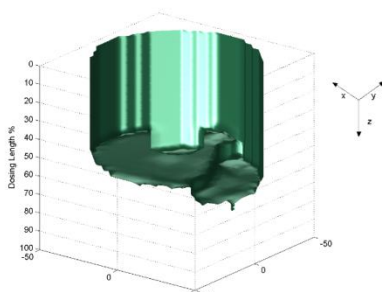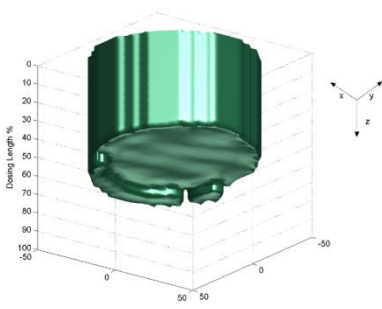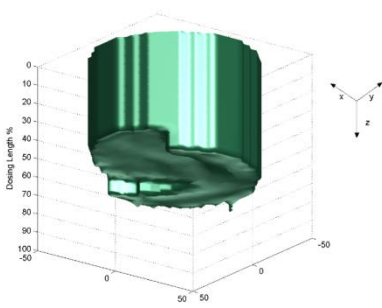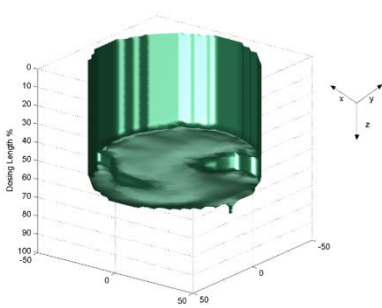
Appendix C – ECT - X-ray comparison
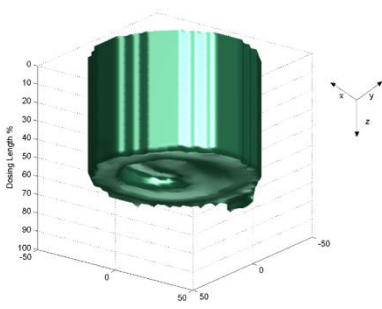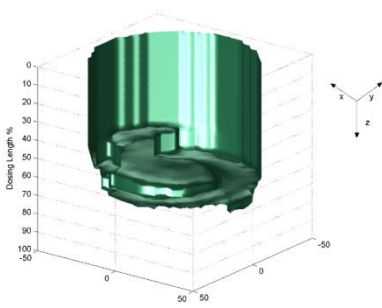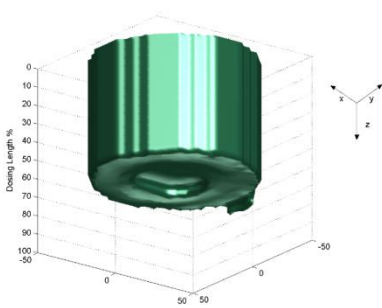
Chapter number of relevant chapter in thesis: 7
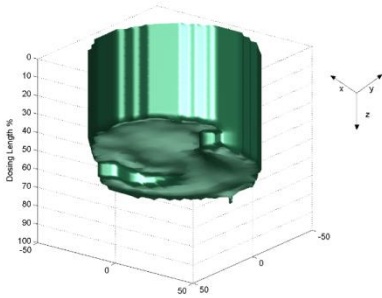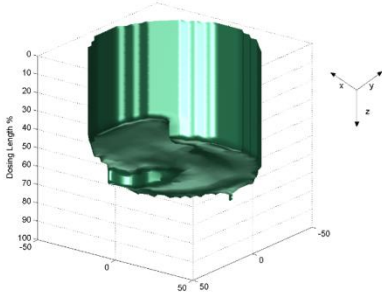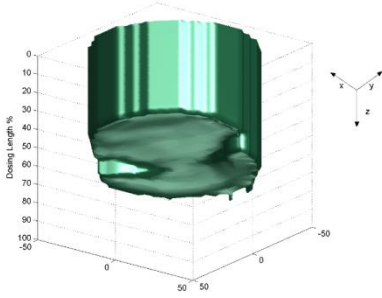
Page numbers of relevant chapter: 199-259
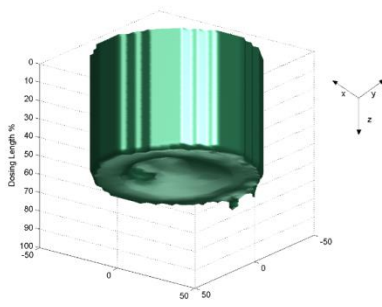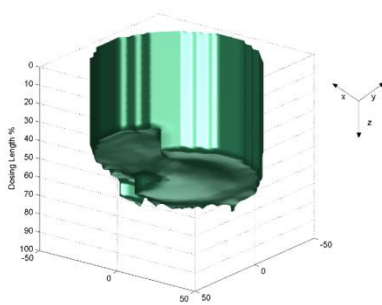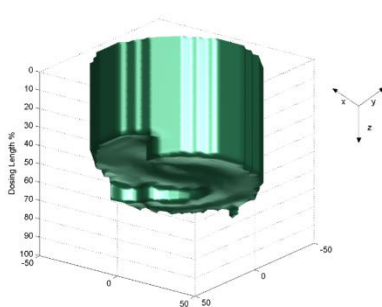
C.1 Flow-Through monoliths
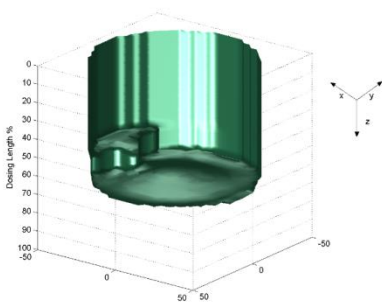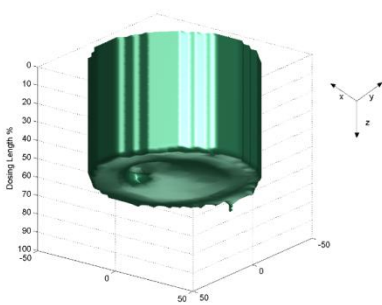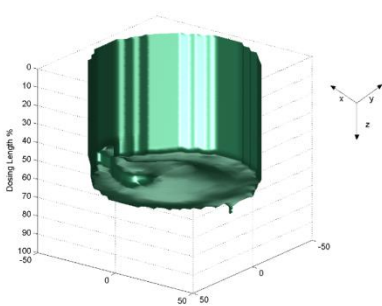
Item nr.	X-Ray		ECT	
	Image	Dosing (%)	3D image	Dosing (%)
1		62.6		57.7
2		64.2		62.8
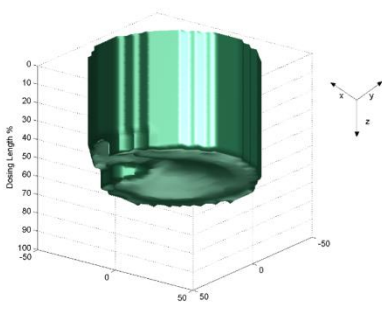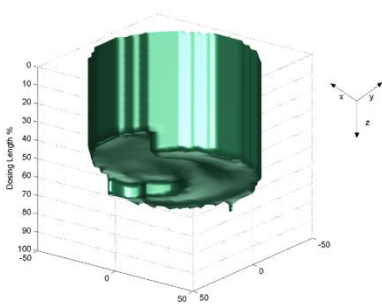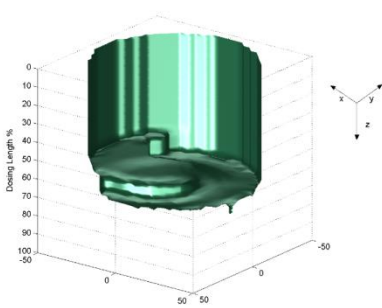
Item nr.	X-Ray		ECT	
	Image	Dosing (%)	3D image	Dosing (%)
3		63.4		59.5
4		64.4		61.8
5		63.2		61.6
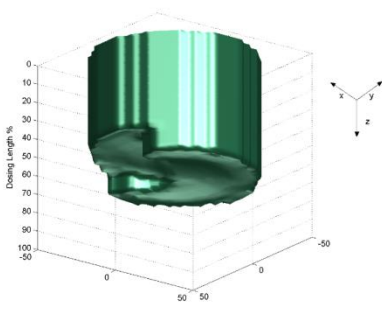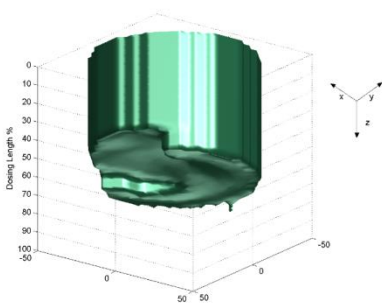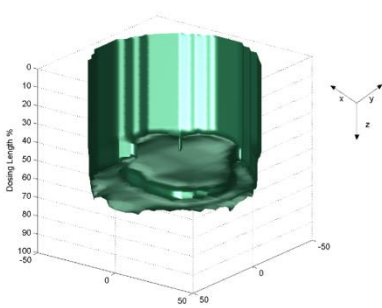
Item nr.	X-Ray		ECT	
	Image	Dosing (%)	3D image	Dosing (%)
6		64.2		64.5
7		63.1		61.8
8		63.1		65.2
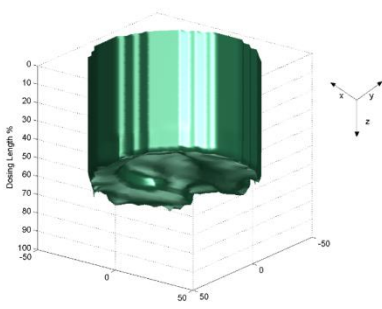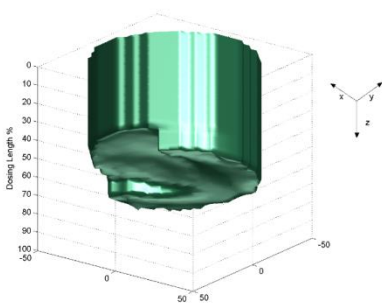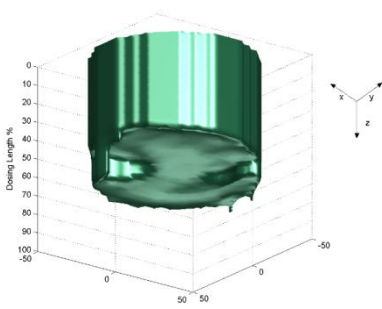
Item nr.	X-Ray		ECT	
	Image	Dosing (%)	3D image	Dosing (%)
9		63.7		61.1
10		63.3		61.1
11		63.0		61.0
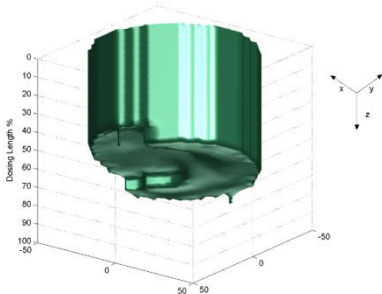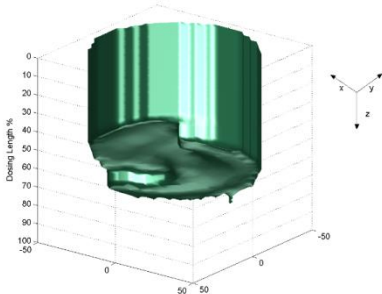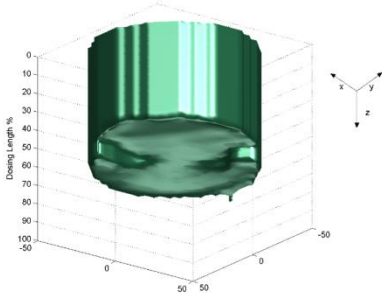
Item nr.	X-Ray		ECT	
	Image	Dosing (%)	3D image	Dosing (%)
12		63.9		59.8
13		64.6		65.3
14		63.9		61.5
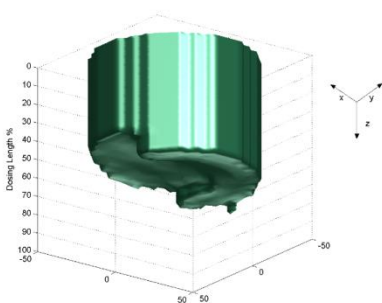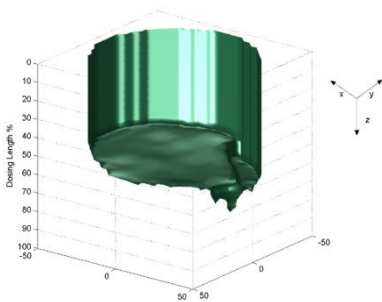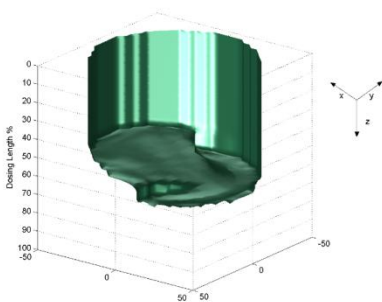
Item nr.	X-Ray		ECT	
	Image	Dosing (%)	3D image	Dosing (%)
15		64.6		61.3
16		64.8		64.4
17		64.0		65.2
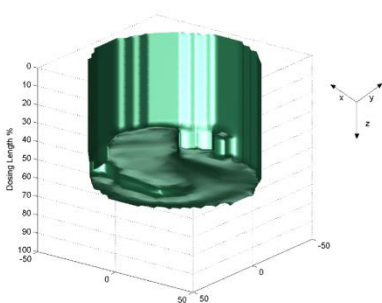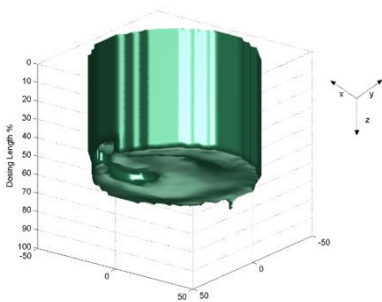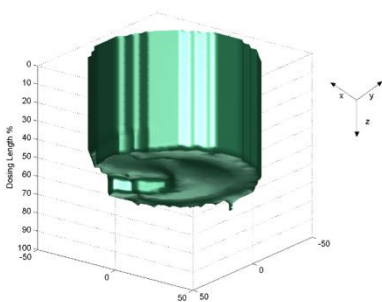
Item nr.	X-Ray		ECT	
	Image	Dosing (%)	3D image	Dosing (%)
18		64.2		63.9
19		63.3		63.2
20		63.0		62.0
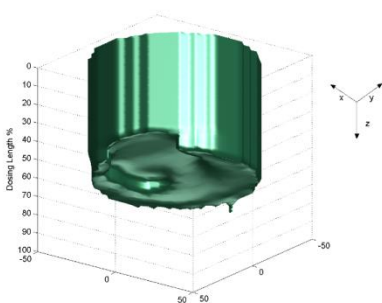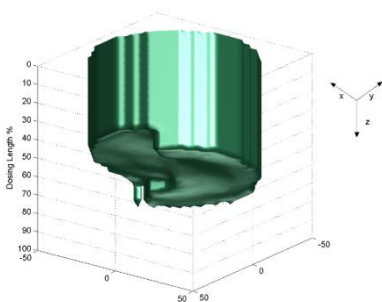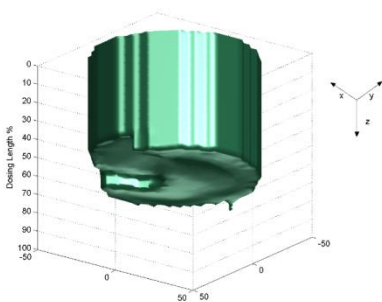
Item nr.	X-Ray		ECT	
	Image	**Dosing (%)**	**3D image**	**Dosing (%)**
21		64.1		62.3
22		63.1		61.7
23		62.8		61.8
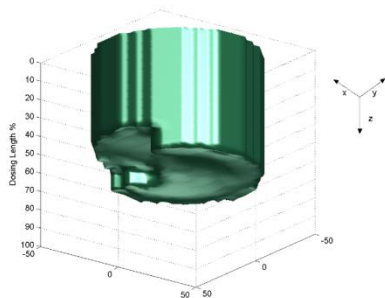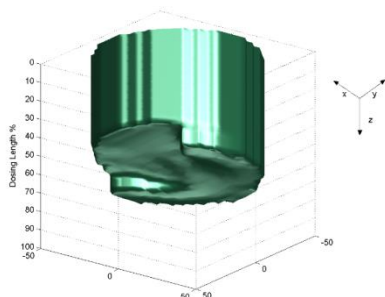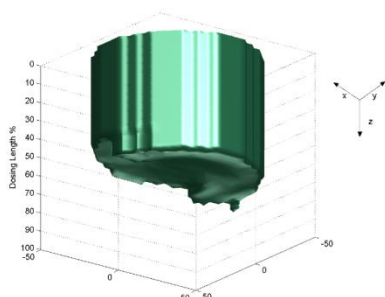
Item nr.	X-Ray		ECT	
	Image	Dosing (%)	3D image	Dosing (%)
24		64.1		63.6
25		63.1		61.2
26		64.6		60.4
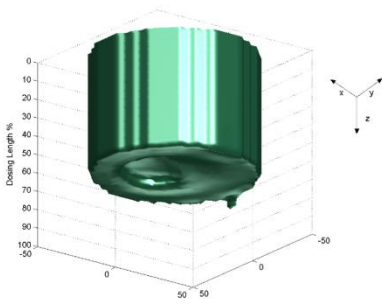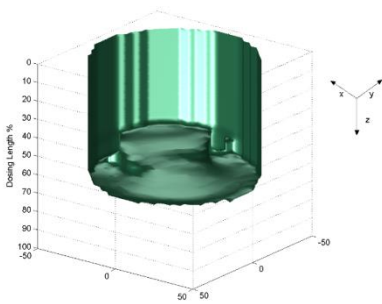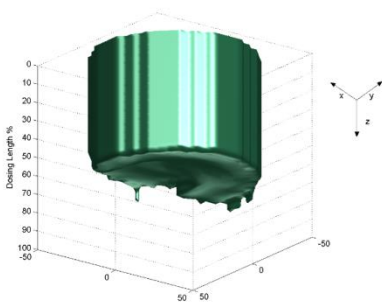
Item nr.	X-Ray		ECT	
	Image	Dosing (%)	3D image	Dosing (%)
27		63.3		61.5
28		63.0		61.5
29		63.0		60.8
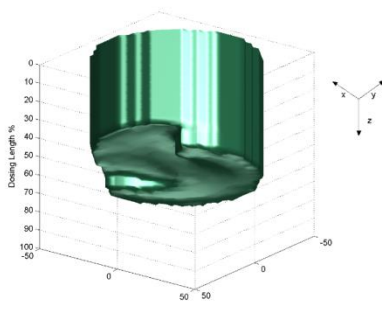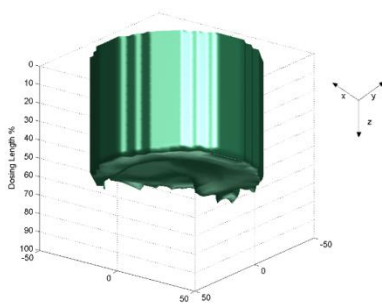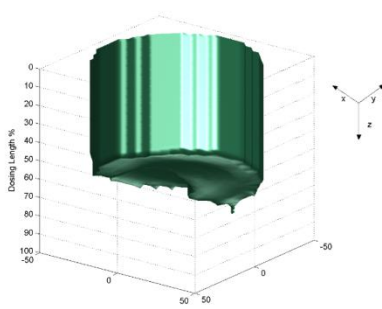
Item nr.	X-Ray		ECT	
	Image	Dosing (%)	3D image	Dosing (%)
30		64.1		60.6
31		62.6		58.7
32		64.8		59.3

298
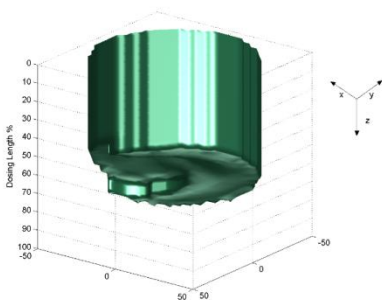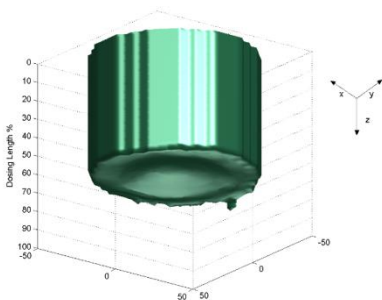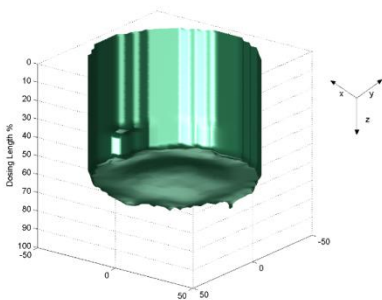
Item nr.	X-Ray		ECT	
	Image	Dosing (%)	3D image	Dosing (%)
33		64.6		62.3
34		63.7		63.6
35		65.0		62.7
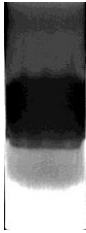
Item nr.	X-Ray		ECT	
	Image	Dosing (%)	3D image	Dosing (%)
36		63.7		62.3
37		63.5		60.9
38		64.8		62.7

Item nr.	X-Ray		ECT	
	Image	Dosing (%)	3D image	Dosing (%)
39		64.8		62.4
40		63.0		61.1
41		64.4		60.8
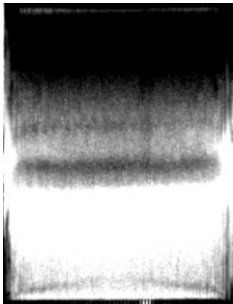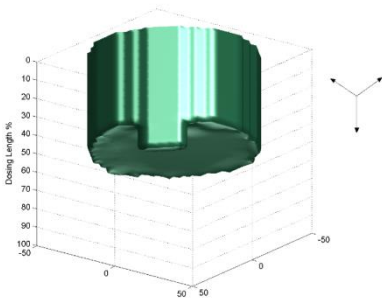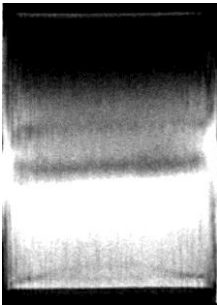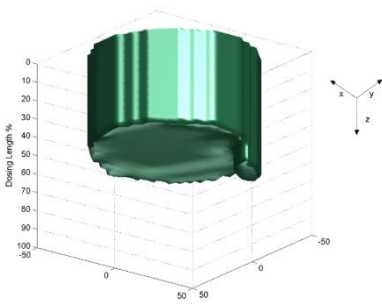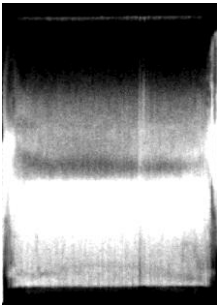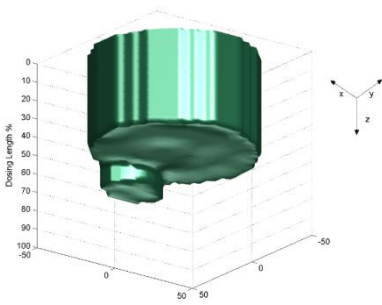
Item nr.	X-Ray		ECT	
	Image	Dosing (%)	3D image	Dosing (%)
42		64.2		64.5
43		63.5		62.6
44		64.2		62.7
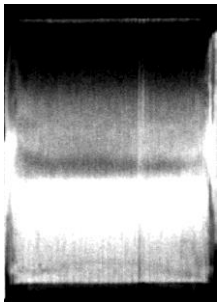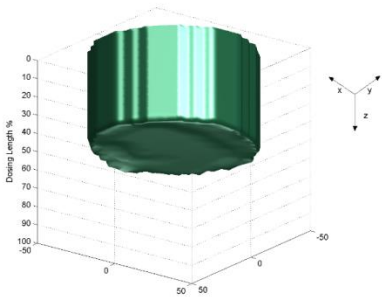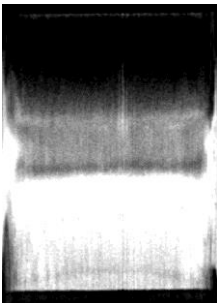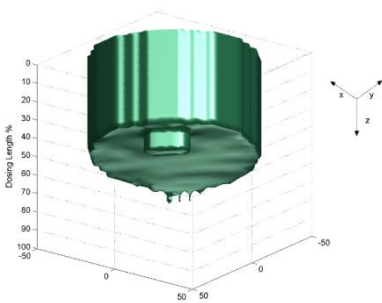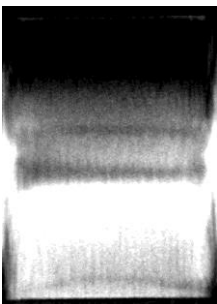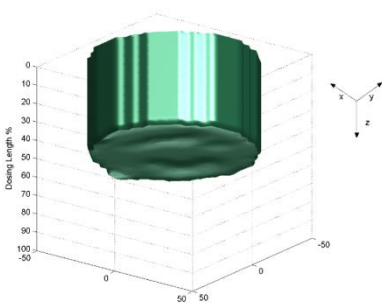
Item nr.	X-Ray		ECT	
	Image	Dosing (%)	3D image	Dosing (%)
45		63.5		61.5
46		63.2		62.6
47		63.7		62.6
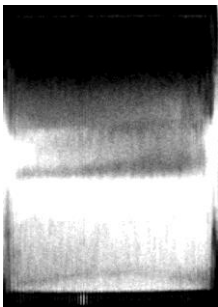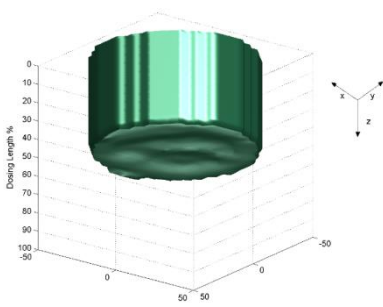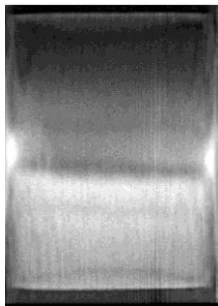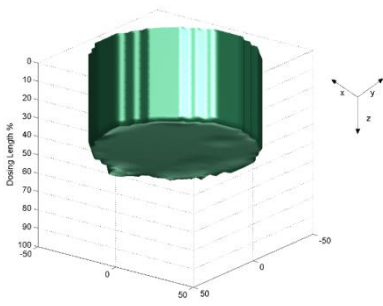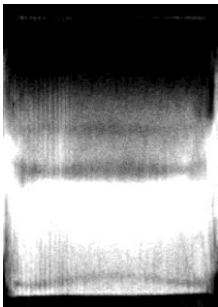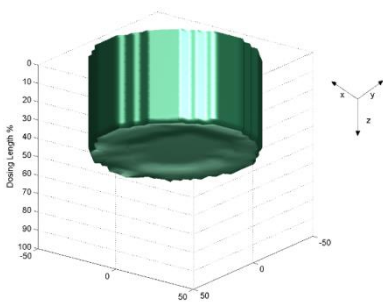
Item nr.	X-Ray		ECT	
	Image	Dosing (%)	3D image	Dosing (%)
48		63.7		61.8
49		66.4		65.5
50		66.6		65.9
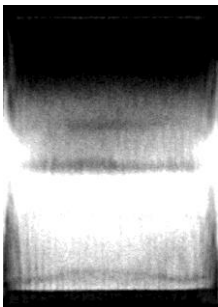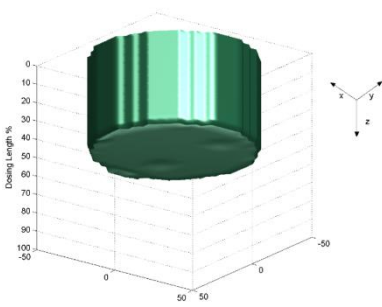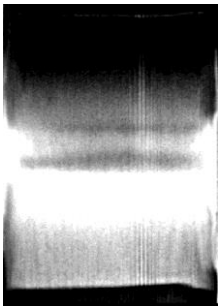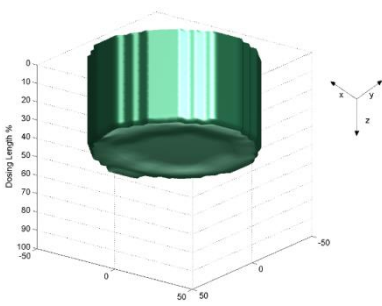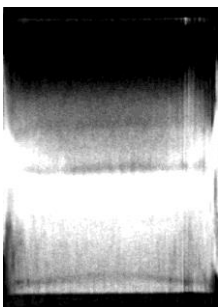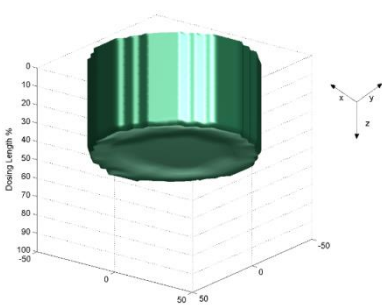
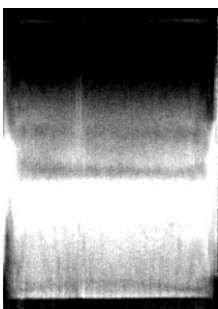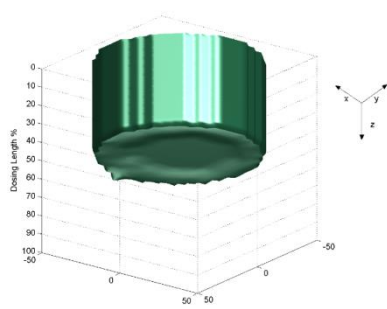| Item nr.	X-Ray		ECT	
	Image	Dosing (%)	3D image	Dosing (%)
-			X-ray image of part used as high permittivity reference.	
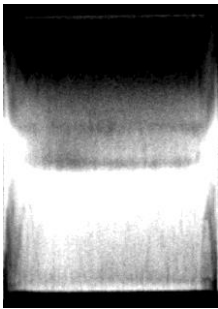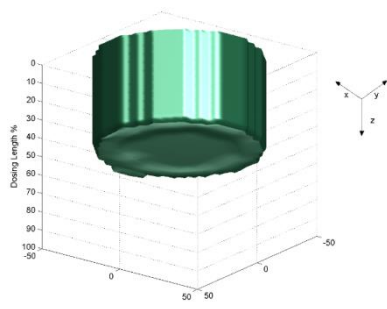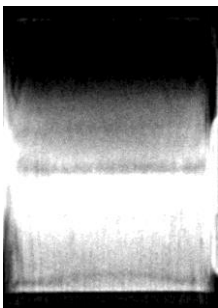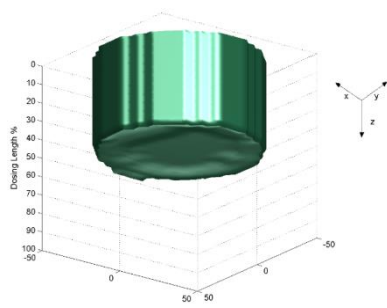
C.2 Gasoline Particulate Filters
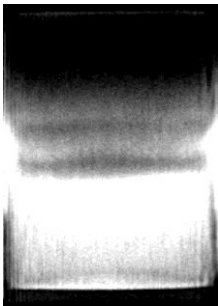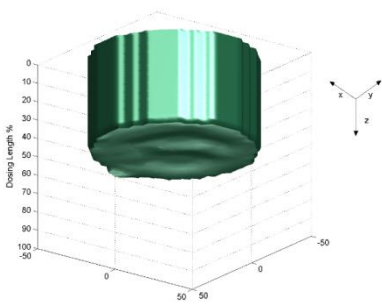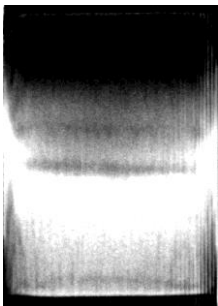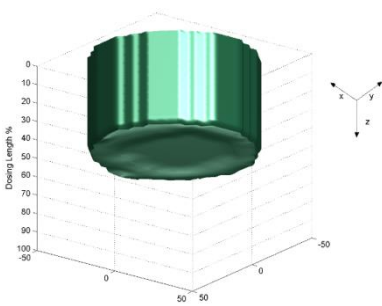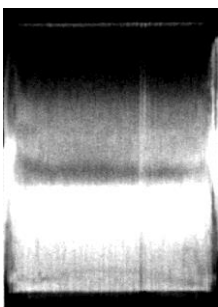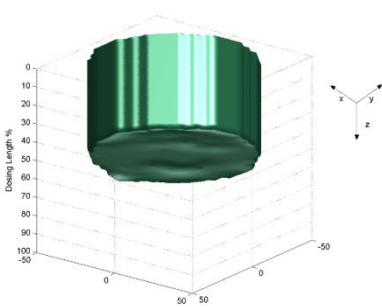
Item nr.	X-Ray		ECT	
	Image	**Dosing (%)**	**3D image**	**Dosing (%)**
1		58.3		53.3
2		56.3		53.3
3		56.5		54.3

Item nr.	X-Ray		ECT	
	Image	**Dosing (%)**	**3D image**	**Dosing (%)**
4		56.8		52.3
5		54		54.7
6		57		51.6

Item nr.	X-Ray		ECT	
	Image	Dosing (%)	3D image	Dosing (%)
7		54.8		51.2
8		55.2		52.0
9		57		51.2

Item nr.	X-Ray		ECT	
	Image	**Dosing (%)**	**3D image**	**Dosing (%)**
10		53.5		51.5
11		53.5		51.0
12		53.6		50.9

Item nr.	X-Ray		ECT	
	Image	Dosing (%)	3D image	Dosing (%)
13		53		50.9
14		54		51.1
15		55.6		51.0

Item nr.	X-Ray		ECT	
	Image	Dosing (%)	3D image	Dosing (%)
16		55.8		51.3
17		54.5		50.9
18		53.3		51.7